BORON ACTIVATION AND DIFFUSION IN SILICON FOR VARYING INITIAL PROCESS CONDITIONS DURING FLASH-ASSIST RAPID THERMAL ANNEALING

By

RENATA A. CAMILLO-CASTILLO

A DISSERTATION PRESENTED TO THE GRADUATE SCHOOL
OF THE UNIVERSITY OF FLORIDA IN PARTIAL FULFILLMENT
OF THE REQUIREMENTS FOR THE DEGREE OF
DOCTOR OF PHILOSOPHY

UNIVERSITY OF FLORIDA

2006

To my son and his father – who will always mean more to me than they will ever know.

ACKNOWLEDGMENTS

You never think that this day will come, when you finally get to acknowledge the people that helped you get through it all. But it has. Before I go any further, however, I would like to say that the individuals I will mention are a small subset of a larger group of people who assisted me in my endeavors throughout my lifetime. The brevity of this chapter does not allow me to make mention of each individual, but I would like to take the opportunity to thank each of them; they know who they are. At this point I think that it is necessary to express my gratitude to my committee members, which include Dr. Cammy Abernathy, Dr. Paul Holloway and Dr. Robert Fox for serving in this capacity during the last few years.

My advisors Drs. Mark E. Law and Kevin S. Jones managed to create a diverse research environment which encouraged independent thinking, while simultaneously providing the guidance and support required for their students to succeed. In addition, they made a concerted effort to ensure that it was fun. This setting coupled with the easy going nature of these individuals was ideal for my progress. I could not have asked for better advisors or for a better graduate experience. Weekly meetings with Dr. Law were very relaxed, which allowed me to share my ideas with him quite easily, knowing that they would be met with respect, no matter how ludicrous they were. I also very much appreciated his open door policy; towards the end of my tenure this proved to be quite useful, since my weekly meetings turned into daily meetings for which he was always

available. These were also opportunities for him to update me on how well, or badly the Trinidad and Tobago football (soccer) team was doing. Thanks Dr. Law!

One of the advantages of being a member of the SWAMP center is the fact that you have access to both Dr. Law and Dr. Jones, and therefore their respective areas of expertise. Dr. Jones was always willing to assist and I never hesitated to get his input in every aspect of my research. The first experiment which I performed at the SWAMP Center was designed in consultation with Dr. Jones and formed the basis of this dissertation. Had it not been for that, this document would not have existed. I appreciated the time that he took to review and discuss my research and personal issues with me and for this I want to say thanks.

The numerous members of the SWAMP center were also responsible for helping to create the research setting and making my stay enjoyable. My first encounters with SWAMPies were the 'BOs" – Ibo (Ibrahim) Avci and Ljubo Radic, who were willing to answer the million questions that I hurled their way about FLOOPS. Then there was Mark Clark, Antonio 'Tony' Saavedra, Chad Linfors, Eric Kuryliw and Dena Wrigley who willingly trained me in TEM sample preparation, how to run Hall measurements, use the Four Point Probe and use the Ellipsometer. Robert Crosby never failed to reminder me about how I loved to 'wasted my time', while Danny Zeenberg ensured that I didn't waste any more time lapping TEM samples, by volunteering to etch my samples for me when it was not physically possible. The members of the SWAMP center that came after me have been very supportive these last two years, in particular Michelle Phen, Diane Hickey and Heather Randell. Thanks guys for everything!

Apart from my colleagues in school, there were others in the Gainesville community who made this experience a much more pleasant one. Jeanne and Jose Diaz opened up their home to me and have been a constant form of support for the entire time I lived in Gainesville. Without their friendship, advice, reminders, food supplies, and most recently baby-sitting – I would not have gotten through any of this as well as I did. They are my family in Gainesville. Thank you guys – including Jordan, Kieran and Gavin - I will never forget you and what you have done for us. Vanessa Harris-Mohajer, and Shirin and Negin Ahadi were my first friends in Gainesville – thanks for the good times, giving me rides, waking up at 5.30am to let me in after long hours at school, feeding me. I will always value your friendship. Finally I would like to thank the Baha'i community of Gainesville and Greater Gainesville, for their loving support, guidance and the opportunities for growth which they have provided over the last few years. I have established many personal relationships with families in the Baha'i community, which I cherish dearly.

Jessica Sawka, ended up living in Gainesville, at a time when I needed assistance desperately. She unselfishly took on the task of taking care of my son and all his needs, so that I could complete the task of writing this document which lay ahead of me. She gave me the sense of security that I needed concerning him, so that I could totally immerse myself in my work at the time when it was most necessary. To her I will be eternally grateful. Thanks Jess for being you.

I have been fortunate to have had the most supportive family. My parents, Frederick and Norma Camillo-Castillo, in particular have always been a source of encouragement and support. They worked extremely hard to provide my siblings and me

with the opportunities they themselves did not have and succeeded in doing that. I would like to sincerely thank them for everything that they did right – their examples of hard work, which they instilled in all of us; their devotion to their children; the balance between work and family they were able to achieve; the valuable lesson that moderation in all things is key; provided us with a unique family experience that not many people are privileged to have. Apart from which their individual qualities such as my father's humility, his willingness to help anyone and his selflessness, served as remarkable examples of the qualities we should strive to attain in our own selves. We could not have had better parents, without them none of us would have been able to achieve the things we have.

My twin sister, Natasha shared every experience with me for the first eighteen years of our lives, without her I probably would not have gotten through any of it. We had the advantage of always of having each other there on first day of school, when we knew no one else. It was really nice to always have her to study with, to encourage me to stay up that one more night burning the midnight oil and to make that cup of coffee and place it strategically on the bed in the hope that I would wake up and get to work. I remember her saying "You will regret it if you don't get up and study", and sure enough I did regret it, when I didn't. She was my biggest source of encouragement in primary and secondary school and continued to be in the years that followed. She has been there for me in all my endeavors and has been supportive in every possible way. I will forever be indebted to her. Thanks Tash for being the best sister. My younger sister, Melissa cannot go unmentioned since she has also been very supportive from the onset. To her I would like to say thanks.

I have looked forward to this day from the first day I met my mentor, Dr. Hamid Farabi. He embodied all the characteristics of the person that I wanted to become; an individual with things in perspective, someone who always gave of his best and expected nothing in return, humble despite his many achievements, to name a few. His personal traits combined with his passion for chemical engineering enkindled in me a desire to achieve more academically and set me on this path in the years which followed our encounter. I probably would not have chosen this course had I not met him; and to him I will be eternally grateful for this and the countless hours he spent guiding, encouraging and supporting me. He has made more of an impact on my life than he will ever know.

Finally, I would like to express thanks to my son, Naysan Victor for being the source of my motivation for completing this work and writing this manuscript. His very nature provided me with the greatest rewards, which I know I will continue to receive throughout my lifetime.

TABLE OF CONTENTS

LIST OF TABLES

LIST OF FIGURES

Abstract of Dissertation Presented to the Graduate School
of the University of Florida in Partial Fulfillment of the
Requirements for the Degree of Doctor of Philosophy

BORON ACTIVATION AND DIFFUSION IN SILICON FOR VARYING INITIAL PROCESS CONDITIONS DURING FLASH-ASSIST RAPID THERMAL ANNEALING

By

Renata A. Camillo-Castillo

May 2006

Chair: Kevin S. Jones
Cochair: Mark E. Law
Major Department: Materials Science and Engineering

Flash-assist Rapid Thermal Processing offers thermal budgets more than three orders of magnitude less than conventional annealing technologies. It therefore presents an opportunity for the continued scaling of complementary metal-oxide-semiconductor (CMOS) technologies, which demand highly doped, ultra shallow junctions for its source/drain extensions. These low thermal budgets are expected to limit dopant diffusion, while the extremely rapid ramp rates enable the attainment of anneal temperatures which were previously not possible. It is the goal of this work to gain a better understanding of the underlying mechanisms which are responsible for the dopant activation and diffusion in silicon material processed by Flash-assist Rapid Thermal Processing.

The extremely fast ramp rates, on the order of $1x10^6$ $^oCs^{-1}$ and short processing times, which are typically less than 1 millisecond, offered by the Flash-assist Rapid

Thermal Process, have enabled investigations into the early stages of the extended defect evolution. These studies of the End of Range defects associated with amorphous layers have revealed the existence of a highly unstable silicon interstitial defect structure, which was found to follow one of two evolutionary paths: evolution into the {311}-type defect or dissolution via the loss of interstitials. The silicon interstitial loss from this defect configuration was shown to be related to the anneal temperature through an Arrhenius relation, with an activation energy of 2.1eV, which differs from previously reported values of known defect structures.

The work herein also clearly established that higher boron activation levels can be achieved subsequent to amorphous layer re-crystallization, for sufficiently high anneal temperatures. This was determined to be a direct consequence of increased diffusion in the tail of the boron profile and activation in the profile peak. At such anneal temperatures the peak active boron concentration was independent of the amorphous layer re-crystallization temperature. The increase in active boron concentration subsequent to the re-crystallization process was also shown to be much larger than the reactivation of boron from the well researched boron interstitial cluster configuration. This fact strongly suggests the existence of boron in an alternative less stable configuration from which additional activation, subsequent to the re-crystallization process is possible.

CHAPTER 1
MOTIVATION

The remarkable changes that the semi-conductor industry has seen over the last forty years have been a direct consequence of a trend which was put forth by Gordon Moore in 1965 [MOO65], and which continues to drive the semiconductor industry today. Moore postulated that the number of transistors on a semiconductor integrated circuit (IC) would double every year, as illustrated in Figure 1-1. The semiconductor industry has endeavored to fulfill Moore's predictions and in so doing have managed to double the number of transistors on the IC every 18 to 24 months. The continued miniaturization of the devices on the IC is required if the industry is to carry on this trend.

1.1 Scaling the MOSFET

The metal-oxide-semiconductor field-effect transistor or MOSFET is the basic building block of electronic devices (Figure 1-2). Reducing the feature size of the MOSFET to fit more in the same planar area is termed scaling [CLA04].The demand for more computing power is one of the main motivations for reducing size of the transistor, because it allows for a faster switching of the device. Scaling the transistor is also economically driven, since a higher yield ultimately reduces the cost of production for each individual transistor. Additionally, the increased demand for more integrated functions necessitates an increase in the number of devices on the IC. Scaling however calls for higher doping levels, ultra-shallow electrical junctions and narrower gate lengths, which induce effects that are deleterious to device operation.

1.1.1 Short Channel Effects (SCE)

An increase in MOSFET speed is accomplished by reducing the channel length, L allowing for faster switching of the transistor. However for the device to operate in the same way, reducing the channel length demands scale-down of the all doped regions by the same factor. This ensures that the electric field patterns are maintained and assumes that the operating voltages are also scaled proportionally [PLU00]. Vertical and lateral scaling have severe operational repercussions; collectively known as Short Channel Effects (SCE). One issue is the interaction of the depletion regions that exist in the immediate vicinity of the source and drain. As the lateral dimensions are reduced, the two dimensional spreading of the electric field from the drain can attract carriers from the source, resulting in the flow of current when the device is turned off, known as the *off-current*. Hence there is current flow for a gate voltage, V_G which is smaller than the threshold voltage, V_{TH} leaving the V_G with limited control of the device. The change in off-current with drain voltage is known as Drain-Induced Barrier Lowering (DIBL).

In order to curb SCE and tailor threshold voltage, a number of different ion implantation steps are necessary. One such option is the HALO or Punchthrough Stop implant [ZIE00]. This implant places dopant just below the active channel adjacent to the source/drain (S/D) regions and serves to minimize the depletion width spread in these areas. The source/drain extension implants are also employed; they provide a concentration gradient from the deep/source drain to the conducting channel in order to reduce the maximum electric field. Furthermore a threshold voltage adjust channel implant is also used to modify threshold voltage for the NMOS and PMOS devices. Although implementation of these implants have been somewhat successful, aggressive scaling of the S/D extension and S/D junction depths is necessary to minimize SCE.

1.1.2 Other Issues with Scaling

Parasitic resistances limit the resistance in the channel and therefore the maximum possible drive current in the channel. These parasitic resistances include the series sum of the silicide contact resistance R_{cs}, the deep drain resistance R_{dd}, the drain extension resistance R_{de}, and the drain extension-to-gate overlap resistance R_{ov}, as illustrated in Figure 1-2 [PLU00]. Hence increasing the concentration of electrically active dopants in the junction can reduce resistance of the drain extension, which enables higher drive currents. Incorporation of high concentrations of active dopant in the drain extension and simultaneous scale-down are inversely related. This can be better understood by considering that the sheet resistance of a layer is inversely proportional to the junction depth. It should be noted that the drain extension referred to above collectively refers to the source and drain regions which are physically identical.

Power consumption is another constraint placed on the device. Leakage currents and DIBL have tremendous impact on the power consumption and dissipation in MOS devices. Correspondingly reductions in leakage as well as off-currents will assist in offsetting these issues.

1.2 CMOS Processing

1.2.1 Current Processing Technologies

Ion implantation has been the dominant technique in the semiconductor industry for introducing dopant atoms into the silicon lattice for more than twenty years. The process offers a number of advantages, such as reproducibility and excellent dose control, which makes it extremely attractive from a manufacturing perspective. However, the non-conservative nature of the implantation technique results in the addition of a large concentration of extra atoms into the lattice [JON88]. Furthermore, there is an inherent

damage to the material due to the nuclear collisions between the incoming atoms and the primary and recoiled silicon atoms, such that Frenkel pairs are produced. The amount of damage incurred by the lattice can result in the transformation of the material from a crystalline to an amorphous phase. In silicon, this phase transformation is believed to occur when the threshold damage density is approximately 10 % of the silicon lattice density [CHR81]. The formation of a continuous surface amorphous layer prior to ion implantation of the dopant atoms is known to eliminate ion channeling of low mass species, which would otherwise travel deeper into the lattice thorough the interstices. Thus preamorphization [TU72, BRO69] is widely used in CMOS processing for ultra-shallow junction formation.

In order to repair the damage accumulated in the crystal structure during the implantation process, an annealing step is required. The thermal anneal effects solid phase epitaxial regrowth (SPER) of the amorphous layer by motion of the amorphous-crystalline interface [DRO82]. End of range (EOR) or Category II defects occur whenever an amorphous layer is formed during ion implantation and occur beyond the amorphous-crystalline interface in the damaged crystalline material [JON88]. These extended defects are detrimental to device performance, since they degrade carrier mobilities and increase junction leakages, so their annihilation is vital. A number of studies have focused on understanding the thermal evolutionary pathways for the EOR defects and it is now widely accepted that sub-microscopic interstitial clusters (SMICs) [BEN97, COF00, LIB98] are the precursors for the formation of {311}-type defects [EAG94, STO97, PAN97], which are metastable and eventually unfault to form dislocation loops [LIJ98]. The dislocation loops eventually dissolve. The silicon

interstitial super-saturation in the vicinity of the EOR defects is a function of the defect size and decreases as the EOR defects grow [BON97]. Additionally, the EOR defects have been shown to contribute to an anomalous diffusion of dopant atoms [ZHA95, STO97]. The phenomenon has been termed transient enhanced diffusion (TED) [ANG86, SER87, MIC87] and is illustrated in Figure 1-3. The tail of the implanted profile is shown to have diffused over 70nm, whereas the equilibrium diffusion length for these annealing conditions is only 2.5nm. An additional feature of TED is that the peak portion of the dopant profile above $1x10^{18}$/cm3 is not electrically activated and has remained immobile during annealing, despite the fact that the equilibrium solubility of B at 800 °C is higher than $1x10^{19}$/cm3, suggesting that the entire B profile should be soluble and mobile.TED is thought to be the result of the silicon interstitials coupling with substitutional boron atoms to form highly mobile pairs which diffuse rapidly throughout the silicon lattice. TED is therefore directly impacted by the silicon interstitial supersaturation, which is inversely proportional to the temperature. Thus at higher temperatures the TED is significantly less. This detail has led to the development of rapid thermal processing (RTP) tools, which have the capability of attaining high temperatures with fast ramp-up rates and switching times, in an effort to shield dopant profiles from TED. Higher anneal temperatures translate into increased dopant activation levels, lower silicon interstitial super-saturation levels and further evolution of the EOR damage. While fast ramp rates lessen the time spent in the low temperature regime, thus reducing the anomalous dopant diffusion. Although the reduced effective thermal budgets offered by RTP techniques have enabled the continued scaling of CMOS technology, TED is still an issue in the early stages of annealing during ramp-up to the desired anneal temperature. The junction

depth and junction abruptness achievable by RTP can no longer sustain the aggressive scaling needed to meet the requirements of the International Technology Roadmap for Semiconductors (ITRS) [SEM05]. Thus alternative annealing technologies are necessitated, which are capable of producing highly active junctions without significant dopant TED and which can appreciably evolve the EOR damage so that carrier mobility degradation and junction leakage are minimized. Flash annealing, Levitor annealing and Laser Thermal annealing are processing technologies that are being developed to meet drain extension scaling requirements. Figure 1-4 compares the thermal profiles of the various annealing techniques.

1.2.2 Flash-Assist Rapid Thermal Processing

Flash-assist RTP is a viable option for thermal annealing which enables annealing schemes in the millisecond regime at exceedingly high temperatures (~1350°C), by utilizing a water-wall arc lamp. In contrast to tungsten lamp heating technology used in the conventional RTA, a water-wall arc lamp provides the means for significantly reducing the heating-cycle time because of its ability to deliver higher power and because of its faster response time [CAM94]. The process entails heating the bulk of the wafer to an intermediate temperature prior to discharging capacitor banks into flash lamps. The ensuing pulse of radiation heats a thin slice on the top-side or device-side of the wafer. The lower effective thermal budget obtainable by Flash-assist RTP and the higher attainable anneal temperatures are attractive from a dopant diffusion and activation perspective.

Flash-assist RTP enables investigations into annealing time and temperature regimes which were not possible with conventional technologies such as Rapid Thermal Annealing (RTA). This provides a unique opportunity to explore the early stages of the

EOR damage evolution and also to investigate the kinetics with which the damage evolves during the high temperature portion of the temperature profile. There are also many unanswered questions regarding the material properties of the doped layer which dictate the final sheet resistance and those stages in the Flash-assist RTP which controls the dopant activation. Understanding these issues is critical to the achievement of highly active shallow layers and the better utilization of this tool.

1.3 Objectives and Statement of Thesis

The goal of this work is to gain an understanding of the stages in the anneal process which control the activation of dopant atoms in the preamorphized silicon. This is done by varying the initial implant condition of the wafer itself and altering the temperatures to which the wafer is initially subjected. It is also aim of this work to explore the early stages of the EOR defect evolution.

The research herein has provided the following scientific contributions

1. Existence of an End of Range extended defect in the silicon lattice preceding the formation of the {311}-type defect.
2. Kinetics of the dissolution of this End of Range defect
3. Evidence of the activation of boron located in high concentration regions of the Gaussian implanted profile, subsequent to the re-crystallization process.
4. Evidence of the existence of boron in an alternative, less stable configuration to the well researched Boron Interstitial Cluster, from which additional activation is achieved
5. Identification of the improvements in sheet resistance achieved by Flash-assist RTP as being due to increases in active concentrations and not to enhancements in mobility.
6. Evidence of the thermal stability of the junctions formed by Flash-assist RTP.

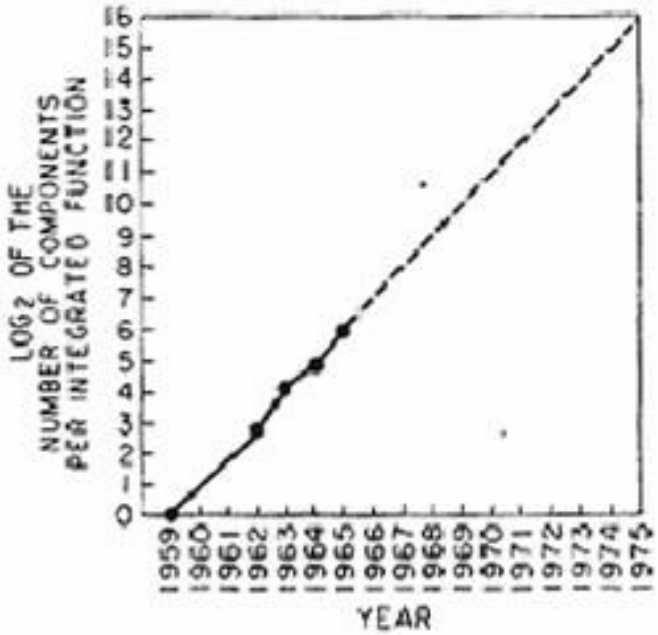

Figure 1-1. Moore's plot of the number of components per integrated function as a function of year [MOO65], which became the benchmark for the semiconductor industry.

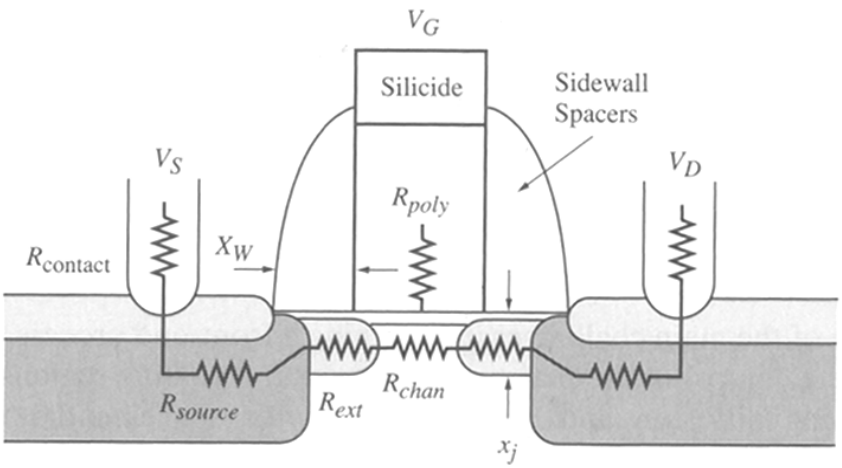

Figure 1-2. Schematic of the cross-section MOSFET, illustrating the parasitic resistances and the intrinsic channel resistance [PLU00].

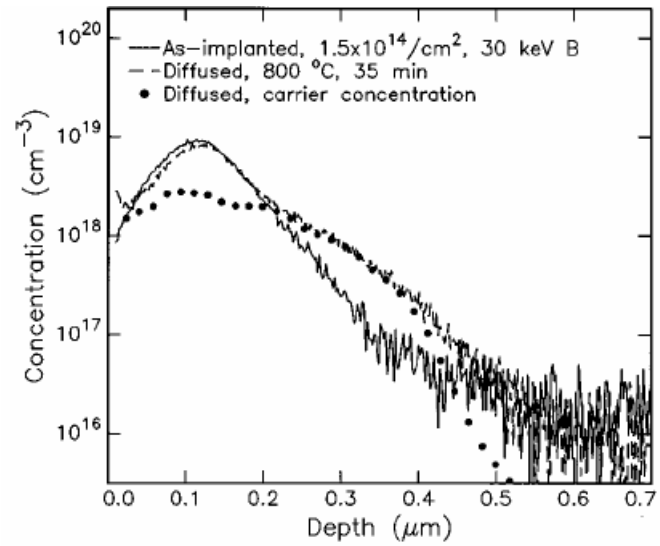

Figure 1-3. Secondary-ion-mass spectrometry (lines) and spreading resistance (solid circles) measurements of an implanted B profile ($1.5 \times 10^{14}/cm^2$, 30 keV ^{10}B) before and after transient enhanced diffusion at 800 °C for 35 min. [STO97]

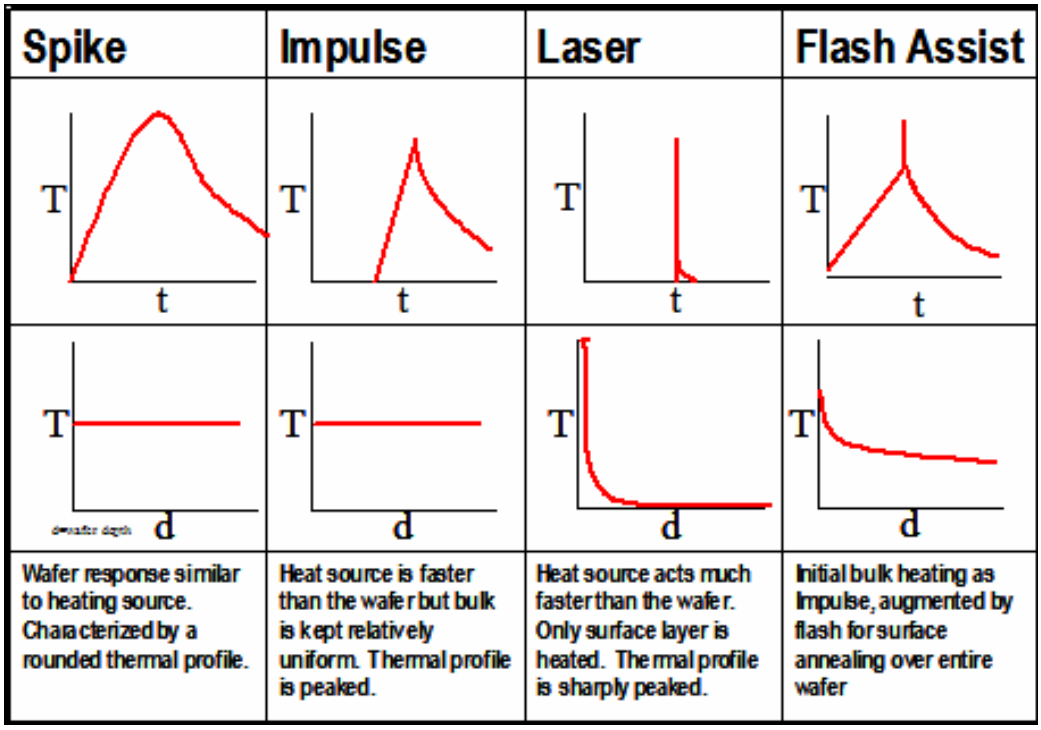

Figure 1-4. Comparison of the thermal profiles of annealing technologies being explored to facilitate the formation of drain extensions which meet the requirements of the International technology roadmap for semiconductors (ITRS).

CHAPTER 2
LITERATURE SURVEY

2.1 Ion Implantation Technology

Ion implantation has been the dominant technique for dopant atom introduction in silicon integrated circuit (IC) manufacture, for the last twenty years. The original patent for this technique was issued to William Shockley in 1954 [SHO03], but it was more than twenty years before it was integrated into the IC manufacturing process [PLU03]. The basic technique entails accelerating dopant ions to extremely high velocities via electric fields. These highly accelerated ions are impacted onto the surface of the material to be implanted, such that a damage cascade results as the atoms are displaced from their lattices positions on impact and subsequently interact with other atoms in structure. In semiconductors, such violent displacement processes cause the accumulation of radiation damage within the lattice [WIL84].

The success of the implantation technique lies largely in the fact that the process can be quantitatively described and predicted. It provides a controlled and precise means of introducing a specific number of atoms into the structure. The technique also meets the requirements of a good manufacturing process, in that it is uniform, reproducible and versatile [PLU00]. However the inherent radiation damage to the crystal is a major disadvantage to ion implantation.

2.1.1 Overview of Ion Implantation Technology

The ion implanter has five major components that include an ion source, an ion extractor, a mass analyzer, an acceleration tube and a target chamber, a schematic of

which is depicted in Figure 2-1. The source gas for the implantation process must be ionized so that acceleration can be achieved. This is accomplished by energetic electrons from a hot filament source or by a plasma discharge. The ions are then extracted by means of a voltage bias applied to a grid positioned immediately in front of the source. They subsequently undergo mass selection by applying a magnetic field perpendicular to direction to the ions, such that those ions which do not meet the required mass to charge ratio are deflected away from the resolving aperture. The mass analysis therefore relies on a balance of the applied magnetic force and the resultant centripetal force due to deflection. Hence the ensuing path is determined by equating the these relations as shown in Equation 2-1 in which m is the mass of the ion, v is the ion velocity, q is the charge on the ion, R is the radius of curvature and B is the magnetic field intensity. The ion velocity, ν is related to the extraction voltage, V_{ext} by the equation

$$\frac{mv^2}{R} = q.\vec{v}\vec{B} \tag{2-1}$$

$$v = \sqrt{\frac{2E}{m}} = \sqrt{\frac{2qV_{ext}}{m}} \tag{2-2}$$

For most situations the ions undergo a further acceleration in a small linear accelerator to the final implant energy. The ion path also undergoes a deflection away from the linear path prior to implantation, to trap any neutrals which may be present in the beam. These neutral atoms cannot be detected on implantation and therefore are not counted. This can have serious repercussions, for instance uncontrolled doping.

The two principle stopping mechanisms of the ion implantation process are elastic nuclear collisions of the primary ions and recoiled atoms with the lattice atoms of the substrate; and electronic stopping associated with the loss of inelastic energy arising from

electrostatic interactions among electrons in the outer shell of the transmitted ions and lattice atoms of the substrate. Figure 2-2 demonstrates these differences. The nuclear energy loss is due to momentum transfer from the incoming ion to the target atoms. This can occur by direct head-on collisions or by interaction of the ion with the electric field of the nucleus. In the latter case, the energy loss is a maximum at the closest distance of approach of the ion to the nucleus or the impact parameter. The ion looses kinetic energy is in accordance with the conservation of momentum. Hence the energy transfer provides the atomic-scale basis for the damage. In the case of silicon, 15eV of energy are required to displace a single atom from the lattice position. These nuclear interactions give rise to the scattering and deflection trajectories.

The nuclear energy loss is small at high energies and dominates at the end of range (EOR) when the ion has lost most of its energy. This can be explained by the reduced interaction of the ion with the scattering nucleus at high velocities. When the ion slows down there is more time for interaction and therefore more damage occurs. This process is responsible for the damage which will be discussed in this document. The nuclear collision process is a function of ion energy, E and can be modeled by Equation 2-3 in which Z_1 and m_1 are the ion and Z_2 and m_2 are the substrate atomic number and mass, respectively.

$$S_n(E) = 2.8\times10^{-15}.\frac{Z_1 Z_2}{\left(Z_1^{\frac{2}{3}} + Z_2^{\frac{2}{3}}\right)^{\frac{1}{2}}}.\frac{m_1}{(m_1+m_2)} eVcm^2 \qquad (2\text{-}3)$$

Electronic stopping in contrast to nuclear stopping is an inelastic process whereby energy loss occurs via a drag component due to polarization of the ion. Generally, this process is modeled by Equation 2-10 in which k is a function of the ion and the substrate.

$$S_e(E) = k\sqrt{E} \tag{2-4}$$

Hence the total energy losses incurred by the implanted ion as it travels through the lattice is the sum of both energy loss mechanisms and is given by Equation 2-5 where N is the atomic density of the material.

$$\frac{dE}{dx} = -N\left[S_n(E) + S_e(E)\right] \tag{2-5}$$

Since the energy loss mechanisms dictate when the ion comes to rest, the range of the ion, R is also a function of these stopping powers and can be determined once they are known in accordance with the relation

$$R = \int_0^R dx = \frac{1}{N}\int_0^E \frac{dE}{S_n(E) + S_e(E)} \tag{2-6}$$

The distribution can be statistically described by a first order Gaussian distribution (Equation 2-7), in which R_p is the projected range normal to the surface, ΔR_p is the standard deviation and C_p is the peak concentration where the Guassian is centered. Most of the ions lie within $\pm\Delta R_p$ of the projected range. The implanted dose, Q or the total number of implanted ions can be extracted from this expression by integrating the concentration with respect to the distance into the material, x and is determined by an equation of the form of Equation 2-8.

$$C(x) = C_p \exp\left[-\frac{(x - R_p)^2}{2\Delta R_p{}^2}\right] \tag{2-7}$$

$$Q = \int_{-\infty}^{\infty} C(x)dx = \sqrt{2\pi} R_p C_p \tag{2-8}$$

An arbitrary distribution can be described by a series of four moments [PLU00]. The projected range, R_p is the first moment described by the equation:

$$R_p = \frac{1}{Q}\int_{-\infty}^{\infty} xC(x)dx \tag{2-9}$$

The second moment is the straggle or the standard deviation.

$$\Delta R_p = \sqrt{\frac{1}{Q}\int_{-\infty}^{\infty}\left(x - R_p\right)^2 C(x)dx} \tag{2-10}$$

Equations 2-9 and 2-10 show that the both the R_p and ΔR_p decrease with increasing ion and substrate mass. The third moment is the skewness (γ), which is dimensionless and indicates the direction of the peak. If the peak is skewed towards the surface the value is negative, while if the peak is skewed away from the surface this it is positive,.

$$\gamma = \frac{\int_{-\infty}^{\infty}\left(x - R_p\right)^3 C(x)dx}{Q\Delta R_p^{\ 3}} \tag{2-11}$$

The kurtosis (γ) is the fourth moment which is also a dimensionless parameter that indicates the extent of the distribution tails. A Guassian distribution corresponds to a value of 3. In general, values from 0 to 3 indicate abbreviated tails and above 3 indicate broad tails. The fourth moment defined by the following Equation 2-12.

$$\beta = \frac{\int_{-\infty}^{\infty}\left(x - R_p\right)^4 C(x)dx}{Q\Delta R_p^{\ 2}} \tag{2-12}$$

2.1.1.1 Channeling

The ion motion in a crystalline target can become constrained into the adjacent rows of atoms along low Miller index crystallographic planes. In these instances the steering forces of the atomic potentials of the rows of atoms are effective in keeping the ion directed along the channel [ZIE00]. The ions are then able to travel much further distances into the crystal lattice as electronic stopping is the only mechanism by which

energy is lost and hence there is reduced energy loss. Consequently there is less damage to the structure. The resultant ion implantation profile has a deeper projected range and long tail and then cannot be modeled by Equation 2-7. In extreme cases the profile exhibits a secondary maximum deeper into the crystal. Channeling is determined by the probability of the ions to enter a channel, which is related to size of the channel and the capability of the ions to hold the ions. The latter depends on the density of the silicon atoms along the channel walls, as higher density walls will maintain more ions.

Channeling can be controlled by a number of techniques. For primary implants, the wafer orientation relative to the ion beam is crucial. The necessary condition to avoid direct channeling is to orient the wafer such that the initial trajectories of the beam are not well aligned along the axes or between planes of the lattice. The two most important parameters are the wafer tilt and twist. Since there is a greater severity for axial channeling than planar channeling, the wafer tilt has a much more significant effect than the twist. For this reason, {100} silicon wafers are typically oriented relative to the beam direction with a tilt of 7° in the [110] direction followed by a twist of 27° around the [100] direction. Screen oxides can also drastically reduce the sensitivity of the profiles to channeling. These oxides are usually amorphous and the implant is done through them. The idea is that the amorphous layer is thin enough such that most of the ions are implanted, however the nature of the layer initiates scattering of the ion beams.

The implant dose can also assist in lessening the effects of channeling. If the dose is high enough, the accumulated damage can affect the channeled portion of the ion beam. As the dose is increased, the damage induced eventually reaches a critical value such that the structure is considered amorphous. The ions cannot channel through the

amorphous region, as the long range order has ceased to exist. However, doses which exceed the critical amorphization dose can punch through the amorphous layer and channel along low index rows in the underlying crystalline material. Although the use of high doses can dramatically reduce channeling effects, it is not available as an adjustable parameter for channeling control [ZIE00]. Pre-amorphization techniques that utilize silicon and non-dopant atoms such as germanium have become very popular for producing ultra-shallow boron junctions. The amorphous layer thickness determines its effectiveness in suppressing channeling. The depth of the amorphous layer is a function of the mass, energy and dose of the pre-amorphizing specie. The formation of amorphous layers has proven to be more effective in reducing the channeling effect than the use of screen oxides.

2.1.1.2 Amorphous Layer Formation

At sufficiently high damage concentrations a crystalline material undergoes a phase transition to an amorphous phase. The transformation is of the first order, as demonstrated by the abrupt amorphous-crystalline interface. The damage required to produce the crystalline to amorphous phase change is dependent on the ion mass, dose rate, implant energy and implant temperature. Several models have been presented which attempt to explain these dependencies. These models may be classified as either heterogeneous or homogenous nucleation, depending on whether they apply to heavy ions implanted at low temperatures or light ions at high temperatures, respectively.

Morehead and Crowder [MOR70] proposed a heterogeneous model in which they assumed that each incoming ion produced an amorphous cylinder of radius R. Experimental evidence for heavier ions confirmed the model's premise that the

amorphous layer formation involved the overlap of amorphous regions [JON93]. The number of displaced atoms per incident ion, N_d was given by

$$N_d = \frac{F_d}{2E_d} \tag{2-13}$$

where F_d is the energy deposited into the nuclear process, E_d is the threshold energy for an atom to remain displaced. For an incident ion dose, Q and nuclear energy loss $(dE/dx)_n$, the density of displaced ions was calculated as

$$N_d = \frac{Q\left(\frac{dE}{dx}\right)_n}{2E_d} \tag{2-14}$$

The critical dose for amorphization, D_{crit} is calculated by considering the condition for full amorphization such that the density of displaced ions is equated to the silicon atomic density. The homogeneous model was based on the assumption that when the point defect concentration reached a critical value, the system relaxed to an amorphous state [GIB77]. The model was subsequently modified to incorporate nucleation of amorphous regions at small amorphous zones created at the end of the light ion track [SHI85, WAS83]. The concept of a critical energy deposition or a threshold damage density was introduced by Stein et al. [STE70]. It represented the amount of energy necessary for nuclear collisions to change the crystalline lattice to an amorphous phase. The threshold damage density was shown to be a strong function of the ion mass, dose rate and wafer temperature during ion implantation.

2.1.2 Solid Phase Epitaxial Regrowth (SPER)

Solid phase epitaxial regrowth, commonly known as SPER is essentially the crystallization of an amorphous layer which is in immediate contact with a crystal

substrate. The process requires some form of heat energy which would allow for the rearrangement of the atoms at the amorphous-crystalline (α-C) interface such that the crystallization can seed of the underlying material. The required amorphous layer may be deposited onto the crystalline substrate by a chemical vapor deposition (CVD) technique or similar processes; however there are inherent disadvantages as this requires a pristine substrate surface to ensure good crystalline quality. An alternate method to forming an amorphous layer is ion implantation [DEA73]; a method that is widely employed in the semiconductor industry today. The use of implantation can provide an amorphous layer in intimate contact with the underlying substrate thus eliminating any contamination at the interface [CSE75]. Regrowth of the amorphous layer may be achieved by supplying thermal energy to the structure such that the atoms can redistribute themselves at the interface. Typically SPER commences at temperatures ranging 400-450°C [POA74] up to temperatures just below the melting point of the amorphous layer. SPER is of particular interest at temperatures below 650°C since these temperatures allow for limited diffusion of any impurities that are intentionally incorporated in the material; an area of great significance to the semiconductor industry. Various techniques have been employed to induce SPER, including thermal heating [POA74, NAR82, NAR83], electron beam heating [TIM85, TIM86], ion beam assisted regrowth [ELL87a, ELL87b] and laser heating [OLS84, OLS85a, OLS85b]. The regrowth however is also dependent on a number of variables such as the substrate orientation, the type of dopants incorporated and off course the temperature at which it is conducted.

Csepregi [CSE75, CSE76, CSE77] carried out several experiments on the temperature and substrate orientation dependence of the regrowth rate from amorphous

layers created by ion implantation at energies between 50 and 250keV. They realized that the growth velocity followed an Arrhenius type relation and was dependent on the orientation of the substrate. The growth rate was determined to be a linear function of the temperature and possessed a well defined activation energy, Ea of approximately 2.35eV over the temperature range 425-575oC for all orientations. The following equation defines the growth velocity, v, where v0 is the pre-exponential factor; k is Boltzmann's constant and T the temperature in Kelvin.

$$v = v_0 \exp\left[\frac{-E_a}{kT}\right] \tag{2-15}$$

Subsequent experiments employed techniques which were more accurate than those of Csepregi since they enabled simultaneous acquisition of the amorphous layer depth by time resolved reflectivity (TRR) measurements. Olson used TRR measurements for laser induced regrowth and established values of 3.07×10^8 cm/sec and 2.68eV for v_0 and E_a, respectively [OLS85a]. The work by Licoppe and Nissim [LIC86] examined a larger temperature range (500-900°C) using furnace and laser heating. Their findings were very similar to those of Olson and produced values of 3×10^8 cms^{-1} and 2.7eV for v_0 and E_a, respectively [LIC86].

The <100> oriented substrate resulted in the fastest growth, while growth on the <110> and <111> oriented substrates was found to be much slower, with growth on the <110> being approximately three times slower. Interestingly the growth dynamics on the <111> differed in that it exhibited two different growth regimes, both of which were linear in time. In the first region, the interface was uniform and the growth rate was a factor of twenty five times slower that that for the <100> [CSE76]. In the second regime the growth rate was faster but the interface was non-uniform. Csepregi later went on to

propose a model to explain the observed orientation dependence. He postulated that the regrowth of the metastable amorphous phase can be explained by a bond-breaking mechanism which allows the transfer of atoms at the α-c interface from irregular positions to regular lattice-sites [CSE78]. Since the measured regrowth was epitaxial he assumed that the atoms were transferred from the amorphous to crystalline phase at sites where at least two nearest-neighboring atoms at the interface were in crystalline positions. Csepregi's model though could not account for the regrowth rate on the <110> oriented substrates. Extended defects such as dislocation loops, stacking faults and microtwins were observed as a result of the recrystallization of amorphous silicon layers. Micro twins and stacking faults were not formed on the <100> and <110> oriented substrates, but only populated the microstructure of the <111> regrown layers [CSE76]. These however, were not evident in those layers which were regrown on the other crystal orientations investigated.

Spaepen et al. [SPA79] presented an atomistic model of the bond arrangements in the amorphous phase at the <111> interface. They demonstrated how bonds could be broken so that the atoms may be transferred from the amorphous to the crystalline phase at defects on a perfect <111> surface. Drosd [DRO82] offered a model similar to the atomistic model of Spaepen, based on the criterion that atoms of the amorphous phase must make two undistorted bonds with the crystal before they were considered to belong to the crystalline phase. Undistorted bonds were defined as those with the characteristic length and angle of the crystalline phase. They suggested that the layers of amorphous silicon in contact with the crystalline substrate, crystallized by the motion of the interface rather than by the nucleation of new crystals within the amorphous phase [DRO78]. This

was in agreement with the work of Blum [BLU72] and Turnball [TUR69] who determined that the time required for the nucleation of new crystals in amorphous silicon was extremely long in the temperature range of interest [DRO78]. For the α-c interface to advance during annealing, single atoms or small groups of atoms must reorient at the interface so as to add to the crystal surface at the correct location and orientation [FAU62], forming two undistorted bonds to the crystal. The requirement for the formation of two undistorted bonds was shown to be easily surmounted by the <100> oriented substrate as only a single atom was necessary. However on flat <110> and <111> surfaces, clusters of two and three atoms respectively were required to arrive at the surface for crystallization to proceed. Thus a crystallization nucleation step was necessary and the formation of new atomic layers posed a greater difficulty, more so, on the <111>, which resulted in longer regrowth times. Their model also accounted for the orientation specific defect structures that were observed by Csepregi and others. The dislocation loops in the <100> and <110> regrowths were attributed to primary point defects at the α-c interface, that are inherent to ion implantation. Microtwins and stacking faults on the other hand were thought to be the result of a non-planar interface and accounted for the accelerated growth observed in the second regrowth regime of the <111> oriented layers.

There has been considerable dispute over the E_a for α-c interface migration, however it has been confirmed that it is constant for a variety of recrystallization directions [LAU78]. Drosd [DRO82] therefore hypothesized that the thermally activated event for growth on any surface must be similar and is perhaps the reorientation of a small group of atoms in the amorphous material at the interface, as proposed by Spaepen

[SPA79]. The difference in growth rates were ascribed to the different probabilities that such an event would result in the placement of atoms at in position to form new regular bonds to the crystal [DRO82].

The incorporation of impurities into the crystal lattice upon regrowth, has been and remains an area of tremendous interest to the semiconductor industry. Therefore the effects of introducing impurities into the crystal lattice have been extensively studied [CSE77, BLO79, ADE88a, LIN00, LIN01]. Csepregi [CSE77] explored the influence of electrically active species with high solid solubilities on the regrowth of these amorphous layers. Their initial work involving the incorporation of boron into <100> silicon indicated that there was a tremendous increase in the regrowth velocity over that of only ^{28}Si-implanted amorphous layers. This increased growth was on the order of twenty-five for concentrations ranging $1x10^{20}cm^{-3}$; higher boron concentrations of $1x10^{21}cm^{-3}$ however only resulted in regrowth velocities that were 10 times greater. The boron incorporation also served to reduce the E_a for regrowth, which was consistent with the observed enhanced growth rate. Csepregi reported an E_a of 1.9eV [CSE77]. The boron enhanced regrowth also resulted in a considerable amount of residual defects. One of the main flaws in these experiments however was in the measurement of the regrowth which was taken over a Gaussian concentration profile.

Further investigations were conducted on the effect of the impurity incorporation on the regrowth. They include the work of Suni et al [SUN88a, SUN88b, SUN88c] who was able to achieve a more uniform concentration over the Gaussian profile of Csepregi, via the use of multiple energy implants. Their findings were similar to Csepregi, with an enhanced growth, but the enhancement reported was lower and was on the order of

fifteen for concentrations on the order of $2x10^{20}cm^{-3}$. However, in their work they failed to measure the intrinsic silicon regrowth velocity which was ultimately compared to that measured by Csepregi. Boron dose effects were explored by Kerkow et al. [KER84] at a temperature of 515°C for a range of concentrations. Their results indicate a maximum growth rate is achieved for a dose of $4x10^{20}cm^{-3}$; which subsequently falls of. Their findings included a reduced growth rate below that of intrinsic silicon for concentrations greater than $1x10^{21}cm^{-3}$. The experimental observations of Adekoya et al. [ADE88b] indicated a linear dependence of the growth rate on the implanted boron concentration, for concentrations ranging $5x10^{19}$ to $3x10^{20}cm^{-3}$. In accordance with the findings of Csepregi [CSE77] there was an observed enhanced regrowth velocity and the E_a also was found to be an inversely proportional function of the dose rate.

Additional work by Lindfors [LIN00] on 0.5keV ultra low energy (ULE) boron implants and regrowth temperatures of 500°C, suggest that high concentrations of boron corresponding to doses in excess of $1x10^{15}cm^{-2}$ can significantly reduce or stop the regrowth process altogether.

2.2 Defects in the Silicon Lattice

2.2.1 Primary Defects

Those defects which are the direct result of the processes of defect generation/annihilation in the time scale of the implantation kinetics are known as primary defects. They exist when the material is said to be in the "as-implanted" condition before any post-implantation processing occurs. The damage is a consequence of the interaction of the ions with the crystal atoms and the presence of the ions themselves in the structure. Momentum transfer between the implanted ions and the atoms results in the displacement of atoms from their lattice positions and hence the

formation of Frenkel pairs, which are pairs of vacancies and interstitials. In accordance with the Monte Carlo calculations of Mazzone [MAZ86], the forward momentum of the incoming ion produces a vacancy rich region from the surface to approximately $0.8R_p$, while an interstitial rich zone is found between R_p and $2R_p$. Thus the surface atoms move deeper into the structure leaving vacancies behind; a natural process of ion implantation commonly referred to as recoil implantation. The non-conservative nature of the implantation process also introduces excess interstitials into the structure, which are far greater than the number of vacancies available for occupation. These excess interstitials dominate the point defect population.

2.2.2 Structure of Secondary Defects

2.2.2.1 Sub-microscopic interstitial clusters

Initial evidence of the existence of the extended defect at the sub-microscopic level came from studies of the phenomenon of transient enhanced diffusion (TED) of boron in the silicon microstructure. The existence of these sub-microscopic interstitial clusters (SMICs) was initially postulated by Zhang (ZHA95) to account for the enhanced diffusion of boron, for which extended defects were not observed. As the name suggests, these defects were too small to be imaged by transmission electron microscopy (TEM), indicating that their dimensions were less than 5nm. Subsequently, Huizing [HUI96] also put forward that an alternate source of interstitials existed, to account for his observation of an ultra-fast diffusion pulse [MIC87, COW99b] which well in excess of the enhancement caused by the known {311}-type defect.

The submicroscopic interstitial clusters were believed to be the precursor for thhe {311}-type defect. Benton et al. [BEN97] presented a quantitative study of the evolution of point defects into clusters and extended defects in ion-implanted silicon. Deep level

transient spectroscopy (DLTS) measurements were used to identify and count the electrically active defects in the damage region. The damage was produced by silicon ion implantation of energies 145keV to 2MeV for doses ranging from $1x10^8$ to $5x10^{13}cm^{-2}$. The defect evolution was observed over the temperature range 100-680^oC. At doses less than $1x10^{10}cm^{-2}$ and temperatures below than 300^oC, the interstitials and vacancies were seen to anneal concomitantly, indicating recombination and no SMICs were observed. Above 350^oC the DLTS spectra revealed signatures inherent to second-order point defects with two or three interstitial-type defects per ion. Silicon implanted at higher fluences of $1x10^{12}$ to $7x10^{13}cm^{-2}$ and annealed at temperatures ≥600^oC exhibited two self-interstitial type defects at E_v+0.29 and E_v+0.48eV. The broadening of the DLTS spectra and the larger thermal stability of the signals provided evidence of the clusters. The interstitial clusters were not detectable by TEM which suggested that they were less than 5nm. At doses exceeding $5x10^{13}cm^{-2}$, thermal treatments at 680^oC achieved a strong decrease in the interstitial cluster signals and produced a different DLTS signal at E_v+0.5eV. Comparison of the formation and the dissolution of this extended defect signal with TEM analyses, substantiated that this signature corresponded to a rod-like {311} defect. On this basis they deduced that small interstitial clusters were precursors for {311} defects or competed with them for interstitials. In a similar experiment for n-type material, Benton et al. [BEN98] identified 5 DLTS signals associated with the interstitial type defects: E_c-0.14, E_c-0.29, E_c-0.37, E_c-0.50, and E^c-0.58eV. They indicate that the defects at E_v+0.29 and E_v+0.48eV were related to those at E_c-0.29 and E_c-0.50eV since they show similar annealing characteristics. The defect at E_c-0.58eV appeared only in the presence of a higher oxygen concentration. They therefore concluded that the thermal

stability of interstitial clusters was enhanced due to an increase in the interstitial concentration as the dose increased.

Coffa's experiments also provided evidence that SMICS underwent a structural change into the known {311}-type defect [COF00]. They utilized DLTS, Photoluminescence (PL) and TEM analyses to monitor the transition of small interstitials, formed from the agglomeration of excess interstitials into {311}-type defects. The dose and anneal temperature ranges examined were $1x10^{12}$ to $5x10^{13}cm^{-2}$ and 600 to 700°C, respectively. The silicon implantation was performed at 1.2MeV. Annealing at 600°C for 4 hours resulted in two well-defined peaks in the DLTS spectra which decreased in absolute magnitude as annealing proceeded. These were attributed to the interstitial clusters that dissolved with time. PL spectra of the same samples demonstrated sharp lines which characterized well defined structures, some of which were associated with interstitial clusters. The appearance of a sharp peak in the PL spectrum at 1376 nm was observed to indicate a structural transformation from SMICs to {311}-type defects [COF99]. However, they were unable to identify the size or configuration of the SMICs present in their specimens.

The SMICs were later shown to undergo Ostwald ripening and provided the interstitial supersaturation required for TED in the absence of extended defects higher in the evolution. DLTS measurements performed by Libertino [LIB99, LIB00] on epitaxial and Czochralski (CZ) silicon implanted with silicon ions at 145keV and 1.2MeV, revealed interstitial cluster formation at doses in excess of $1x10^{12}cm^{-2}$ and at annealing temperatures higher than 550°C. Analysis of the annealing kinetics for this dose in the temperature range 550 to 750°C indicated that the clusters underwent Ostwald ripening

and annealed out with dissociation energy of ~2.3eV. This value was consistent with the characteristic TED energy value in the absence of extended defects. The anneal temperature was also determined to increase with the fluence, owing to the augmented stability of the larger clusters. It was therefore deduced that the dissociation energy and the time for interstitial release would also increase for larger doses.

The inability to successfully identify the structure of the SMIC led to a number of studies which attempted to do so using ab initio total-energy calculations [PAY92] and inverse modeling techniques. Aria's electronic energy calculation showed that the four self-interstitial clusters (I4) were more stable than isolated interstitial configurations [ARI97]. The results of Kohyama quantitatively supported the possible existence of the I4 clusters as primary clusters or embryos of extended agglomerates [KOH99]. Most recently, Cowern [COW99] results showed the occurrence of minima in the cluster formation energy, E_{fc} for clusters composed of 4 and 8 self-interstitials. Figure 2-3 is a plot of the formation energy as a function of the number of self-interstitials in different extrinsic defects. It important to note that for larger clusters sizes, the formation energy tends to 1.1eV, the value expected for {311}-type defects of small sizes [CLA03]. This observation demonstrates that clusters of more than 20 atoms are similar in terms of formation energy, if not structurally, to small {311}-type defects [CLA03].

2.2.2.2 {311}-type defects

Research conducted at AT&T Bell Laboratories by Eaglesham [EAG94] in the early nineties identified the structural source of the silicon interstitials which enhanced implanted boron and phosphorous diffusion, as the {311}-type defect. Shallow 40keV silicon implants were selected for these experiments because the effects were shown to be more marked for narrow initial profiles and implant doses ranging from $5x10^{12}$ to

$5x10^{14}cm^{-2}$ were utilized. Furnace anneals were conducted at 670 and 815°C. Cross-sectional transmission electron microscopy (XTEM) revealed a high density of large extended defects whose structure was consistent with the well-known "rod-like" or {311}-type defects, in the implanted region throughout the TED [EAG94].

Quantitative TEM (QTEM) indicated that as the anneal progressed, the {311}-type defects evolved in accordance with a non-conservative Ostwald ripening process, in which large defects grew at the expense of small ones. Ostwald ripening is a competitive process which takes place through the exchange of atoms between all precipitates and hence maintains a supersaturation of host atoms in the region [CLA02]. The driving force for the formation of bigger defects is the dependence of the chemical potential of an interstitial silicon atom on the size of the extended defect it is bound [CLA02]. The width of the defects were found to be independent of anneal time and so their coarsening was denoted by an increase in length only. Figure 2-4 shows the variation of the {311}-type defect density and size with anneal time observed by Eaglesham and co-workers. Eaglesham correlated the dissolution of the {311}-type defects with the length of the diffusion transient and demonstrated a link between the number of interstitials emitted by the defects and the flux of interstitials driving TED [EAG94]. The net loss of interstitials associated with the dissolution and decay of the {311}-type defects was shown to be an exponential decay with time given by Equation 2-15

$$[Si_I] = Si_0 \exp\left(-\frac{t}{\tau}\right) \qquad (2\text{-}15)$$

in which Si_I is the planar density of interstitials trapped in {311}-type defects, Si_0 is the pre-exponential factor, t is the anneal time, and τ is the time constant for dissolution. This

time constant obeyed first order reaction kinetics (Figure 2-5) and yielded an activation energy for dissolution via the Arrhenius relationship

$$\tau = \tau_0 \exp\left(-\frac{E_a}{kT}\right) \tag{2-16}$$

where τ_0 is the pre-exponential, E_a the activation energy for {311}-type defect dissolution, k Boltzmann's constant, and T the temperature in Kelvin. The value of E_a for {311}-type defect dissolution was determined to be approximately 3.8eV [EAG94, SOL91]. This value corresponds to the sum of the binding and migration energies of a free silicon interstitial and also to the difference between the activation energy for self-diffusion and the formation energy of the defect [CLA00].

Figure 2-6 depicts a three dimensional representation of the {311}-type defect in the silicon lattice. The defect consists of interstitials precipitating on {311} habit planes as a single monolayer of hexagonal silicon, along <110> directions with a burger's vector, b of a/25<116> [TAK94]. It is now generally accepted that {311}-type defect consist of condensates of interstitials forming five-, six-, seven- (I) and eight- (O) membered rings, as shown in Figure 2-7. The silicon interstitials are contained in the six-membered ring (hexagonal). This atomic arrangement of a monolayer of hexagonal rings provides a way to insert planes of interstitials without introducing dangling bonds, which further reduces the energy of the silicon interstitial, hence the stability of these defects [EAG94]. Consequently, these defects do not significantly change in width and are approximately 4nm wide [EAG94]. Hence they almost one-dimensional precipitates [CLA00]. Takeda [TAK94] determined that the areal density of interstitials ranged 5.1 to 5.5nm^{-2} along the {311}-type defect cross section, hence the total interstitials within a rod-like {311}-type defect can be estimated to be approximately 26nm^{-1}. This value is

commonly used in quantitative TEM studies to estimate trapped interstitial densities. Figure 2-8 is a high resolution TEM image of a {311}-type defect as it occurs in the silicon lattice, taken by Eaglesham [EAG94].

The {311}-type defect is believed to evolve from the SMIC, which was previously discussed [COF00]. Coffa's experiments provided experimental evidence that SMICS underwent a structural change into the known {311}-type defect. Silicon self-implant doses exceeding $1x10^{13}cm^{-2}$ demonstrated a different peak in the spectra which increased with dose. Correlation of the TEM analyses for these samples verified the presence of {311}-type defects for a threshold dose of $1x10^{13}cm^{-2}$ at $600^{o}C$. Coffa went further to propose a nucleation barrier for {311}-type defect formation due to the apparent morphological changes required for evolution from interstitial clusters. They suggested that at low temperatures there was insufficient energy to overcome this nucleation barrier, hence the clusters simply dissolved. At elevated temperatures and higher doses, the probability for {311}-type defect formation was believed to be much higher. Impurities were also shown to influence the threshold dose for which {311}-defect formation was observed [COF00]. By comparing the PL spectra of epitaxial and CZ-silicon, Coffa determined that a lower threshold dose was required for high purity silicon. CZ-grown silicon had an inherently larger carbon impurity concentration and therefore, required a higher dose before {311}-type defects were detected. Carbon is known to trap interstitials; it therefore prevented the formation of large self-interstitial clusters, thus a higher interstitial concentration was required for {311}-type defect formation.

The driving force for such a precipitation process is a reduction of the chemical potential for an interstitial silicon atom entering such a defect structure. The formation

energy, which is the energy increase due to the incorporation of an extra silicon atom, for the {311}-type defect has been found to fall between 1 and 1.3eV [SEI94, GIL95, RAF96]. This value slowly decreases as the {311}-type defect decreases in size, with an asymptotic limit of in the range 0.5 to 0.9eV [TAK94].

2.2.2.3 Dislocation loops

There are two types of dislocation loops reported which include the faulted Frank dislocation loop and the perfect prismatic loop. The circular Frank dislocation loop is interstitial in nature and consists of two circular extra {111} net planes of silicon atoms, with a stacking fault displacement vector R= a/3<111> [CLA03]. The fault is bounded by a Frank partial dislocation whose Burgers vector, b = a/3<111>, hence it is a pure edge dislocation that can only grow by climb [CLA03]. The perfect prismatic loop on the other hand have nearly {111} habit planes and are elongated along <110> directions perpendicular to their Burgers vector, b=a/2<110>. They both have a planar density of $1.566 \times 10^{-8} cm^{-2}$.

Extensive analysis of the structure of these defects was conducted by de Mauduit [DEM90] via weak beam dark field (WBDF) methods. They determined that anneals at $1000^{o}C$ for 10 seconds resulted in a distribution of defects that was approximately 75% Frank loops and 25% perfect prismatic loops for a germanium amorphizing implant. It should be noted that for such thermal budgets, dislocation loops of both types are observed, whereas at higher temperatures only faulted dislocation loops are present [CLA00]. The predominant extrinsic circular Frank loops were observed to exist as four variants, while the there were twelve variants of the perfect elongated prismatic loops with each (111) plane containing three <110> directions.

The threshold dose required for dislocation loops to be observed in the silicon microstructure was demonstrated to be $1x10^{14}cm^{-2}$ [EAG95]. At higher energy implants however the threshold dose decreases owing to the higher implant damage as well as the increased distance between the Frenkel pairs, which reduces the probability of the interstitial-vacancy recombination [LAN95]. The precursor for the dislocation loop has been demonstrated to be the {311}-type defect for both non-amorphizing and amorphizing implants. Li and Jones [LI98] verified by in-situ TEM experiments that {311}-type defects unfaulted into both types of dislocation loops, for non-amorphizing implants. Subsequently, Robertson [ROB00] showed for amorphizing implants, that {311}-type defect either unfaulted to form dislocation loops or dissolved releasing the trapped interstitials. They went further to suggest that {311}-type defect sites served as the preferential site for dislocation loop nucleation.

The thermal evolution of faulted dislocation loops has been extensively studied [JON96, PAN97, BON98] and it is now widely accepted that the number of interstitials trapped within then remain constant, while they grow and decrease their density. This is formally known as a conservative Ostwald ripening process. This process can be understood by considering the Gibbs-Thompson equation, which relates the size of a precipitate (hence an extrinsic defect) of diameter 2r, to its equilibrium interstitial supersaturation. Equation 2-17 depicts the Gibbs-Thompson equation in which S(r) is the supersaturation of free interstitials, E_f is the formation energy of the defect, k is the Boltzmann constant and T is the temperature in Kelvin.

$$S(r) = \exp\left(\frac{E_f}{kT}\right) \qquad (2\text{-}17)$$

In general the interstitial supersaturation in the vicinity of a given defect is smaller as the defect increases in size, owing to a corresponding decrease in its formation energy. Hence the difference in the interstitial supersaturation in the vicinity of different size defects triggers atomic diffusion between the defects from regions of high interstitial supersaturation to those of lower interstitial supersaturation until a steady state is achieved, as demonstrated by Bonafos [BON98]. This steady state is defined as simply when the growth of the defects consists of the exchange of atoms between the loops. In such an instance the loop density varies inversely with time i.e. 1/t and the mean radius of the loops increases with $t^{1/2}$ independent of the limiting phenomenon (i.e. diffusion or interface reaction) [CLA03].

In the steady state condition the dislocation loops are the only sources and sinks of the interstitials. Therefore in the instance where both types of dislocation loops exist, there is an exchange of atoms such that the perfect prismatic loops undergo dissolution and the released interstitials contribute to the growth of the Frank dislocation loops [OMR99, GIL99]. Clearly, the perfect prismatic loops are less stable than Frank dislocation loops, hence based on the above discussion it can be inferred that the formation energy of the perfect prismatic loop is higher than that of the Frank dislocation loop. Faulted dislocation loops are very stable defects which are in equilibrium with the interstitial supersaturation around them; hence they require a high activation energy of 4.5eV for growth to occur [CLA00]. This energy is very similar to the interstitial self-diffusion (5eV). Figure 2-2, highlights the fact that the formation energies of both types of dislocation loops are much smaller than that of {311}-type defects and SMICs. This

suggests that the formation of a dislocation loop from a {311}-type defect requires that a reaction barrier be overcome by the {311}-type defect.

The presence of a particular extrinsic defect in the microstructure does not preclude the occurrence of other defects. Jones [JON96, JON97] established the simultaneous existence of both {311}-type defects and dislocation loops for temperatures below 800°C. Their experiments revealed both loops and {311}-type defects after the regrowth of an amorphous layer at 600°C. On additional annealing the {311}-type defects coarsened and dissolved between 700 and 800°C. The dislocation loops only entered a coarsening phase when the temperature was further increased. This has been accurately modeled by Lanaab [LAN93] and Liu [LIU95]. More recently Claverie showed that all four types of defects including SMICs, {311}-type defects, perfect dislocation loops and faulted dislocation loops can be simultaneously present as EOR defects [JAI02]. The extrinsic defects were observed for a 150keV germanium implant at a dose of $2x10^{15}cm^{-2}$ after a 400 second anneal at 750°C and are depicted in Figure 2-9.

2.2.2.4 Boron interstitial clusters

Boron interstitial clusters (BICs) are known to severely deteriorate the electrical properties of the silicon host due to boron electrical deactivation [COW90, LIL99, MIR03], such that that active concentrations are lower than the equilibrium solid solubility levels in the silicon lattice [TRU60]. They also adversely affect the carrier mobility by severely degrading it [MIR03]. These clusters are known to be very stable, existing for up to 4 hours after TED at 800°C [STO95, MIR03].

Evidence that boron exhibited clustering was demonstrated in the experiments performed by Stolk [STO95]. They showed that the peak regions of a boron marker layer close to the surface were immobile. Boron marker layers 10nm in width were grown in a

silicon epitaxial layer and subsequently implanted with $1x10^{13}cm^{-2}$, 40keV silicon. The structure was then annealed at $790^{o}C$ for 10 minutes. Figure 2-xx depicts the resultant diffusion. It was clear from the SIMS profile that there was very little diffusion of the boron in the shallowest peak. The lower boron concentration parts of the profile indicated broadening due to TED, which was most for the shallowest marker and decreased progressively with depth. They were also not visible via TEM analyses, which indicated that these clusters were smaller than 5nm, the TEM resolution limit.

The kinetics of BIC dissolution [HUA98, PEL99b, SOL00, MAN00, MAN01, MAN02, LIL02, RAD02, MIR03, DES05a, DES05b] has been the focus of a vast number of studies. Although these studies have yielded substantial information about these structures, there are still many unknowns regarding for example their configuration, whether they form in the amorphous phase during SPER and if they occupy substitutional sites or the lattice interstices or both. Boron is known to cluster for concentrations exceeding the range $1x10^{18}$ to $1x10^{19}cm^{-3}$ in crystalline material. The clustering reaction also seems to depend on the distance between the regions of high boron concentrations and the interstitial population. Clustering has been demonstrated for boron concentrations overlapping the interstitial population, but has not been observed in a re-grown amorphous layer [JON96]. Lilak [LIL02] and Mirabella [MIR03] performed extensive studies on the dissolution kinetics of BICS, which yielded respective thermal activation energies of 3.0 and 3.2eV, respectively. These are significantly less than that found by Mokhberi, of 4.7 eV [MOK02]. More recently, De Salvador established that they were two regimes of BIC dissolution, characterized by a fast dissolution, similar to that of Mirabella and Lilak, and a slow dissolution [DES05a, DES05b]. BICs formed for

concentrations on the order of $2x10^{20}cm^{-3}$, which exceeded solid solubility limits, were shown to dissolve with an activation energy of 4.8eV [DES05a, DES05b]. Figure 2-10 illustrates the Arrhenius fit for these two BIC regimes, observed by De Salvador. This value is remarkably similar to the value obtained by Mokhberi [MOK02], whose boron dose was $1x10^{15}cm^{-2}$. It is therefore likely that the boron concentrations in his experiments were comparable to DeSalvador.

In an effort to determine the most probable BIC configurations, a number of computational studies have been conducted. These include *Ab initio* and tight binding calculations which have provided useful information on the relative stability of specific BIC configurations [ZHU96, CAT98, PEL99a, LIU00, LEN00, LUO01, ADE03, HWA03]. Pelaz's model in particular has been able to demonstrate that BICs on their dissolution emit interstitials which can contribute to TED. Figure 2-11 illustrates the formation energies required for evolution of BICs up to a size of B_4I_4 [PEL99a] from Pelaz's model. They came to the conclusion that BICs with a high interstitial content (e.g., BI_2, B_3I_3, B_4I_4) form at early times when the interstitial supersaturation is greatest. As annealing proceeds, the BICs emit interstitials that can contribute to TED leading to BICs with a lower interstitial content. Therefore, the most stable configurations are those where $m < n$ for a B_nI_m cluster. When the BICs completely dissociate the immobile peak is observed to diffuse, but this occurs long after TED has ended.

2.3 Diffusion

In order to repair the damage created by the implantation process an annealing technique is required. The thermal input enables the process of diffusion. Diffusion may be defined as the system's attempt to reduce its chemical potential gradient by redistributing the atoms to eliminate an existing concentration gradient.

2.3.1 Fickian Diffusion

The analyses presented by Fick are a macroscopic interpretation of the diffusion process. Fick's first law of diffusion states that the concentration flux per unit area of the diffusing species under steady state conditions is proportional to the concentration gradient and is expressed as

$$J = -D\left(\frac{\partial C}{\partial x}\right)_t \tag{2-18}$$

where J is the flux per unit area, D is the diffusion coefficient, C is the concentration of the diffusing species, x is the gradient direction, and t is time. This relation however does not take into consideration that concentration may vary as a function of time; hence Fick defined a second law which takes both of these parameters into account and is expressed in Equation 2-19.

$$\frac{\partial C}{\partial t} = \frac{\partial}{\partial x}\left(D\frac{\partial C}{\partial x}\right) = D\frac{\partial^2 C}{\partial x^2} \tag{2-19}$$

In this case the diffusivity, D is assumed to be independent of time and space and is represented by an Arrhenius expression of the form of Equation 2-20.

$$D = D_0 \exp\left(\frac{-E_a}{kT}\right) \tag{2-20}$$

where D_0 is the pre-exponential factor, E is the activation energy for the diffusing species, k is Boltzmann's constant, and T is temperature. These constants differ for different species; the values of which can be found in Table 2-1 for diffusion in the silicon lattice.

The simplest solution to these equations arise for steady state conditions, which results in a linear concentration profile with distance, x given by

$$C(x) = a + bx \tag{2-21}$$

While for a lightly doped region, a Gaussian solution exits for a narrow peak of dopant introduced into the lattice, which can be described by a delta function. The solution of which is given by Equation 2-22, from which the characteristic dopant diffusion length, x can be determined as shown in Equation 2-23.

$$C(x,t) = \frac{Q}{2\sqrt{\pi Dt}} \exp\left(-\frac{x^2}{4Dt}\right) = C(0,t)\exp\left(-\frac{x^2}{4Dt}\right) \tag{2-22}$$

$$x = 2\sqrt{Dt} \tag{2-23}$$

For a heavily doped region, the error function solution applies and is

$$C(x,t) = \frac{C}{2}\left[erfc\left(\frac{x}{2\sqrt{Dt}}\right)\right] \tag{2-24}$$

In equations 2-22 through 2-24, C is the concentration of the dopant atom, Q is the implant dose, D is the diffusivity, x is the dopant diffusion length and t is the anneal time. It should be noted that modifications to Fick's laws have been made to account for electric field effects, concentration dependant diffusion, dopant pile up and other physically observed defects which will not be reviewed here.

2.3.2 Point Defect Interactions

It is now generally accepted that dopants diffuse through the silicon lattice via interactions with both the interstitials and vacancies. The subsitutitonal dopant atom is immobile by itself unless it interacts with a point defect [PLU00]. The dopant atom may couple with an interstitial (I) or vacancy (V) to become a mobile specie [FAH89] as follows

$$A + V \leftrightarrow AV \tag{2-25}$$

$$A + I \leftrightarrow AI \tag{2-26}$$

$$A + I \leftrightarrow A_i \tag{2-27}$$

$$A \leftrightarrow A_i + V \tag{2-28}$$

where A represents an impurity atom in a substitutional configuration, I is a self-interstitial, V is a vacancy, and A_i is an impurity atom in an interstitial position. Equation 2-25 depicts dopant diffusion by the vacancy mechanism. The next three equations describe the dopant diffusion by the substitutional/interstitial/interstitialcy mechanisms. In Equation 2-26 a substitutional dopant pairs with a self-interstitial to form a dopant-interstitial pair, which shares the lattice site as the pair diffuses. This is known as the interstitialcy mechanism. While in the interstitial mechanism of Equation 2-27 a self-interstitial or substitutional dopant is completely “kicked” off the lattice site. It should be mentioned that the distinction between the interstitialcy/interstitial mechanisms is rarely made. In the last reaction a substitutional dopant hops into an interstitial position, leaving behind a vacancy. This is known as the dissociative reaction or Frank-Turnbull mechanism diffusion.

Both interstitials and vacancies contribute to dopant diffusion in silicon. The effective diffusivity accounts for both vacancy and interstitial contributions to diffusion and can be described at low dopant concentrations by

$$D_A^{eff} = D_A^0 \exp\left(\frac{-E_A}{kT}\right) \tag{2-29}$$

where E_A is the activation energy of diffusion, D_A^0 is the pre-exponential factor, T is the temperature in Kelvin and k the Boltzman constant. The activation energy for self-diffusion is generally 1eV higher than that for dopant diffusion which range between 3 and 4eV.

The effective, intrinsic diffusivity is the sum of the contributions of the diffusivities for each mechanism, D_{AI} and D_{AV}, the interstitial and vacancy contributions respectively, such that

$$D_A^{eff} = D_{AI} + D_{AV} \tag{2-30}$$

$$D_A^{eff} = d_{AI}\left[\frac{C_{AI}}{C_A}\right] + d_{AV}\left[\frac{C_{AV}}{C_A}\right] \tag{2-31}$$

where D_A is the diffusion coefficient of species A, D_{AI} is the interstitial diffusion coefficient of species A, C_{AI} is the concentration of species A occupying interstitial positions in the host lattice, C_A is the concentration of species A, D_{AV} is the vacancy diffusion coefficient of species A, and C_{AV} is the concentration of species A occupying host lattice sites with adjacent vacancies [FAH89]. D_{AI} and D_{AV} are therefore dependent on the fraction of mobile species and their diffusivities, d_{AI} and d_{AV}.

Alternatively, the fractional diffusion of a species through each mechanism may be defined for the interstitial and vacancy mechanisms as

$$f_{AI} = \left(\frac{D_{AI}}{D_A}\right)\left[\frac{C_{AI}}{C_A}\right] \tag{2-32}$$

$$f_{AV} = \left(\frac{D_{AV}}{D_A}\right)\left[\frac{C_{AV}}{C_A}\right] \tag{2-33}$$

where f_{AI} and f_{AV} are the fractional interstitial and vacancy diffusion components for species A, respectively, such that the sum of the fractional components is unity. Under intrinsic conditions, the ratio of the diffusivity of species A to its equilibrium diffusivity is given by the relation

$$\frac{D_A}{D_A^*} = f_{AI}\frac{C_{AI}}{C_{AI}^*} + (1 - f_{AI})\frac{C_{AV}}{C_{AV}^*} \tag{2-34}$$

where D_A*, C_{AI}*, and C_{AV}* are the equilibrium diffusivity component, equilibrium interstitial concentration, and equilibrium vacancy concentration of species A, respectively. Clearly from the equation the diffusivity is proportional to the supersaturation of interstitials and vacancies.

2.3.3 Transient Enhanced Diffusion

Three basic characteristics define what has become known as transient enhanced diffusion (TED); transient, enhanced and depth dependant diffusion. This diffusion behavior was classified as transient because its amplitude was a decaying function of time; the impurity diffusion was considerably faster than regular thermal diffusion and therefore it appeared to be enhanced; and finally, there seemed to be a dependence of the effect on the distance between impurity atoms, the defects and surface. These specific elements collectively contribute to what has commonly become known as TED.

Enhanced diffusion of dopant atoms in silicon were first observed over forty years ago in 1960 in bipolar devices. Abnormally rapid diffusion of base dopant impurity near

the emitter region of a doubly diffused n-p-n semiconductor was detected. This effect is now known as the emitter push effect [JAI02]. Since then a number of reports of anomalous diffusion have been made and it has become an area of extensive research within the semiconductor industry. Hofker [HOF73] reported enhanced diffusion of boron in silicon in 1973, in which the anomalous motion was attributed to a fast diffusing interstitial component of the boron. Ten years later studies employing rapid thermal processing techniques by Hodgson [HOD84] demonstrated that anomalous transient displacements of 50-100nm, occur in short times on the order of 1-2 seconds at temperatures ranging 860 to 1200°C. Sedgwick [SED85] and Oehrlein [OEH84] also demonstrated similar results at longer anneal times of 10s, in which displacements of 40nm were obtained between 900 and 1100°C. The diffusion was credited to an enhanced point defect concentration related to ion implanted damage. Cho [CHO85] later confirmed that channeled interstitial boron was not responsible for the anomalous transient. In their experiments different isotopes of boron were employed to illustrate that a stabilized boron implant underwent an additional displacement when a second boron implant was annealed. These experiments conclusively proved that substitutional boron atoms experienced TED due to point defects created by the implantation. It was later confirmed that the boron diffused by an interstitialcy mechanism.

The first clear evidence for TED was presented by Michel [MIC87] in which it was apparent that the anomalous diffusion of ion implanted boron into silicon was a transient effect. The decay time was observed to rapidly decrease on increasing the anneal temperature. At 800°C the transient lasted 35 minutes and the boron diffusion was on the order of 150-200nm, compared to a regular thermal diffusion of 3nm. The transient was

reduced to a few seconds at 900°C with a corresponding decrease in the diffusion amplitude. Subsequently, the dependence of boron TED on the defect depth position relative to the as-implanted boron profile was investigated by a number of authors. They elucidated that the enhanced diffusion occurred when the junction was localized in an interstitial rich region, just beyond the amorphous-crystalline interface [SOL86, ANG86]. They further postulated that the dissolution of the interstitial clusters in the damage tail gave rise to a supersaturation of interstitials. These interstitials interacted with the extended defects formed at the original amorphous-crystalline interface and were able to enhance the diffusion of the boron.

Although post implantation thermal processing effects the recombination of interstitials and vacancies produced by the implantation process, there is a net interstitial population which does not recombine which is approximately equal to the implanted dose. This is known as the “plus 1 dose” [GIL91]. There are cases however for which the plus-1 model breaks down as it underestimates the number of interstitials in implanted and annealed samples. This has been observed for cases in which the implanted dose is low [LAW00] and also when TED is independent of the implanted species for a given energy [GRI93, CHA96]. Pelaz examined the ion mass effect on TED via atomistic simulations and proposed an effective plus-factor or plus-n factor [PEL98]. This proposal was based on the fact that heavy ions because of their inherent larger cross-section and mass, contribute more energy to momentum transfer and therefore the displaced ions travel further distances, in accordance with the conservation of momentum. Hence there is a reduction in the probability of recombination of the interstitials (I) and vacancies (V), as the V may recombine at the surface which is closer. The plus-n factor also accounted

for lower doses. At lower doses there is a smaller concentration of interstitials and vacancies, hence longer distances need to be traveled before recombination occurs, which again reduces the probability of such an event. The plus-n factor has been defined for a boron concentration of $2x10^{13}cm^{-2}$ as +1.2.

As previously discussed, extended defects form on annealing due to coalescence of these excess interstitials. These defects are metastable and exist as SMICs, {311}-type defects and dislocation loops. The types of defects present in the silicon microstructure are a function of the dose and implant conditions. At lower doses the SMICs and {311}-type defects occur, whereas at higher doses and thermal budgets dislocation loops and can be observed [EAG95a]. In accordance with precipitation theory the defects maintain an equilibrium interstitial supersaturation in their vicinity, which is a function of the defect size and anneal temperature [BON97]. When this interstitial supersaturation falls the defects dissolve and emit interstitials, which contribute to and sustain TED. At low temperatures the TED lasts longer times than at high temperatures. This can be explained by the fact that there is a lower supersaturation of interstitials at higher temperatures, which is a direct consequence of the higher equilibrium concentration, C_i^* available. This is more apparent on examining the relation that defines the interstitial supersaturation, S_i.

$$S_i = \frac{C_i}{C_i^*(T)} \tag{2-35}$$

The increase in junction depth accompanied by TED [RAF96] is captured in the equation

$$\Delta x_j = NR_p \exp\left[-\left(-\frac{1.4}{kT}\right)\right] \tag{2-36}$$

where N is the number of interstitials trapped in the defects, R_p is the projected range and Δx_j is the junction depth. The relation demonstrates a linear dependence of the junction depth on the dose which is reflected in the trapped interstitial concentration. An increase in dose results in an increase in the interstitial supersaturation and therefore a diffusion enhancement. Also the projected range determines the surface recombination and therefore the interstitials available for diffusion. This relation also captures the temperature dependence of the TED, which is larger at smaller temperatures and accounted for in the negative exponential expression [JAI02]. This is an important result, from a processing standpoint. It has encouraged the development of anneal processes which were able to achieve very high temperatures in the shortest possible time, such as Rapid Thermal Anneals (RTA) in which ramp rates of approximately 200-400°Cs^{-1} are possible.

2.4 Rapid Thermal Processing

Various thermal annealing techniques such as Rapid Thermal Processing (RTP) using soak cycles, and, more recently, RTP spike anneals have met the needs of mainstream CMOS for many years. Consequently, a lot of research activity has been devoted to investigating annealing techniques, which minimize the thermal budget imparted to the wafer and therefore reduce the corresponding diffusion. Researchers in RTP have improved the thermal cycles by increasing ramp up and cool down rates and by increasing the sharpness of the spike anneal to try to reduce the effective time of the anneal cycle and hence reduce the diffusion. This has produced some marginal improvements in junction depth and sheet resistance, but this has proven inadequate for future device generations. The minimum cycle times in conventional RTP techniques are limited by the maximum power delivered to the wafer and the minimum response time of

the relatively large thermal mass incandescent tungsten lamps. These factors dictate the ramp-up rate, the soak time and the ramp-down rate. Without being able to minimize the soak time and the ramp-down rate, increasing the ramp-up rate above 100°Cs^{-1} results in no additional improvement in terms of forming a highly-activated ultra-shallow junction [MAN01]. The progress towards meeting the needs of future technology nodes as defined in the ITRS Roadmap [SEM05] has also recently slowed, as the combination of implantation and spike RTP seems to have reached a barrier [SHI99]. Accordingly, alternative annealing techniques are being investigated.

Laser thermal processing (LTP) has shown extremely shallow junctions with very high activation [FEL00]. But, there have been reports of dopant deactivation upon application of subsequent thermal processing, as well as integration issues [YAN01]. Another disadvantage of the LTP technique is fact that the entire wafer cannot be laser processed at the same time and the laser beam must be raster scanned across the wafer. This significantly increases the time required to process one wafer, which is undesirable from an economic standpoint. The non-uniform heating of the entire wafer surface makes this an inherently low throughput process and the possibility of lateral thermal gradients in the wafer is very high and can result in residual defects. Hence, although a promising technique, if these issues are not sorted out, LTP will not make it to manufacturing facilities.

More recently considerable research has been conducted on Flash lamp annealing in the millisecond regime. Flash technology has been investigated for more than twenty years as an alternative annealing technique for reducing the thermal budget imparted to the silicon wafer, in an effort to produce shallow junctions. The process is commercially

known as Flash-Assist Rapid Thermal Processing (RTP) or fRTP and was designed to operate within the time gap between spike RTP and LTP. The process uses a continuous arc lamp to heat the bulk of the wafer to an intermediate temperature (iRTP). This heating is slower than the thermal conduction rate through the wafer, thus the entire wafer remains at approximately the same temperature [STU02]. Subsequently a capacitor bank is discharged through an arc lamp which adds additional power to the device side of the wafer, at a rate much faster than the thermal conduction rate. Short time pulses only allow for heating of the surface of the wafer while the substrate never attains these high temperatures. This is possible since the time constant of the flash which is on the order 1ms is much shorter than the thermal time constant of the wafer (~10-20ms). Therefore a thin slice of the device side of the wafer is heated and cooled rapidly at rates on the order of $1x10^6$ °Cs^{-1}. The fast cooling is achieved since the bulk of the wafer acts as a heat sink removing heat from the top layer via conduction much more efficiently and faster than can be accomplished in bulk cooling. The high absorbance of the reactor chamber also complements the cooling rates. However, as the flash time pulse approaches the time constant of silicon the flash elevates the bulk temperature considerably, therefore only allowing for cooling by radiative and convective methods, resulting in much slower cooling rates. Heating rates up to the intermediate temperature are similar to conventional spike annealing (50 to 300 °Cs^{-1}) as are cooling rates during the bulk radiative cooling (up to ~150 °C/s).

The basic features of Vortek's 300mm Flash-assist RTP tool include two arc lamps which are mounted at either end of the chamber. The lamps are positioned to allow both sides of the wafer, which is mounted on four quartz pins in the center of a reflective

chamber, to be irradiated. Lamp 2 is typically used to achieve the intermediate temperature, while the capacitor bank is discharged through Lamp 1 to generate the flash. Water-cooled windows are located between the chamber and the each arc-lamp, which transmits light in the UV and visible regions of the electromagnetic spectrum, but absorbs near IR radiation [STU02]. Two radiometers are employed in the temperature measurement; the Fast Radiometer (FR) measures the radiance from the substrate side of the wafer, whereas the Ultra-Fast Radiometer (UFR) measures radiance from the device-side of the wafer. The FR and UFR differ in their sampling rates and resolution, which are higher and lower, respectively for the UFR. The camera located to the side of Lamp 2, serves two purposes; one of which is to measure the emissivity of the substrate side of the wafer, in combination with the emissometer source. The other function of the camera is to provide a temperature map of the wafer.

The advantages of the Flash-assist RTP over conventional RTA systems, stem from the differences in the heating technology. There are three main advantages of using water-walled arc lamps over tungsten filament lamps used in conventional RTA systems; the ability to deliver greater power, faster response time of the arc and the spectral distribution of the incident radiation. Radiation is produced in a tungsten lamp by heating the filament to approximately 3500K, with a resultant power on the order of $1x10^3$W [CAM94]. This compares to powers of $1x10^6$W obtainable by heating a high pressure argon plasma to 12000K in an arc lamp, which enables ramp rates that are more than four orders of magnitude higher than that of the conventional RTA. The arc lamps also respond much faster than the tungsten filament lamps, owing to the smaller thermal mass of argon, which yields a response time of 25ms compared to 300ms for the tungsten

lamps [CAM94]. In general the transition from heating to cooling is limited by the thermal time constant of the wafer, which is approximately 15ms and the time constant of the heat source. Hence the flashed wafer will transition much faster from heating to cooling that the wafer processed by conventional RTA [CAM94]. These differences in the transitions times account for the rounded profile of the conventional RTA compared to the sharp peak of the Impulse (iRTP) anneal, shown in Figure 2-13. The short wavelength radiation produced by the arc lamp is also more effective in heating the silicon substrate. Figure 2-14 shows the spectral distribution of the emitted radiation and the corresponding integrated spectra as a function of wavelength. It is evident that over 95% of the arc radiation is below the 1.2μm band gap absorption of silicon compared to 40% for radiation generated by the tungsten lamps [CAM94]. Additionally, tungsten filament lamps degrade with time due to deposits on the lamp as well as changes in the filaments themselves, hence the irradiance distribution shifts to longer wavelengths with time and the absorption consequently drops below 40%. Conversely, water-walled arc lamps are high quality optical sources with well-defined positions and negligible change in radiance with lifetime, provided the electrical power is maintained [CAM94]. Hence they are more reliable heating source.

One of the key issues with integrating the Flash-assist RTP tool into the CMOS manufacturing process is the difference in optical properties of the complex patterned wafer. These patterns inherently introduce temperature uniformities [VAN89] arising from the disparities in the emission, reflectance and absorbance. In order to understand the design concepts which were implemented in the tool design to counteract these issues, one needs to consider a wafer at uniform temperature that is totally exposed to black

body radiation at the same temperature. Assuming that the system is in equilibrium, temperature uniformity is maintained despite the patterns on the wafer, provided the patterns do not absorb and emit the radiation at different rates. This effects differences in the heating and cooling rates in different sections of the wafer. Additionally edge effects are a concern; due to the increased surface area to volume ratio at the wafer edges, heat flux can be lost through the edges. Hence the key to minimizing the pattern and edge effects is to minimize the heat transfer through the wafer and at the edges [CAM94]. These issues are countered by the use of a ring to extend the wafer diameter and a highly reflective cavity above the wafer's device side [CAM94]. Another feature of the tool is the implementation of a water-walled arc lamp and reflector cavity that absorbs all the secondary radiation emitted from the wafer. If the secondary radiation is absorbed and the optics designed to give uniform primary radiation, then the limit to the temperature uniformity is estimated at $\pm 1^{o}C$ at $1100^{o}C$ [CAM94].

Accurate and reliable temperature measurement on a real time basis is absolutely essential for any manufacturing process in which this tool is to be utilized. This is achieved due to the inherent characteristics of the water-walled arc lamp and the absorbing chamber. The rapid response time of the arc lamp enables the lamp to be turned off, the thermal radiation of the wafer measured and the lamp switched back on, before the wafer changes temperature. Measurement of the radiation reflected from the wafer is obtained by comparing the measurements with the lamp on and off. An estimate of the reflectivity can be made from the angular and spatial distribution of the primary radiation on the wafer and the measured reflected radiation [CAM94]. These real time measurements of the reflectivity are used to estimate the emissivity. The wafer

temperature is determined from the emissivity together with the thermal radiation measurements, in accordance with the equation for emission from a gray body

$$I = \varepsilon \frac{2\pi c^2 h \Delta\lambda}{\lambda^5 \left(e^{hc/\lambda kT} - 1\right)} \tag{2-37}$$

where I is the emitted intensity at the wavelength λ in a band Δλ wide and h is Plank's constant, k is Boltzmann's constant and c is the speed of light [LEF99]. A reference object at fixed temperature, T_{ref}, with known emissivity, ε_{ref} is placed in the field of view so that simultaneous measurements of reference, I_{ref}, and wafer radiation, I, are obtained in one image [LEF99]. Both the reference and wafer obey Equation 2-37, hence solving the simultaneous equation yields the wafer temperature, T.

$$T = \frac{hc}{\lambda k} \left\{ \frac{1}{\ln\left[\frac{I_{ref}\varepsilon}{I\varepsilon_{ref}} \left(e^{hc/\lambda kT_{ref}} - 1\right) \right]} \right\} \tag{2-38}$$

The wavelength can be accurately selected by placing an interference filter in front of the camera. At a wavelength of 900nm, where the wafer is opaque, the emissivity, ε is estimated from the reflectivity, r

$$r = 1 - \varepsilon = \frac{I_{reflected}}{I_{incident}} \tag{2-39}$$

The reflected light is measured directly by a charge-coupled device (CCD) camera, the incident light can be calibrated before hand or determined by reflection off a reference. The CCD camera can measure thermal radiation from the wafer to give relative temperature measurements within ±0.25°C. Emissivity measurements within 1% give absolute temperature to within ±3°C at 1050°C [LEF99].

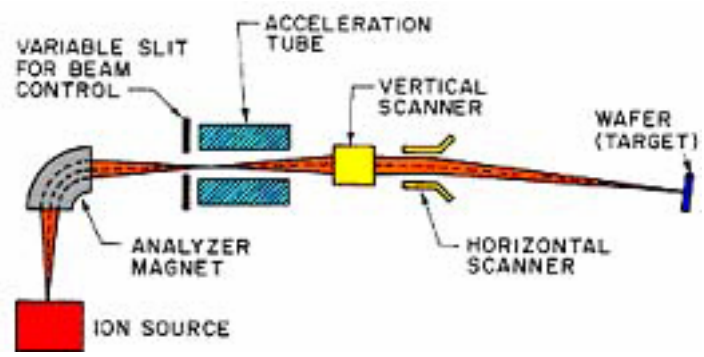

Figure 2-1. Schematic of an ion implanter

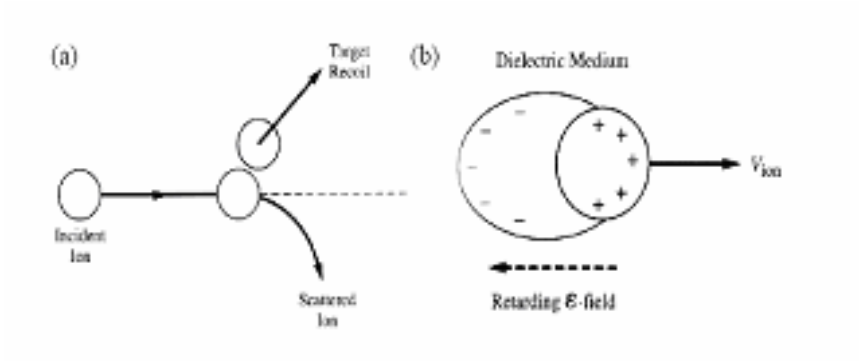

Figure2-2. Schematic representation of loss mechanisms associated with the ion implantation technique. (a) nuclear energy loss and (b) electronic energy loss [PLU00].

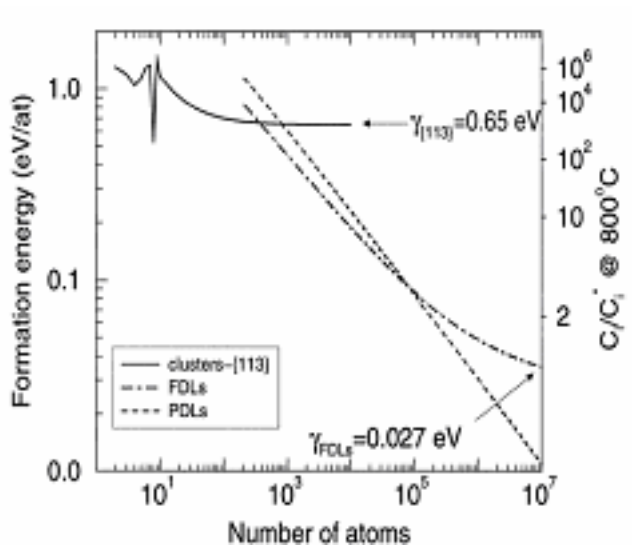

Figure 2-3. Formation energy (left axis) of the different types of extrinsic defects as a function of their size and corresponding values of the silicon interstitial supersaturation (right axis) [CLA03].

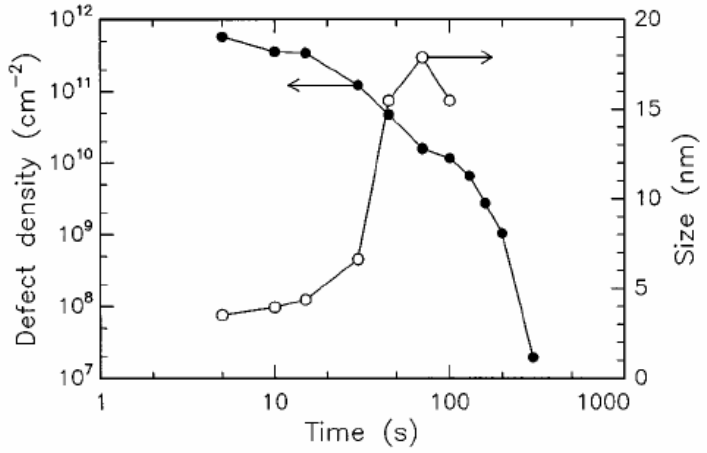

Figure 2-4. Development of the density and the average length of {311}-type defects during annealing at 815 °C. [EAG94].

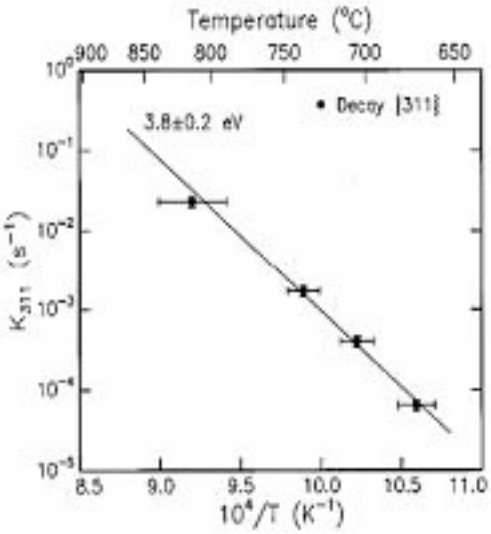

Figure 2-5. Arrhenius graph of the time constant for {311}-type defect decay derived from the annealing curves [EAG94].

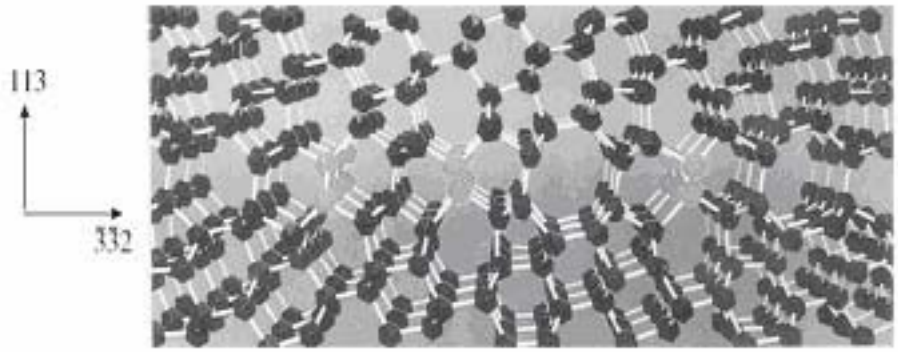

Figure 2-6. 3D representation of {311}-type defect in the silicon lattice. Light gray balls show interstitial chains along <110> direction [TAK91].

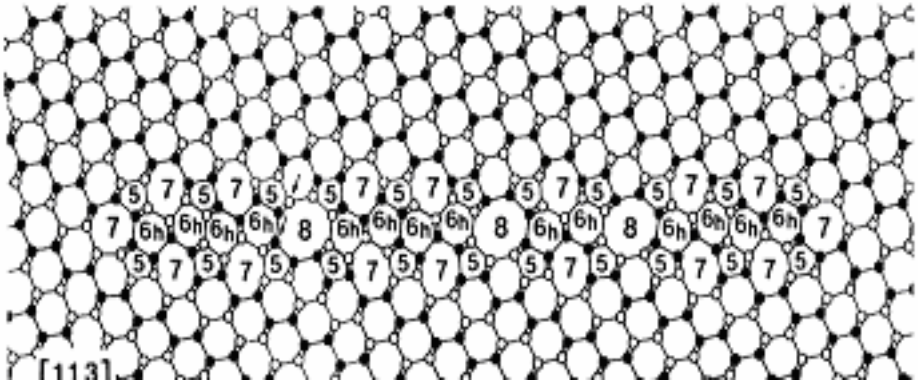

Figure 2-7. Atomic structure of a planar {311}-type defect in which the numbers represent rings different from those in a perfect crystal [TAK94].

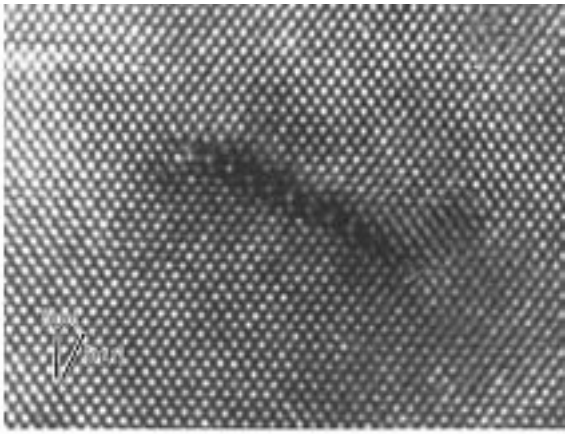

Figure 2-8. Plan-view high-resolution transmission electron microscopy image of a {311}-type defect in the silicon lattice. [EAG94].

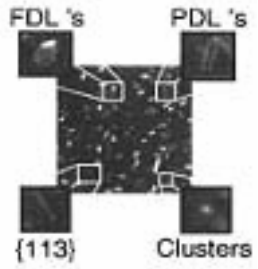

Figure 2-9. Different types of extrinsic defects after annealing at 750◦C for 400s: clusters, {113}-type defects, perfect prismatic dislocation loops (PDL) and Frank dislocation loops (FDL) [CLA03].

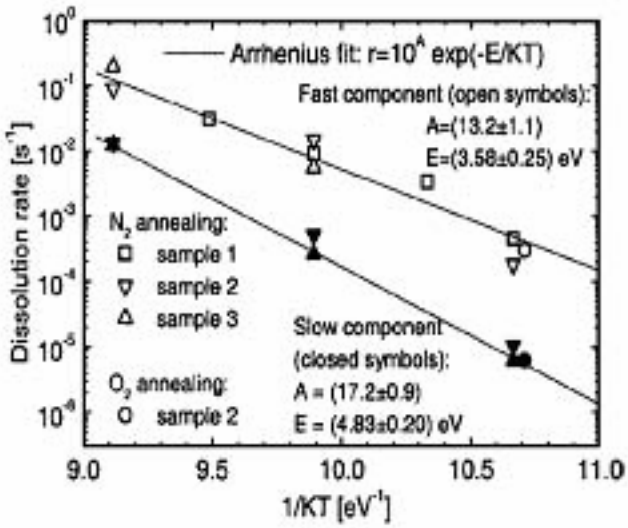

Figure 2-10. Arrhenius plot of the dissolution rates of boron clusters. Open and closed symbols represent the faster and slower dissolution processes, respectively. Continuous lines are the best Arrhenius fits for the fast (upper line) and the slow (lower one) process obtained by a fit of all the data weighted by their errors (not shown) [DES05].

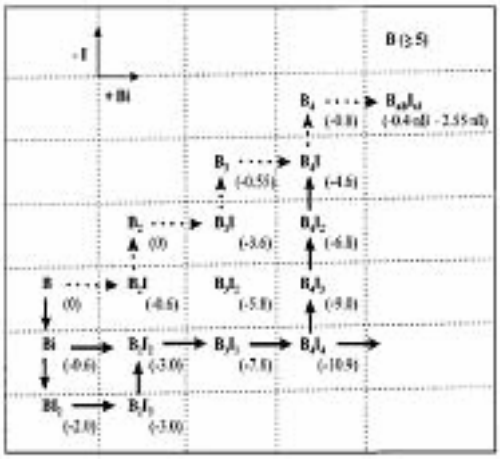

Figure 2-11. Schematic of the different paths for the growth of boron clusters. The dashed line corresponds to a generic low interstitial content path. The solid line corresponds to a high interstitial content path. The energies in the table determine a predominant high interstitial content path. The clusters with high interstitial content release silicon interstitials when the interstitial supersaturation decreases. The energy of boron clusters is also shown in eV [PEL99a].

Table 2-1. Approximate fractional interstitial and vacancy components for various dopants in the silicon lattice [PLU00].

Impurity	Fractional Interstitial	Fractional Vacancy
Boron	0.8 - 1	0 - 0.2
Phosphorus	0.9 - 1	0 - 0.1
Arsenic	0.4	0.6
Antimony	0.02	0.98
Silicon	0.6	0.4

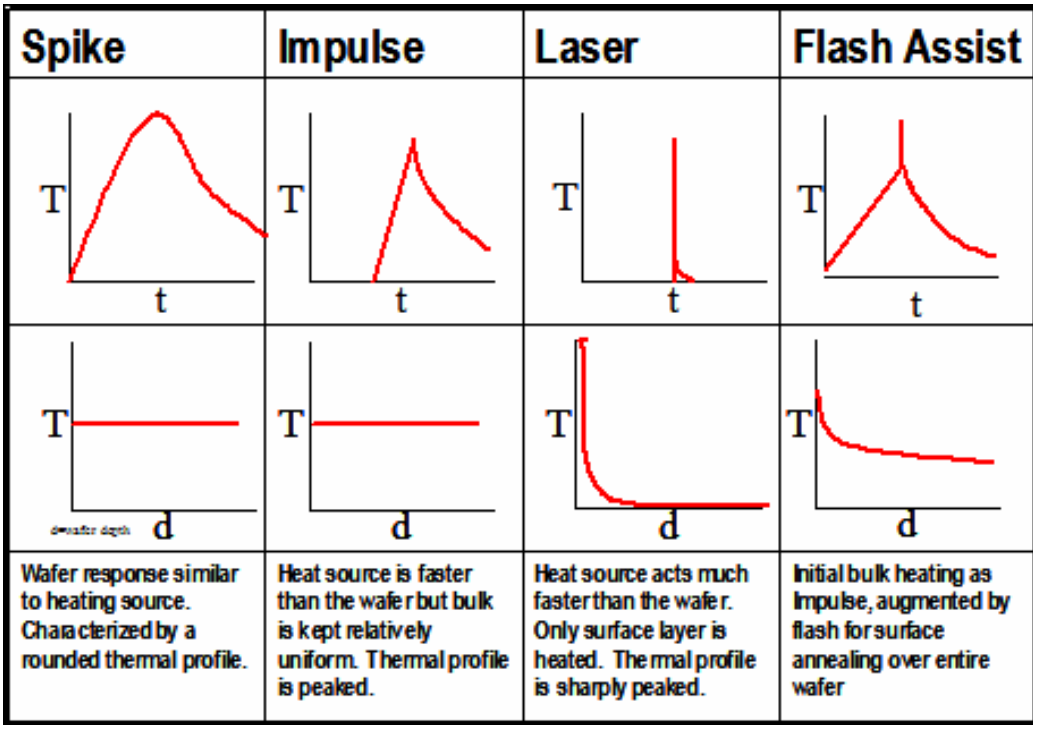

Figure 2-12. Characteristic temperature-time profiles of various annealing techniques, which demonstrates the differences in the transition from heating to cooling. Clearly a more rounded transition is obtained for the spike anneal compared to the Impulse, Laser and Flash-assist RTP anneals.

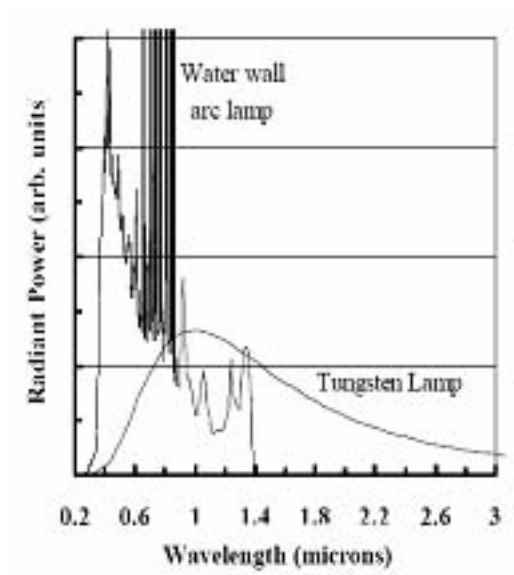

Figure 2-13. Spectra distribution for a water-walled arc lamp and tungsten lamp heated to 2900K.

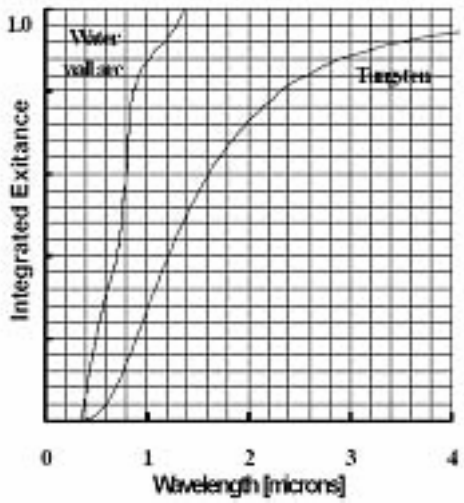

Figure 2-14. Integrated spectra for a water-walled arc lamp and tungsten lamp at 2900K.

CHAPTER 3
ANALYTICAL TECHNIQUES

This chapter discusses gives an overview of the operating principles of the analytical techniques which have been used in this work. The goal is for the reader to become familiar with the capabilities of each technique and its limitations, such that the reader can better understand the results and analyses presented in the subsequent chapters. There is no specific order of presentation.

3.1 Transmission Electron Microscopy

Transmission electron microscopy is a very powerful imaging tool, which can be used for high-resolution imaging, with a resolution of 2nm. The electron beam is generated by thermionic emission from a tungsten filament, which occurs when the work function of the filament is exceeded such that electrons can escape from the filament. The beam of electrons is subsequently converged to a point by a negative voltage applied to a Wehnelt cap, which acts as the first electrostatic lens in the microscope. The electron beam should be coherent and monochromatic and is typically 100-400kV. The electrons that leave the gun area are focused to a small coherent beam by the use of two condenser lenses. The first of the two lenses determines the spot size of the beam, whereas the second lens changes the size of the spot on the sample from a widely dispersed spot to a focused beam. The interaction volume of the sample depends on a number of factors including the atomic number of the material, the accelerating voltage being used, and the angle of incidence for the electron beam. Smaller interaction volumes occur for higher atomic number materials, smaller accelerating voltages and higher angles of incidence.

As the beam passes through the specimen it undergoes a number of elastic and inelastic scattering processes, which are shown in Figure 3-1. The transmitted beam comprises both the unscattered as well as scattered electrons. The elastically scattered electrons are of interest. In accordance with Bragg's law all incidents scattered by the same atomic spacing will be scattered by the same angle. Bragg's law is shown in Equation 3-1.

$$\lambda = 2d\sin\theta \tag{3-1}$$

where λ is the wavelength of the incident beam, d is the interplanar spacing for a particular set of planes and θ is the angle conditioned between the incident beam and the lattice plane of interest. Constructive interference of the diffracted beams together with the structure factor, specimen orientation relative to the beam direction, and the lattice spacing, determine the diffraction pattern Material properties such as the interplanar spacing, d can be determined from the relation

$$Rd = \lambda L \tag{3-2}$$

where R is the measured distance from the diffraction spot to the transmitted beam, λ is the wavelength of the incident beam and L is the camera length. The Miller indices (h,k,l) of the atomic plane can the be determined from the Equation 3-3 which relates the interplanar spacing, d to the lattice parameter, a.

$$d = \frac{a}{\sqrt{h^2 + k^2 + l^2}} \tag{3-3}$$

The inelastically scattered electrons produce the Kikuchi bands which appear as alternating dark and light lines which are related to the atomic spacing. The transmitted portion of the electron beam is focused by the objective lens into an image. Dark field (DF) imaging, allows for viewing along specific crystallographic directions, usually

results in excellent contrast relative to imaging with the direct transmitted beam in bright field (BF) mode.

Plan-view transmission electron microscopy (PTEM) was used to investigate the effects of flash-assist RTP on the end of range (EOR) defect evolution and morphology. PTEM sample preparation entailed cutting a 3mm disc of each sample, chemically mechanically thinning the sample using 15μm alumina slurry and chemically etching the backside of the sample with a 1:3 49%HF: HNO_3 solution, until electron transparent regions were evident. The nitric acid serves to oxidize the silicon, while the fluoride etches the oxide according to the equations

$$Si(s) + 4HNO_3(l) \Leftrightarrow 3SiO_2(s) + 4NO(g) + 2H_2O \quad (3\text{-}4)$$

$$SiO_2(s) + 6HF(l) \Leftrightarrow H_2SiF_6(l) + 2H_2O(l) \quad (3\text{-}5)$$

PTEM images of the EOR damage in these regions were then captured using a JEOL 200CX microscope, operating at an accelerating voltage of 200keV in weak-beam-dark-field (WBDF), g_{220} two-beam imaging conditions. The WBDF images were obtained by selecting the g_{220} beam in DF mode and aligning it with the direct beam in BF mode. The specimen was then tilted slightly off the <001> zone axis and the deficit and excess <220> Kikuchi lines aligned with the beam direction and g_{220}, respectively in BF. This was coupled with aligning the lines along the g_{220} and 2g in DF. The Kikuchi bands were then shifted slightly off the g_{220} and 2g to excite the 3g beam to its intersection with the Ewald sphere. Although the g_{220} was not exactly at Bragg conditions, scattering from the 3g allowed for the excellent contrast around the strain field of the defects. Figure 3-2 illustrates the principle behind weak beam dark field imaging in TEM for an edge dislocation, in which it can be seen that the highest intensity occurs close to dislocation

core because planes are bent back to Bragg condition [WIL96]. The resultant images of the EOR damage were analyzed using the quantification technique of Bharatan et al. [BHA97].

One of the main drawbacks of TEM is it is extremely time consuming. A single PTEM sample can take several hours before it can be imaged. Additionally the technique is destructive and therefore the sample cannot usually be used for any other analysis.

3.2 Secondary Ion Mass Spectrometry

Dynamic secondary ion mass spectrometry (SIMS) utilizes a primary monoenergetic ion beam to bombard a solid surface; such that a mixing zone is produced from which atoms are sputtered. The sputtered atoms are known as secondary ions and may be neutral or charged and are subsequently mass selected in a mass spectrometer, via the application of electrostatic and magnetic fields. Ions of different mass-to-charge ratios are measured by changing the strength of the magnetic field. A typical SIMS depth profile is collected as ion counts per second versus sputtering time which is converted to a concentration-depth profile. The relative sensitivity factor (RSFs) is used to convert the vertical axis from ion counts into concentration; while the depth of the sputtering crater, measured using a profilometer, is used to convert the time to depth. The depth of the mixing zone limits the depth resolution of SIMS to between 2 to 30nm. A smaller primary ion energy, smaller angle of incidence and larger mass primary ions effects better depth resolution, since these factors decrease the depth of the mixing zone.

SIMS can be used to measure any elemental impurity from hydrogen to uranium and any isotope of these elements [BRU92]. The detection limit is also much lower than any other technique which claims a similar lateral and depth profiling, and is y between $1x10^{12}$ and $1x10^{16}cm^{-3}$ for most impurities. The detection limit of the element however is

dictated by how efficiently it ionizes. Other advantages of SIMS include the ability to provide composition images, limited sample preparation, excellent vertical resolution, and very low detection limits. The disadvantages are that the process is destructive, need for standards, and generally poor lateral resolution.

One of three kinds of primary beams is used in SIMS analyses, including oxygen (O_2^+ or O^-) and cesium (Cs^+). The ion yield is defined as the fraction of sputtered ions that become ionized. An oxygen beam is used for boron profiling since it increases the ion yield of positive ions, while cesium is used to increase the ion yield of negative ions. The enhancement in the ion yield can be understood by considering that the oxygen bombardment results in the formation of oxygen bonds in the oxygen-rich mixing zone. These bonds are subsequently broken in the ion emission process, such that the oxygen becomes negatively charged due to its higher ionization potential and the dissociated boron atom, for example becomes positively charged. In the case of cesium, the formation of cesium bonds in the mixing zone drastically decreases the work function, so that more secondary electrons are excited over the surface potential barrier such that there is an enhancement in the formation of negative ions [BRU92].

SIMS is used in the context of this work to determine the concentration-depth profiles for the as-implanted boron dopant profile and the subsequent boron diffusion on application of the thermal anneals.

3.3 Hall Effect

The Hall Effect can be understood by considering the consequence of applying a magnetic filed perpendicular to a moving electron. The result is that the carrier undergoes a deflection which is perpendicular to both to the magnetic field and the plane in which it was originally traveling, due to a Lorenz force, illustrated in Figure 3-3. This behavior

was originally observed by Hall and is now commonly applied to an electric current flowing in semiconductors. The result of the charged carriers being deflected to a given side of the sample is a potential difference across the material, which effects a Hall voltage. It should be noted that electrons and holes are deflected in the same direction owing to their opposite velocity and opposite charge. An electric field is set up due to the potential gradient which exists between the opposite sides of the sample. The Hall voltage, V_H can be determined by equating the force due to the electric field, E to the force due to the magnetic field, B such that

$$Eq = \frac{V_H q}{d} = Bqv \tag{3-6}$$

$$V_H = Bvd \tag{3-7}$$

where q is the charge on the carrier (1.6×10^{-19}C), d is the length of the sample across which the potential exists and v is the drift velocity of the electrons which is determined from

$$I = pqvA \tag{3-7}$$

$$A = td \tag{3-8}$$

where p is the number of holes (or electrons for n-type) per unit volume, A is the cross-sectional area of the semi-conductor, and t is the thickness. Hence substituting the for the drift velocity, v

$$V_H = \frac{BI}{pqt} \tag{3-9}$$

A Van der Pauw [PAU58] geometry, consisting of a number of shapes, is typically used, but is not a requirement for doing Hall experiments. The most common shapes include a circle, cloverleaf, square, and bridge-shape. The objective of the Hall measurement in the

van der Pauw technique is to determine the sheet number, ρ_s by measuring the Hall voltage,V_H. The Hall voltage is measured by forcing a current, I through opposing pair of contacts, the Hall voltage is measured across the remaining pair of contacts 2 and 4. This is demonstrated in Figure 3-4. Once the Hall voltage is acquired, the sheet number, ρ_s can be calculated from the following equation, in which I is the current, B is the magnetic field, q is the carrier charge

$$\rho_s = \frac{IB}{qV_H} \tag{3-10}$$

The Sheet resistance, R_s of the semiconductor can be conveniently determined by use of the van der Pauw resistivity measurement technique. Since sheet resistance includes the sheet number, ρ_s and mobility μ. The mobility is calculated by substituting Equation 3- into the following equation for R_s

$$R_s = \frac{1}{q\mu\rho_s} \tag{3-11}$$

Hence the mobility, μ is

$$\mu = \frac{V_H}{R_s IB} = \frac{1}{q\rho_s R_s} \tag{3-12}$$

Since ion implantation results in a Gaussian profile then the carrier density and mobility values obtained from the Hall measurements are averaged over the profiles. The Hall coefficient, R_H is given by the inverse of the product of the carrier charge, q and the active hole concentration, p

$$R_H = \frac{1}{qp} \tag{3-13}$$

Simple Hall measurements do not consider effects of light-hole, heavy-hole, and spin-orbit split bands together, therefore correction factors need to be added into data [LI79, LIN81]. Li derived an expression for the Hall coefficient, R_H, that includes the Hall factor, r [LI93].

$$R_H = \frac{r}{qp} \tag{3-14}$$

To obtain true values of dose activation one needs to multiply the measured active dose by the Hall factor, while the conductivity mobility is determined by dividing the Hall mobility by the Hall factor. The Hall factor varies from ~0.8 for boron concentrations around $1x10^{18}cm^{-3}$ to ~0.7 for concentrations $>1x10^{20}$ cm^{-3} [Li79, Lin81]. In this work a Hall factor of 0.7 is assumed as a conservative estimate since active boron concentrations $>1x10^{20}cm^{-3}$ is realized.

There are practical aspects which must be considered when carrying out Hall and resistivity measurements. Primary concerns are include ohmic contact quality and size, sample uniformity and accurate thickness determination, thermomagnetic effects due to nonuniform temperature, and photoconductive and photovoltaic effects which can be minimized by measuring in a dark environment.

The Hall measurements were performed to track how the active dopant dose and the carrier mobility changed with application of the Flash-assist RTP. The measurements were performed using a system manufactured by MMR Technologies that includes the M-50 bench top electromagnet, MPS-50 programmable magnet power supply, K-20 programmable temperature controller, and H-50 Hall, van der Pauw controller. Soft indium contacts were used during the measurement.

3.4 Four Point Probe

The Four Point Probe measurement is the simplest of all the techniques used in this work. It provides a sheet resistance, R_s measurement, which is valuable to the semiconductor industry since it relates the active impurity level to the carrier mobility. The measurement is obtained by applying a voltage across two outer probes, such that the voltage drop across two inner probes is measured, which is representative of the sample. To understand the measurement, consider a rectangular layer of doped silicon of length l, width w, and thickness t. The resistance measured between the parallel faces of width w and thickness t is described by

$$R = \frac{\rho(t)}{t}\frac{l}{w} = R_s \frac{l}{w} \tag{3-15}$$

where ρ is the specific resistivity of the measured layer in units of ohm distance (ohms·cm) and varies with thickness, t. R_s is the sheet resistance of the layer in units of ohms, but usually reported as ohms/sq.

The resistivity, ρ of the layer is related to the carrier mobility, μ and concentration of charge carriers, n for electrons and p for holes, according to relation 3-16 in which q is the carrier charge.

$$\rho = \frac{1}{q\mu_e n + q\mu_h p} \tag{3-16}$$

For uniform spacing of the probes in the instrument,

$$\rho = 2\pi s \frac{V}{I} \tag{3-17}$$

In very thin samples, where the thickness of the conducting layer is thin compared to the probe spacing (e.g. implanted layers, as in these experiments) the resistivity, ρ becomes

$$\rho = \frac{\pi t}{\ln 2}\frac{V}{I} = 4.532\frac{V}{I}x_j \tag{3-18}$$

from which the sheet resistance is determined using Equation 3-15.

The Four point probe measurements in these experiments were used to determine the sheet resistance and used to confirm the sheet resistance measured by Hall.

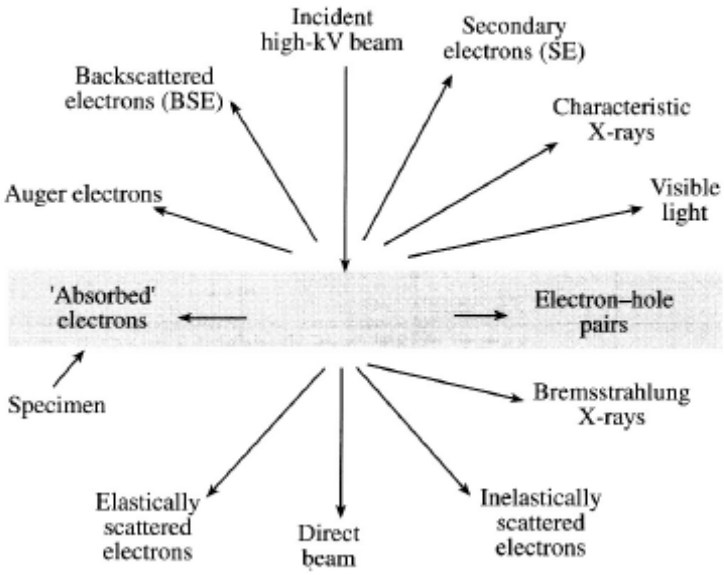

Figure 3-1. Signals generated when a high-energy beam of electrons interacts with a sample. The directions shown indicate where the signal is strongest or where it is detected.

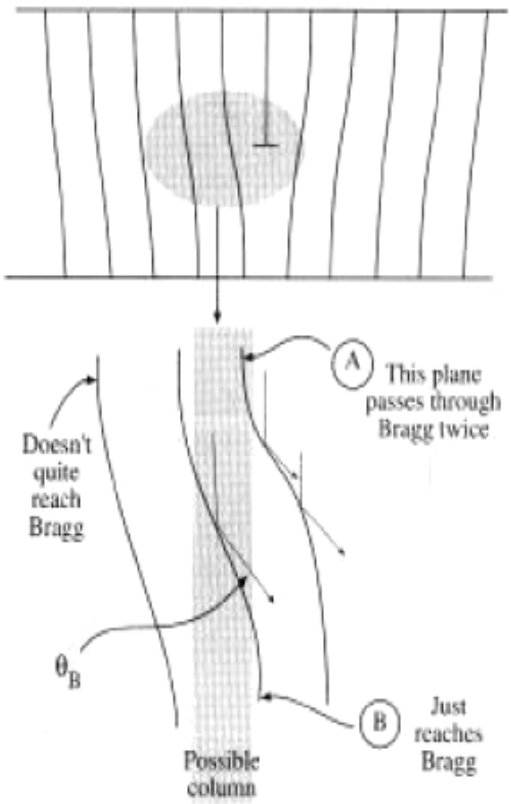

Figure 3-2. Principle behind weak beam dark field imaging in TEM for a edge dislocation. High intensity occurs close to dislocation core because planes are bent back to Bragg condition. [WIL96]

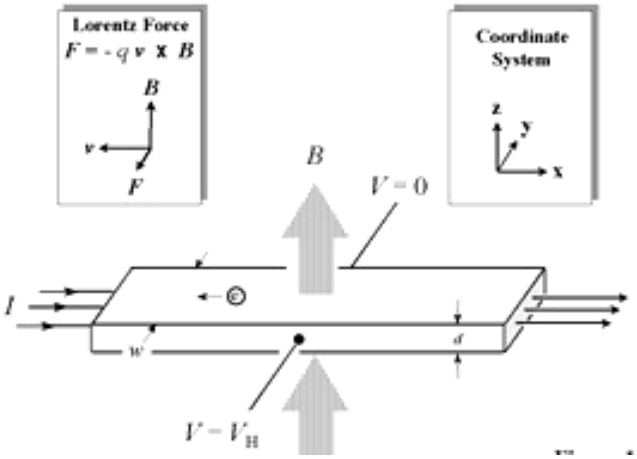

Figure 3-3. Illustration of the Hall Effect occurring in an n-type specimen.

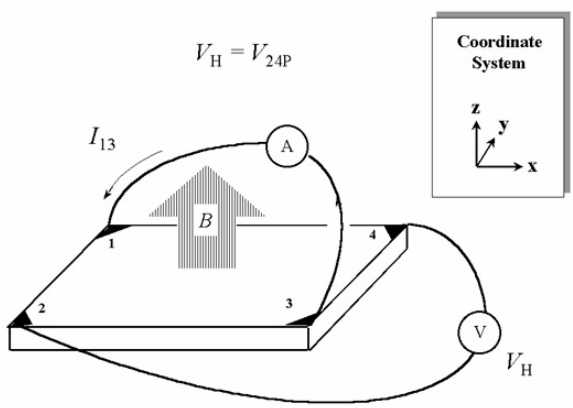

Figure 3-4. Schematic of a van der Pauw configuration used in the determination of the Hall voltage, V_H.

CHAPTER 4
INVESTIGATIONS OF THE EFFECT OF FLASH-ASSIST RAPID THERMAL PROCESSING ON THE END OF RANGE DAMAGE EVOLUTION

4.1 Introduction

Flash-assist Rapid Thermal Processing (RTP) enables investigations into annealing time and temperature regimes which were not possible with conventional technologies such as Rapid Thermal Annealing (RTA). This provides a unique opportunity to explore the early stages of the EOR damage evolution and also to examine how the damage evolves during the high temperature portion of the temperature profile.

Knowledge of the defect structures which exist in the silicon lattice is crucial to understanding the variations in the silicon interstitial supersaturation, during thermal annealing process. It has been previously demonstrated that the silicon interstitial supersaturation in the vicinity of the End of Range (EOR) damage drives the anomalous diffusion of dopant atoms or TED [BON97]. Additionally the release of interstitials which accompanies dissolution of the EOR damage also contributes to TED. TED is known to occur during the early stages of the annealing process, when the interstitial supersaturation is high. The interstitial supersaturation is also known to be a function of the defect size and also the anneal temperature, being high for smaller defects and lower anneal temperature. Hence, investigations which can provide further insight into the processes that occur in the early stages of the thermal anneal of an implanted wafer, when the defects are very small, are beneficial. This chapters examines the defect evolution of the during Flash-assist Rapid Thermal Processing.

4.2 Experimental Design

200mm 12ohm-cm (100) n-type Czochralski (CZ) grown silicon wafers were amorphized with a 30keV germanium ion implant at a dose of $1x10^{15}cm^{-2}$. The ion implantations were performed in deceleration mode on an Applied Materials XR80 Leap Implanter at a twist of 27° and a tilt of 7°. The silicon wafers were then annealed by Flash-assist RTP at Vortek technologies in Vancouver, Canada. These thermal anneals comprised heating the bulk silicon wafers by arc irradiation at a heating rate of 150^oCs^{-1} to an intermediate temperature (iRTP) of 700^oC, where the dwell time was 0s. The iRTP served as the initial temperature for the flash anneal. The flash anneal (fRTP) which arises by discharging capacitor banks into flash lamps, produced a pulse of radiation with a full width at half maximum ranging 0.85-0.9ms, enabling temperatures of 1100, 1200 and 1300^oC at a heating rate of $10^6\ ^oCs^{-1}$. During the fRTP anneal only the near surface regions of the wafers were heated, this allowed for conductive heat loss through the cooler layers on the backside of the wafer, and rapid cooling rates which very similar to the heating rates attained. These rates were on the order of $1x10^6\ ^oCs^{-1}$. Throughout the course of the flash pulse the backside of the wafers experienced an increase in temperature of approximately 100^oC. Once the flashed wafer surface was in thermal equilibrium with the bulk of the wafer, subsequent cooling was dominated by radiative heat loss to the surrounding black environment at a maximum rate of 90^oCs^{-1}. Figure 4-1 depicts the thermal profile of the flash anneal which was used in this experiment.

Plan-view transmission electron microscopy (PTEM) was used to investigate the effects of flash-assist RTP on the end of range (EOR) defect evolution and morphology. PTEM sample preparation entailed cutting a 3mm disc of each sample, chemically mechanically thinning the sample using 15μm alumina slurry and chemically etching the

backside of the sample with a 1:3 49%HF: HNO_3 solution, until electron transparent regions were evident. PTEM images of the EOR damage in these regions were then captured using a JEOL 200CX microscope, operating at an accelerating voltage of 200keV in weak-beam-dark-field (WBDF), g_{220} two-beam imaging conditions. The resultant images of the EOR damage were analyzed using the quantification technique of Bharatan et al. [BHA97].

Cross-sectional TEM (XTEM) was also performed using a JEOL 200CX TEM operating at an accelerating voltage of 200keV. However the images were taken under g_{110} bright field conditions. The XTEM samples were prepared via a Focused Ion Beam and the method was used to determine amorphous layer depths and track layer re-growth.

4.3 Results

The 30keV germanium implant produced a continuous amorphous layer from the surface to a depth of 50nm, as measured by VASE and confirmed by XTEM. Figure 4-2 depicts XTEM images of the flash annealed material, in which the EOR damage layer can be discerned just beyond the original amorphous-crystalline interface at a depth of approximately 55nm. It is also evident that the iRTP anneal resulted in total re-crystallization of the amorphous layer.

The WBDF PTEM images of the end of range (EOR) damage observed for the Flash-assist RTP are illustrated in Figure 4-3. Examination of the damage due to the 30keV germanium PAI reveals the presence of small dot-like interstitial clusters of very high density, immediately after the 700°C iRTP anneal. On application of the 1100°C fRTP, some signs of coarsening become apparent. The EOR defects appear somewhat larger and of smaller areal density. This trend is sustained as the fRTP temperature is

raised to 1200 and 1300°C, in which cases the defects are observed to coarsen into {311}-type structures and dislocation loops.

Defect density as a function of the fRTP anneal temperature is shown in Figure 4-4, which exhibits a decreasing defect density with increasing fRTP anneal temperature. Defect densities on the order of $1x10^{11}cm^{-2}$ are attained for anneal temperatures of 700, 1100 and 1200°C. However, the density rapidly plummets two orders of magnitude on application of the 1300°C fRTP anneal. An analysis of the defect size indicates that the defect diameter does not significantly change between 700 and 1100°C averaging between 5 and 7nm, respectively. As the fRTP temperature is increased to 1200°C the predominant {311}-defects present in the microstructure are of an average length of 14nm, whereas, the dislocation loops observed at 1300°C are approximately 18nm in diameter.

Quantification of the interstitials trapped in the EOR defects were conducted using the average defect sizes summarized above. As the fRTP anneal temperature was increased the number of interstitials trapped by the EOR defects were observed to decrease. The trapped interstitial dose decreased from values on the order of $1x10^{14}cm^{-2}$ between 700 and 1200°C to $1x10^{13}cm^{-2}$ for the 1300°C fRTP, as shown in Figure 4-5. This trend is very similar to that observed for the defect density and demonstrates an exponential decay with anneal temperature.

4.4 Discussion

The re-crystallized layer depth as a function of the anneal temperature was determined using the intrinsic re-growth velocity relation of Roth and Olson [ROT90]. The process simulator FLOOPS [LAW03] was utilized to calculate the re-crystallized layer depth (velocity-time product) by integrating the velocity as the temperature was

varied with time for each thermal profile. Thus accurately accounting for the variations in the re-crystallization with the simultaneous change in temperature and time as the wafer was annealed. The calculations of the intrinsic re-growth indicated that the velocities were insufficient to completely re-crystallize the layer during the ramp up to the iRTP temperature, with only the first 20nm of the layer re-crystallized. Hence the subsequent thermal budget completed the re-crystallization process. In the case of the 700°C iRTP this occurred during the ramp down from 700°C to the ambient temperature. The layers which were subjected to the higher temperature fRTP anneals were all re-crystallized at the same temperature of ~1000°C, during the ramp-up from the iRTP to the final fRTP temperature. Figure 4-6 shows the re-growth at a given temperature which was determined by taking the integral of the velocity-time plots.

The damage observed in the microstructure can be classified as Type II, which results when an amorphous layer is present and occurs beyond the amorphous-crystalline interface in the EOR region [JON88]. The evolution of Type II defects from point defects to extrinsic dislocation loops upon annealing is believed to occur via intermediate defect configurations and it is now widely accepted that sub-microscopic interstitial clusters (SMICs) [BEN97, COF00, LIB98] are the precursors for the formation of {311}-type defects [EAG94, STO97, PAN97]. The {311}-type defects which are metastable, eventually unfault to form dislocation loops [LIJ98]. The fact that different defect structures were identified at different annealing temperatures in this work is not unexpected. Isochronal anneals although a valid experimental approach to temperature dependent studies, do not yield EOR defects in the same phase of their evolution. At a given isochronal annealing time, lower temperature anneals would generate EOR defects

in their earlier nucleation, growth and coarsening stages, while high temperature anneals would result in defects further along in their evolution, possibly in the dissolution regime [KEY01]. The evolution of the Type II damage observed in this study concurs with previous findings, as the EOR defects are observed to evolve from {311}-type defects into dislocation loops with increasing fRTP anneal temperature. However, there has been no previous evidence of the EOR defects evolving from these dot-like structures to {311}-type defects.

The structure of the dot-like interstitial clusters observed after the 700°C iRTP and 1100°C fRTP anneals proved difficult to discern from the PTEM images. The exact configuration of small interstitial clusters has been the center of a number of investigations, yet very little is still known. Recent experimental and theoretical data [KIM89, GIL95, COW99 and CHI02] demonstrates that precise cluster sizes exhibit enhanced stability, indicated by the existence of minima and maxima in the cluster binding energy curve. However, considerable debate remains over the exact sizes of the stable clusters. Cowern [COW99] found that interstitial clusters which consisted of more than twenty atoms had a similar differential formation energy to the {311}-type defect, suggesting that the interstitial clusters undergo a transition to {311}-type defects at a smaller cluster size. Other investigations [DES00, CLA01 and CLA02] support this idea and suggest that the transition from small interstitial clusters to {311}-type defects occur for interstitial clusters containing eight atoms. Hence the small interstitial clusters observed at 700°C iRTP and the 1100°C fRTP may in fact be {311}-type defects, since the total number of atoms in these structures exceeds 8 atoms and the smallest defect that can be imaged by a conventional TEM is approximately 100 atoms [ROB00]. Other

studies [GUT01, KIN03b] of lower energy germanium amorphizing implants propose that small interstitial clusters may exhibit defect morphologies very similar to plate-like dislocation loops. These dislocation loops have been shown to be very unstable, dissolving with an activation energy of 1.13 ± 0.14eV [KIN03a]. If the dot-like interstitial clusters in these experiments are analogous to the loops observed by Gutierrez and King then any additional thermal budget applied to them should result in a defect dissolution behavior in accordance with their kinetics.

In an effort to corroborate that the defect evolution captured during the lower fRTP temperatures, was in its initial stages, post flash thermal anneals were conducted. The experimental selection was based on the notion that the additional thermal budget would coarsen or evolve the EOR damage if it was in its infancy or dissolve the damage if the dissolution adhered to the findings of King et al [KIN03a]. The modification to the original experiment entailed cleaving the wafer which was annealed at a 700°C iRTP, 1100°C fRTP thermal condition into 3x3cm^{2} pieces. The sample surfaces were then cleaned with a solution of acetone and subsequently annealed in an AG Associates 210 Rapid Thermal Annealer under nitrogen ambient. The thermal profile comprised a ramp up to an intermediate soak temperature of 600°C at a heating rate of 100°Cs^{-1}; at which the temperature was held constant for 10 seconds. After which the temperature was increased at the same heating rate to 950°C, where the dwell time was 0 seconds. The wafer was then cooled by radiative heat loss at a rate of approximately 50°Cs^{-1}. The anneal temperature was selected based on past studies [CAM02] conducted on 30keV germanium pre-amorphizing implants, which demonstrated the presence of dislocation loops in the microstructure after a similar anneal. PTEM images of the EOR defects both

before and after the 950°C spike RTA are illustrated in Figure 4-7. It is obvious that the 950°C spike RTA evolved the EOR defects from dot-like interstitial clusters, which were present after the 1100°C fRTP anneal, to dislocation loops of much lower density. The defect density and trapped interstitial population determined for the sample after the 950°C spike RTA are shown in Figure 4-8. This critical data provided the evidence needed to substantiate the supposition that at the lower fRTP anneal temperatures, the system was in fact in the early stages of evolution. Robertson [ROB00] demonstrated for amorphizing implants that approximately 75% of {311}-type defects unfaulted to dislocation loops. Hence it can be inferred that a possible evolutionary path from the dot-like interstitials to dislocation loops involved the formation of {311}-type defect. This inference is supported by the existence of the {311}-type defect in the microstructure after the 1200°C fRTP anneal. The evolution of {311}-type defects from dot-like interstitial clusters have not been previously reported and strongly suggest the existence of another defect regime prior to the formation of the {311}-type defect and dislocation loop. Additionally, it was concluded that the dot-like interstitial clusters observed were not similar to the structures investigated by Gutierrez and King [GUT01, KIN03a, KIN03b], since defect dissolution did not occur upon annealing.

{311}-type defects have been shown to be relatively unstable, dissolving after only 3 minutes at 815°C with an activation energy of 3.7eV [EAG94, STO97]. These dissolution kinetics indicate that such defect structures can only exist at very high anneal temperatures for extremely short anneal times. Keys et al [KEY01] demonstrated that it is possible to effect similar defect structures and diffusion states at different anneal temperatures by determining an “equivalent” anneal time. Knowledge of the time, t_1

required for {311}-type defect dissolution at a given anneal temperature, T_1 allows one to calculate the anneal time, t_2 required to effect similar defect structures at another temperature, T_2 from the ratio of the time constants for decay, τ in accordance with the relation

$$t_2 = \frac{\tau_1 t_1}{\tau_2} \tag{5.1}$$

in which τ is related to the anneal temperature, T by an Arrhenius relation given by equation 5.2 that includes an activation energy, E_a, a pre-exponential factor, τ_0 and the Boltzmann constant, k

$$\tau = \tau_0 \exp\left(\frac{E_a}{kT}\right) \tag{5.2}$$

The value of the E_a used in the calculation is based on the dominant defect structure present in the microstructure. Thus in the case of the {311}-type defect, the activation energy for {311}-type dissolution, 3.7eV [EAG94, STO97] is used. Table 4-1 shows the estimated times at the fRTP temperatures required for {311} defect dissolution. Approximately 5ms at 1200°C is required to effect total {311}-type defect dissolution. This time exceeds the size of the radiation pulse produced by the flash lamps by an order of magnitude. Hence the presence of {311}-type defect in the microstructure after the 1200°C fRTP is plausible, since the time of the flash anneal was insufficient to effect dissolution based on the equivalent anneal time calculation. A similar argument holds for the occurrence of dislocation loops upon annealing at 1300°C. Dislocation loops are known to be more stable than {311}-type defects and to dissolve with an activation energy of ~5.0eV [SEI85]. Such defect structures formed for low energy germanium PAI have been shown to be completely removed by RTAs conducted at 1050°C for 10s

[JAG87] and 1100°C for 2s [JON93]. Applying the relation in equation 5.1 and an activation energy, E_a of 5.0eV [SEI85], to determine the time required for total dissolution of these extrinsic defects at 1300°C, yields an anneal time of roughly 9ms, as shown in Table 4-2. This value is also an order of magnitude greater than the time for which the wafer was subjected to this temperature during the flash-assist RTP anneals. Hence it is conceivable that dislocation loops would still be present in the microstructure after the 1300°C fRTP anneal.

The number of interstitials trapped by the EOR defects remained effectively unchanged for the sample subjected to the 700°C iRTP and the 1100°C fRTP anneals. The extremely small defect sizes at these temperatures made it exceedingly difficult to determine the exact area of the dot-line interstitial clusters which were present in the microstructure at this time, introducing a larger error in the analysis. However the values obtained are in agreement with previous studies which examined the number of trapped interstitials for germanium amorphizing implants [GUT01, AVC02]. At the higher fRTP anneal temperatures, the larger defect sizes allowed for the determination of the trapped interstitial density with more confidence. Hence, the reduction in the number of trapped interstitials observed between 1100 and 1300°C fRTP anneal temperatures is believed to be accurate. This reduced number can possibly be accounted for by defect dissolution and interstitial recombination at the surface.

It is important to recognize that no one process is occurring at any single time during the thermal cycle but a series of complex simultaneous reactions, which includes amorphous layer re-crystallization, changes in interstitial supersaturation as the temperature is varied, nucleation of defects, their growth and dissolution, and interstitial

diffusion and recombination, to name a few. Immediately after the implantation process, at the beginning of the thermal cycle, the interstitial supersaturation is at its maximum level. During this time nucleation of the interstitial clusters occurs in an attempt to reduce the free energy of the system. This has been shown to occur almost instantaneously, within the first second of the anneal [BON96, BON97, CLA97]. Once nucleation has occurred the interstitial clusters enter the growth regime, in which they increase in size by binding interstitials until a dynamic equilibrium is attained with the interstitial supersaturation in their vicinity. It is widely believed that the amorphous-crystalline interface initially acts as a barrier to interstitial diffusion to the surface during the amorphous layer re-crystallization. Consequently, only when the amorphous layer is completely re-grown can the surface act as a recombination site. However, it has also been suggested that the moving interface itself acts as a recombination site for the interstitials. This is not totally unreasonable, since models postulated for the amorphous to crystalline transition require the formation new bonds with the atoms at the interface in the crystalline phase [DRO82]. Hence, it is plausible that these dangling bonds are satisfied by free interstitials.

The interstitial supersaturation gradient between the EOR defect band and the silicon surface drives the surface recombination reaction. Therefore, a higher interstitial supersaturation at the defect band results in a higher recombination rate, as demonstrated by Law [LAW98]. Thus throughout the growth process interstitials are continually lost to the surface provided the interstitial supersaturation gradient to the surface is high enough. Only when the system enters the Ostwald ripening regime, in which there is an exchange of silicon atoms between the defects such that the larger defects grow at the expense of

the smaller defects, is the surface no longer a strong recombination site for the silicon interstitials [BON97]. The system is then viewed as a closed box in which the interstitial flux flows from the small defects to the larger defects due to the differences in the defect equilibrium interstitial supersaturation levels. The likelihood that an interstitial is re-captured by a defect then is much higher than it diffusing to the surface, since the inter-defect distance is much smaller than the distance to the surface.

The nature of the Flash-assist RTP employed in these experiments was such that the system effectively had zero dwell time at any given temperature, except at the final fRTP temperature, which was less than a millisecond. A direct consequence of this is that the system was always in a dynamic condition, in which the temperature was continually changing with resultant changes in temperature dependent properties such as the silicon interstitial diffusivity and supersaturation. Presumably, since the iRTP ramp rate and temperature were held constant for the experiment, the nucleation of interstitial clusters, which is believed to occur almost instantaneously on annealing [BON96, BON97, CLA97], would be very similar for all cases despite the final flash temperatures attained. It can therefore be inferred that the differences in the subsequent thermal profiles effected the changes observed in the EOR damage, provided that the assumption of the same initial nucleation condition is valid. An increase in temperature translates into higher interstitial diffusivities and lower interstitial supersaturations [COW99] and vice versa. Higher interstitial diffusivities mean an increase in the probability of an interstitial reaching the surface; while a decrease in the interstitial supersaturation in the defect layer reduces the driving force for interstitial diffusion to the surface. Both these factors have a direct impact on the interstitial surface recombination rate, which has been shown to be a

di-interstitial mechanism proportional to the square of the interstitial supersaturation [LAW98]. The effect of the surface can only be considered however, once the amorphous layer re-crystallization is completed.

In this work, complete amorphous layer re-growth was shown to occur at different points in the thermal cycle. Hence the surface served as a recombination site at different stages of the anneal sequences. The duration of time for which the surface is available for interstitial recombination can have an enormous impact on the interstitial supersaturation and consequently on the number of interstitials captured by the defects as they evolve. Additionally the temperatures attained directly impact the silicon interstitial diffusivity and interstitial supersaturation, which also influences the recombination rate. As previously discussed total re-growth of the amorphous layer required the entire duration of the anneal for the wafer which was only subjected to a 700°C iRTP anneal. This suggests that the surface probably was not an effective recombination site for interstitials during the nucleation and growth of the EOR damage. Therefore it is not unreasonable to assume that this anneal would have yielded the highest concentration of interstitials captured by the EOR defects. However, for the higher fRTP anneal temperatures total re-crystallization was estimated to occur during the ramp up, at a temperature of 1000°C. Hence, the surface was available for interstitial recombination for temperatures exceeding this value and throughout the high temperature portion of the thermal anneal. Thus the reduction in interstitial concentrations during the fRTP is plausible. It is conceivable that the surface recombination rate is higher as the fRTP temperature is increased, owing to the higher attainable interstitial diffusivities. However, the inherent reduction in the interstitial supersaturation with increasing temperature yields a smaller recombination

rate as demonstrated by Law et al [LAW98]. These competing factors determine the final number of interstitials in the EOR which are available for growth of the extended defects. Thus the continual loss of interstitials from the defect band to the surface as the defects grow may be a valid contributing factor to the reductions in trapped interstitials observed between 1100 and 1300°C fRTP anneals. This continual loss of interstitials leads one to imagine the system as a "leaky box" in which the EOR defects coarsen.

Robertson et al. [ROB00] demonstrated, for amorphizing implants, two possible evolutionary pathways for {311}-type defects; ~ 25% dissolution and ~75% unfaulting to dislocation loops. In accordance with Eaglesham's studies, alluded to previously, {311}-type defects have started to dissolve for anneal times less than 30 seconds at a temperature of 815°C [EAG94]. It is therefore likely the 1200°C fRTP resulted in some {311}-type defect dissolution, which would account for the reduced number of trapped interstitials observed between 1100 and 1200°C fRTP. A similar argument may hold for the rapid decline in the interstitials contained in dislocation loops observed at 1300°C, since sufficient time was spent at the fRTP temperature to induce dissolution in accordance with Seidel's kinetics. [SEI85]. Another possible theory therefore for the reduced number of interstitials observed with increasing fRTP temperature is dissolution of the extended defects.

It proves difficult to pinpoint the origin of the reductions in the number of trapped interstitials since isochronal anneals were performed due to the nature of the Flash-assist RTP. Thus, snapshots of the damage for given fRTP temperatures were examined opposed to isothermal anneals in which the defect evolution could be more carefully tracked. Therefore it cannot be said without any reasonable doubt whether the interstitial

loss to the surface or defect dissolution or both processes played a role in the decline in trapped interstitial densities. It seems unlikely in such a complex system that one mechanism will solely dominate the reduction in interstitials observed. The author is inclined to believe that both interstitial losses to the surface and defect dissolution play a role in the reduced interstitial concentrations evident in the EOR damage.

4.5 Conclusions

The effects of increasing the fRTP temperature in Flash-assist RTP on the EOR damage formed for a 30keV, $1x10^{15}cm^{-2}$ germanium amorphizing implant into (100) silicon has been investigated. Analysis of the microstructure revealed the presence of dot-like interstitial clusters following the 700°C iRTP and the 700°C iRTP, 1100°C fRTP anneals. An increase in the fRTP anneal temperature to 1200°C fRTP and 1300°C fRTP resulted in the formation of {311}-type defects and dislocation loops, respectively. This defect evolution concurred with the widely accepted theories that the EOR defects evolve from point defects to extrinsic dislocation loops via intermediate defect configurations. Sub-microscopic interstitial clusters (SMICs) [BEN97, COF00, LIB98] are thought to be the precursors for the formation of {311}-type defects [EAG94, STO97, PAN97], which are metastable and eventually unfault to form dislocation loops [LIJ98].

The very fast ramp rates and short anneals offered by the Flash-assist RTP has allowed investigations into the early stages of the defect evolution, which have not been probed before. Dot-like interstitial clusters are observed to dominate the microstructure in the early stages of the evolution and have been shown to evolve into dislocation loops, via a {311}-type defect configuration. This is the first experimental evidence which suggests that the dot-like interstitial cluster is a precursor for the formation of the {311}-type defect, which is an important result of this work.

Additionally, as the fRTP temperatures were increased they effected advanced stages of the EOR defect evolution, which proved that the Flash-assist RTP is capable of evolving the EOR damage. The reduced defect densities and trapped interstitial doses observed with increasing fRTP temperatures were attributed to both interstitial losses to the surface and defect dissolution.

These findings are technologically important from a leakage and carrier mobility perspective for CMOS processing.

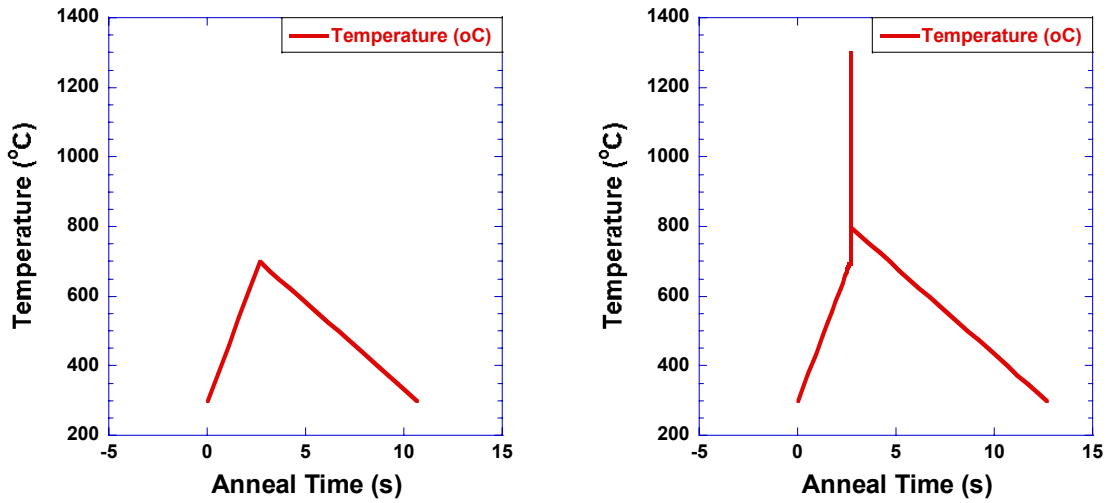

a) b)

Figure 4-1. Temperature-time profiles of the thermal anneals used in this study. a) iRTP anneal and b) fRTP anneal.

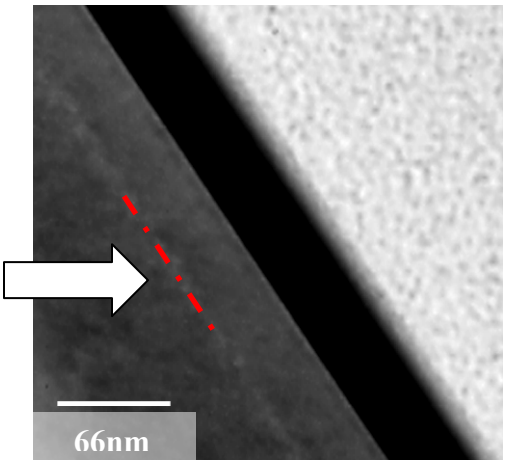

Figure 4-2. XTEM images, taken under g_{110} BF conditions, of the re-grown amorphous layer subsequent to the 700°C iRTP anneal in which the EOR damage can be seen at a depth of ~55nm.

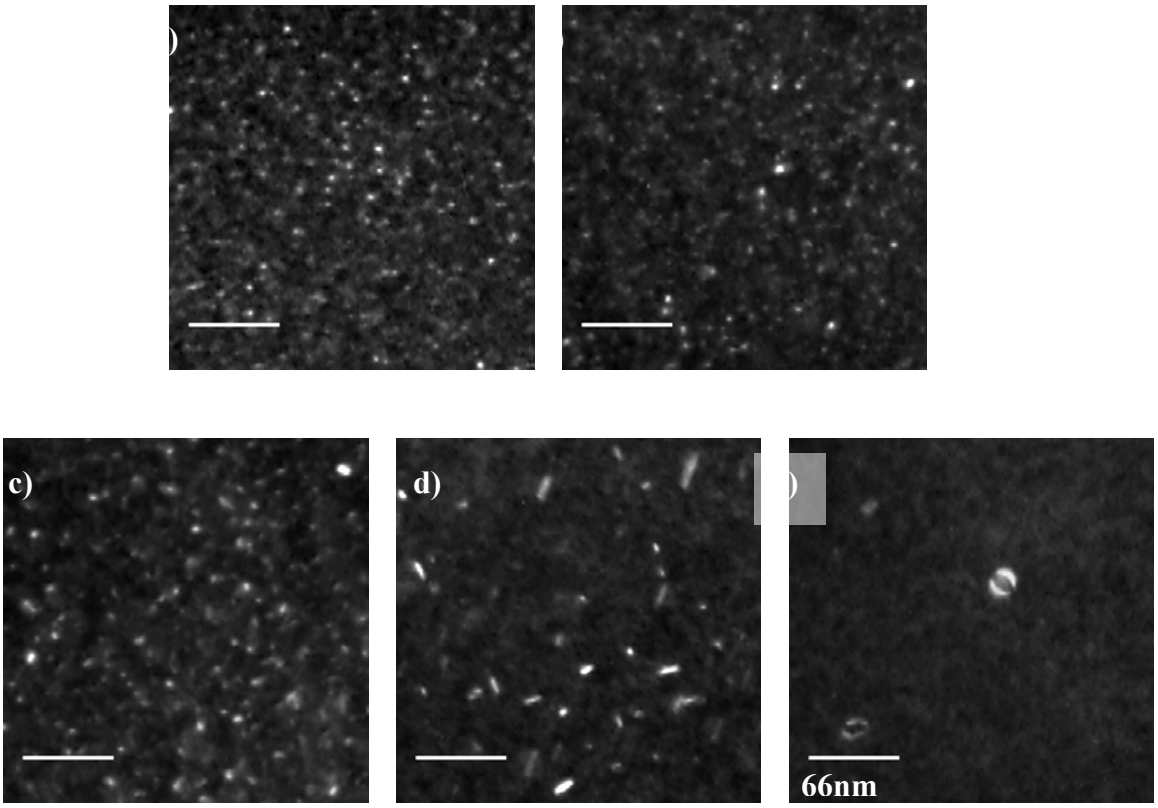

Figure 4-3. WBDF PTEM images of the EOR defects imaged under g_{220} two-beam conditions of the 30keV $1x10^{15}cm^{-2}$ germanium amorphizing implant. a)700°C iRTP, b) 700°C iRTP,1000°C fRTP, c) 700°C iRTP, 1100°C fRTP, d) 700°C iRTP, 1200°C fRTP, e) 700°C iRTP, 1300°C fRTP

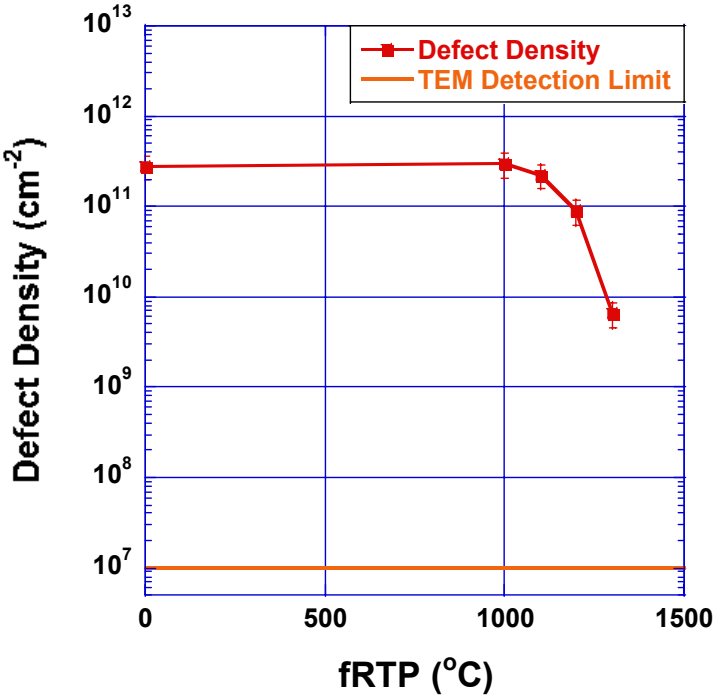

Figure 4-4. Defect density as a function of fRTP anneal temperature for a $1x10^{15}cm^{-2}$ 30keV Ge amorphizing implant

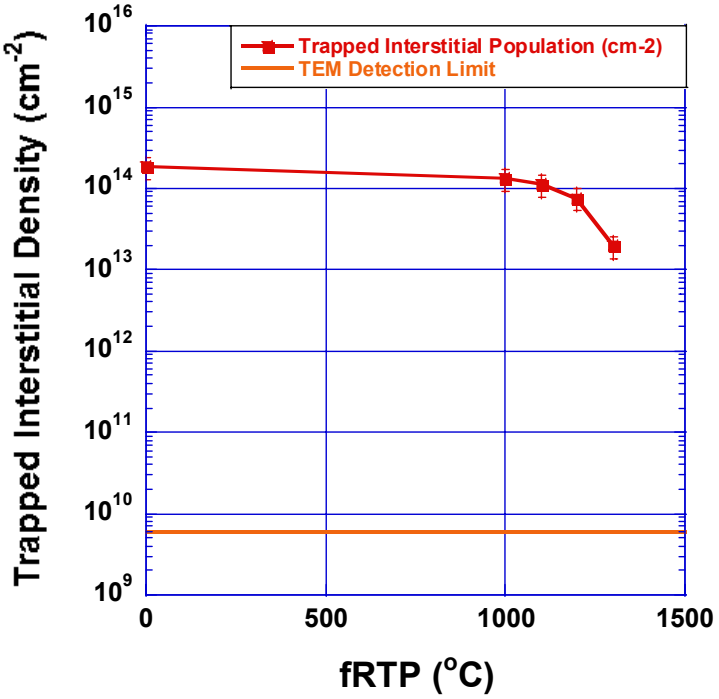

Figure 4-5. Trapped interstitial density as a function of fRTP anneal temperature for a $1x10^{15}cm^{-2}$ 30keV germanium amorphizing implant

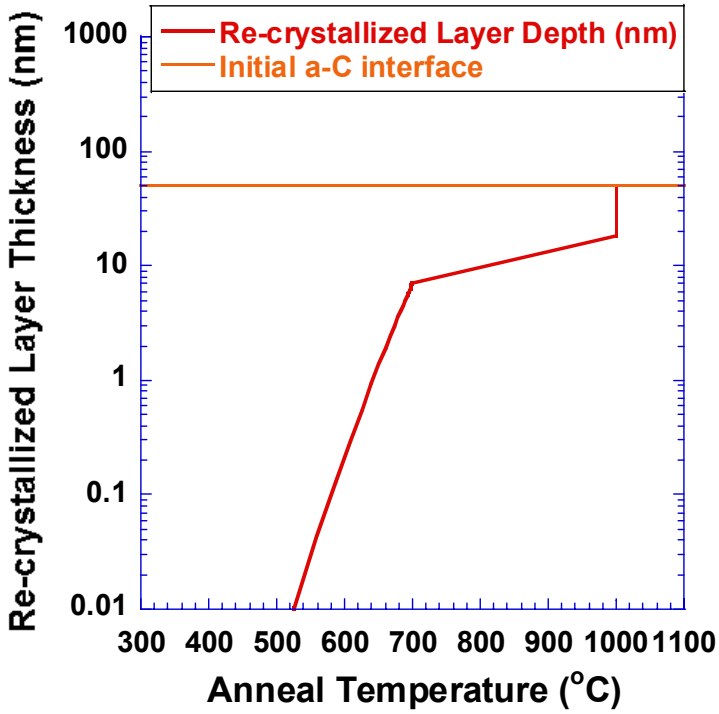

Figure 4-6. Estimated re-crystallized layer thickness for the 700°C, 1000°C iRTP anneal as a function of the anneal temperature determined by taking the integral of the regrowth velocity-time variation.

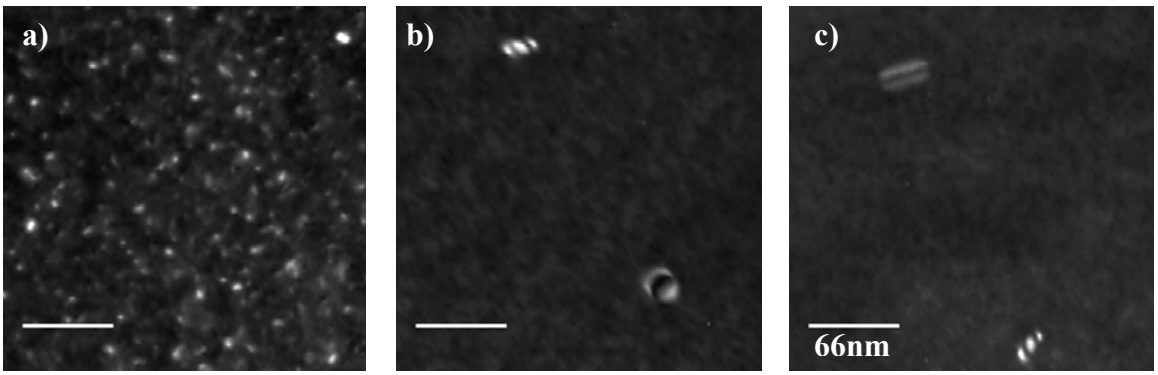

Figure 4-7. WBDF PTEM images of the EOR defects imaged under g_{220} two-beam conditions of the 30keV $1x10^{15}cm^{-2}$ Ge amorphizing implant. a) 700°C iRTP, 1100°C fRTP b) 700°C iRTP, 1100°C + 950°C spike RTA c) 950°C spike RTA only

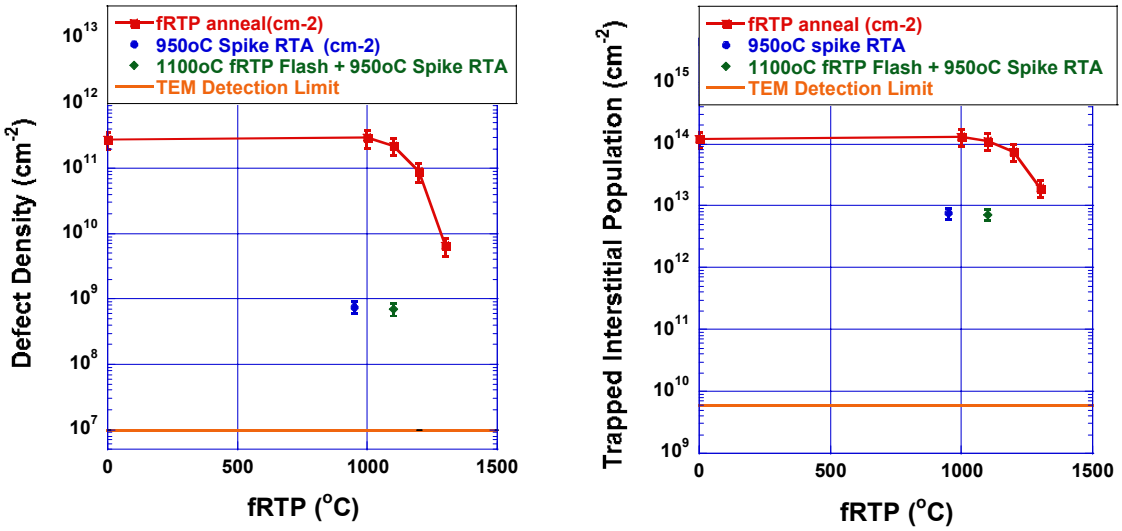

a) b)

Figure 4-8. Quantitative transmission electron micrsocopy results for a $1x10^{15}cm^{-2}$ 30keV germanium amorphizing implant subjected to a 700°C iRTP, 1100°C fRTP anneal only and 700°C iRTP, 1100°C fRTP anneal + 950°C spike RTA. a) Defect density and b) Trapped Interstitial density as a function of fRTP anneal temperature.

Table 4-1. Estimated equivalent anneal times for {311}-type defect dissolution at the fRTP anneal temperatures, based on a known dissolution time of 180s at 815°C

Anneal Temperature (^{o}C)	Anneal Time (s)
815	1.80×10^{2}
1000	5.79×10^{-1}
1100	4.96×10^{-2}
1200	5.93×10^{-3}
1300	9.28×10^{-4}

Table 4-2. Estimated equivalent anneal times for dislocation loop dissolution at the fRTP anneal temperatures, based on a known dissolution time of 10s at 1050°C

Anneal Temperature (^{o}C)	Anneal Time (s)
1050	1.00×10^{1}
1000	5.61×10^{1}
1100	2.02×10^{0}
1200	1.15×10^{-1}
1300	9.35×10^{-3}

CHAPTER 5
KINETIC ANALYSIS OF THE END OF RANGE DAMAGE DISSOLUTION FOR FLASH-ASSIST RAPID THERMAL PROCESSING

5.1 Introduction

The nature of the Flash-assist RTP makes it is extremely difficult to reasonably compare it to alternative annealing techniques, largely because the annealing time at a given temperature is dictated by the FWHM of the radiation pulse. The FWHM for current flash tools vary between 0.85 and 1.38ms, which compares to a FWHM of 2s for a RTA to achieve similar temperatures. Since the annealing time at the target temperature for the Flash-assist RTP is essentially fixed to very small times on the order of milliseconds, isochronal anneals are a logical experimental approach to temperature dependent studies. However, such anneals yield defect morphologies at different stages of the defect evolution. For instance a lower temperature anneal is expected to probe the early stages of the evolution such as nucleation and growth, whereas a high temperature anneal may capture the defects further along in their evolution, possibly in the dissolution regime. Traditionally, the kinetics of the extended defect have been studied by time dependent studies utilizing isothermal anneals [SIE85, EAG94, STO97, KIN03]; in which specific defect structures could be isolated. The characteristics of Flash-assist RTP do not allow for such investigations in which the EOR defect evolution could be closely tracked with time. This fact presents a challenge in the data analysis and comparison, since different defect structures are detected at each fRTP anneal temperature investigated.

Another feature of Flash-assist RTP which makes the analysis complex is the ramp time relative to the dwell time spent at the peak fRTP temperature. The ramp up to and ramp down from the desired anneal temperature becomes increasingly important in analyzing an anneal process, as the time spent at the target temperature is decreased. The corresponding ramp up and ramp down times required for each fRTP anneal is shown in Table 5-1, in which it is evident that the ramp times are on the same order as the FWHM of the anneal pulse itself. The ratio of the FWHM value to the total ramp time which is also shown, illustrates that as the fRTP temperature is increased the total ramp time can exceed the dwell time at the peak temperature. This simple calculation emphasizes the importance of accounting for these portions of the thermal profile, which may play a significantly larger role in dictating the final material properties.

The inherent characteristics of Flash-assist RTP have consequently required the development of another approach to analyzing the attainable experimental data, such that a meaningful comparison could be made to past studies. The adopted analysis method entailed the selection of a reference anneal, from which the decay in the trapped interstitial density was tracked with the fRTP anneal temperature, allowing for the kinetics of the interstitial decay to be extracted. This analytical procedure as well as the data analysis is discussed in the ensuing sections.

Appendix B contains the respective data for the 8keV germanium amorphizing implant.

5.2 Data Analysis

Past studies which focused on investigating the kinetics of the EOR damage [SIE85, EAG94, STO97, KIN03] have tracked the decline in interstitials trapped in the extended defects with time over various temperatures. However, as alluded to in the

introduction, the inherent attributes of Flash-assist RTP do not allow for time dependent studies in which the defect evolution could be carefully tracked. As a result, an alternative approach was necessitated for the data analysis in which the attainable information could be beneficially analyzed.

In the previous chapter, the trapped interstitial density was observed to decrease as the fRTP anneal temperature was increased above the iRTP temperature. This plot is reproduced for convenience and is shown in Figure 5-1. The reductions in trapped interstitial density suggested that the additional thermal budget associated with the fRTP anneal effected the interstitial losses from the EOR damage. In order to extract the kinetics associated with the interstitial decay, it was necessary to estimate the rate at which these interstitials were being lost. This calculation required at least two data points. The experiment yielded the number of trapped interstitials for each fRTP anneal, which served as one data point. However, the initial trapped interstitial concentrations were not available; hence an assumption had to be made. Since the iRTP anneal temperature from which all the fRTP anneals were conducted was not varied for the experiment, it was assumed that the interstitial density obtained for this temperature could serve as an initial trapped interstitial value, as all the wafers were subjected to this temperature prior to the fRTP anneal. This allowed for the decay in the trapped interstitials during the flash portion of the thermal profile i.e. fRTP anneal, to be extracted such that the effect of the flash on the defects could be isolated.

Figure 5-1 noticeably demonstrates that the trapped interstitial decay follows an exponential relation with fRTP temperature. Hence, in accordance with kinetic rate theory the interstitial decay was approximated by the relation

$$\frac{\partial C_{interstitials}}{\partial t} = -\frac{C_{interstitials}}{\tau} \qquad (5\text{-}1)$$

where $C_{interstitials}$ is the concentration of trapped interstitials (cm^{-2}), t(s) is anneal time and τ(s) is the captured interstitial lifetime, which is related to the anneal temperature, T (K) by an Arrhenius expression that includes an activation energy, E_a.

$$\tau = \tau_0 \exp\left(\frac{E_a}{kT}\right) \qquad (5\text{-}2)$$

The process simulator FLOOPS [LAW03] was utilized to calculate the trapped interstitial density for each fRTP anneal temperature from an initial trapped interstitial density (value for the 700°C iRTP anneal), by fitting the parameters τ_0 and E_a. The simulation incorporated the temperature-time variation for each anneal, thus enabling τ to be accurately accounted for in time as the temperature was varied. This facilitated a precise integration of the trapped interstitials with time. Figure 5-2 is a plot generated from the FLOOPS simulation, which indicate the simulated temperature profiles. The FLOOPS simulation code can be found in Appendix B. Table 5-2 contains the simulated and experimental trapped interstitial values, which are well within the 20% error associated with data extracted from TEM plan-view micrographs. The close agreement between the trapped interstitial populations for the simulations and the experiment is also demonstrated in Figure 5-3. While the decay rates derived from the fits of the experimental trapped interstitial populations are illustrated in Figure 5-4. The interstitial decay rate varied linearly with the inverse fRTP temperature, yielding an activation energy, E_a of 2.1 ± 0.05eV and pre-exponential factor, K_0 of 3.3×10^{10} s^{-1}. The interstitial

decay rates varied over two orders of magnitude for the fRTP temperatures investigated, from approximately $100s^{-1}$ at $1000^{o}C$, compared to $2000s^{-1}$ at $1200^{o}C$.

5.3 Discussion

In an effort to extract useful information from the data obtained in these experiments, it was necessary to employ a new approach to analyzing the data compared to the methods that have been previously used, owing to the inherent nature of the Flash-assist RTP. In Flash-assist RTP there is limited control over the annealing time as this is dictated by the FWHM of the radiation pulse. The FWHM in current available flash tools is limited to 0.85-1.38ms, which makes it impossible to conduct time dependent studies; therefore a logical experimental approach is the use of isochronal temperature dependent studies. However, such studies yield information on the different phases of the defect evolution, which presents a challenge to the data analysis and comparison. Investigations of the kinetics of the defect decay were traditionally performed by fitting the interstitial density with time over various temperatures to an exponential function of the form of Equation 5-1. In these cases isolated defect structures such as {311}-type defects [EAG94, STO97] and dislocation loops [SIE86, KN03] were examined, enabling the kinetics for each defect type to be extracted. In these experiments a similar approach is used, in which the interstitial decay is tracked with time, but over the fRTP anneal portion of the thermal profile. However, it was impossible to follow the interstitial decay for a single isolated defect structure; hence the interstitial data obtained was for the evolved structures as the fRTP temperature was varied.

It is important to recognize that a number of simultaneous complex reactions are occurring during the thermal cycle, which impacts the interstitial population in the microstructure. The nature of the Flash-assist RTP is such that the system is in a

continuous dynamic state as the time spent at the target temperature is on the order of milliseconds. Hence a significant portion of the thermal anneal is spent in either the ramp up or ramp down stages of the thermal profile, as demonstrated in Table 5-1. As a consequence, the interstitial supersaturation and diffusivities are directly impacted and are not fixed values. These parameters have a large influence on the interstitial recombination rate, which has been demonstrated to be a di-interstitial mediated mechanism proportional to the square of the interstitial supersaturation [LAW98]. Hence at higher temperatures, the recombination rate should decrease with the reductions in supersaturation levels. Conversely, larger interstitial diffusivities at higher anneal temperatures increases the probability of interstitial recombination. These competing mechanisms dictate the interstitial recombination rate, which varies with the system temperature. At the fRTP anneal temperatures investigated, both the defect and trapped interstitial densities of the dot-like structures were seen to simultaneously fall of as the temperature is increased, which was discussed in the previous chapter. These events suggest that the defects may be in a coarsening regime in which a fraction of the interstitials is not re-captured by other defect structures. The likelihood that interstitials are continually lost by recombination at the Si-SiO_2 interface or at the amorphous-crystalline interface during the re-crystallization process is therefore high. Consequently, the system is viewed as a “leaky box” from which interstitials are lost as the EOR defects undergo coarsening.

Interstitial loss from the EOR by defect dissolution is also a likely process to account for the reductions detected. Robertson et al. [ROB00] demonstrated approximately 25% of the {311}-type defects undergo dissolution versus the unfaulting

process to form dislocation loops. Furthermore, application of the dissolution kinetics for {311}-type defects [EAG94, STO97] and dislocation loops [SEI85], established that this process was a viable explanation for the diminished interstitial densities observed at 1200 and 1300°C fRTP temperatures. Both of these processes of interstitial losses via recombination and defect dissolution have therefore been attributed to the fall in trapped interstitial densities, as concluded in the previous chapter. The kinetic parameters extracted in this work therefore are pertinent only to the interstitial loss from the EOR defects during the flash portion of the thermal profile (i.e. fRTP anneal), since the root cause for the drop in trapped interstitials could not be pinned to any particular process and more than one defect structure was analyzed to yield the trapped interstitial data presented herein.

Figure 5-5 depicts the interstitial decay rates for {311}-type defects [EAG94] and dislocation loops [SEI85, KIN03] obtained from the literature as a function of the inverse anneal temperature, on which the experimental data from this work is also included. The present study clearly investigates the interstitial decay from the EOR defects at temperatures which have not been studied in the past. In all cases the interstitial decay rate increases with temperature, in accordance with the relation of equation 5-2. One of the most striking features of the plot is the much higher interstitial decay rates obtained for Flash-assist RTP compared to the former studies. The interstitial decay rates obtained for the Flash-assist RTP ranged two orders of magnitude between $1x10^{2}$ and $1x10^{3}s^{-1}$ for fRTP temperatures from 1000 through 1300°C. The work of Seidel et al. [SEI85] determined the maximum rate previously reported for interstitial decay from the EOR damage, on the order of $1x10^{-1}$; three orders of magnitude lower than the minimum value

obtained in this work. Seidel obtained rates for these temperatures which were on the order of $1x10^{-2}$ and $1x10^{-1}s^{-1}$, compared to $1x10^{2}$ and $1x10^{3}s^{-1}$ for Flash-assist RTP. The decay rates were clearly very different. The interstitial diffusivities were expected to be comparable, since the diffusivity is related to the temperature by an Arrhenius expression [GUE96] and the anneal temperatures in both experiments are similar. Hence this argument does not hold for the differences in the interstitial reduction rates. Additionally, Seidel examined the dissolution of stable dislocation loops, while in this work the interstitial counts of various defect structures were taken into account. The high decay rates obtained in this study suggest the interstitial loss is probably not from a defect similar in structure to the dislocation loops investigated by Seidel. Rather it is suggestive of the existence of a highly unstable defect structure.

Examination of the differences in the activation energies for defect dissolution in the literature may provide further insight into the characteristics of the proposed highly unstable defect. The extracted activation energy for Flash-assist RTP was found to be approximately 2.1eV, which is 2.7eV and 1.6eV smaller than the values obtained for dislocation loop and {311}-type defect dissolution, respectively. Seidel extracted an activation energy of approximately 4.8eV [SEI85] for interstitial loss from dislocation loops, which is remarkably similar to the activation energy value for silicon interstitial self-diffusion [URA98, BRA98], whereas the activation energy for {311}-type dissolution was determined to be 3.7eV [EAG94]. Most recently, King's studies revealed the existence of dot-like dislocation loops which dissolved with an activation energy of 1.13eV [KIN03]. In the previous chapter, it was demonstrated that the dot defects observed in this work did not adhere to the dissolution kinetics of those defects, thus

ruling out this possibility. The fact that the activation energy determined for the interstitial decay in this work is not similar to those previously extracted values, strongly suggests that the interstitial loss may not be from comparable defect structures. Rather, it hints at the existence of a less stable defect structure; possibly the dot-like defects which were observed at the lower fRTP anneal temperatures of 1000 and 1100°C, prior to {311}-type formation.

The fact that the dot-like defects were not observed in the microstructure for fRTP anneal temperatures greater that 1100°C, signifies that these defects only exist during the very early stages of annealing, which Flash-assist RTP has enabled to be investigated. At temperatures exceeding 1100°C this highly unstable defect structure may have therefore followed one of two evolutionary paths. The defects either dissolved or evolved into {311}-type defects. Since the trapped interstitial population, illustrated in Figure 5-1, fell an order of magnitude between the 1100 and 1200°C fRTP anneals, it is reasonable to assume that some defect dissolution occurred, in which a number of the interstitials were either lost to the surface or the bulk. The remaining dot-like defects must have therefore evolved into the {311}-type defect detected at higher anneal temperatures. Inspection of the microstructures annealed at 1200 and 1300°C, revealed the presence of {311}-type defects and dislocation loops, respectively, but there was no indication of this dot-like defect structure. This fact validates the supposition that the dot-like defect is a precursor for the {311}-type defect. Consequently, the extracted kinetics for the decrease in trapped interstitial density as a function of the temperature applies to the dissolution to this dot-like defect structure.

The observed defect configurations at 1200 and 1300°C, shown in Figure 5-6, are in accord with the widely accepted evolution of the EOR damage, in which {311}-type defects are known to either dissolve or unfault into dislocation loops when annealed [LIJ98, ROB00]. Since no dot-like defects were detected in the structure at 1200°C, then the difference in the interstitial count between 1200 and 1300°C should adhere to the kinetics for {311}-type dissolution [EAG94]. In Figure 5-6, Eaglesham's data is extrapolated to yield the {311}-type defect decay rate at 1300°C, which was determined to be approximately 4000s^{-1}. Application of this rate to the exponential relation in Equation 2-15, generated an anneal time of 0.3ms, which is the time required to account for the differences in the interstitial densities between the 1200 and 1300°C fRTP anneals. As the FWHM of the radiation pulse in this experiment ranged 0.85-0.9ms, the time spent at 1300°C during the fRTP cycle was sufficient to effect {311}-type defect dissolution. This detail also substantiates the hypothesis that the dot-like defects only exist in the very early stages of the defect evolution and either dissolved or evolved into {311}-type defects, with additional thermal budget.

5.4 Conclusions

The inherent nature of Flash-assist RTP which makes it attractive as a possible annealing technique for ultra shallow-junction formation, presents challenges in evaluating its effectiveness in eliminating the EOR damage. These challenges stem from the very short anneal times, on the order of milliseconds, that Flash-assist RTP offers. These short anneal times makes time dependent studies of the damage evolution impossible. Consequently, the use of isochronal anneals for temperature dependent studies of the EOR defect evolution is necessitated. This experimental approach yields the extended defects at different stages of their evolution, requiring an alternate method

to conventional data analysis techniques. The method employed in this work tracks the interstitial decay with anneal temperature by utilizing the initial interstitial density as that for the iRTP anneal, which was not varied for the experiment. Thus the interstitial decay rate over the fRTP portion of the anneal could be isolated, enabling the effectiveness of the flash to be evaluated.

The short anneal times and high temperatures attainable with Flash-assist RTP have enabled investigations of the early stages of the EOR defect evolution, which have revealed the existence of a highly unstable defect structure preceding the {311}-type defect. This defect is believed to be a precursor for the {311}-type defect and is thought to go through one of two evolutionary paths, defect dissolution or evolution into the {311}-type defect.

The defect dissolution kinetics was extracted using the process simulator FLOOPS [LAW03]. In order to capture the interstitial decay rate as a function of the anneal time, the captured interstitial lifetime, τ was coupled to the thermal profile of the anneal by an Arrhenius expression. This enabled τ to be accurately accounted for in time and hence the variations in the interstitial density to be precisely determined. An activation energy of 2.1eV was determined for dissolution of these dot-like defects. This is the first experimental evidence of the existence of such a defect, whose dissolution kinetics differ from previously reported defect structures.

Table 5-1. Estimated ramp times for the fRTP anneal temperatures for a ramp rate of $1x10^6$ $^oCs^{-1}$

fRTP Anneal Temperature (^{o} C)	Ramp up time from 700°C iRTP temperature(ms)	Ramp down time from fRTP anneal to wafer temperature (ms)	Ratio of the FWHM (0.9ms) to total ramp time
1000	0.30	0.20	0.50
1100	0.40	0.30	0.77
1200	0.50	0.40	1.00
1300	0.60	0.50	0.12

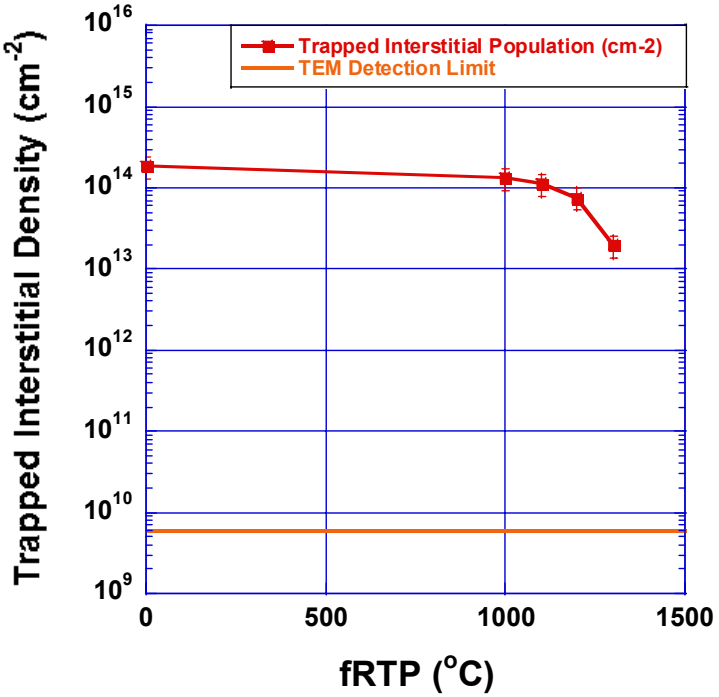

Figure 5-1. Trapped interstitial density as a function of fRTP anneal temperature for a $1x10^{15}cm^{-2}$ 30keV germanium amorphizing implant

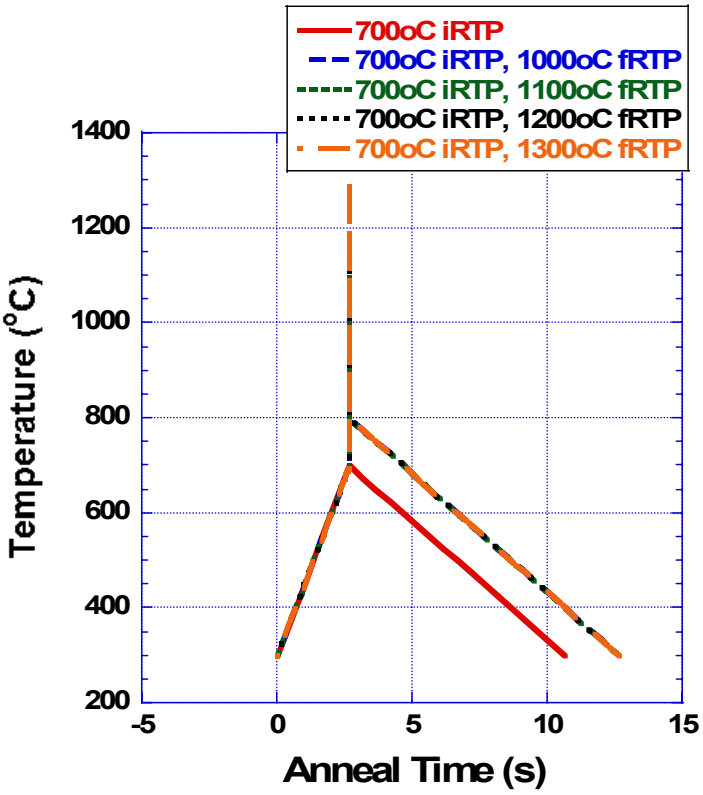

Figure 5-2. fRTP anneal temperature-time profiles generated from FLOOPS during the trapped interstitial density simulation.

Table 5-2. Simulated and experimental trapped interstitial densities and associated errors for a 30keV germanium amorphizing ion implant into (100) silicon

fRTP Anneal Temperature (^{o}C)	Simulated Trapped Interstitial Density (cm^{-2})	Experimental Trapped Interstitial Density (cm^{-2})	Error (%)
1300	1.88E+13	1.94E+13	2.93
1200	7.19E+13	7.53E+13	4.52
1100	1.06E+14	1.11E+14	4.70
1000	1.16E+14	1.31E+14	11.58

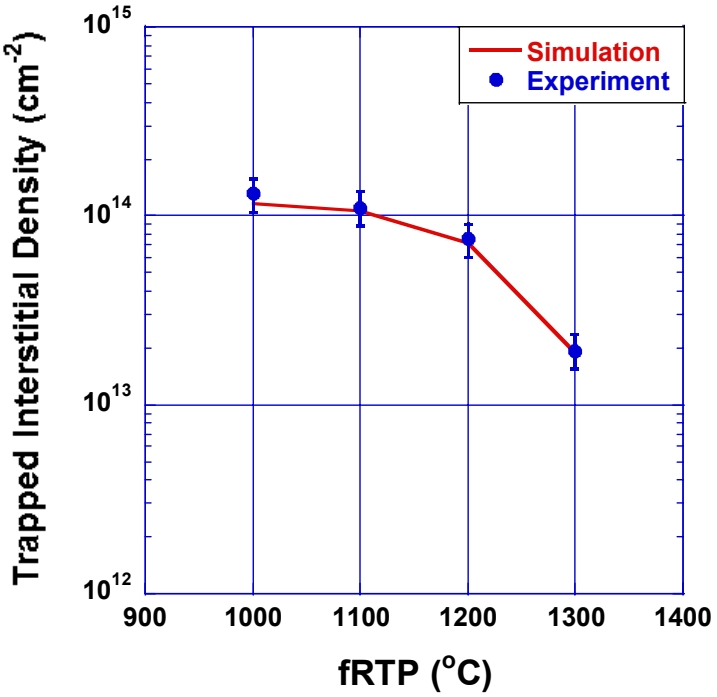

Figure 5-3. Simulated and experimental trapped interstitial densities for a 30keV, $1x10^{15}cm^{-2}$ germanium amorphizing ion implant into (100) silicon

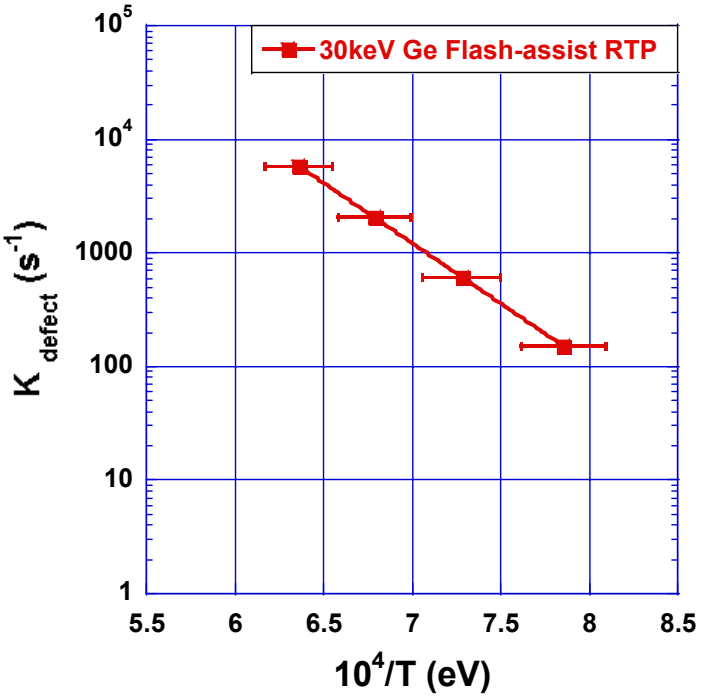

Figure 5-4. Arrhenius plot of the time constant derived for defect decay extracted from the simulated experimental data, indicating an activation energy, E_a of 2.1 ±0.05eV for dissolution

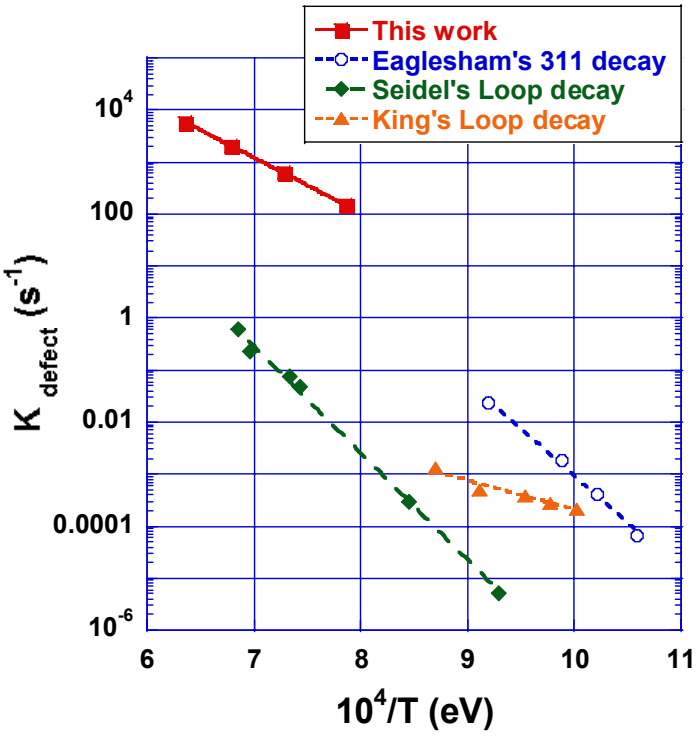

Figure 5-5. Arrhenius plot of the time constant derived for defect decay from the literature, including decay rates for {311}-type defects [EAG94, STO97], dislocation loops [SEI85, KIN03] and the dot-like defects observed in this work.

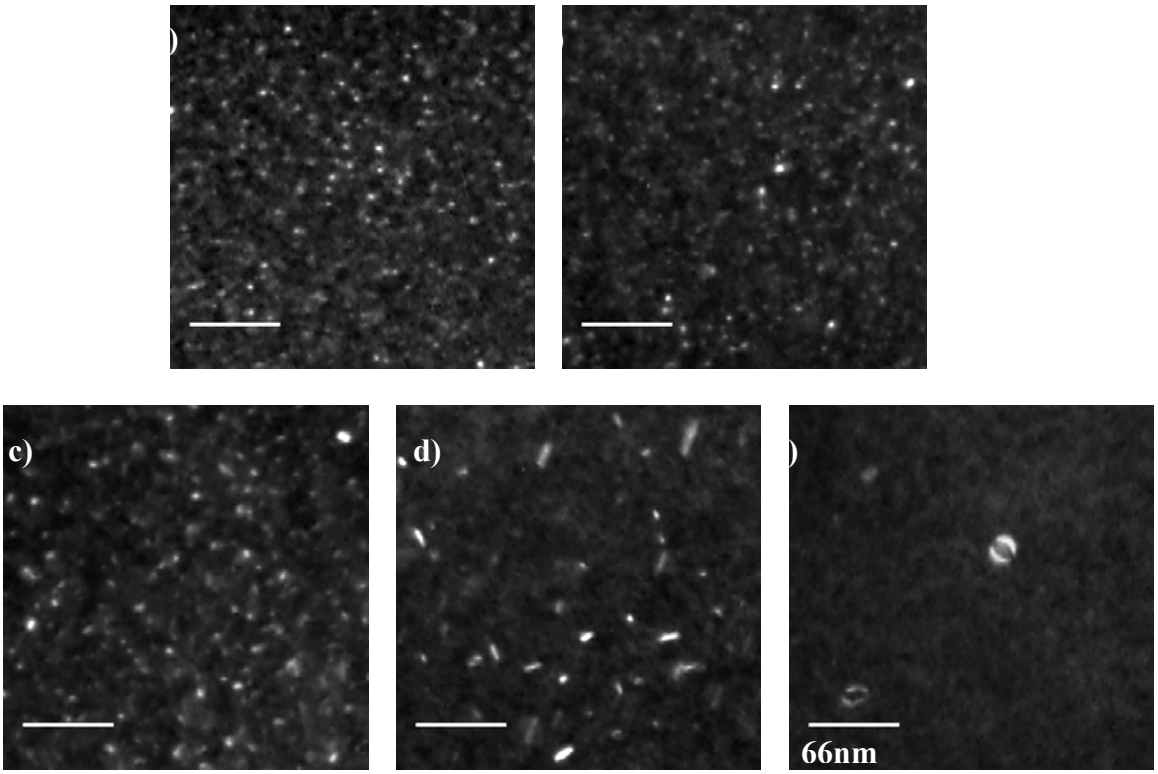

Figure 5-6. WBDF PTEM images of the EOR defects imaged under g220 two-beam conditions of the 30keV $1x10^{15}cm^{-2}$ germanium amorphizing implant subjected to flash anneals. a)700°C iRTP, b) 700°C iRTP,1000°C fRTP, c) 700°C iRTP, 1100°C fRTP, d) 700°C iRTP, 1200°C fRTP, e) 700°C iRTP, 1300°C fRTP

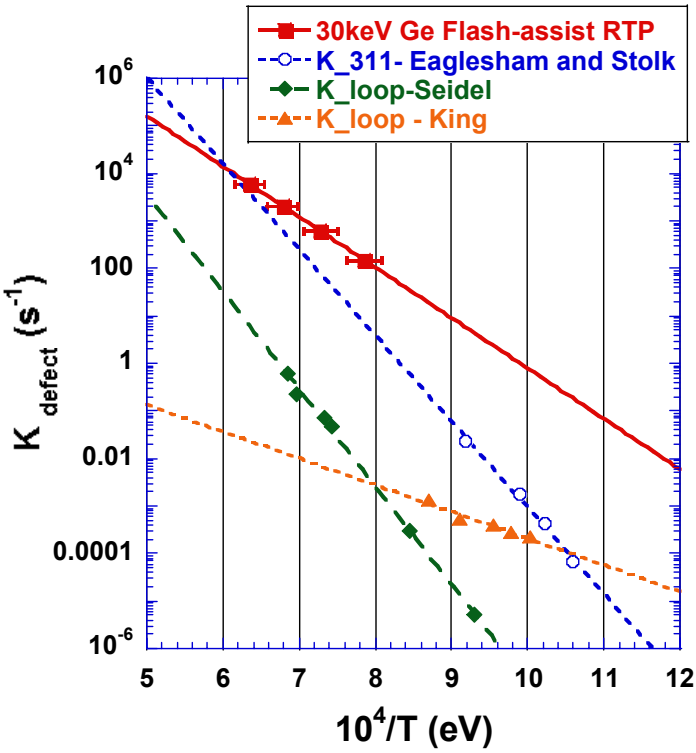

Figure 5-7. Extrapolated defect decay rates for an Arrhenius plot of the time constant derived for defect decay from the literature. Decay rates include those for {311}-type defects [EAG94, STO97], dislocation loops [SEI85, KIN03] and the dot-like defects observed in this work.

CHAPTER 6
INFLUENCE OF GERMANIUM PRE-AMORPHIZATION ENERGY ON THE JUNCTION CHARACTERISTICS OF FLASH-ASSIST RAPID THERMAL PROCESSED SILICON WAFERS

6.1 Introduction

Germanium has gained vast acceptance as amorphizing specie since it has several advantages over silicon. These advantages stem from germanium's bigger atomic size relative to that of silicon, which allows for a greater contribution to nuclear collisions. Hence an enhanced degree of disorder can be induced by germanium atoms of the same energy as a silicon amorphizing implant, and therefore a lower dose can be employed to achieve the same result. This is extremely important as it reduces the concentration of interstitials in the structure, which contribute to defect formation and anomalous diffusion of the boron. Germanium amorphization also allows for room temperature implantation; an advantage over the low liquid nitrogen temperatures required for silicon preamorphization. More recently, the amorphous interface formed with a germanium amorphizing implant has been shown to be approximately four times smoother than that formed with silicon for doses of $1x10^{15}cm^{-2}$ [ALB00], which is beneficial from a regrowth perspective.

Germanium preamorphization at low energies has the potential to take the industry through to the 35nm node [BOR01] as demonstrated on the ITRS roadmap [SEM05]. Lower energy amorphizing implants are attractive from a junction engineering perspective, since they inherently produce less damage in the silicon lattice, which immediately translates into a reduction in the probability of junction leakage.

Additionally, the number of interstitials trapped by the EOR range defects is also proportional to the implant energy [JON91]. Hence subsequent annealing processes geared towards dissolving this damage, would result in the release of a reduced number of silicon interstitials, which are known to contribute to TED [ANG86, SER87, MIC87]. However, a reduction in the energy of the implant also positions the EOR damage closer to the surface and to the shallow dopant profiles, which can have severe repercussions. The reduced relative distance between the dopant profile and the silicon interstitial supersaturation in the vicinity of the EOR damage, increases the probability of clustering reactions [COW90, STO94, LIL99], which can significantly degrade the carrier mobility [MIR02] and effect dopant deactivation [PEL99]. These issues will be explored for two germanium preamorphizing implants processed by Flash-assist RTP the following sections.

6.2 Experimental

This study utilized 200mm 12ohm-cm (100) n-type Czochralski (CZ) grown silicon wafers, which were pre-amorphized with either an 8keV or a 30keV germanium implant at a constant dose of $1x10^{15}cm^{-2}$. Boron was subsequently implanted into all wafers at an energy of 1keV and a dose of $1x10^{15}cm^{-2}$. The ion implantations were performed in an Applied Materials XR80 Leap Implanter at a twist of 27° and a tilt of 7°, in deceleration mode. Following the implantation process, the wafers were thermally annealed by a Flash-assist Rapid Thermal Process (RTP) at Vortek Technologies, Vancouver, Canada. The thermal profiles consisted of heating the wafers to an intermediate temperature (iRTP) of $700^{o}C$ at a heating rate of $150^{o}Cs^{-1}$. The material temperature was then rapidly increased to the target flash temperatures (fRTP) of 1000, 1100, 1200 and $1300^{o}C$ by an arc radiation pulse, at a heating rate of $1x10^{6}\ ^{o}Cs^{-1}$. The full width at half maximum of the

radiation pulse ranged 0.85-0.90ms. Subsequent wafer cooling was governed by radiation heat loss to the surrounding black environment at a maximum rate of $90^{o}Cs^{-1}$, once thermal equilibrium was achieved between the surface and the bulk of the wafer. A depiction of the thermal profiles to which the wafers were subjected can be seen in Figure 6-1.

Cross-sectional transmission electron microscopy (XTEM) was utilized to determine the depth of the amorphous layers formed by the germanium implants and to confirm re-crystallization of the layers upon subsequent thermal processing. The XTEM was performed on a JEOL 200CX microscope operating at an accelerating voltage of 200keV and the images were taken under g_{110} bright field conditions. The extended defects associated with the amorphizing implants were also examined on a JEOL 200CX microscope operating under similar conditions, but via Plan-view transmission electron microscopy (PTEM). Images of the defects were captured in weak-beam-dark-field (WBDF), g_{220} two-beam conditions and analyzed via the technique developed by Bharatan et al [BHA97]. In order to track the boron diffusion, the dopant concentration as a function of depth was assessed for each anneal condition by dynamic secondary ion mass spectrometry (SIMS) using an Adept 1010 Dynamic SIMS System by Physical Electronics. The data acquisition parameters included a 25nA, 1kV oxygen beam with a 10% gating and a raster area of 250μm x 250μm. Electrical characterizations of the junctions formed included sheet resistance measurements which were conducted on a Four Dimensions 333A Four Point Probe system. Type M probe tips placed 1mm apart with a 5mm edge exclusion were used in the measurements. Hall measurements were also performed to determine carrier densities and mobilities. An MMR Technologies Van der

Pauw Hall System (MPS-50, K-20 and H-50) was employed with a constant field of 3000G and the measurements performed for variable currents of 0.00001, 0.0001 and 0.001A.

6.3 Results

The 8 and 30keV germanium preamorphizing implants resulted in the formation of continuous amorphous layers that extended to respective depths of 16 and 50nm below the silicon surface. Figure 6-2 contains XTEM images of the material subjected to the 700°C iRTP anneal, in which only crystalline regions can be seen which indicates that total re-crystallization of the amorphous regions occurred during the 700°C iRTP anneal for both cases. In these images the EOR defects can be discerned beyond the original amorphous layer interface, at approximately 20 and 55nm, respectively for the 8 and 30keV germanium preamorphizing implants. The as-implanted boron concentration profiles as a function of depth are shown in Figure 6-3 for both germanium amorphizing cases. The boron implant produced a peak boron concentration on the order of $1x10^{21}cm^{-3}$ with a projected range of roughly 3nm and junction depth, measured at a concentration of $1x10^{18}cm^{-3}$, of 30nm. Additionally, the boron implant punched through the amorphous layer formed by the 8keV germanium implant such that the concentration of boron in the EOR region was approximately $5x10^{18}cm^{-3}$. In the case of the 30keV germanium implant the high concentration regions of boron were confined to the amorphous layer, with boron concentrations in the vicinity of the EOR being an order of magnitude lower than that of the 8keV germanium implant, ranging $3x10^{17}cm^{-3}$.

PTEM images of the annealed material revealed very similar microstructures for both germanium amorphizing implants. Figure 6-4 indicates the WBDF PTEM images of the extended defects for the flashed 8keV germanium preamorphized material. Dot-like

interstitial clusters populated the microstructure after the 700°C iRTP anneal. On application of the 1000°C flash temperature, few differences could be discerned in the extended defects. However, as the flash temperature was increased to 1100°C, the defect density clearly decreased and the defects appeared as small loops. At 1200°C, the defect evolution was more apparent as {311}-type defects and larger dislocation loops of smaller density were present in the microstructure. Additional coarsening and defect dissolution occurred as the flash temperature was raised to 1300°C, at which very few dislocation loops were seen. Inspection of the WBDF PTEM images for the 30keV germanium preamorphizing implant revealed an analogous defect evolution. The images are also depicted in Figure 6-5.

A plot of the defect density as a function of fRTP anneal temperature is shown in Figure 6-6, which exhibits a decreasing density with increase in fRTP temperature for both germanium cases. It is important to note that the data points located on the y-axis represent the samples which were only subjected to the 700°C iRTP anneal. One of the most striking features of the plot is the fact that the densities overlapped for all the anneal temperatures investigated, except at the 1300°C, with values on the order of $1x10^{11}cm^{-2}$. At 1300°C the density plunged two to three orders on magnitude respectively, for the 30 and 8keV germanium energies, to values of approximately $7x10^{9}$ and $3x10^{8}cm^{-2}$. A similar trend was realized for the trapped interstitial densities, in which case the densities differed for fRTP temperatures exceeding 1100°C, with the defects formed for the 8keV germanium implant exhibiting lower trapped interstitial concentrations. The trapped interstitial density variation with fRTP anneal temperature is plotted in Figure 6-6.

Figure 6-7 depicts the boron concentration versus depth profiles for the material which was subjected to Flash-assist RTP. Figure 6-7a which portrays the boron diffusion in the wafers preamorphized with the 8keV germanium implant will be discussed first. From the plot it is evident that application of the 700°C iRTP resulted in some noticeable diffusion, for concentrations between 1x10^{19} and 2x10^{18}cm^{-3}, which coincides with the estimated depth of the EOR damage region. Furthermore, application of the flash anneals resulted in additional diffusion of the boron. As the flash temperature was increased from 1000 to 1300°C there was a concomitant increase in boron diffusion. In particular, the boron pile up observed in the vicinity of the EOR region, seemed to increase for flash temperatures ranging 1000 to 1200°C. However, at 1300°C the distinct pile up was no longer visible, but the higher concentration regions were observed to diffuse deeper into the structure. Scrutiny of the near surface region revealed that boron also diffused toward and piled up within the first 2nm at the surface, for the range of temperatures investigated. This concentration of piled up boron at the surface was found to increase with fRTP anneal temperature and was largest for the highest flash temperature, with a value of 1.6x10^{21}cm^{-3}. A corresponding fall in boron concentration was detected within the first 20nm into the wafer. The additional thermal budget associated with the 1300°C fRTP was clearly sufficient to initiate significantly more boron diffusion as the concentration variation with depth appeared appreciably different from those obtained for the lower fRTP anneals. The conspicuous features of the 1300°C fRTP boron profile included a substantially larger decrease in boron concentration within the first 10nm, accompanied by much higher re-distribution of boron at the surface and into the bulk of the wafer. Examination of the boron profile tails revealed that there was no significant

junction motion during the 1000 and 1100°C flash anneals. The junction depths at these temperatures coincided with that of the as-implanted profile at 30nm, measured at a concentration of $1x10^{18}cm^{-3}$. However, as the flash temperature was increased to 1200 and 1300°C the tail of the profiles appeared to also correspond, diffusing to an estimated 35nm. It is important to note in these analyses the boron dose was conserved for all the diffused profiles.

Inspection of the boron diffusion for the samples which were preamorphized with a 30keV germanium implant, shown in Figure 6-7b revealed some differences to those obtained for the 8keV germanium implant. The profiles obtained for the 700°C iRTP anneal and the 1000°C and 1100°C fRTP anneals demonstrated many similarities. Firstly, they all seemed to coincide. Secondly, an inflexion point occurred for these temperatures at a concentration of approximately $2x10^{20}cm^{-3}$ below which the profiles were seen to diffuse into the bulk and above which diffusion took place toward the surface resulting in a pile up of boron at the surface. As the fRTP temperature was increased to 1200°C, the concentration at which the inflexion occurred appeared to decrease with a corresponding increase in both the boron concentration at the surface and diffusion into the bulk. Conversely, the fRTP anneal at 1300°C resulted in a remarkably similar profile to that observed for the 8keV germanium preamorphizing implant, with a boron pile up peak concentration of $1.6x10^{21}cm^{-3}$ and a junction depth of 35nm.

Figure 6-8 is plot of the measured sheet resistance as a function of fRTP temperature. An increase in the fRTP temperature clearly effected decreases in the sheet resistance in both instances. In the 8keV germanium preamorphized material, the gains in sheet resistance between 1000 and 1200°C were minimal within experimental error, with

values ranging 550 through 468ohms/sq. However as the flash temperature was increased to 1300°C, the sheet resistance rapidly fell off to a value of 287ohms/sq. Conversely, application of the fRTP anneal subsequent to the iRTP anneal realized immediate improvements in the sheet resistance for the 30keV germanium amorphizing case, not observed for the 8keV germanium implant. A reduction of approximately 100ohms/sq. over the measured sheet resistance of the 700°C iRTP anneal, was attained on application of the 1000°C fRTP. This improvement trend was sustained for the remaining fRTP anneal temperatures, with the 1300°C fRTP yielding an analogous sheet resistance to that attained by the lower amorphizing energy case, for the same temperature. Evidently, the sheet resistances achieved for the flashed samples which were amorphized with the higher energy implant were consistently lower, with values between 400 and 350ohms/sq for fRTP temperatures ranging 1000 and 1200°C.

The active dose and carrier mobility data obtained from the Hall measurements are shown in Figures 6-9 and 6-10. Once again subtle differences were observed between the two amorphizing implants. As the fRTP anneal temperature was increased above the 700°C iRTP the active dose in the 8keV germanium amorphized material fell from a value of $1.8x10^{19}$ to $1.4x10^{19}cm^{-3}$ for the 1000 through 1200°C fRTP anneals, which represents more than a 20% drop in active concentration. The opposite effect occurred for the 30keV germanium amorphizing implant. In this case, the active dose was observed to increase above that of the 700°C iRTP by more than 40% for the same range of fRTP temperatures. Similar to the results of previously discussed analyses employed in these experiments, the values attained at 1300°C appeared to be comparable, with values of $2.8x10^{19}$ and $3.0x10^{19}cm^{-3}$, respectively for the 8keV and 30keV germanium amorphizing

energies. Finally, very little change in carrier mobility was detected for the 30keV germanium amorphizing implant, with an average value of $45cm^2V^{-1}s^{-1}$ and a standard deviation of 2.8% over the entire temperature range. The variation in the data for the 8keV germanium amorphizing implant was much higher. The data indicated that the application of the fRTP anneal effected higher hole mobility values than that attained for the 700°C iRTP. Application of the 1000 through 1200°C fRTP anneals resulted in a 30 to 50% increase in mobility, respectively above that of the iRTP anneal. Additionally the mobility values attained for the 1300°C fRTP anneals were very similar for both germanium amorphizing cases.

6.4 Discussion

6.4.1 EOR Defect Evolution

The extended defects observed in the microstructure for both germanium amorphizing implants can be classified as Type II damage, which is present beyond the amorphous-crystalline interface in the EOR region when an amorphous layer occurs [JON88]. These defects were observed to evolve in accordance with accepted theories on the EOR damage evolution, which explains that point defects form sub-microscopic interstitial clusters (SMICs) [BEN97, LIB98, COF00], that are thought to be the precursors for {311}-type defect formation [EAG94, STO97, PAN97]. The {311}-type defects in turn unfault into dislocation loops [LIJ98]. In these experiments the above mentioned defect structures were detected at different temperatures; which is anticipated for isochronal anneals [KEY01]. Additionally, the dot-like defect present in the microstructure for the 700°C iRTP and 1000 and 1100°C fRTP anneals concurred with the findings presented in chapter 5. These dot-like structure were observed to evolve into dislocation loops via the formation of the intermediate {311}-type defect, which is the

first experimental evidence of the existence of such a precursor for the {311}-type defect. Figure 6-11 and 6-12 compares the defect and trapped interstitial densities obtained in this experiment to the data presented in chapter 5. These plots undoubtedly confirm that the EOR damage evolutions in both experiments agree. The experiments presented in chapter 5 were not implanted with boron, hence it can be inferred that the boron presence did not influence the EOR damage evolution. The reader is referred to chapters 5 and 6 for a more comprehensive discussion on the evolution.

Inspection of Figure 6-5 revealed that the defect densities matched for all anneal temperatures except the 1300°C fRTP anneal, despite the differences in germanium implant energy. This is peculiar since one would expect more damage to the lattice for a higher energy amorphizing implant. An increase in implant energy may be translated into an increase in the concentration of excess interstitials near the projected range due to an increased separation of Frenkel pairs [COF97], which means an increase in the supersaturation of the interstitials. If defect formation is viewed as the homogeneous nucleation of a precipitate then the number of defects and their size is controlled by the supersaturation of excess self interstitials. Based on this theory, the number of nucleated defects should be higher for the 30keV germanium implant at a given temperature. The data indicates that this is not the case for all temperatures investigated. However one also needs to consider that as the energy of the implant increases, the straggle of the implant also increases, with a consequential reduction in the supersaturation of interstitials [JAS99]. Thus there are two competing processes occurring simultaneously as the implant energy is increased, but it is not clear which effect dominates. The data seems to suggest that the combined effects of the increased interstitial concentration and straggle

for the higher amorphizing energy case resulted in interstitial supersaturation levels comparable to that of the 8keV germanium implant, owing to the remarkably similar defect densities. However, no firm conclusions can be made at this point. Nevertheless, the defect densities attained for the 1300°C fRTP anneal differed with the 8keV germanium implant effecting a smaller density. These differences at 1300°C may be attributed to the difference in proximities of the EOR defect layer from the surface. Raman et al [RAM99b] demonstrated the surface proximity from the EOR damage layer significantly affected the dissolution kinetics of dislocation loops, such that the dissolution rate had an inverse depth dependence. The EOR damage layer for the 8 and 30keV germanium implants were measured at depths of 20 and 55nm, respectively. It is therefore plausible that the dislocation loop density differences were due to the higher dislocation loop dissolution rate in the shallower damage layer. It should be noted that dislocation loops were not the dominant defect structure at the other anneal temperatures. Mostly {311}-type defects were detected at 1200°C, whose rate of dissolution has been previously shown not to be significantly affected by the surface [RAM99a].

For amorphizing implants the number of interstitials in the tail region of the profile includes the recoil atoms from the projected range in addition to the plus one concentration. As the germanium implant energy is reduced, the integrated recoil atom concentration below the amorphous-crystalline interface has been demonstrated to also decrease [GAN89, JON90]. Therefore one can expect the number of trapped interstitials in the EOR to be greater for the 30keV germanium implant. In Figure 6-6, the trapped interstitial densities for both germanium implants appear to be essentially the same for anneal temperatures lower than 1200°C. The extremely small defect sizes at these

temperatures presented some difficulties in the area determination, introducing a larger error in the analysis, which may explain the coincidental data. At 1200 and 1300°C the defects were much larger and therefore the trapped interstitial densities could be calculated with more confidence. The observed differences in interstitial densities at these temperatures conform to the theories of Ganin and Jones [GAN89, JON90], with the trapped interstitial concentration being lower for the 8keV germanium implant. Additionally, the position of the EOR relative to the boron profile could have possibly influenced the interstitial population, with a resultant effect on the defect kinetics. Lilak demonstrated an enhanced {311}-type defect dissolution rate with increasing boron concentration due boron interstitial cluster formation [LIL99]. Since the damage produced by the 8keV implant was in close proximity to boron concentrations on the order of $1x10^{19}cm^{-3}$, it is highly probable that the {311}-type defect dissolution was influenced by the boron. In contrast, the boron concentration in the vicinity of the EOR damage layer for the 30keV germanium implant was $2x10^{17}cm^{-3}$, hence the effect of the boron on the {311}-defect dissolution rate is expected to be lower. Thus the boron presence may be a contributing factor to the observed differences in trapped interstitial densities.

6.4.2 Amorphous Layer Recrystallization

In an effort to estimate the temperature at which the amorphous layers were completely re-crystallized, it was necessary to employ both the intrinsic and extrinsic regrowth velocities for silicon [OLS85a, OLS85b, ROT90]. It is well known and widely accepted that impurity atoms such as boron influences the regrowth velocity [CSE77, SUN82, TIM85, OLS85a, OLS85b]. Hence regions in which the boron concentration was sufficiently high the extrinsic regrowth velocity relation was employed. In the case

of the 8keV germanium implant, the boron implant punched through the amorphous layer resulting in concentrations on the order of $2x10^{19}cm^{-3}$ at the interface, which was high enough to instigate an enhanced regrowth of the layer [OLS88] (see Figure 6-7a). Therefore, the extrinsic relation was used in the regrowth calculation. However, as discussed previously, the boron implant into the amorphous layer formed by the 30keV germanium implant resulted in the regions of high boron concentration being confined to the amorphous layer (see Figure 6-7b). Olson and Roth demonstrated that the solid phase epitaxy rate was not strongly affected by boron concentrations less than $2x10^{19}cm^{-3}$ and significantly increased with concentration up to a concentration of approximately $2x10^{20}cm^{-3}$ [OLS88]. Based on these findings, the recrystallization rate was assumed to be intrinsic for the first 31nm of the regrowth. Only when boron concentrations exceeding $2x10^{19}cm^{-3}$ were encountered by the moving interface was the extrinsic regrowth relation utilized. It should be noted that the extrinsic regrowth relation does not capture the changes in boron concentration inherent to the Gaussian distribution of an ion implant. Hence, only the temperature variations were accounted for in the regrowth velocity determination.

The process simulator FLOOPS [LAW03] was utilized to calculate the re-crystallized layer depth (velocity-time product) by integrating the velocity as the temperature was varied with time for each thermal profile. Thus accurately accounting for the variations in the re-crystallization with the simultaneous change in temperature and time as the wafer was annealed. Appendix B contains the simulation code used for this calculation. The calculations revealed that the velocities attained during the ramp up to the $700^{o}C$ iRTP temperature were sufficient to fully re-crystallize the amorphous layer

formed by the 8keV germanium implant. Based on the extrinsic regrowth velocity relations, complete regrowth was achieved at approximately 580°C. Figure 6-12 contains a plot of the re-crystallized amorphous layer thickness generated by FLOOPS as a function of anneal temperature, which indicates the temperature at which total re-crystallization occurred. The amorphous layer formed by the 30keV germanium preamorphizing implant was evidently not fully re-crystallized on attaining the 700°C iRTP anneal temperature, since the calculation indicated 7nm of regrowth during this portion of the thermal profile. Hence the control wafer which was subjected to only the iRTP anneal must have re-crystallized on the ramp down from the iRTP anneal, since the XTEM images shown in Figure 6-2, indicated no amorphous regions. Those wafers which were annealed at the fRTP temperatures were estimated to undergo complete recrystallization during the fRTP portion of the thermal profile at approximately 1000°C. This is illustrated in Figure 6-12 for the 1000°C fRTP anneal. The regrowth achieved during the ramp up to the 700°C iRTP anneal followed the intrinsic silicon regrowth behavior, with an estimated 20nm of the layer undergoing re-crystallization. The remaining amorphous layer was re-crystallized with velocities characterized by both the intrinsic and extrinsic relation based on the boron concentration encountered, as mentioned previously [CSE77, SUN82, TIM85, OLS85a, OLS85b].

6.4.3 Boron Diffusion Characteristics

Comparison of the plots in Figure 6-7 clearly demonstrates that the diffusion characteristics were a function of the germanium preamorphizing energy. The differences result largely due to the differing positions of the EOR damage relative to the boron profiles and the corresponding depths of the amorphous layers formed.

6.4.3.1 Diffusion in the amorphous phase

The regrowth calculations above demonstrated that the amorphous layer re-crystallization for the 8keV germanium implant occurred at an estimated temperature of 580°C during the ramp up to the 700°C iRTP anneal, approximately 2 seconds into the anneal. From Figure 6-7a, it is evident that application of the 700°C intermediate temperature resulted in some noticeable boron diffusion below the amorphous-crystalline interface, for concentrations between 1x10^{19} and 2x10^{18}cm^{-3} for the 8keV germanium implant. This region coincided with the EOR damage layer and the boron motion is believed to be the initial stages of boron gettering to the EOR damage [BON97b]. Above concentrations of 1x10^{19}cm^{-3}, which overlaps the original amorphous layer, no apparent motion of the profile could be discerned which suggests that the diffusion in the amorphous region was not resolved by SIMS [GAB04]. The regrowth calculations which were performed in FLOOPS, discussed above, indicated only 1nm of the amorphous layer was re-crystallized on attaining a temperature of 530°C, during the ramp up to the iRTP temperature. Thus based on a ramp rate of 150°Cs^{-1}, the boron profile spent approximately 1.5s in the amorphous phase prior to the occurrence of a substantial amount of layer regrowth. Elliman [ELL98] determined the diffusivity of boron in amorphous silicon to be 2.6±0.5 ×10^{-16} cm^{2}s^{-1} at 600 °C. Assuming that boron spent 1.5s at a temperature of 600°C, the expected diffusion length should be 0.40nm in accordance with Elliman's findings. Since it is known that the material was in a dynamic ramp up state and was actually at lower temperatures during this 1.5s interval, the diffusion length should be less than 0.40nm. This calculation confirms that insufficient time spent was in the amorphous regime to allow for any noticeable diffusion in this phase which could be resolved by SIMS.

Alternatively, one could argue that boron interstitial cluster formation [STO95] may be responsible for the apparent immobility of the profile. Certainly the conditions exist to facilitate cluster formation. The temperatures for which the re-growth occurred support high levels of supersaturation, which were determined by Cowern [COW99] to be on the order of $1x10^4$, for temperatures between 600 and 700°C, respectively. Additionally, boron concentrations in the region are high enough and in very close proximity to the interstitial supersaturation. This is therefore a very likely process, which will be explored in the subsequent chapter. It is worth noting that the observed diffusion behavior and any subsequent diffusion occurred in the underlying or re-grown crystalline material.

The boron pile up in the EOR continued to increase for flash temperatures ranging 1000 to 1100°C. This behavior correlates very well with the PTEM analyses which confirmed the presence of the EOR damage and its non-conservative coarsening with increased flash temperature. In Figure 6-6 it can be seen that the interstitial losses from the EOR damage between the iRTP anneal at 700°C and 1000°C fRTP anneal accounts for approximately 15% of the total loss of interstitials observed for the experiment, whereas at 1100°C fRTP a 35% loss of interstitials occurred. The increase in interstitial loss from the EOR defects with increase in fRTP temperature qualitatively matches the increased boron motion observed for this temperature range. At 1200 and 1300°C a distinct bump in the profile was no longer visible, as the profiles were observed to undergo somewhat more diffusion at these temperatures, resulting in much larger concentrations in vicinity of the EOR damage. Since the density of {311}-type defects is quite high at 1200°C, it is expected that these extended defects will continue to getter the

boron. The same applies to the 1300°C anneal, as dislocation loops were still present in the structure at this time, although at a much lower density.

One could argue that the lower defect density hints at a lower gettered boron concentration, but the number of boron atoms which decorate a single defect is not known. Hence a firm conclusion cannot be drawn based on the available data. Reference to Figure 6-6 clearly illustrates much higher interstitial losses occur from the EOR damage on application of the 1200°C fRTP anneal, than detected at the lower fRTP temperatures, with roughly 80% of the entire trapped interstitial population being released. This is 45% more interstitials than that at 1100°C, which correlates with the higher levels of boron diffusion observed between these diffused profiles. The interstitial loss from the defects at 1300°C was 20% more than that at 1200°C, which may account for the substantially less difference in motion observed compared to the differences observed between the 1100 and 1200°C anneals. These arguments also hold for the differences observed in the junction depths measured at a concentration of $1x10^{18}cm^{-3}$. Examination of the diffusion profile tails indicated that there was no significant junction motion during the 1000 and 1100°C fRTP anneals. The junction depths at these temperatures coincided with that of the as-implanted profile at 30nm. However, as the flash temperature was increased to 1200 and 1300°C the junction depth was measured at 35nm. This increased motion was most likely due to, if not in part to, the interstitial release from the EOR.

Conversely, inspection of the diffused profiles in Figure 6-7b indicated that most of the diffusion occurred in early stages of the anneal, compared to the progressive diffusion observed with increasing fRTP anneal temperatures for the 8keV germanium implant.

This was demonstrated by the occurrence of concurrent diffusion profiles for the 700°C iRTP and 1000 and 1100°C fRTP anneals for the 30keV germanium amorphizing implant. In these cases the boron diffusion occurred from much higher concentrations than obtained for the 8keV germanium implant, between concentrations of $2x10^{20}$ and $2x10^{18}cm^{-3}$. Boron diffusion in the amorphous silicon phase during SPER of the implantation-induced amorphous layer has been reported previously [DUF04, GAB04]. In both Gable's and Duffy's investigations the boron profiles were observed to diffuse at a concentration of $2x10^{20}cm^{-3}$ and lower, which is consistent with the diffusion observed in this study. The reasons why motion is observed below this specific concentration are not fully understood at this time. Similar boron diffusion behaviors have been extensively reported in the past in crystalline silicon, which has been attributed to the formation of boron interstitial clusters that are known to be immobile [ANG87, FAI90, SOL91, STO95, PEL99]. Concentrations below the clustered regions diffuse in a comparable manner to the diffusion detected here. However, the diffusion has occurred from concentrations which are much lower than $2x10^{20}cm^{-3}$ and is usually below the solid solubility levels in crystalline silicon. At 700°C the solid solubility of boron in crystalline silicon is on the order of $2x10^{19}cm^{-3}$ [TRU60]. Most of the motion in these experiments occurred for during the ramp up to the 700°C iRTP temperature. The results therefore indicate that diffusion occurs from much higher concentrations in the amorphous phase than in the crystalline phase. Since little is known about clustering in the amorphous phase [DUF04], it cannot be conclusively said that clustering is responsible for the immobile regions of the boron profile.

As previously discussed, the ramp-up to the iRTP anneal resulted in a mere 20nm of layer regrowth. Therefore at least this much time (approximately 3 seconds) was available for diffusion in the amorphous phase before the boron profile was encountered by the moving crystalline interface. In the case of the 700°C iRTP anneal only, the re-growth was completed on the ramp down. Once the boron profile was encountered, boron atoms were positioned on substitutional sites due to the effective solute trapping associated with SPER. Thus the observed diffusion for the 700°C iRTP anneal occurred in the amorphous phase. A prominent feature of the diffusing portion of the profile is the steep gradient, which is analogous to profiles which exhibit concentration enhanced diffusion (CED). CED is the system's attempt to reduce any chemical potential differences, such that regions of high concentrations have higher diffusivities than regions of lower concentrations [PLU00]. The resultant box-like profile formed as a result of CED is very attractive from a junction engineering perspective [DUF04].

6.4.3.2 Transient enhanced diffusion (TED)

It is striking that the diffusion at 1000 and 1100°C fRTP coincides with that of the 700°C iRTP anneal. Earlier, it was demonstrated that total amorphous layer regrowth occurred on the ramp up to the target fRTP temperatures at approximately 1000°C, compared to on the ramp down for 700°C iRTP anneal. Thus the regrowth for the fRTP anneals was completed at a much higher temperature and since the regrowth velocity is a function of the temperature and boron concentration, at a much faster rate; allowing little time for additional diffusion beyond what occurred in the amorphous phase during the ramp up to the iRTP. On this basis therefore it seems plausible that the initial diffusion profiles will be similar after the 700°C iRTP anneal, but the additional thermal budget is expected to effect some diffusion. The data indicates that the thermal budget associated

with the 1000 and 1100°C fRTP portions of the thermal profile did not effect any detectable additional diffusion. Reference to Figure 6-6 indicates less than 10% of the total interstitial loss, which represents on the order of $1x10^{12}cm^{-2}$ interstitials, occurred when the fRTP temperature was increased to 1000 and 1100°C. It is highly probable that these very small levels of released interstitials did not induce diffusion levels which could be detected within the resolution limits of SIMS. If one considers the intrinsic boron diffusivity expression of Hadarra et al [HAD00] the calculated intrinsic diffusion lengths, shown in Table 6-1, cannot account for the detected diffusion, particularly at the higher fRTP anneal temperatures. In determining the diffusion length, the intrinsic diffusivity was calculated as a function of the change in temperature with time, which allowed for the accurate integration of the diffusivity with time. Clearly, the observed diffusion was enhanced and may be attributed to the phenomenon of TED, which is known to be directly related to the interstitial supersaturation levels. The interstitial supersaturation was extracted by Cowern [COW99] for temperatures ranging 600 through 800°C, based on Fair's diffusivity data [FAI81].

$$S_{\text{int}} = S_0 \exp\left(\frac{-E_a}{kT}\right) \qquad (6\text{-}1)$$

where S_{int} is the interstitial supersaturation, the pre-exponential factor, S_0 is $2.63x10^{-1}$ and the activation energy, E_a is -0.82eV. Table 6-2 contains the calculated interstitial supersaturation values and the calculated enhanced diffusion at the anneal temperatures of interests. The estimated values attained were found to be a little higher than the diffusion lengths detected by SIMS. However, the accuracy of the calculation lies in the ability to precisely determine the interstitial supersaturation, which was extracted from diffusivity data available for much lower anneal temperatures than the temperatures used

in this experiment. Hence it is expected that any errors associated with the supersaturation relation would be magnified as the temperature is increased. The calculation yielded enhanced diffusion lengths at 1000 and 1100°C that ranged 1 to 3nm. Within the resolution limits of SIMS this may be difficult to discern from the noise, therefore it is plausible that this enhancement was not detected. In the cases of the 1200 and 1300°C anneals the enhanced diffusion lengths were estimated at 5 and 10nm, respectively, while the actual detected diffusion at a concentration of $1x10^{18}cm^{-2}$ were 1 and 5nm. The predicted diffusion lengths were on the same order of magnitude, which confirms the enhancement in the diffusion observed. The diffusion also corresponded to the reductions in the trapped interstitials observed between these two temperatures. Comparing the difference in the interstitial release from the EOR for these two temperatures (see Figure 6-6), it was obvious that a much larger fraction of interstitials were lost from the defects at 1300°C, with approximately 56% of the total released interstitials versus 35% at 1200°C. These differences concur with the disparities in boron diffusion detected for these fRTP anneals.

6.4.3.3 Boron pile up at the Si-SiO_2 interface

In both germanium preamorphizing cases, boron concentrations were observed to move toward the surface and pile up at the Si-SiO_2 interface with an increase in the fRTP temperature. There have been many reports in the literature that boron can exhibit an uphill diffusion [WAN01, DUF03], and in some cases boron pile up has been observed to be in the vicinity of the surface or an interface [SHI01]. On comparing the reported characteristics associated with boron uphill diffusion to the diffused profiles in this study, it is evident that the profiles do not exhibit the traits associated with uphill diffusion. For instance, the uphill diffusion was reported to be bigger when the amorphous layer was

closer to the surface [DUF03]. But in this work, no distinction can be made in these regions, between the boron profiles for the germanium energies investigated. Also, the regions above concentrations on the order of $5x10^{18}cm^{-3}$ were described to shift in the direction of the surface during uphill diffusion [DUF03]. But the plots in this work do not depict this feature. Inspection of the plots in Figure 6-7 reveals that the motion is more consistent with a redistribution of the boron from the profile peak to the $Si\text{-}SiO_2$ interface, which was confirmed from the SIMS data. The observed motion in the peak of the profile certainly indicates that the entire profile is not immobile and leads one to speculate whether the dissolution of the immobile, clustered fractions alluded to previously yielded the apparent motion. This will be further explored in the subsequent chapter.

6.4.3 Electrical Measurements

The electrical measurements of these junctions generated very interesting results. In particular one of the most salient findings were obtained from the four point probe measurements, which indicated that much higher sheet resistances were attained for the lower germanium energy amorphizing implant. The 8keV germanium implant consistently produced sheet resistances which were approximately 35% higher than that attained for the 30keV germanium implant, in the 1000 through 1200°C fRTP range. Additionally, an estimated 8% higher sheet resistance was obtained for the 700°C iRTP and 1300°C fRTP temperatures. Another striking feature of the plot was the fact that the application of the fRTP anneal resulted in marginal improvements in sheet resistance for the 8keV germanium implant, in particular for the 1000 and 1100°C fRTP temperatures. Similar fRTP anneal temperatures applied to the layer formed by the 30keV germanium PAI, however produced gains in sheet resistance of 20% and more. The larger sheet

resistances attained for the 30keV germanium implants hint at differences in carrier mobilities or active concentrations or both. In Figure 6-9 the active dose measurements for both germanium implants were compared. The values obtained for the 30keV germanium implant are undoubtedly more than 50% higher than those of the 8keV germanium implant, for fRTP temperatures ranging 1000 through 1200°C. Although within experimental error the trend in this temperature range for the 30keV germanium implant could be assumed to be constant, there was an apparent increase in the active dose as the fRTP temperature was varied from 1000 to 1200°C, which was not observed for the active dose corresponding to same temperatures for the 8keV germanium implant. The active dose remained almost constant for the lower germanium energy. In order to understand the trends observed for the sheet resistance, it is also necessary to inspect the carrier mobility values. The opposite behavior was observed for the carrier mobility, in that the values attained for the mobility were almost constant for the sample preamorphized with 30keV germanium. While an increase in mobility was detected for 8keV germanium case. Table 6-3 and Table 6-4 contain the percentage improvements in active dose and mobility for the fRTP anneals over the 700°C iRTP anneal for both germanium preamorphizing energies. Since the 700°C iRTP represents the baseline for the comparison a value of 0% was assigned for easy comparison. In the instance of the 30keV germanium implant, the fRTP anneal resulted in increases in active dose which ranged approximately 40 to 80%, with less than a 10% change in the mobility as the fRTP temperature was increased above the iRTP anneal. Clearly, the active dose was the more dominant factor and therefore it can be inferred that the active dose dictated the sheet resistance trend observed. Whereas for the 8keV germanium implant, decreases in

the active dose which ranged 20 to 25% were detected for fRTP temperatures between 1000 and 1200°C. Corresponding increases in the mobility of roughly 40 to 50% occurred. It is difficult to resolve an increase in mobility with a corresponding decrease in active dose, since a high probability for cluster formation exists which is known to degrade the mobility [STO95]. But it is apparent that the combined product yields a higher sheet resistance than that attained by the 30keV germanium implant. This analysis suggests that different processes may be controlling the activation, which may be tied to the germanium implant energy. There results will be further analyzed in relation to the other characterization techniques, in chapter 8.

6.5 Conclusions

The effect of altering the germanium pre-amorphization energy on the junction characteristics of doped silicon wafers processed by flash-assist rapid thermal processing was investigated. The germanium ion implantation consisted of an 8 and 30keV implant energy at a constant dose of $1x10^{15}cm^{-2}$. Subsequently boron dopant atoms were introduced into the structure at an energy and dose of 1keV and $1x10^{15}cm^{-2}$, such that the boron profile punched through the amorphous layer formed by the 8keV germanium implant, spilling over into the EOR regions, but was wholly confined to the amorphous layer formed by the 30keV germanium. TEM analyses indicated that the EOR damage associated with the germanium amorphizing implant was consistent with Type II damage [JON88] and followed a very similar evolution. As the fRTP anneal temperature was increased the damage evolved from small dot-like interstitial clusters to {311}-type defects and dislocation loops. Only at 1200 and 1300°C were differences in the size and density of the defects observed, with the 8keV germanium implant demonstrating a smaller defect density and size. The disparity in defect density was thought to be the

result of the differences in the interstitial supersaturation, owing to the separation of Frenkel pairs, which was thought to be higher for the 30keV germanium implant. However, one needs to consider that the straggle of the implant is also larger for the 30keV germanium case, which would result in a reduction in the supersaturation. It was not clear which effect would dominate. Although the data suggested that the resultant interstitial supersaturation may have been comparable since at the lower temperatures the defect densities were almost identical. If this is the case, then the disparities observed at 1300°C were thought to be associated with the faster dislocation loop dissolution rate of the 8keV germanium implant, which was previously demonstrated proportional to the distance of the damage layer from the surface [RAM99]. The size discrepancies were attributed to the expected smaller concentration of atoms (recoil atoms and the "plus one" concentration) beyond the amorphous-crystalline interface, for the lower energy implant. The defect behavior was analogous to the experimental findings presented in chapters 5 and 6, which indicated that the boron presence in the microstructure did not effect changes in the EOR defects.

The diffusion behavior of the boron atoms was also found to have an energy dependence. This was largely due to the differences in the amorphous layer thickness and the corresponding location of the EOR damage. Regrowth calculations performed in FLOOPS which took into account the effect of the boron concentrations, indicated that the regrowth of the layers occurred at different rates and consequently at different temperatures. The amorphous layer formed by the 8keV germanium implant was re-crystallized on the ramp-up to the 700°C iRTP temperature, at an estimated temperature of 580°C. The corresponding diffusion indicated that most of the observed boron motion

occurred in the crystalline silicon, subsequent to the re-crystallization process and was enhanced. This motion entailed boron concentrations re-distributing to the EOR region [BON97] and the Si-SiO_2 interface. In the case of the layer formed by the 30keV germanium implant, the re-crystallization was not completed on the ramp up to the 700°C iRTP temperature, but subsequent to this. Hence the boron atoms had sufficient time to diffuse in the amorphous phase from a concentration of $2x10^{20}cm^{-3}$[GAB04, DUF04], which is much higher than similar diffusions observed in crystalline silicon. Concentrations above this were observed to be immobile in the amorphous silicon, which is similar to clustering phenomenon in crystalline silicon. It was clear that most of the diffusion detected at the lower fRTP anneal temperatures was dictated by the diffusion which occurred in the amorphous phase. The subsequent thermal budget associated with the fRTP anneals effected an enhanced diffusion, which was shown to be too small to be resolved by SIMS at 1000 and 1100°C, hence these profiles appeared to coincide with the diffused profile for the 700°C iRTP anneal. At 1200°C and 1300°C the enhancement could be clearly discerned. The boron peak concentrations exhibited very similar behavior for both germanium energies, with an evident pile up at the Si-SiO_2 interface which increased as the fRTP temperature was increased. This mobile boron seemed to diffuse from the originally immobile boron concentrations, leading one to speculate whether the fractions which were thought to be clustered were dissolved by the thermal budget, resulting in the apparent motion.

Investigations into the electrical characteristics showed that the sheet resistance obtained for the lower energy implant was consistently higher. An examination of the carrier density and mobility data gave further insight into the processes which may be

governing this behavior. It became clear that the sheet resistance was dictated by carrier density, which was much higher than for the 30keV germanium implant versus the 8keV germanium. However, a direct inference could not be made for the 8keV germanium implant, as there was a simultaneous increase in mobility and decrease in carrier density which cannot both be resolved by the formation of clusters, which are believed to be present in the microstructure. In Chapter 7 we will attempt to resolve this issue and further correlate the data presented herein.

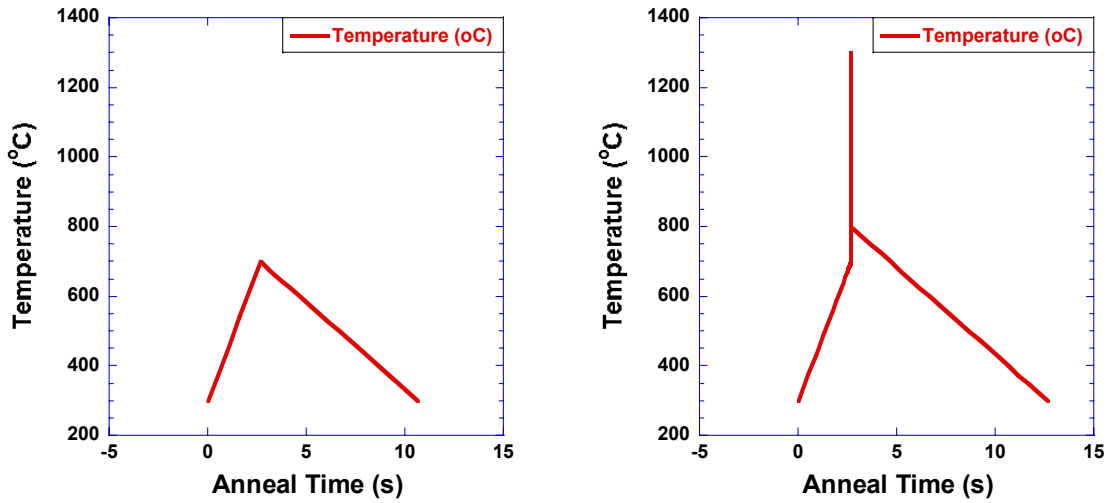

a) b)

Figure 6-1. Illustration of the temperature-time variations of the Flash-assist RTP thermal profiles used in these experiments. a) iRTP anneal b) fRTP anneal.

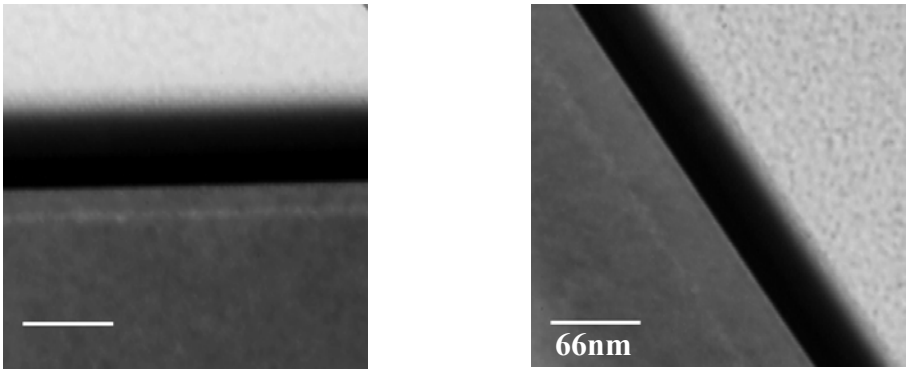

a) b)

Figure 6-2. Cross-section TEM images taken under g_{110} BF diffraction conditions of the re-crystallized amorphous regions for an 8 and 30keV germanium preamorphizing implants subjected to a 700°C iRTP anneal. a) 8keV germanium PAI and b) 30keV germanium PAI. The EOR damage regions can also be seen at depths of 20 and 55nm, respectively.

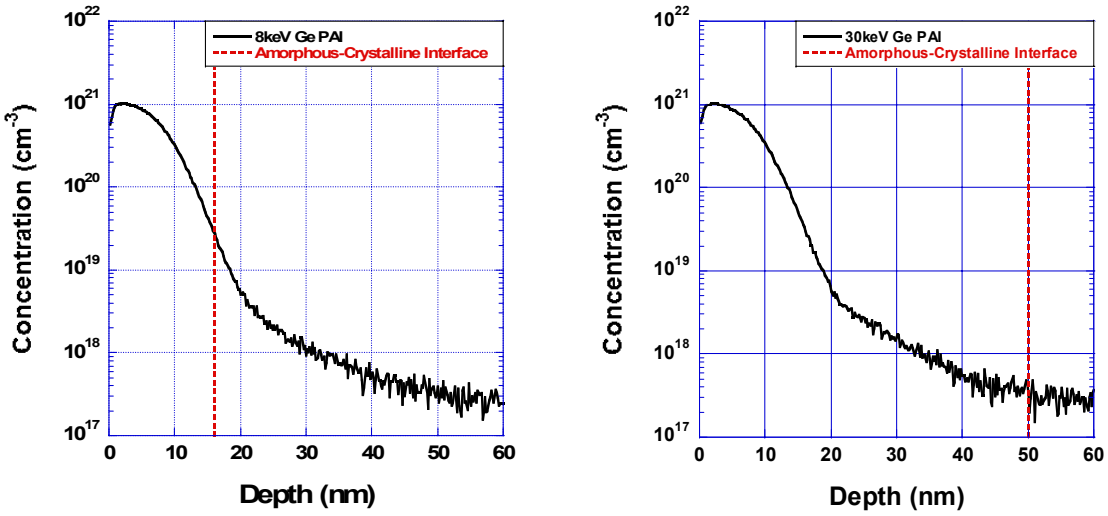

a) b)

Figure 6-3. Concentration-depth profiles of the as-implanted boron profiles into amorphous layers formed by 8 and 30keV germanium preamorphizing implant, obtained from SIMS analyses. a) 8keV germanium PAI and b) 30keV germanium PAI.

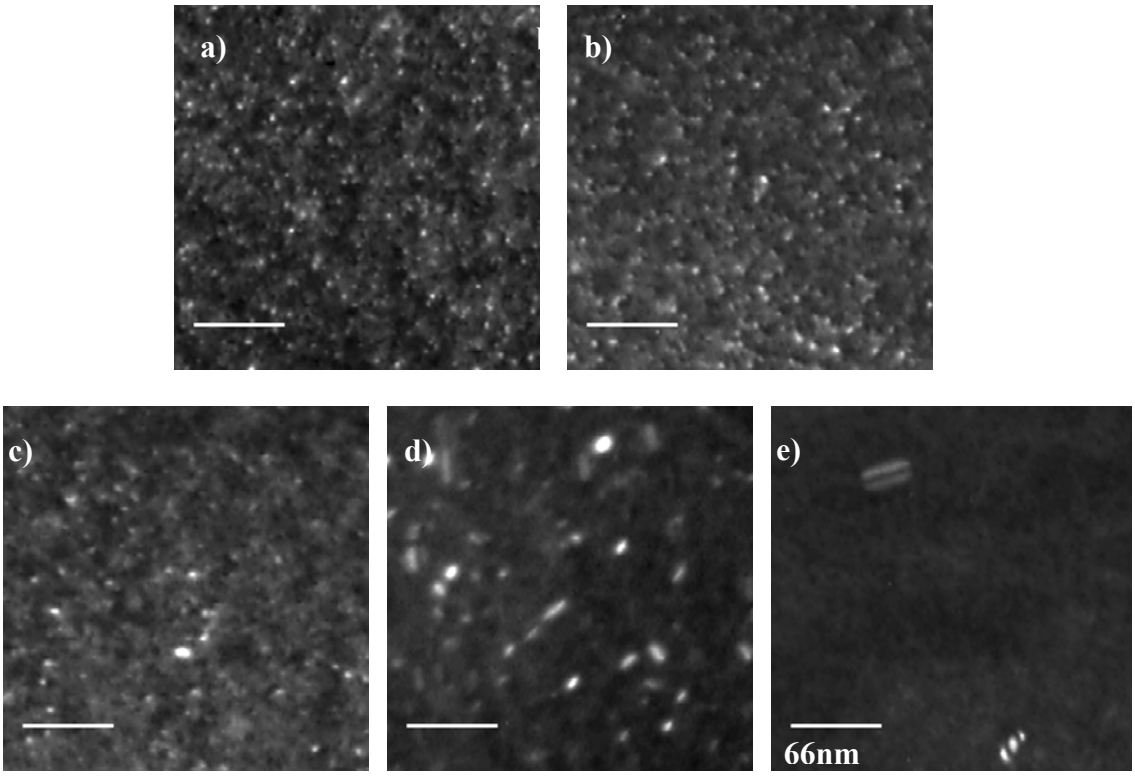

Figure 6-4. WBDF PTEM images of the EOR defects imaged under g_{220} two-beam conditions of the 8keV germanium PAI. a)700°C iRTP, b) 700°C iRTP,1000°C fRTP, c) 700°C iRTP, 1100°C fRTP, d) 700°C iRTP, 1200°C fRTP, e) 700°C iRTP, 1300°C fRTP

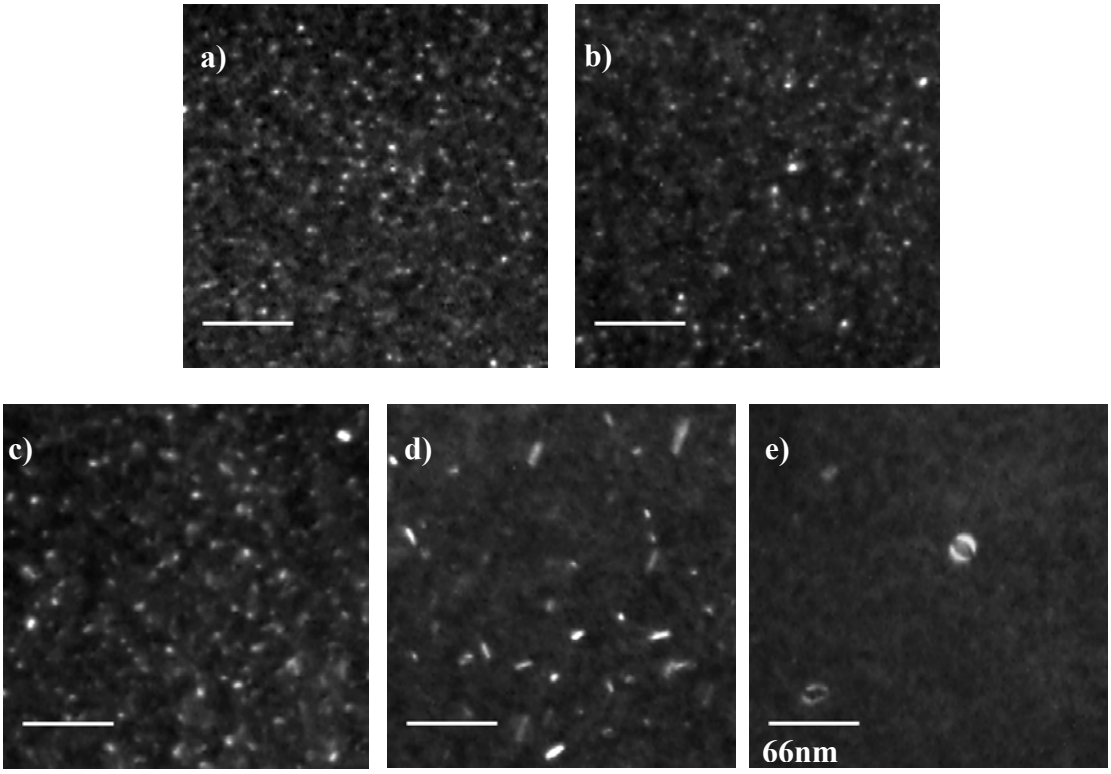

Figure 6-5. WBDF PTEM images of the EOR defects imaged under g_{220} two-beam conditions of the 30keV germanium PAI. a)700°C iRTP, b) 700°C iRTP,1000°C fRTP, c) 700°C iRTP, 1100°C fRTP, d) 700°C iRTP, 1200°C fRTP, e) 700°C iRTP, 1300°C fRTP

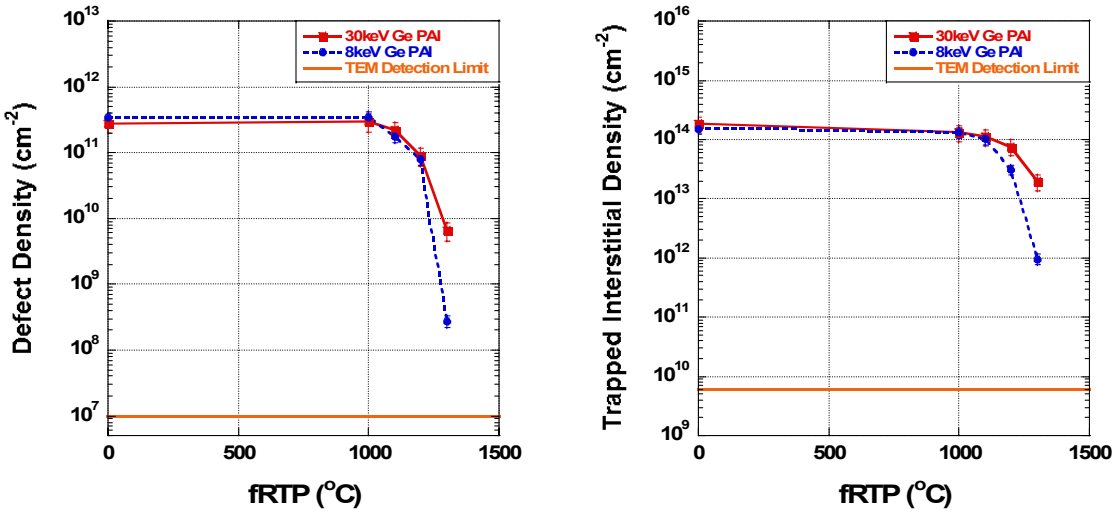

a) b)

Figure 6-6. Quantitative transmission electron microscopy results for 8 and 30keV germanium preamorphizing implants subjected to flash anneals. a) Defect density and b) Trapped Interstitial Density as a function of fRTP anneal temperature.

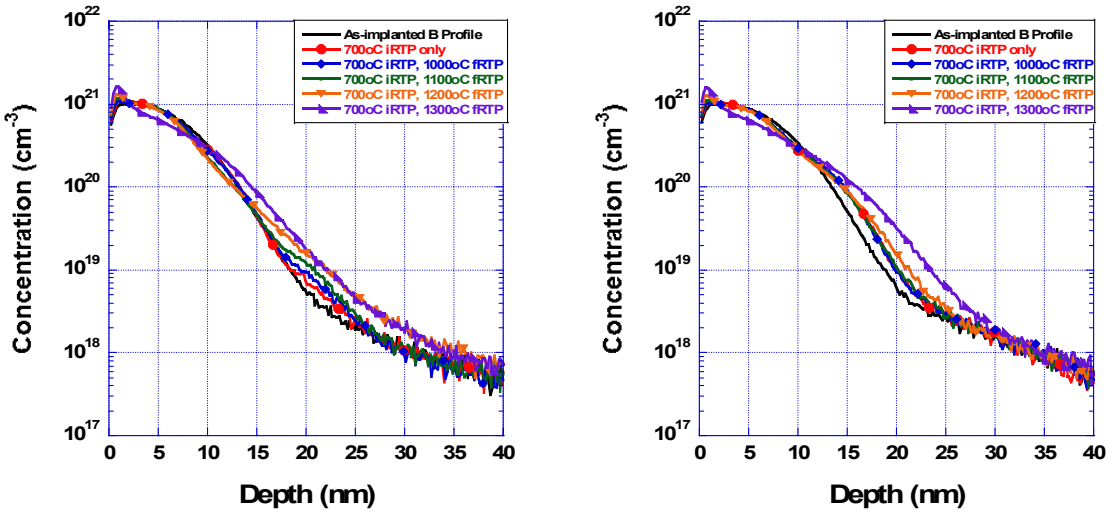

a) b)

Figure 6-7. Concentration-depth profiles of the diffused boron implant obtained from SIMS analyses for samples subjected to flash anneals. a) 8keV germanium PAI and b) 30keV germanium PAI.

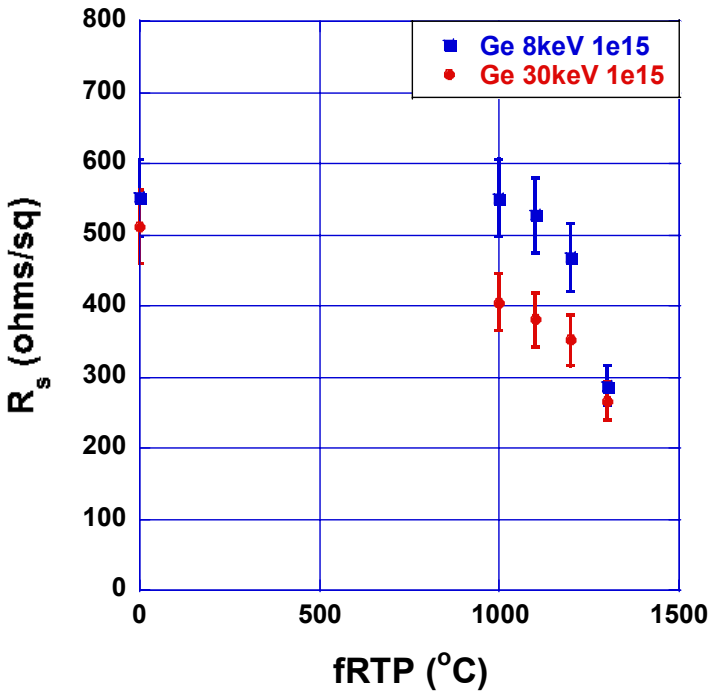

Figure 6-8. Sheet resistance, R_s as a function of fRTP anneal temperature for 8 and 30keV germanium PAI obtained from Four-Point probe measurements

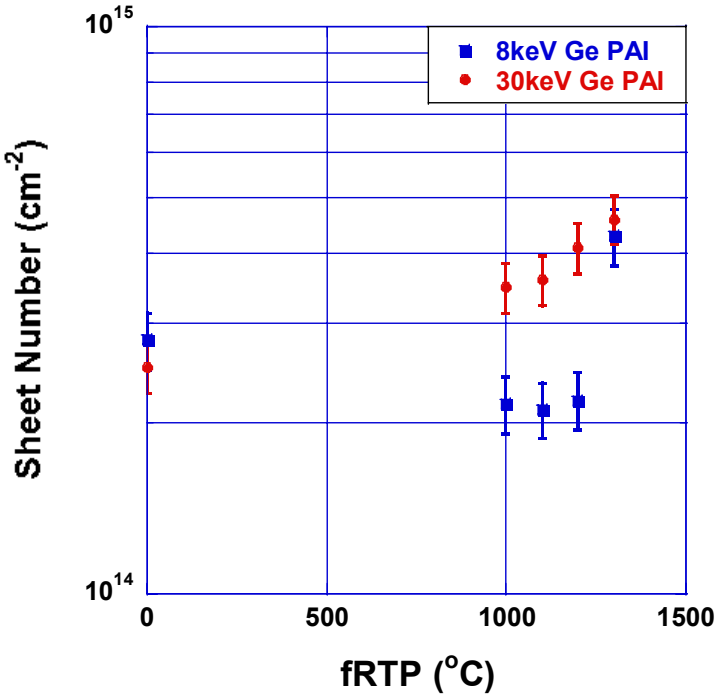

Figure 6-9. Active dose as a function of fRTP anneal temperature for 8 and 30keV germanium PAI obtained from Hall measurements

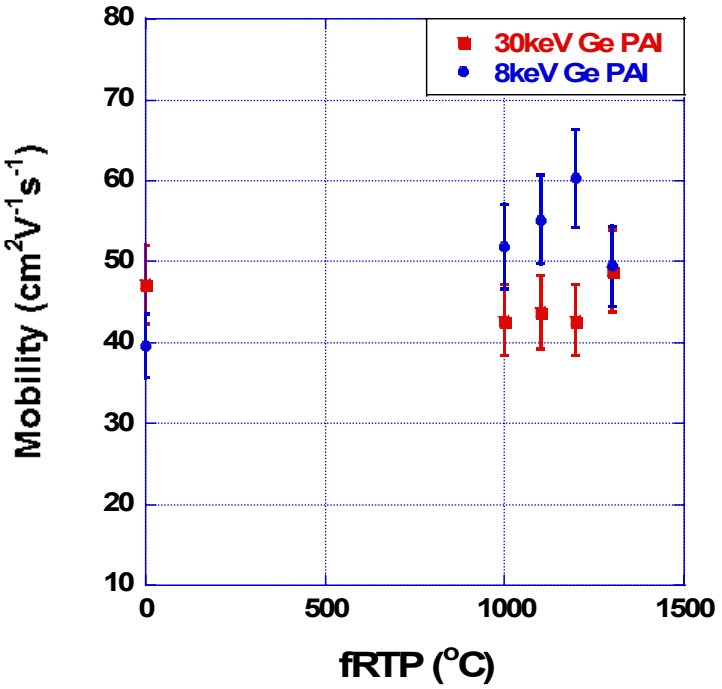

Figure 6-10. Carrier mobility as a function of fRTP anneal temperature for 8 and 30keV germanium PAI obtained from Hall measurements

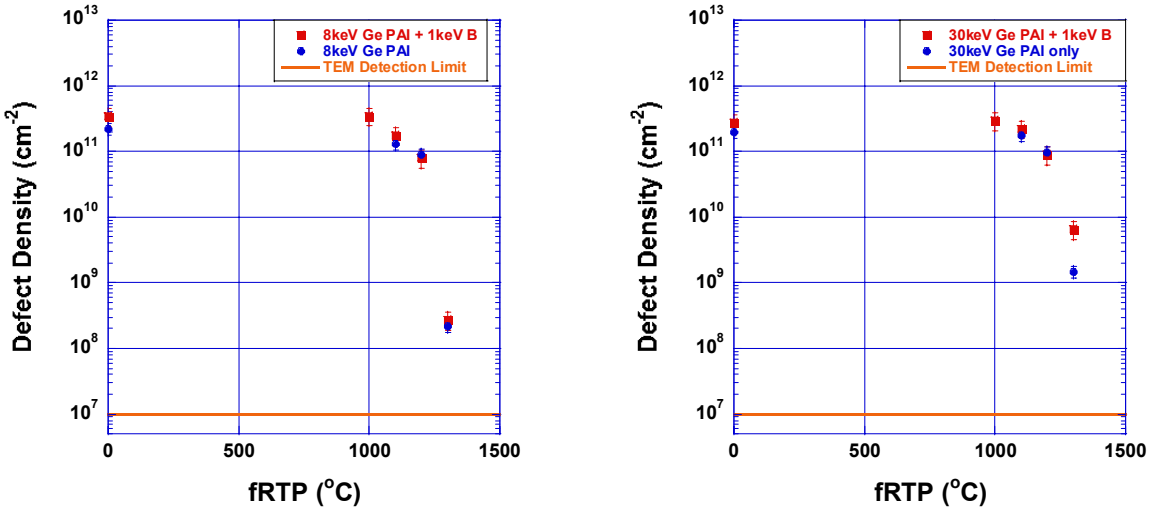

a) b)

Figure 6-11. Effect of boron on the defect density as a function of fRTP anneal temperature. a) 8keV germanium PAI and b) 30keV germanium PAI with and without a 1keV $1x10^{15}cm^{-2}$ B implant.

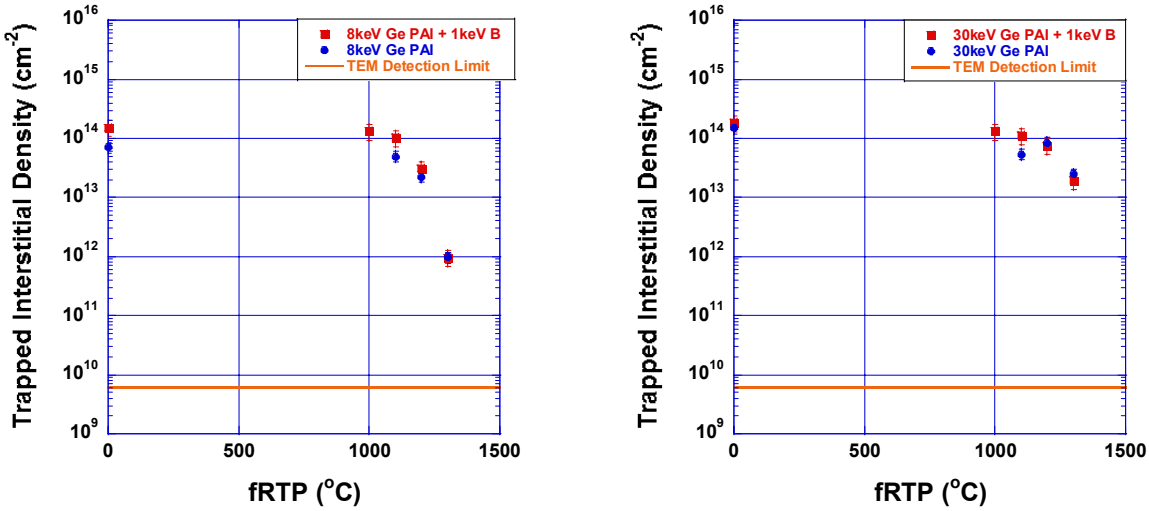

a) b)

Figure 6-12. Effect of boron on the trapped interstitial density as a function of fRTP anneal temperature. a) 8keV germanium PAI and b) 30keV germanium PAI with and without a 1keV $1x1^{015}cm^{-2}$ B implant.

Table 6-1. Calculated boron intrinsic diffusion lengths in crystalline silicon for the fRTP temperatures investigated

fRTP Temperature (^{o}C)	Intrinsic boron diffusion length (nm)
1000	0.05
1100	0.17
1200	0.44
1300	1.03

Table 6-2. Estimated silicon interstitial supersaturation and boron enhanced diffusion length in crystalline silicon for the fRTP temperatures investigated

fRTP Temperature (^{o}C)	Silicon interstitial supersaturation	Boron enhanced diffusion length (nm)
1000	4.62E+02	1
1100	2.68E+02	3
1200	1.68E+02	5
1300	1.11E+02	10

Table 6-3. Percent changes in active dose and mobility values on application of the fRTP anneals over the 700°C iRTP for the 30keV germanium preamorphizing implant

fRTP Temperature (°C)	Active Dose (cm^{-2})	Mobility ($cm^2V^{-1}s^{-1}$)	% change in Active Dose	% change in Mobility
700	2.50E+14	47	0	0
1000	3.48E+14	43	39	-9
1100	3.57E+14	44	43	-7
1200	4.08E+14	43	63	-9
1300	4.58E+14	49	83	4

Table 6-4. Percent changes in active dose and mobility values on application of the fRTP anneals over the 700°C iRTP for the 8keV germanium preamorphizing implant

fRTP Temperature (°C)	Active Dose (cm^{-2})	Mobility ($cm^2V^{-1}s^{-1}$)	% change in Active Dose	% change in Mobility
700	2.80E+14	40	40	0
1000	2.16E+14	52	52	31
1100	2.11E+14	55	55	39
1200	2.19E+14	60	60	52
1300	4.27E+14	49	49	25

CHAPTER 7
BORON ACTIVATION DURING FLASH-ASSIST RAPID THERMAL PROCESSING

7.1 Introduction

The goal of this chapter is to present a more in depth analysis of the experimental data presented in the previous chapter in relation to the activation of boron during Flash-Assist Rapid Thermal Processing (RTP) for different germanium preamorphization energies. A direct consequence of altering the preamorphization energy for a given boron implant was a change in the position of the amorphous-crystalline interface relative to the profile. This variation of the initial wafer condition proved to have a significant impact on the amorphous layer re-crystallization velocity which influenced the boron diffusion and electrical properties of the junctions. Although these differences in material properties stemmed from the variations in germanium energy for these experiments, the critical factor was found to be the relative positions of the as-implanted boron profile and the amorphous-crystalline interface. The following discussion will explore these ideas in more detail and elucidate the processes which dictate the boron activation during Flash-assist RTP.

7.2 Discussion

7.2.1 Differences in the Initial Implant Conditions

The 8keV and 30keV germanium implant resulted in the formation of amorphous layers which were 16 and 50nm deep, respectively. Figure 7-1 is a plot of the as-implanted profile for a 1keV, $1x10^{15}cm^{-2}$ boron implant into silicon preamorphized with 8 and 30keV germanium energies, in which the amorphous-crystalline interface is

illustrated. The figure shows that the boron implant produced a peak boron concentration on the order of $1x10^{21}cm^{-3}$ with a projected range of roughly 3nm and junction depth, measured at a concentration of $1x10^{18}cm^{-3}$, of 30nm. Additionally, the boron implant punched through the amorphous layer formed by the 8keV germanium implant such that the concentration of boron at the amorphous-crystalline interface was on the order of $1x10^{19}cm^{-2}$. In the case of the 30keV germanium implant the high concentration regions of boron were confined to the amorphous layer, with boron concentrations in the vicinity of the EOR being an order of magnitude lower than that of the 8keV germanium implant, ranging $3x10^{17}cm^{-3}$. Hence varying the energy of the preamorphization implant and therefore the layer thickness, effected changes in the boron levels at the amorphous-crystalline interface and consequently in the EOR damage region. These initial conditions are important for the remaining discussion.

7.2.2 Influence on the Amorphous Layer Re-crystallization

The boron position relative to the amorphous-crystalline interface and the EOR damage region proved to be significant. It is well known that the impurity atoms such as boron in the silicon lattice at high enough concentrations can effect noticeable changes in the re-crystallization velocity [CSE77, SUN82, TIM85, OLS85a, OLS85b]. Olson and Roth demonstrated that the solid phase epitaxy rate was not strongly affected by boron concentrations less than $2x10^{19}cm^{-3}$ and significantly increased with concentration up to a concentration of approximately $2x10^{20}cm^{-3}$ [OLS88]. Thus examining the as-implanted boron profile relative to the original amorphous-crystalline interface for each germanium implant revealed that the concentrations in the region had an immediate impact on the re-crystallization. In the case of the 8keV germanium implant, the regrowth was instantly enhanced relative to the intrinsic velocity owing to the high boron concentrations at the

interface. However, since the concentrations were much lower at the amorphous-crystalline interface of the 30keV germanium implant, the initial velocity was characterized by an intrinsic relation for the first 30nm of the regrowth. Consequently, from the onset of the thermal anneal there were differences in the kinetics of the regrowth. Figure 7-2 contains plots of the re-crystallized layer depth as a function of anneal temperature generated by FLOOPS [LAW03] for both germanium energies. Based on the extrinsic regrowth velocity relations, the 8keV germanium amorphous layer was determined to recrystallize at a temperature of 580°C, during the ramp up to the iRTP anneal temperature. The deeper layer of the 30keV germanium implant took a longer time for re-crystallization to be completed. The FLOOPS simulation discussed in the previous chapter indicated a mere 20nm re-crystallized during the ramp up to the 700°C iRTP anneal, owing to a much lower intrinsic regrowth velocity used for the first 30nm of regrowth. Consequently, complete re-crystallization of the layer occurred during the remaining portions of the thermal profile. In the case of the 700°C iRTP anneal, this coincided with the ramp down, whereas for the fRTP anneals total re-growth was achieved at an estimated temperature of 1000°C.

7.2.3 Analyses of the Electrical Data

The sheet resistance measurements for both the 8keV and 30keV germanium preamorphizing implant, shown in Figure 7-3, demonstrated very different trends. In particular, the values attained for the fRTP anneals conducted at 1000 through 1200°C were found to be higher for the lower germanium energy implant, by an average 26% over that of the 30keV germanium implant. In an effort to understand the processes which were responsible for these differences it was necessary to take a closer look at the active dose and carrier mobility data, which dictate the final sheet resistance of the layer.

The electrical data obtained from the Hall measurements were pertinent to gaining an understanding into the processes which were occurring. In Figure 7-4 the active dose for both germanium energies as a function of fRTP anneal temperature is illustrated. It is evident that the active dose obtained for the 30keV germanium implant case was consistently higher than that attained for boron in the layer amorphized by the 8keV implant. After the 700°C iRTP anneal it was obvious that approximately 75% of the total implanted dose existed in some inactive, immobile configuration, for both amorphizing implants. However the trends varied considerably for fRTP anneal temperatures ranging 1000 through 1200°C.

Similarly, the mobility as a function of the fRTP temperature was found to be a function of the germanium preamorphizing energy, as seen in Figure 7-5. The mobility values extracted by the Hall measurement were consistent for the 30keV germanium implant, with values on the order of the 40-50cm^{2}/Vs, but much higher values were observed for the lower germanium energy implant in the temperature range 1000 through 1200°C.

7.2.3.1 8keV germanium preamorphizing implant

Consider the 8keV germanium implant; at 1300°C the active dose almost doubled that attained by the 700°C iRTP anneal. However, the active dose appeared to be independent of the fRTP anneal temperature between 700 and 1200°C. The apparent reduction in active dose on application of the 1000°C fRTP anneal, subsequent to the 700°C iRTP anneal are within error of the Hall measurement, which is a reasonable assumption. One may be likely to agree with this since similar active doses were obtained at 1100 and 1200°C indicating no substantial change in the active dose. Further examination of the numbers, revealed that the application of fRTP anneals at

temperatures of 1000 to 1200°C, subsequent to the 700°C iRTP instigated a 25% decrease in the active dose. This trend was peculiar and fell outside of the 10% error associated with the Hall measurements, leading one to believe that this seeming deactivation was real. These differences compelled the author to consider the probability of the occurrence of another physical mechanism which may have been responsible for this discrepancy.

The formation of boron interstitial clusters in crystalline silicon (BICs) is known to occur when a thermal treatment subjected to high boron concentrations in the presence of an interstitial supersaturation. This is generally accepted to occur for boron concentrations exceeding the range $1x10^{18}$ to $1x10^{19}cm^{-3}$ [STO97, RAC02, LIL02, MIR03]. The clusters are known to be immobile and inactive and are therefore often observed as stationary peaks in SIMS profiles and reduced active Hall doses. [LIU96]. The boron concentrations in the vicinity of the interstitial supersaturation in these experiments were within the range for which BICs have been demonstrated to occur. Furthermore, the interstitial supersaturation at the temperatures in the initial stages of the anneal should have been on the order of $1x10^{4}$, as demonstrated by Cowern [COW99] for temperatures ranging 600 to 700°C. Hence the conditions necessary for BIC formation existed, increasing the probability of their occurrence. Consequently the drop in active concentration may also be explained by the formation of BICs, which are known to deactivate already active boron concentrations. This theory will be explored in relation to additional experimental measurements later on in the discussion.

Since the amorphous layer re-crystallization occurred on the ramp up to the iRTP anneal temperature of 700°C, all the boron profiles in the case of the 8keV germanium implant were subjected to the same temperature profile and the layers were re-crystallized

at the same time and temperature. As a result they were all activated at the same time. If the activation was a function of the re-crystallization temperature [GAB04, JAI04] then the activation levels of boron should be similar at the onset of the fRTP anneals, owing to the activation during the SPER. Assuming that the decrease in the active dose which occurred between the 700°C iRTP and application of the 1000°C fRTP anneal can be accounted for by error in the Hall measurement, the active boron doses are very similar for temperatures up to 1200°C. This supports the postulation that the activation is a function of the re-crystallization temperature. But this premise does not account for the higher activation levels achieved by the 1300°C anneal.

To resolve the factors which were responsible for the higher activation levels attained for the 1300°C fRTP anneal, the active portions of the SIMS boron profiles were determined by matching the integrated area below the curve to the active boron dose obtained from the Hall measurement. This yielded the maximum active concentrations achieved by each anneal. Any concentrations above these values were assumed to be in an inactive state. It should be noted that this also entailed an additional assumption that all boron atoms in the tail of the profile were in fact in an active configuration; which may not necessarily be fully correct. However, it was not possible to otherwise establish the location of the active boron concentrations and it was more probable that lower boron concentrations would be activated. Hence the assumption seemed reasonable.

The maximum active concentrations for the 8keV germanium preamorphizing implant can be seen in Figure 7-6, in which it is clear that they differ with anneal temperature. The maximum active concentration achieved for the 700°C iRTP anneal was found to be roughly $2x10^{20}cm^{-3}$, which is approximately an order of magnitude higher

than the equilibrium boron solid solubility in crystalline silicon for the corresponding temperature [TRU60]. Thus this concentration was much higher than the equilibrium solid solubility in crystalline silicon at the estimated re-crystallization temperature of 580°C [TRU60]. The active concentrations obtained herein were found to be in agreement with the findings of other authors who reported comparable active concentrations [SOL90, LIN03, JAI04]. The active concentrations obtained for the 1000 through 1200°C fRTP anneals were found to be slightly lower with an average value of $1.4x10^{20}cm^{-3}$, which was a direct result of the reduced active boron doses detected by the Hall measurement. However, they too concurred with previous findings [SOL90, LIN03, JAI04]. In particular Lindfors' studies demonstrated that active concentrations of $1.2x10^{20}$ to $2.2x10^{20}cm^{-3}$ for a similar boron dose can be achieved for furnace anneals conducted at 600°C for 1 to 4 minutes. Thus leading one to believe that the discrepancy in active dose between the 700°C iRTP and the fRTP anneals in the range 1000 through 1200°C may not necessarily be due to the formation of BICs, but may simply represent the boron fraction incorporated at lattice sites during the SPER. It can therefore be deduced that the differences in the active dose associated with these anneal temperatures (700-1200°C) were a direct consequence of the boron tail motion, since the maximum active concentration matched reasonably well.

Active concentrations on the order of $3x10^{20}cm^{-3}$ were achieved for the 1300°C fRTP anneal, which represents more than a 33% increase in the active concentration over the lower temperature anneals. Analyses of the diffusion profiles divulged that the majority of the increase in active dose above that of the lower temperature anneals did not lie in the diffused region of the profile, rather in the profile peak. The difference in

active dose between the 1200°C and 1300°C fRTP anneals was estimated at $2x10^{14}cm^{-2}$, of which 20% resided in the tail region and the remaining 80% in the peak of the profile. Hence, the much higher levels of active boron achieved by the 1300°C fRTP anneal were not totally due to diffusion of the profile into the bulk, but additional activation of boron in the peak from some initial, immobile, inactive configuration. This activation in the profile peak clearly occurred subsequent to the re-crystallization of the layer and therefore could not be attributed to the regrowth.

To more accurately evaluate the effect of the increased temperature post the re-crystallization process, the active concentrations of the 700°C iRTP were compared to the 1300°C. Figure 7-7 highlights the differences in active regions for these anneals. The reasons for choosing these temperatures were simply due to the fact that the re-crystallization was known to be completed during the ramp up to the iRTP anneal temperature, so that it served as an initial condition; while the 1300°C demonstrated a substantial increase in active dose of approximately 50%. This increase in active dose of the 1300°C fRTP over the 700°C iRTP was determined to occur both in the peak of the profile and the diffused tail. Approximately 60% of the augmented active dose was located in the peak and the remaining 40% was the direct result of diffusion of the profile. The inactive portion of the boron dose in the peak was estimated at 70% subsequent to the 700°C iRTP, but this value decreased by 10% on application of the 1300°C fRTP anneal. This is a significant result from the standpoint that enhanced activation was possible without diffusion subsequent to re-crystallization of the amorphous layer. The question of the origin of this 10% supplemental boron activation in

the peak then arises. Clearly the boron was activated from some other immobile configuration.

The active dose cannot be examined solely without considering the trends in mobility. Figure 7-5 contains the mobility data obtained from the Hall measurements as a function of the anneal temperature, in which it is noticeable that the mobility achieved on application of the fRTP anneals were higher than that of the 700°C iRTP anneal. Within experimental error one can argue that the mobility of the 1300°C fRTP anneal relative to the 700°C iRTP did not change. However, it was peculiar that the mobility exhibited an increasing trend with anneal temperature in the fRTP temperature range 1000 through 1200°C, since the corresponding active concentrations were determined to be almost identical in the range with values on the order of $1x10^{20}cm^{-3}$. Accepted mobility models [KLA92] predict a constant mobility at such dopant concentrations which lies between 40 and $50cm^{2}/Vs$. The mobility for the 700°C iRTP and the 1300°C fRTP anneals were consistent with the model predictions, however those values attained for all other fRTP anneals were above the predicted mobility range and exceeded this range by as much as 20%. The higher mobility values correspond to the active doses which were determined for this temperature range, and therefore offer an explanation for the decrease in active dose detected between the 700°C iRTP and the 1000 to 1200°C fRTP anneals. Since the sheet resistance is inversely related to the product of the mobility and the active dose, then a higher mobility automatically means a smaller active dose for a given sheet resistance.

An increase in the mobility is expected if there is an increase in the time between scattering events. If one considers scattering by the ionized impurities in the material, one

cannot argue substantial differences between the anneal temperatures since the active concentrations were observed to be similar and therefore the probability of such scattering should have been similar. Hence this argument cannot explain the differences observed. The prime cause for such a mobility enhancement is unclear at this time and would need to be the focus of additional investigations which are not encompassed in this work.

7.2.3.2 30keV germanium preamorphizing implant

In the case of the deeper amorphous layer formed by the 30keV germanium implant, the re-crystallization temperature was not the same for all the boron profiles for two reasons. Firstly, the amorphous layer was deeper and secondly, an intrinsic velocity dictated the initial stages of the regrowth since the boron implant was shallow. Hence when the 700°C iRTP temperature was realized, less than half of the layer was estimated to have re-grown and the boron profile was not yet encountered. Consequently, the recrystallization temperature differed for the control sample (700°C iRTP only) and the samples which were annealed at the fRTP temperatures. Since the peak temperature of the iRTP anneal was 700°C, the remaining recrystallization occurred during the ramp down, at which time boron activation occurred. But for the fRTP anneals, upon achieving the iRTP temperature the fRTP anneal was introduced, hence the remaining amorphous region was crystallized on the ramp up to the target fRTP temperature at an estimated 1000°C, in all cases. Thus boron activation occurred during the ramp up to the fRTP from the iRTP anneals.

Jain's findings indicated the boron activation had a monotonically increasing dependence on the temperature [JAI04]. The increased boron activation above that of the 700°C iRTP, on application of the fRTP temperatures, can therefore be attributed to the

higher temperatures at which the re-crystallization occurred, which was shown to be approximately 1000°C for all fRTP anneals. Similar to the case of the 8keV germanium implant, the activation levels detected at 1300°C cannot be accounted for by the proposed theory based on the recrystallization temperature. If this theory holds true, then the supplemental activation of boron must be the result of another physical mechanism, post amorphous layer re-crystallization.

One could argue that the active doses between 1000 and 1200°C are the same, since they lie within the experimental error associated with the Hall measurements. However, there seems to be an increase in the active dose for the 1200°C fRTP anneal above that of the 1000 and 1100°C anneals. If this is the case, it suggests that the additional thermal budget applied to the material subsequent to amorphous layer re-crystallization effected additional activation of boron at the 1200°C fRTP anneal as well.

In order to gain further insight into the responsible mechanisms for the increased activation, the active portions of the SIMS boron profiles were determined. This was conducted using a similar method described above for the 8keV germanium preamorphizing implant; by matching the integrated area below the curve to the active boron dose obtained from the Hall measurement. This yielded the maximum active concentrations achieved by each anneal and is shown in Figure 7-8. Any concentrations above these values were assumed to be in an inactive state. Scrutiny of the active boron concentrations in the re-crystallized layer of the 30keV germanium preamorphization implant, revealed different characteristics to that of the lower germanium amorphizing energy. In this situation a progressive increase in active concentration could be seen as the peak anneal temperature was increased from 700°C to 1100°C. This data substantiated

the theory that the temperature at which the re-crystallization was completed, dictated the amount of active boron in the silicon lattice. However, it was evident that the 1200°C anneal effected increases in the active concentration which were not due to diffusion of the profile into the bulk, but were mainly due to activation of boron atoms in the peak, subsequent to SPER. An estimated 90% of the activated boron dose above that of the 1100°C fRTP anneal was contained in the peak of the profile. Similarly, most of the elevated active boron concentrations above the 1100°C fRTP at 1300°C were located in profile peak, which accounted for 60% of the increase in active boron, versus 40% in the tail. One may be compelled to assume that the increase in the active dose associated with the 1200°C fRTP anneal above that of the 1100°C fRTP may be the within the errors of the Hall measurement. But if this holds then the same error must be attributed to the peak active concentration observed for the 1300°C fRTP anneal. Assuming this is the case the increases in the active concentration observed at 1300°C, must be attributed to additional activation resulting from diffusion of the profile tail. Figure 7-9 illustrates the active concentration levels attained for the 1200 and 1300°C fRTP anneals relative to the 1100°C fRTP.

The mobility values attained for this experiment were in accord with model predictions [KLA92], both in terms of the value and the trends observed. Figure 7-5 contains the measured mobility as a function of the anneal temperature. The values ranged between 40 and 50cm^{2}/Vs which correspond to the predicted values for the concentration range of the active dopants for the 30keV germanium implant. The fact that the mobility did not change substantially as the anneal temperature was increased corroborates the trends observed for the active dose.

7.2.3.3 Activation subsequent to solid phase epitaxial regrowth

If the above theory proposed for the 30keV germanium energy case, which postulates that the increased activation at 1300°C is only associated with diffusion of the profile, holds, then it invalidates the supposition that the additional thermal budget subsequent to the re-crystallization effected supplemental activation of boron in the peak of the profile. The latter was proposed to account for the enhanced activation observed at this temperature for the 8keV germanium implant. In an attempt to resolve the responsible processes, the 1300°C fRTP anneals for both germanium energies were compared since they demonstrated comparable material properties.

In the case of the 8keV germanium implant, the amorphous layer re-crystallized during the ramp up to the 700°C iRTP anneal, at an estimated temperature of 580°C compared to 1000°C for the 30keV germanium preamorphizing implant. Hence given the supposition that the activation was a function of the re-crystallization temperature, upon complete re-crystallization of the layer the activation levels were expected to be lower for the 8keV germanium implant. Therefore to account for the high levels of activation detected for the 1300°C anneal, the additional thermal budget imparted to the wafer subsequent to re-crystallization, must have effected increases in activation. The source of this supplemental activation may be due to diffusion or activation from a previous immobile state or both.

The initial active condition in both cases was assumed to be that for which re-crystallization occurred. These were taken as the 700°C iRTP and the 1000°C fRTP anneals for the 8 and 30keV germanium energies, respectively. The differences in the active portions of the boron profiles between these assumed initial conditions and the respective 1300°C fRTP anneals were therefore expected to indicate the source of

enhanced activation. Figure 7-7 illustrates the active concentrations for the 700°C iRTP and 1300°C fRTP anneals for the 8keV germanium implant. It indicated that the augmented dose of the 1300°C was located in both the peak and the diffused tail of the profile, with respective fractions of 60 and 40% of the increase in active dose above the active crystallization dose (active dose upon re-crystallization). Similarly, the enhanced activation of the 30keV germanium implant occurred both in the peak and the diffused profile tail, as seen in Figure 7-10. However, in this case the higher portion was positioned in the profile tail which constituted approximately 70% of the increased active dose. If one compares the peak active concentration for the 1300°C anneals for the 8keV and 30keV germanium preamorphizing implants, essentially no differences could be discerned, except in the tails of the boron profiles. These diffusion differences observed in the tails could be explained by considering that the boron positioned in the layer formed by the 30keV germanium implant underwent some diffusion in the amorphous phase which resulted in a more abrupt, deeper profile. Hence the initial condition was deeper, yielding a deeper profile which constituted a higher fraction of the newly activated dose. Alternatively, one could consider that the boron segregation to the EOR loop layer may have also contributed to less diffusion in the tail for the 8keV germanium PAI.

Since both analyses indicated that a significant fraction of the dose was located in the peak of the profile, the author is inclined to believe that the both processes of diffusion and supplemental activation from a previous immobile state in the profile peak are responsible for the increases in active dose observed. The configuration of this initial immobile fraction of boron is unknown. It is unclear at this time why the maximum

active concentrations coincide for both germanium energies despite the fact that the initial active fraction immediately subsequent to amorphous layer re-crystallization differ. One would have expected the sample with the higher initial active concentration prior to the fRTP anneal to yield a higher active dose, assuming the source of the additional boron activation was the same. The total dose activated in the peak after re-crystallization was determined to be smaller for the 30keV germanium implant. The differences in additional thermal budget applied subsequent to the re-growth, may account for the different activated fractions of boron in the peak. Since the layer formed by the 30keV germanium implant re-crystallized at the higher temperature, less thermal budget was available for additional activation in the peak, hence a smaller fraction of boron was activated. Alternatively, the existence of a threshold for boron activation subsequent to the re-crystallization is proposed to account for the similar peak active concentrations obtained despite the differences in the active dose upon re-crystallization.

Furthermore, the increase in active concentration in the peak observed at 1200°C for the 30keV germanium preamorphizing implant may be the attributed to the error in the Hall measurement. It seems unlikely that the thermal budget was insufficient to activate boron from this inactive unknown configuration in one instance and not in the other, given that the fRTP anneals were performed simultaneously. If it were sufficient to activate the boron atoms in the layer formed by the 30keV germanium implant, then it should have also initiated a similar boron activation for the 8keV germanium implant. One could argue that this was the case if boron existed in different configurations for the 8 and 30keV germanium energies, however, the fact that very similar behavior was observed for the 1300°C fRTP anneal in both cases nullifies this presumption.

The active dose and mobility measurements for the 30keV presented a clearer picture of the processes which controlled the sheet resistance. In this case, it was evidently the differences in the active doses, which changed with the recrystallization temperature that governed the sheet resistance, since the mobility was found to remain almost the same. On the contrary, the variation in the mobility detected for the 8keV germanium implant presented some inconsistencies. If the activation was a function of the re-crystallization temperature then they should have all been the same for anneal temperatures of 1200°C and below. The differences in this temperature range were found to fall within the error of the Hall measurement. Assuming this was correct then the changes in the sheet resistance over this temperature range must be accredited to the changes in the mobility. This suggests that processes which control the sheet resistance vary with the germanium preamorphization energy. But a firm conclusion cannot be drawn from this experimental data set, since the reasons for the changes in the mobility are not understood at this time.

7.2.4 Models for Boron Activation during Re-crystallization

It is widely accepted that low temperature anneals are capable of producing activation levels which exceed solid solubility limits in crystalline silicon [BLO79, NAR82, LIN03]. This has been attributed to solute-trapping at the amorphous-crystalline interface which occurs provided the impurity residence time at the interface exceeds time required for re-growth of the monolayer [CAM80]. It has also been postulated that impurity solubility in amorphous silicon is significantly greater than that in crystalline silicon. The increased solubility has been ascribed to the large density of defects trapping and gettering the impurities [ELL85, POL90, COF92], as well as to the distorted atomic structure of the amorphous phase [CAL89]. To account for the higher boron activation

levels yielded by higher re-crystallization temperatures a number of theories have been proposed which stem from these hypotheses.

One such model was presented by Jain [JAI04] and is based on the assumption that clusters of boron form in the amorphous phase. Thus as the amorphous-crystalline interface is swept across the boron profile during the re-growth, those concentrations which exist as clusters form the inactive portion of the profile, while the boron concentrations which have eluded cluster formation are trapped at substitutional sites and account for the active dose. They attributed the lower inactive concentrations attained at the higher fRTP temperatures to the reduced time for cluster formation owing to the fact that the re-growth velocity had an exponential dependence on the temperature. Examination of the calculated re-growth velocity for the 8keV germanium preamorphizing implant indicated significant re-growth of the layer did not occur for temperatures below 550°C. Hence the boron layer spent approximately 1-2 seconds in the amorphous phase, which may have been sufficient time for boron to cluster before the interface began to sweep over the profile. The boron profile for the 30keV germanium implant was also shown to spend a similar time in the amorphous phase before the interface encountered the profile. This suggested that similar fractions of boron should have clustered. But recall that the re-growth velocity varies exponentially with temperature; hence the rate at which the interface swept over the boron profile was much faster for the 30keV germanium implant for those re-crystallizations which occurred on the ramp up to the fRTP at 1000°C. Conversely, the interface traversed the boron profile in the amorphous layer of the lower energy implant at temperatures below 600°C and consequently at lower rates. Theoretically, the boron atoms for the lower energy

germanium preamorphization had more time to cluster in the amorphous phase, which may account for the lower active doses. Nevertheless this argument does not account for the similar active doses observed for the 700°C iRTP anneals, for which the 30keV germanium amorphous layer was re-crystallized on the ramp down from the 700°C peak temperature compared to on the ramp up for the 8keV germanium amorphous layer. The boron implant for the 30keV germanium spent more time in the amorphous phase, thus the clustering reactions should have been more yielding a lower active dose for the 700°C iRTP anneal. Clearly this hypothesis cannot account for all the experimental data.

An alternative proposal to account for the higher activation levels achieved by higher recrystallization temperatures [JAI04] takes into account the exponential dependence of the re-crystallization velocity. The faster sweeping velocity is believed to trap much larger concentrations at substitutional sites, since the re-growth velocity is much higher than the corresponding dopant atom diffusion [CAM80, CLA04]. Melt laser annealing represents the extreme end of this spectrum, where all the dopants are incorporated onto lattice sites because of the exceptionally high regrowth velocity [JAI04]. In the case of the 8keV germanium preamorphizing implant the re-crystallization occurred on the ramp up to the iRTP at an estimated temperature of 580°C, hence the regrowth velocity varied accordingly and was much lower than that of the layer formed by the 30keV germanium preamorphizing implant. In the latter instance the amorphous-crystalline interface swept over the boron profile for temperatures between 700 and 1000°C, at a much higher re-growth velocity, hence in accordance with the proposed theory the faster re-growth should have resulted in higher concentrations of boron atoms trapped at substitutional sites. Higher activation levels immediately

subsequent to the re-crystallization were observed for the 30keV germanium preamorphizing implant layers subjected to the fRTP anneals, which agreed with this conjecture.

More recently, Gable [GAB04] proposed that boron exhibited a higher solubility in the amorphous phase relative to the crystalline phase. This was thought to be the responsible factor for the higher active fractions obtained at higher re-crystallization temperatures. Since the boron profiles in amorphous silicon were subjected to different temperatures owing to the differences in the re-growth velocity, it is plausible that the solubility differed. For the shallower amorphous layer the maximum temperature to which the amorphous region was raised prior to re-crystallization was below the re-crystallization temperature of 580°C. On the contrary, the amorphous region experienced much higher temperatures on the ramp up to the 1000°C anneal. The boron solubility in the amorphous phase was therefore much higher for the 30keV germanium preamorphization, which concurred with the higher active doses attained subsequent to re-crystallization of the layer. Gable's supposition can account for the higher active doses achieved at the higher re-crystallization temperatures in these experiments. However, the reasons why a higher solubility was attained in the amorphous phase have not been presented.

Based on the most recent discussion, the author is inclined to believe that the higher active doses achieved at higher re-crystallization temperatures could be the result of either the effective solute trapping at substitutional sites during the re-growth or the higher boron solid solubility in the amorphous phase.

7.2.5 Kinetics of Boron Activation

The active concentrations detected for the 1300°C fRTP anneals discussed above demonstrated that the additional activation occurred subsequent to the re-crystallization process. This supplemental activation was shown to be due to not only diffusion but also to activation in the peak of the profile. The activation of boron from some immobile, inactive concentration was hypothesized to account for the high activation levels for the 1300°C fRTP anneal. Although there was a lack of evidence to support the presence of BICs of the type, which has been extensively studied by a number of researchers [STO95, LIL99, MIR03, DES05], it was deemed necessary to determine whether the detected supplemental activation of boron subsequent to SPER adhered to similar activation kinetics. Confirmation of a lack of adherence to this kinetics would support the concept of boron existence in an alternative, inactive, immobile configuration.

BICs have been shown to dissolve with an activation energy of 3.2eV [LIL02, MIR03]. This kinetics applies to BICs which have been formed for concentrations on the order of $1x10^{19}cm^{-3}$. More recently, De Salvador established that they were two regimes of BIC dissolution, characterized by a fast dissolution, similar to that of Mirabella and Lilak, and a slow dissolution [DES05a, DES05b]. BICs formed for concentrations on the order of $2x10^{20}cm^{-3}$, which exceeded solid solubility limits, were shown to dissolve with an activation energy of 4.8eV [DES05a, DES05b]. The concentrations in this work overlap both of these regimes. Based on this dissolution kinetics, the reactivated boron fraction was determined for the fRTP temperatures of interest and is shown in Tables 7-1 and 7-2. It was clear that for these thermal budgets only a small fraction of the clustered boron should be reactivated. An estimated 1.5% of the originally clustered boron should have been reactivated for the 1300°C fRTP anneal, which was much lower than the actual

active dose measured by Hall for both germanium preamorphizing energies. The measured active dose was found to be almost double the active dose attained after the 700°C iRTP anneal for both germanium preamorphizing implants. This disparity in the active concentration and the low estimated reactivated fraction precluded activation of boron from a configuration similar to the clusters studied by Lilak, Mirabella and DeSalvador [LIL02, MIR03, DES05]. Rather it was suggestive of boron activation at these temperatures from another inactive, immobile boron configuration.

7.2.6 Validity of the Plateau Concentration as an Indication of Active Concentration

Gable [GAB04] postulated that boron concentrations above a plateau concentration, which was defined as the concentration at which the diffusion produced an inflexion point in the concentration-depth profile, were inactive for a 3keV, 1x10^{15}cm^{-2} BF_2 implant into an amorphous region formed by a 48keV 6x10^{14}cm^{-2} germanium implant. Consequently the maximum active concentration was assumed to correspond to the plateau concentration extracted from the diffused boron profiles. Figure 7-11 contains the active concentrations obtained for these experiments as a function of inverse anneal temperature, on which Gable's data was also illustrated. The active concentrations for this work matched those obtained from Gable's assumptions remarkably well for the 30keV germanium preamorphizing implant, which validated Gable's hypothesis. To determine whether this supposition held up for the 30keV germanium preamorphizing implant the active concentrations were examined relative to the diffused profiles to determine whether they coincided with an inflexion point in the concentration-depth profile. Within the limits of the accuracy of the active dose measurements and the SIMS analyses these values coincided reasonably well. In the case of the lower energy germanium preamorphizing implant, the inflexion points were not as noticeable but could

still be discerned. Here too, the inflexion points were a relatively good indication of the peak active concentrations.

A significant finding of these experiments was the fact that the peak active concentrations were found to be more than an order of magnitude greater than the solid solubility in crystalline silicon for relatively low re-crystallization temperatures. This detail supports the both postulated theories; the solute trapping at substitutional sites during the re-growth was more effective at the higher re-crystallization temperature and the solid solubility of boron in amorphous silicon was much higher than that in crystalline silicon. Additionally, the slight temperature dependence that was observed validated the theory that the activation was a function of the recrystallization temperature.

7.2.7 Boron Interstitial Clusters

Previously the formation of BICs was proposed to account for the apparent deactivation observed for the iRTP anneal and the 1000, 1100 and 1200°C fRTP anneals for the 8keV germanium preamorphization energy. This hypothesis was thought to be conceivable since high boron concentrations were in very close proximity to the EOR damage region, in which a high interstitial supersaturation was available. BICs are known to severely deteriorate the electrical properties of the silicon host due to boron electrical deactivation [COW90, LIL99, MIR03] and carrier concentration mobility lowering [MIR03]. They have also been shown to be very stable, existing for up to 4 hours after TED at 800°C [STO95, MIR03]. The following discussion is aimed at highlighting the experimental evidence which led to the conclusions drawn.

Consider Figure 7-12 which contains the diffused boron profiles for the 8keVgermanium preamorphizing implant. The boron profiles clearly underwent some diffusion in the peak region (shallower than the amorphous-crystalline interface), which

exceeded intrinsic boron diffusion lengths for the anneal temperatures investigated. The magnitudes of these diffusion lengths were found to be comparable with the enhanced diffusion lengths and are shown in Tables 7-3 and 7-4, respectively. Annealing is known to induce transient enhanced diffusion (TED) [HOF74, MIC87, COW90] of boron which arises from the fact that ion-generated self-interstitials accelerate boron diffusion through the interstitialcy or kick-out mechanism [FAH89]. The observed enhanced diffusion in this work was therefore indicative of silicon interstitials interacting with the boron profile. Enhanced diffusion does not preclude clustering phenomenon. It has been observed [MIC87, COW90] that above an apparent critical boron concentration, the peak portion of the boron profile remains static and electrically inactive upon annealing [STO95]. In these experiments the static peak associated with BIC formation was not observed, although there was evidence of the silicon interstitials interacting with the high concentration regions of the profile, which suggested that BICs may not have formed.

In these experiments the high concentration regions of the profile were located in the regrown amorphous material. Jones [JON96] demonstrated for a boron marker layer located in an amorphous region that clustering phenomenon did not occur when the material was re-grown. This was attributed to the lack of sufficient interstitial backflow subsequent to layer re-growth to enable clustering reactions. The interstitial backflow was later shown to decrease with increase in implant temperature owing to the reduction in EOR damage density [JON97]. Above it was shown that the silicon interstitials from the EOR region in this work were not diffusion limited, since TED of the boron profile was observed. Hence the interstitials were able to interact with the boron profile. However, it is not the absolute number of interstitials that governs BIC formation; rather the

interstitial supersaturation is the critical condition. If the interstitial supersaturation was not high enough BICs would not form. Table 7-2 contains the interstitial supersaturation levels determined from Cowern's data [COW99] for the temperatures used in these experiments, in which it is clear that the supersaturation levels varied over two orders from $1x10^4$ at 700^oC to $1x10^2$ for the fRTP anneals. As the anneal temperature increased, the probability of BIC formation therefore decreased since the interstitial supersaturation fell, which corroborated the notion that BICs were not present in the microstructure.

Another compelling piece of information which substantiated this supposition was the mobility data for the temperature range over which the reduction in active dose was observed. BICs are known to lower the carrier concentration mobility [MIR03], but the mobility was found to increase in the temperature regime for which BIC existence was postulated. Hence this also pointed to the fact that these clusters may not be present in the microstructure.

Based on the above discussion which highlighted the factors the author believed were relevant, it was concluded that BIC formation was most likely not responsible for the apparent deactivation observed as the anneal temperature was increased from 700^oC iRTP to 1000, 1100 and 1200^oC fRTP temperatures. This decrease in active concentration was believed to be due to the errors in the Hall measurement.

7.3 Conclusion

The analyses contained in this chapter attempted to resolve the experimental findings presented in the previous chapter; the aim of which was to determine whether the germanium preamorphization energy had an impact on the final characteristics of p-type junctions formed in silicon by Flash-assist Rapid Thermal Processing. The experiment entailed varying the germanium preamorphizing energy for values of 8 and

30keV at a constant dose of $1x10^{15}cm^{-2}$. Boron was subsequently implanted at a constant energy and dose of 1keV and $1x10^{15}cm^{-2}$, respectively.

Analyses of the experimental results revealed that the initial conditions had a significant impact on the junction characteristics. Specifically the position of the amorphous-crystalline interface relative to the boron profile effected differences in the re-growth velocities and hence the time the dopant profile spent in the amorphous phase and the temperatures to which these profiles were subjected to during the recrystallization process. These differences dictated the final activation levels which were found to be a function of the re-crystallization temperature. The corresponding activation mechanisms were attributed to the much more effective trapping of solute atoms at substitutional sites at the higher temperatures. The experimental findings also concurred with the possibility of higher boron solid solubility levels in amorphous silicon. Naturally, the shallower amorphous layer re-crystallized at a lower temperature. However, the additional impact of the enhanced regrowth due to the boron presence resulted in a reduced re-crystallization temperature, which effected an active dose in the 8keV germanium preamorphizing case that was much smaller than that for the 30keV germanium preamorphizing implant. The amorphous layer formed by the 30keV germanium implant was shown to re-crystallize at a much higher temperature resulting in the observation of the higher active dose.

Subsequent to the re-crystallization process thermal budgets associated with fRTP anneal temperatures as high as $1200^{o}C$, were determined to be insufficient to result in increased activation levels, thus the final activation was controlled by the re-crystallization temperature. But at $1300^{o}C$ fRTP increases in activation levels above the

re-crystallization activation, of approximately 50 and 30% were detected for the 8 and 30keV germanium implants, respectively. These were observed to be a direct consequence of two processes which included increased diffusion in the tail of the boron profile and activation in the profile peak. This find demonstrated that boron was activated from some initial unknown, immobile, inactive configuration. Comparisons of the kinetics associated with the dissolution of the extensively studied BICs [LIL02, MIR03, DES05], revealed that these thermal budgets were insufficient to activate boron from such a configuration, to yield the high active concentrations observed. Hence it was concluded that the supplemental activation was the result of boron activation from another inactive configuration. This is a significant finding of this research, since it was demonstrated that the high anneal temperatures enabled by Flash-assist RTP enabled additional activation of boron in the profile peak, subsequent to the re-crystallization process.

Additionally, despite the differences in the active dose upon completion of the re-crystallization process, identical peak active concentrations were attained for the 1300°C anneal which hinted at a possible threshold concentration for activating boron at these temperatures. The final junction characteristics attained for the 1300°C fRTP anneal appeared to be independent of the germanium preamorphization energy, since they exhibited similar electrical and diffusion profiles. However, the diffused tail of the boron profile in the layer formed by the 30keV germanium preamorphizing implant was found to be more abrupt. This too was a direct consequence of the deeper position of the amorphous layer relative to the boron profile, which facilitated obvious levels of boron

diffusion in the amorphous layer prior to the amorphous-crystalline interface encountering the dopant.

It was also concluded that the sheet resistance was dictated by the active dose for the 30keV germanium preamorphizing implant. Conversely, the mobility appeared to be the dominant parameter which governed the final sheet resistance for 8keV germanium implant for temperatures of 1200°C and below, since the active dose was demonstrated to be controlled by the re-crystallization temperature. But a firm conclusion could not be drawn for the 8keV germanium preamorphizing implant, as the mobility changes are not fully understood at this time and needs to be further investigated.

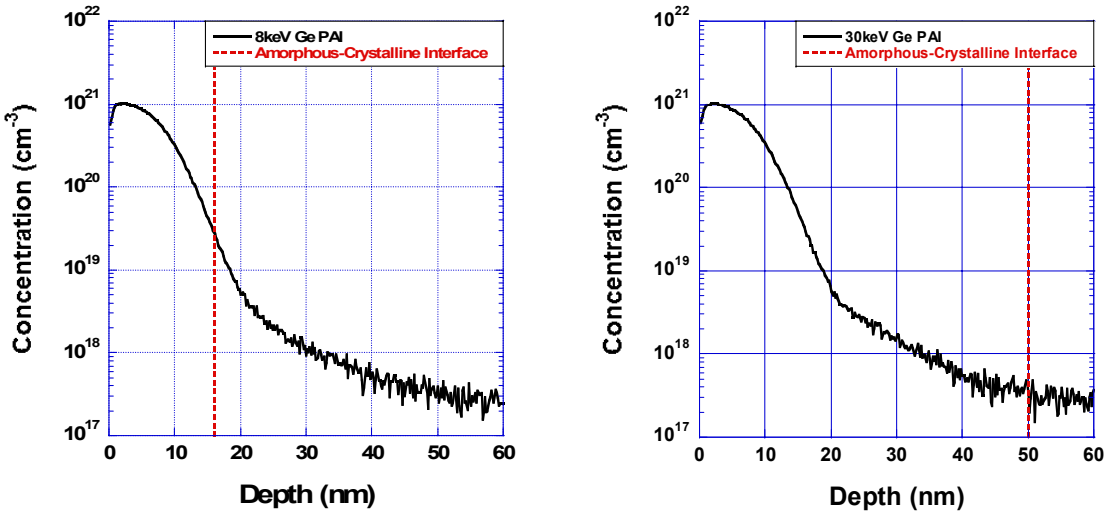

a) b)

Figure 7-1. Concentration-depth profiles of the boron implant into amorphous layers formed by an 8 and 30keV germanium preamorphizing implant, obtained from SIMS analyses. a) 8keV germanium PAI and b) 30keV germanium PAI

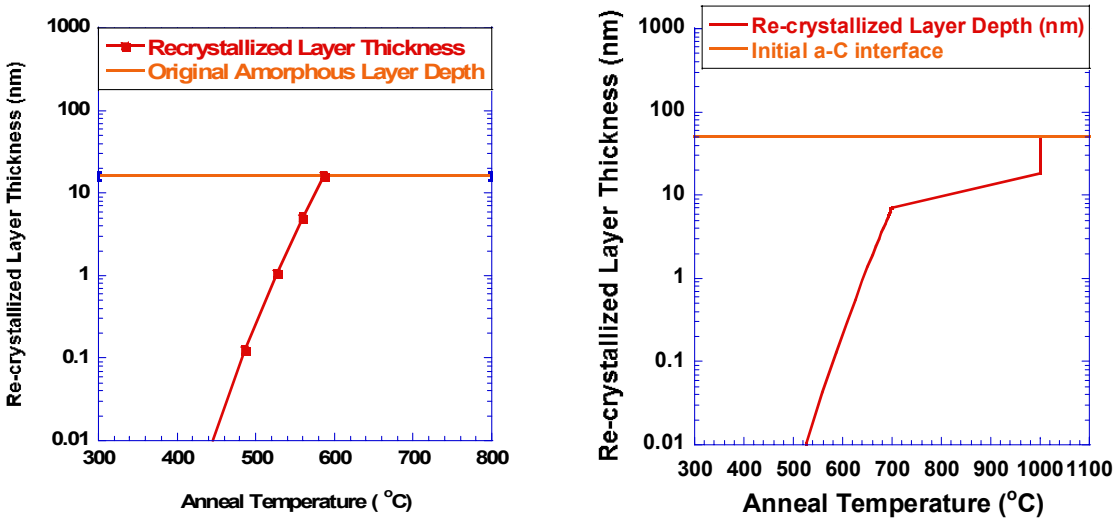

a) b)

Figure 7-2. Re-crystallized layer depth as a function of anneal temperature generated in FLOOPS, utilizing both an intrinsic and extrinsic regrowth velocity relations, for an 8 and 30keV germanium preamorphizing implant. a) 8keV and b) 30keV germanium PAI.

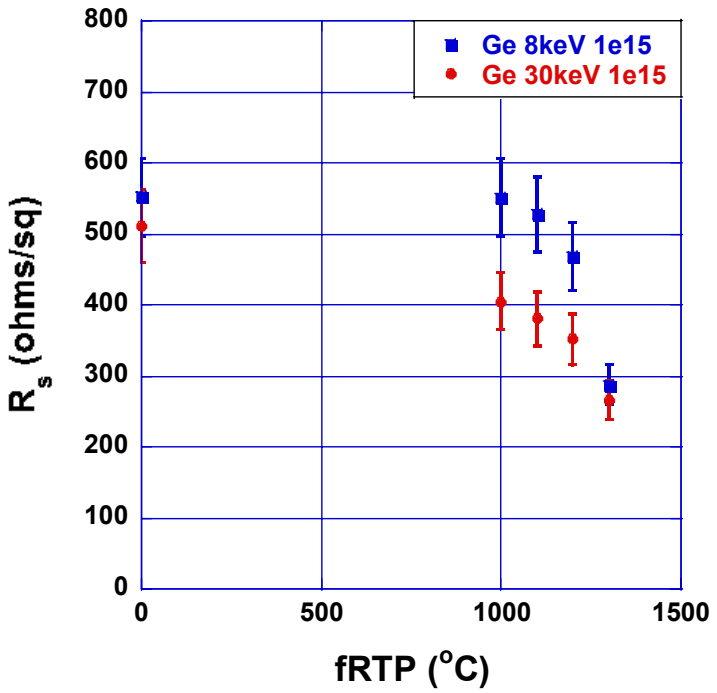

Figure 7-3. Sheet resistance, R_s as a function of fRTP anneal temperature for 8 and 30keV germanium PAI obtained from Four-Point Probe measurements.

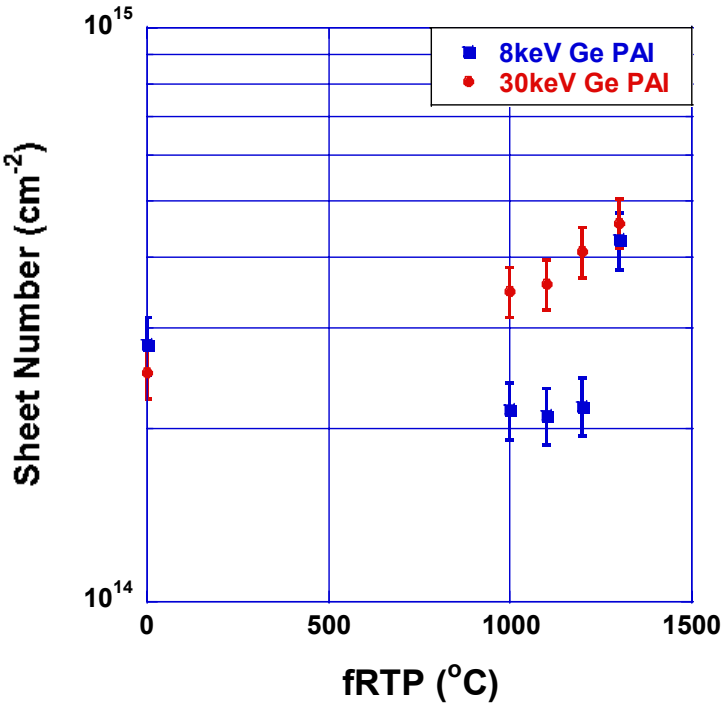

Figure 7-4. Active dose as a function of fRTP anneal temperature for 8 and 30keV germanium PAI obtained from Four-Point Probe measurements.

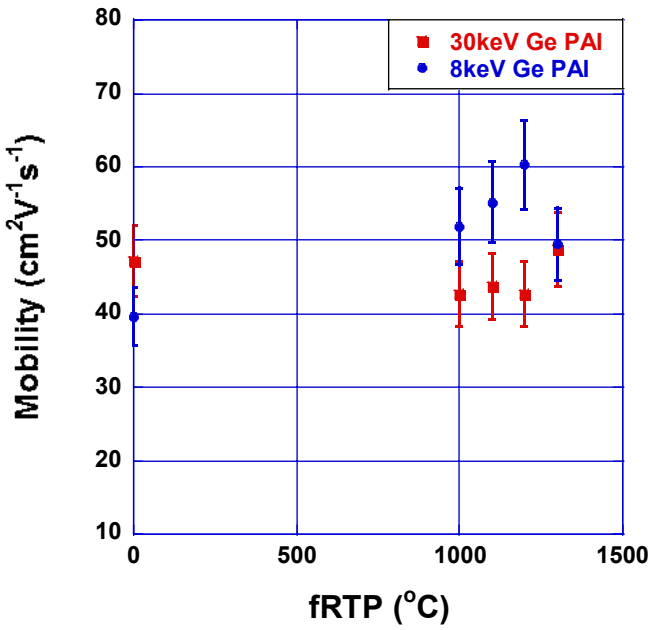

Figure 7-5. Hole mobility as a function of fRTP anneal temperature for 8 and 30keV germanium PAI obtained from Hall measurements.

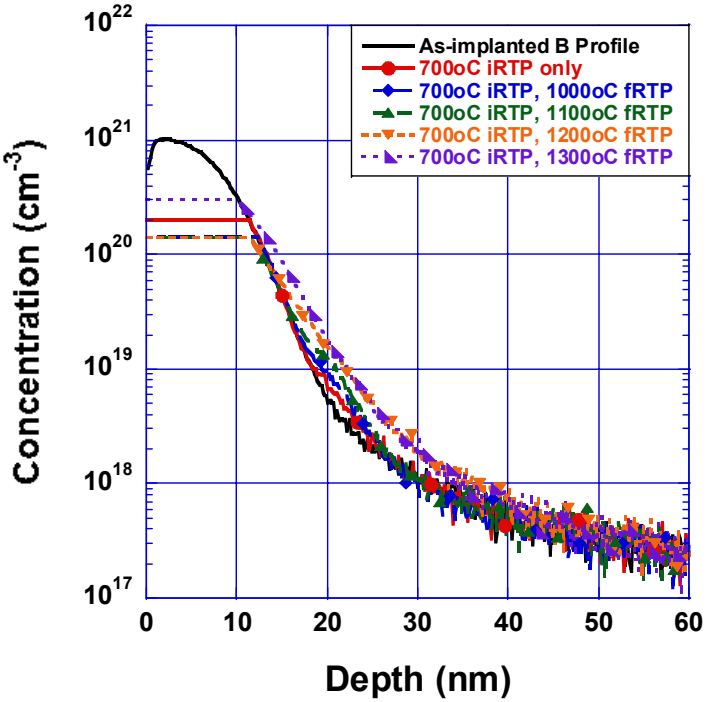

Figure 7-6. Active portions of the SIMS boron profile, determined by matching the integrated area below the curve to the active boron dose obtained from the Hall measurement for an 8keV germanium PAI. Peak active concentrations are also highlighted for each anneal

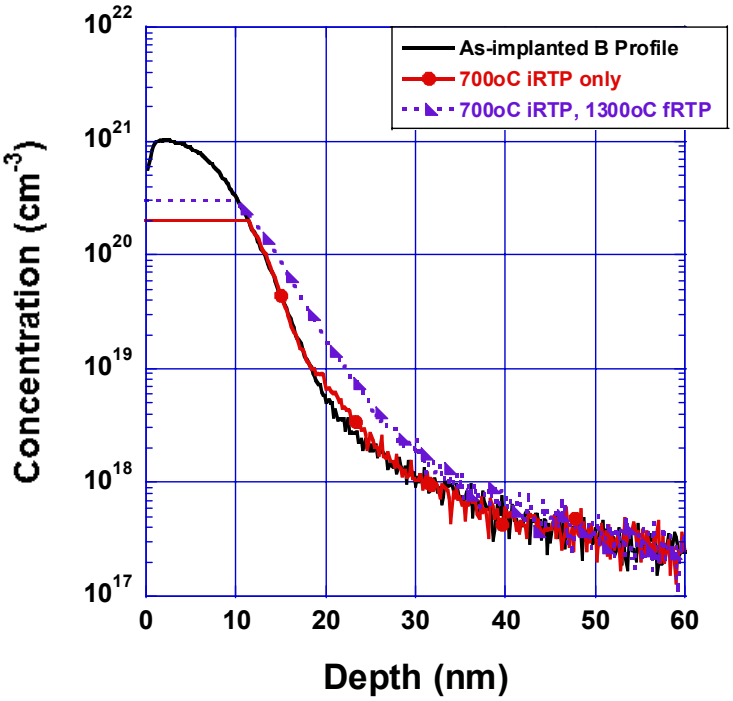

Figure 7-7. Active portions of the SIMS boron profile for the 700°C iRTP and 700°C iRTP/1300°C fRTP anneals. These were determined by matching the integrated area below the curve to the active boron dose obtained from the Hall measurement for a 8keV germanium PAI. Peak active concentrations are also highlighted for each anneal.

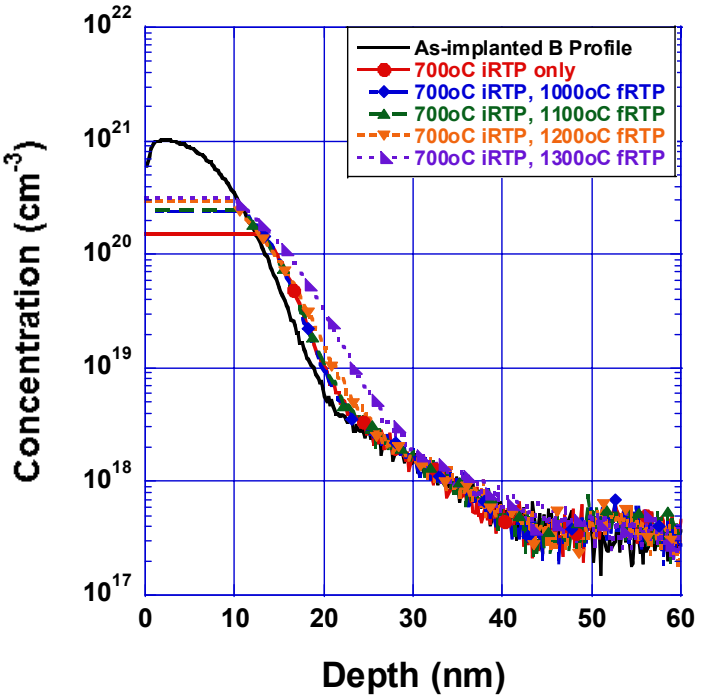

Figure 7-8. Active portions of the SIMS boron profile, determined by matching the integrated area below the curve to the active boron dose obtained from the Hall measurement for a 30keV germanium PAI. Peak active concentrations are also highlighted for each anneal

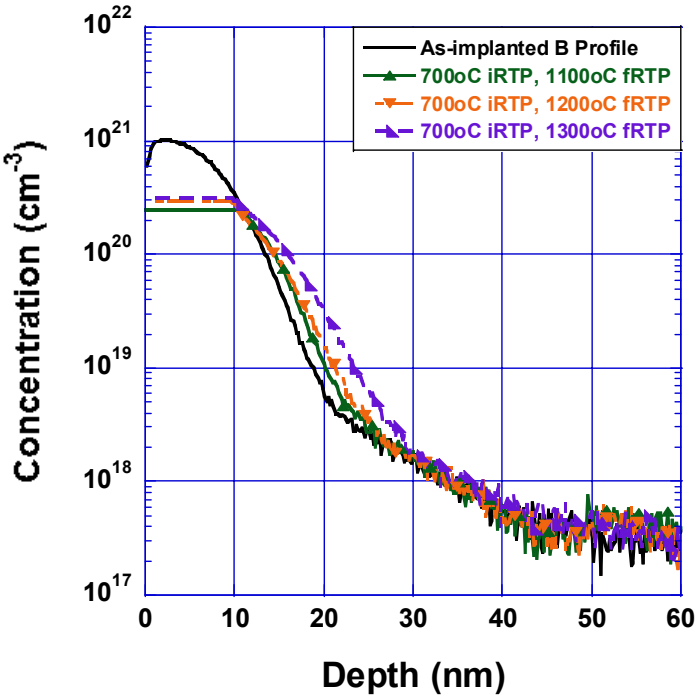

Figure 7-9. Active portions of the SIMS boron profile for the 700°C iRTP/1100°C fRTP, 700°C iRTP/1200°C fRTP and 700°C iRTP/1300°C fRTP anneals. These were determined by matching the integrated area below the curve to the active boron dose obtained from the Hall measurement for a 30keV germanium PAI. Peak active concentrations are also highlighted for each anneal.

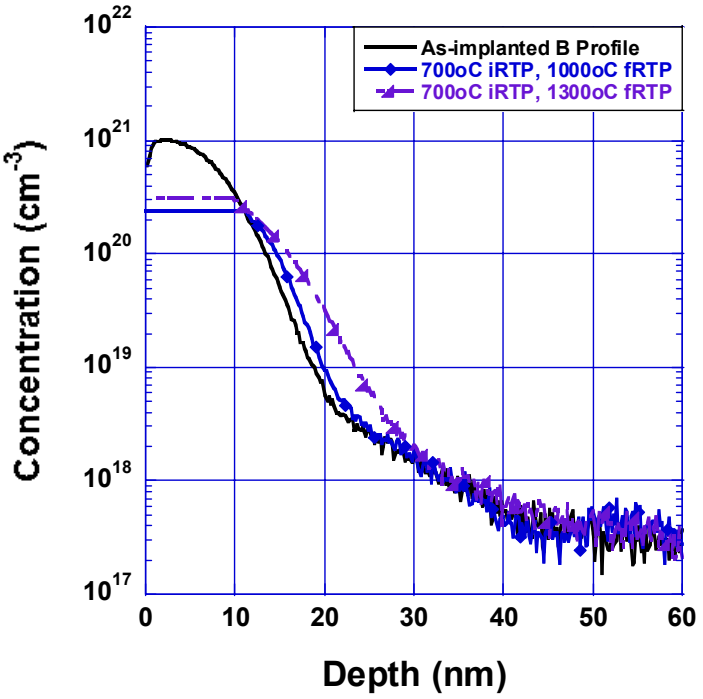

Figure 7-10. Active portions of the SIMS boron profile for the 700°C iRTP/1100°C fRTP, and 700°C iRTP/1300°C fRTP anneals. These were determined by matching the integrated area below the curve to the active boron dose obtained from the Hall measurement for a 30keV germanium PAI. Peak active concentrations are also highlighted for each anneal.

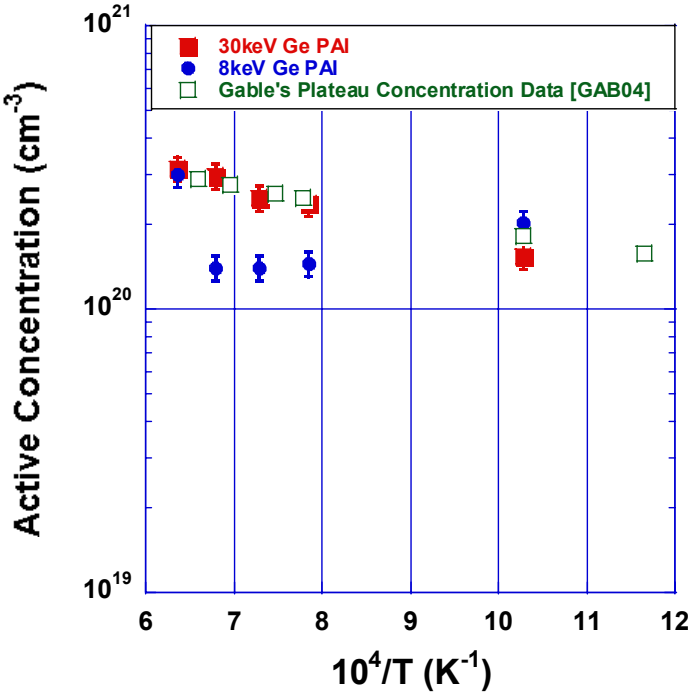

Figure 7-11. Peak active concentration as a function of the inverse peak anneal temperature for both the 8 and 30keV germanium PAI.

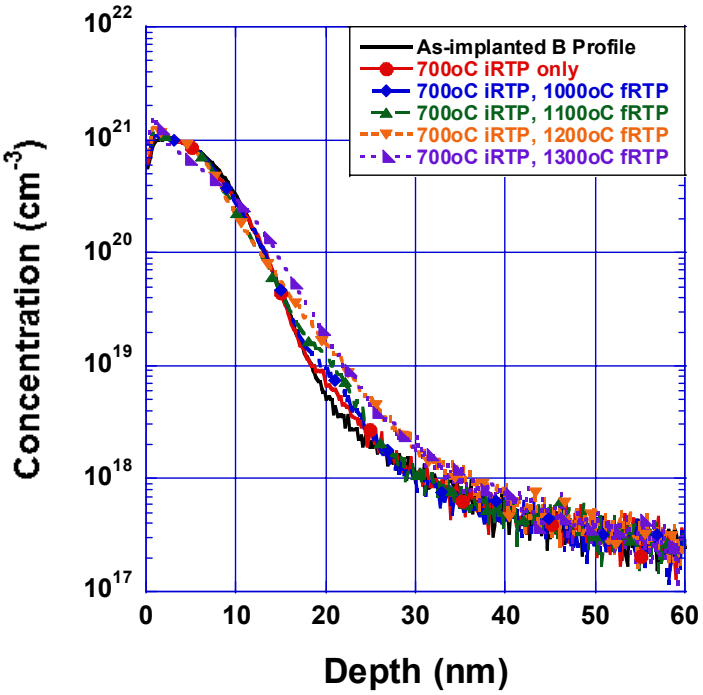

Figure 7-12. Concentration-depth profiles of the diffused boron implant processed by Flash-assist RTP for the 8keV germanium PAI obtained from SIMS analyze

Table 7-1. Estimated fraction of boron reactivated from a boron interstitial cluster of the type studied by Lilak [LIL02] and Mirabella [MIR03] for boron concentrations ranging 1x1019cm-3, based on an activation energy of 3.2eV.

T(oC)	% (Breactivated/Bclustered)
1000	0.01
1100	0.07
1200	0.38
1300	1.52

Table 7-2. Estimated fraction of boron reactivated from a boron interstitial cluster of the type studied by DeSalvador [DES05] for boron concentrations exceeding $2x10^{20}cm^{-3}$, based on an activation energy of 4.8eV.

T(^{o}C)	% ($B_{reactivated}/B_{clustered}$)
1000	0.00
1100	0.01
1200	0.19
1300	1.58

Table 7-3. Calculated boron intrinsic diffusion lengths in crystalline silicon for the fRTP temperatures investigated

fRTP Temperature (^{o}C)	Intrinsic boron diffusion length (nm)
1000	0.05
1100	0.17
1200	0.44
1300	1.03

Table 7-4. Estimated silicon interstitial supersaturation and boron enhanced diffusion length in crystalline silicon for the fRTP temperatures investigated.

fRTP Temperature (^{o}C)	Silicon interstitial supersaturation	Boron enhanced diffusion length (nm)
1000	4.62E+02	1
1100	2.68E+02	3
1200	1.68E+02	5
1300	1.11E+02	10

CHAPTER 8
ALTERING THE RE-CRYSTALLIZATION TEMPERATURE OF THE AMORPHOUHS LAYER AND ITS IMPACT ON FINAL BORON ACTIVATION

8.1 Introduction

In the previous two chapters the effect of changing the germanium preamorphization energy on boron activation and diffusion were investigated for Flash-assist RTP. One significant finding of this investigation was that the activation levels of boron in an amorphous layer may be a function of the temperature at which the amorphous layer was re-crystallized. This deduction was obtained for experiments in which the amorphous layer depth was varied by changing the germanium preamorphization energy. Changing the energy of the preamorphizing implant effected differences in the relative distances of the amorphous-crystalline interface and the end of range damage from the boron profile. This in turn effected changes in the velocities at which the amorphous layer re-crystallized since boron is known to effect enhanced regrowth velocities and consequently, the temperature at which the re-crystallization of the layer occurred. Clearly there were many variables in the experiments.

In an effort to further explore this concept the experiments presented in the previous chapters were modified by the introducing a low temperature anneal prior to the application of the Flash-assist RTP thermal anneal step. The goal of which was to re-crystallize the amorphous layer before the material was annealed by the Flash-assist RTP, such that this hypothesis could be tested, for fewer experimental variables. These experiments were performed for two germanium preamorphizaton energies, an 8keV and

30keV, at a constant dose of $1x10^{15}cm^{-2}$. Two low temperature anneals were also investigated, which entailed either an 8hour anneal at 450^oC or a 30minute anneal at 500^oC. Both of which were selected to ensure re-crystallization of the amorphous layer. The experimental results are too lengthy to all be presented in this chapter; hence the results for the 30keV germanium preamorphizing implant annealed at 500^oC for 30 minutes will be discussed. The results not included in this chapter can be found in Appendix D.

On reading the experimental results section, the reader may be overwhelmed with the vast amount of data offered. It is recommended that the reader proceed to the discussion section, where the data is further discussed and analyzed. The discussion serves to clarify and relate the experimental results, which cannot be solely understood.

8.2 Experiment

This study utilized 200mm 12ohm-cm (100) n-type Czochralski (CZ) grown silicon wafers, which were pre-amorphized with a 30keV germanium implant at a constant dose of $1x10^{15}cm^{-2}$. Boron was subsequently implanted into all wafers at an energy of 1keV and a dose of $1x10^{15}cm^{-2}$. The ion implantations were performed in an Applied Materials XR80 Leap Implanter at a standard tilt of 7° and twist of 27°. Low temperature furnace anneals were then carried out on the whole wafers under N_2 ambient, in an atmospheric oxide tube of an ASM International A400 furnace, shown in Figure 8-1. The annealing chamber was brought to a temperature of 450^oC prior to the wafer loading. Once the wafers were loaded into the chamber the temperature was allowed to stabilize for a 20 minute period, subsequent to ramp up to the desired 500^oC anneal temperature. A ramp rate of 5^oCmin^{-1} was employed in the anneal sequence, such that the total anneal time spent at 500^oC was estimated at 20 minutes. Figure 8-2 is a picture of the captured

thermal profile during the course of the anneal. The annealed wafers were then subjected to another anneal step which was performed Vortek Technologies using a Flash-assist Rapid Thermal Process (RTP). The Flash-assist RTP anneal temperature profile entailed a ramp up to a 700°C intermediate temperature (iRTP) at a heating rate of 150°Cs^{-1}, where the dwell time was 0s. The temperature was then rapidly increased to flash temperatures of 1100 and 1300°C at a rate 1x10^{6} ^{o}Cs^{-1}. The experimental control wafers were only subjected to the flash anneal for temperatures of 1000, 1100, 1200 and 1300°C. The full width at half maximum of the radiation pulse ranged 0.85-0.90ms. Subsequent wafer cooling was governed by radiation heat loss to the surrounding black environment at a maximum rate of 90°Cs^{-1}, once thermal equilibrium was achieved between the surface and the bulk of the wafer. A depiction of the thermal profiles to which the wafers were subjected can be seen in Figure 8-3.

Cross-sectional transmission electron microscopy (XTEM) was utilized to determine the depth of the amorphous layers formed by the germanium implants and to confirm re-crystallization of the layers upon subsequent thermal processing. The XTEM was performed on a JEOL 200CX microscope operating at an accelerating voltage of 200keV and the images were taken under g_{110} bright field conditions. The extended defects associated with the amorphizing implants were also examined on a JEOL 200CX microscope operating under similar conditions, but via Plan-view transmission electron microscopy (PTEM). Images of the defects were captured in weak-beam-dark-field (WBDF), g_{220} two-beam conditions and analyzed via the technique developed by Bharatan et al [BHA97]. In order to track the boron diffusion, the dopant concentration as a function of depth was assessed for each anneal condition by dynamic secondary ion

mass spectrometry (SIMS) using an Adept 1010 Dynamic SIMS System by Physical Electronics. The data acquisition parameters included a 25nA, 1kV oxygen beam with a 10% gating and a raster area of 250μm x 250μm. Electrical characterizations of the junctions formed included sheet resistance measurements which were conducted on a Four Dimensions 333A Four Point Probe system. Type M probe tips placed 1mm apart with 5mm edge exclusion were used in the measurements. Hall measurements were also performed to determine carrier densities and carrier mobilities. An MMR Technologies Van der Pauw Hall System (MPS-50, K-20 and H-50) was employed with a constant field of 3000G and the measurements performed for variable currents of 0.00001, 0.0001 and 0.001A.

8.3 Results

The 30keV germanium preamorphizing implant resulted in the formation of a continuous amorphous layer which extended to a depth of 50nm into the wafer. The layer was shallow enough such that the 500°C 30 minute furnace anneal resulted in its complete re-crystallization. An XTEM image of the regrown amorphous layer is demonstrated in Figure 8-4, in which the EOR damage which lies just beyond the original amorphous-crystalline interface can be discerned at a depth of approximately 55nm. The layer was sufficiently deep such that the subsequent boron implant was wholly confined to the amorphous region. Figure 8-5 contains the concentration-depth profiles for the as-implanted profile, on which the depth of the original amorphous layer is indicated. It can be seen that the projected range of the boron implant was roughly 3nm, with a peak concentration on the order of $1x10^{21}cm^{-3}$.

In the experimental control (wafers which were not subjected to the low temperature furnace anneal) dot-like interstitial clusters populated the microstructure after the 700°C iRTP anneal. On application of the 1000°C flash temperature, few differences could be discerned in the extended defects. However, as the flash temperature was increased to 1100°C, the defect density clearly decreased and the defects appeared as small loops. At 1200°C, the defect evolution was more apparent as {311}-type defects and larger dislocation loops of smaller density were present in the microstructure. Additional coarsening and defect dissolution occurred as the flash temperature was raised to 1300°C, at which very few dislocation loops were seen. The PTEM weak beam dark field (WBDF) images of the experimental control are depicted in Figure 8-6.

Inspection of the WBDF PTEM images of those wafers which underwent the low temperature anneal step revealed that the additional low temperature thermal step did not effect any noticeable micro structural change. The defect morphology and evolution appeared to follow a similar pathway to the experimental control. Figure 8-7 portrays the PTEM WBDF images of the EOR damage formed for the samples which were preannealed at 500°C for 30minutes and then subjected to the Flash-assist RTP anneal step. It should be noted that the EOR defects formed after the 500°C 30 minute anneal alone were extremely difficult to image due to the small defect size, therefore they are not shown here. After the low temperature preanneal however, the defects appeared as a high density of tiny dot-like structures. Reference to Figure 8-6 indicates that a similar defect structure existed post the 700°C iRTP anneal, and this structure evolved as the peak anneal temperature was increased to 1100 and 1300°C with application of the fRTP anneals. At 1100°C, the defect density clearly decreased and the defects appeared as

small loops, suggestive of a coarsening process. Additional coarsening and defect dissolution occurred as the flash temperature was raised to 1300°C, at which very few dislocation loops of much larger dimensions were seen. In Figure 8-8 PTEM WBDF images for both the experimental control and those wafers which were preannealed are compared.

The corresponding defect and trapped interstitial obtained for the samples which were preannealed and those only subjected to the Flash-assist RTP process are compared in Figure 8-9. The data point corresponding to the 700°C iRTP anneal was plotted on the y-axis, to represent 0°C fRTP, since the fRTP portion of the thermal anneal was not applied. It was obvious that the application of the preanneal had virtually no impact on either of these parameters. At temperatures below 1200°C the defect density remained almost constant on the order of $1x10^{11}cm^{-2}$, before a rapid decay was observed between 1200 and 1300°C to values on the order of $1x10^{10}$ and $1x10^{9}cm^{-2}$, respectively. The number of trapped interstitials in the EOR damage demonstrated a similar behavior to the defect density, with the interstitial density commencing a decline from $1x10^{14}cm^{-2}$ at 1100°C to $1x10^{13}$cm-3 at 1300°C.

The boron diffusion for the control samples which were annealed via Flash-assist RTP only are illustrated in Figure 8-10. The profiles obtained for the 700°C iRTP anneal and the 1000°C and 1100°C fRTP anneals demonstrated many similarities. Firstly, they all seemed to coincide. Secondly, an inflexion point occurred for these temperatures at a concentration of approximately $2x10^{20}cm^{-3}$ below which the profiles were seen to diffuse into the bulk and above which diffusion took place toward the surface resulting in a pile up of boron at the surface. As the fRTP temperature was increased to 1200°C, the

concentration at which the inflexion occurred appeared to decrease with a corresponding increase in both the boron concentration at the surface and diffusion into the bulk. Conversely, the fRTP anneal at 1300°C resulted in a boron pile up at a peak concentration of $1.6x10^{21}cm^{-3}$ and a junction depth of 35nm. Very similar diffusion behavior was recognized for the samples which were subjected to the low temperature furnace anneal. In Figure 8-11 the diffused profiles for the preannealed samples and the experimental control are more closely compared. Clearly few differences could be discerned in the profiles, which indicates that the low temperature preanneal effected very little change in the boron diffusion, if any at all.

The measured sheet resistance as a function of the fRTP temperature can be seen in Figure 8-12. An increase in the fRTP temperature clearly effected decreases in the sheet resistance in both instances. Application of the fRTP anneal subsequent to the iRTP anneal realized immediate improvements in the sheet resistance for the experimental control (no preanneal), which was not the case for the samples which were preannealed. A reduction of approximately 100Ω/sq. over the measured sheet resistance of the 700°C iRTP anneal, was attained on application of the 1000°C fRTP, in the experimental control. This improvement trend was sustained for the remaining fRTP anneal temperatures, with the 1300°C fRTP yielding a sheet resistance of 260Ω/sq. At an fRTP temperature of 1100°C, the preanneal clearly effected much higher sheet resistances which were not apparent at the other coincident data points, with a value not very different from the 700°C iRTP anneal, of 480Ω/sq.

In the experimental control, the active dose was observed to increase above that of the 700°C iRTP by more than 40% for increasing fRTP temperatures ranging 1000

though 1300°C. This trend is depicted in Figure 8-12 on which it is clear that the active dose obtained for the 700°C iRTP were very similar for both the experimental control and the preannealed sample, with a value of approximately 2.5x10^{14}cm^{-2}. At 1300°C the active doses were also observed to coincide within experimental error. However for the fRTP anneal temperature of 1100°C which fell between these two temperatures, there was an obvious effect of the preanneal on the active dose. The active dose did not appear to increase above that of the iRTP anneal, as in the case of the experimental control, where a 40% increase was detected. Rather the active dose was consistent with that of the 700°C iRTP anneal. A similar trend was observed for the mobility, which is shown in Figure 7-13. The mobility appeared to be independent of the fRTP anneal temperature, with values ranging 40-50cm^{2}/Vs for those wafers which were only processed by Flash-assist RTP. This was found to be consistent with the samples which were preannealed, in particular for the 700°C iRTP and the 1300°C fRTP temperatures. The values attained at these temperatures virtually coincided with those of the experimental control. But the mobility seemed to be much higher for the 1100°C fRTP anneal with a value greater than 50cm^{2}/Vs. One could argue that this value fell within the experimental error of the Hall measurement, but for a similar temperature the corresponding value for the experimental control was much lower.

8.4 Discussion

8.4.1 EOR Damage

The damage created by the germanium preamorphization implant was consistent with Type II or EOR damage, which is associated with the formation of continuous amorphous layers [JON88]. Hence the defects detected at different stages in the anneal sequence corresponded to the well documented EOR defect evolution. They were

observed to evolve from dot-like interstitial clusters to {311}-type defects [EAG94, STO97, PAN97] which unfaulted into stable dislocation loops [LIJ98]. The dot-like interstitial cluster observed in this work is believed to be the precursor for the {311}-type defect. This is the first experimental evidence of the existence of such a structure. Previous studies have postulated the existence of the sub-microscopic interstitial cluster as the precursor for the {311}-type defect [BEN97, LIB98, COF00]. The dot-like interstitial cluster herein is thought to evolve from the sub-microscopic interstitial cluster, which has been discussed in more detail in chapter 5. Clearly the low temperature anneal prior to the Flash-assist RTP process had no observable effect on the EOR damage nor its evolution; as illustrated in Figures 8-8 and 8-9. This was concluded since the defect morphologies, densities and trapped interstitial densities could not be differentiated from the experimental control. The reader is referred to chapters 5 and 6 for a more extensive discussion on the defect evolution.

8.4.2 Amorphous Layer Re-crystallization

The XTEM image of the wafer which was subjected to the 500°C 30min furnace anneal only, shown in Figure 8-4, indicated that this anneal was sufficient to completely re-grow the amorphous layer. In an effort to determine the anneal time which was required to fully re-grow the 50nm amorphous layer formed by the 30keV germanium preamorphizing implant in the experimental control, the intrinsic and extrinsic velocity relations of Olson and Roth were utilized [OLS85a, OLS85b, ROT90]. The intrinsic velocity relation was employed in the initial stages of the anneal since the boron concentrations were to low to effect enhanced re-crystallization rates [CSE77, SUN82, TIM85, OLS85a, OLS85b]. At concentrations exceeding $2x10^{19}cm^{-3}$ the extrinsic relation was used. Based on the chemical boron concentration-depth profile of the as implanted

structure, this concentration was not encountered until approximately 30nm of the layer was re-grown. Figure 8-13 contains a plot of the re-crystallized amorphous layer thickness generated by FLOOPS as a function of anneal temperature, which indicates the temperature at which total re-crystallization occurred. The amorphous layer formed by the 30keV germanium preamorphizing implant was evidently not fully re-crystallized on attaining the 700°C iRTP anneal temperature, since the calculation indicated 20nm of regrowth during this portion of the thermal profile. Hence the control wafer which was subjected to only the iRTP anneal must have re-crystallized on the ramp down from the iRTP anneal, since the XTEM images shown in Figure 8-14, indicated no amorphous regions. Those wafers which were annealed at the fRTP temperatures were estimated to undergo complete recrystallization during the fRTP portion of the thermal profile at approximately 1000°C. This is illustrated in Figure 8-13 for the 1000°C fRTP anneal. The regrowth achieved during the ramp up to the 700°C iRTP anneal followed the intrinsic silicon regrowth behavior, with an estimated 20nm of the layer undergoing re-crystallization. The remaining amorphous layer was re-crystallized with velocities characterized by both the intrinsic and extrinsic relation based on the boron concentration encountered, as mentioned previously [CSE77, SUN82, TIM85, OLS85a, OLS85b]. This calculation will prove beneficial for the remaining analyses.

8.4.3 Boron Diffusion Characteristics

8.4.3.1 Diffusion in the amorphous phase

In the Chapter 7 the occurrence of boron diffusion in the amorphous phase was postulated to occur for the 30keV germanium preamorphizing implant for concentrations below $2x10^{20}cm^{-3}$. Previous reports have been made of diffusion of boron during SPER of the implantation-induced amorphous layer below a similar concentration [DUF04,

GAB04], but the reasons why diffusion occurs below this particular concentration are uncertain. It has been postulated that boron clustering in the amorphous region [MAT04] above $2x10^{20}cm^{-3}$ may be responsible for the lack of diffusion in the profile peak. But since little is known about clustering in the amorphous phase [DUF04], it cannot be conclusively said that clustering is responsible for the immobile regions of the boron profile.

The diffusion characteristics of those wafers subjected to the low temperature preanneal, did not appear to differ substantially from the experimental control which was demonstrated in Figure 8-11, suggesting that the low temperature anneal did not effect any difference in the boron diffusion behavior. In an attempt to resolve the reasons why there were no evident differences in the profile, the initial wafer condition prior to the second anneal step (Flash-assist RTP) was considered. Figure 8-15 illustrates the concentration-depth profile for the $500^{o}C$ 30 minute furnace anneal. It is evident from the plot that there was a significant amount of diffusion during the low temperature preanneal. In this case an inflexion point in the profile occurred at approximately $1x10^{20}cm^{-3}$ below which concentrations were observed to diffuse into the bulk of the material. Above this concentration boron diffused toward the surface, at which boron pile up at the oxide interface could be discerned. Previous reports for similar boron implant and into a deeper germanium preamorphized layer, the inflexion point in the boron profile was observed at $2x10^{20}cm^{-3}$ for an anneal conducted at $500^{o}C$ for 40minutes [DUF04]. In their experiments the amorphous layer was much deeper which allowed for more motion in the amorphous phase.

The intrinsic diffusivity of boron in silicon was at 500°C was estimated to be $2.76x10^{-24}cm^{2}s^{-1}$, in accordance with the relation of Hadarra [HAD00]. Hence boron is expected to diffuse no more than $7.0x10^{-4}$nm in 30 minutes at this temperature (shown in Table 8-1). The observed diffusion was on the order of 1nm, which was three orders of magnitude greater than the determined intrinsic diffusion length. It was therefore plausible that, like the experimental control, boron had sufficient time to diffuse in the amorphous phase prior to the amorphous-crystalline interface was swept over the profile. Figures 8-16 and 8-17 compares the diffused profiles for the 500°C 30 minute furnace anneal to the as-implated profile and the 700°C iRTP, respectively. This comparison can be justified as it was previously demonstrated that boron diffusion in the amorphous phase during the ramp up to the iRTP anneal, was responsible for the shape of the profile. Since the XTEM analysis confirmed that the amorphous region was completely re-crystallized during the 500°C 30 minute furnace anneal, any diffusion must have occurred in the amorphous phase.

To corroborate this postulation, it was necessary to determine the time that boron spent in the amorphous phase and therefore the time that was available for boron to diffuse. The re-growth velocity calculation at 500°C yielded an intrinsic velocity of approximately $1x10^{-2}nms^{-1}$. At this rate, more than 50 minutes were required to regrow 30nm of the layer before the high concentration regions of the boron profile were encountered for an extrinsic relation to apply. However, the duration of the anneal at this temperature was much shorter, which suggested that the anneal time should have been insufficient to effect total re-growth of the amorphous layer. But, the XTEM WBDF image subsequent to the 500°C 30min furnace anneal, shown in the Figure 8-4 indicated

that the layer was fully regrown, since no amorphous regions were observed. The velocity relations used were clearly not able to accurately account for the regrowth, hence it was not possible to determine the time at which the layer re-grew and therefore the time which was available for boron to diffuse in the amorphous phase via this relation.

Gable [GAB04] proposed that boron diffused in the silicon amorphous phase with an activation energy of approximately 2.2±0.26eV. Unfortunately, they were unable to determine the pre-exponential factor for the diffusivity. Hence without knowing the exact time frame for which boron diffusion occurred at a given temperature it was impossible to accurately determine the pre-exponential factor. In the case of the 700°C iRTP anneal of the experimental control, the time for which boron resided in the amorphous silicon phase was estimated based on the regrowth and thermal profile. Therefore the pre-exponential factor could not be conclusively extracted. In an effort to circumvent this matter, the ratio of the anneal times required to effect the same diffusion length at 500°C and during the ramp up to the 700°C iRTP anneal was calculated. Examination of the profiles in Figure 8-16, revealed the diffusion lengths were similar at the steepest parts of the profile for a concentration of 2x10^{19}cm^{-3}. Hence the ratio of the anneal times was determined from the following relation, in which D is the boron diffusivity

$$D_1 t_1 = D_2 t_2 \qquad \text{8-1}$$

In the previous chapter it was shown that boron spent approximately 2s in the amorphous phase during the ramp up to the iRTP anneal prior to re-crystallization. Based on this relation the equivalent time at 500°C for the ramp up to the 700°C iRTP anneal was estimated to be 208s, which is approximately 3minutes. It is therefore plausible that there was sufficient time to allow for boron diffusion before re-crystallization, which is known

to have occurred sometime during the 30min 500°C anneal. More recently, Jacques [JAC05] extracted an activation energy and pre-exponential factor for boron diffusion in the silicon amorphous phase of 2.5eV and 0.32cm^{2}/s, respectively. The corresponding estimated diffusion length for the 500°C 30minute anneal was found to be approximately 1.6nm, which was consistent with the diffusion observed. These calculations therefore substantiated the postulation that the boron diffusion observed during the low temperature preanneal occurred while in the amorphous phase.

8.4.3.2 Transient enhanced diffusion (TED)

The concurrent diffused boron profiles of Figure 8-10b for the 700°C iRTP and 1100°C fRTP anneals indicated that the low temperature anneal had clearly dominated the diffusion, since the additional thermal budget did not seem to effect any detectable diffusion levels. Although no substantial change was detected, the difference in the trapped interstitials between the 700°C iRTP and the 1100°C fRTP ranged 5x10^{13}cm^{-2}, which should be enough to result in an enhanced diffusion. Table 8-1 contains the intrinsic boron diffusion lengths at the fRTP anneal temperatures of interest, determined using the diffusivity relation of Hadarra [HAD00]. In determining the diffusion length, the intrinsic diffusivity was calculated as a function of the change in temperature with time, which allowed for the accurate integration of the diffusivity with time. Clearly, the diffusion lengths could not have account for the observed diffusion, particularly at the higher anneal temperatures.

Interstitial supersaturation levels were extracted by Cowern [COW99] for temperatures ranging 600 through 800°C, based on Fair's diffusivity data [FAI81].

$$S_{\text{int}} = S_0 \times \exp\left(\frac{-E_a}{kT}\right) \tag{8-2}$$

where S_{int} is the interstitial supersaturation, the pre-exponential factor, S_0 is $2.63x10^{-1}$ and the activation energy, E_a is -0.82eV. Table 8-2 contains the calculated interstitial supersaturation values and the calculated enhanced diffusion at the anneal temperatures of interest. The estimated values attained were found to be a little higher than the diffusion lengths detected by SIMS. However, the accuracy of the calculation was dependant on the ability to precisely determine the interstitial supersaturation, which was extracted from diffusivity data available for much lower anneal temperatures than the temperatures used in this experiment. Hence it is expected that any errors associated with the supersaturation relation would be magnified as the temperature is increased. The calculation yielded enhanced diffusion length at 1100°C of approximately 3nm. Within the resolution limits of SIMS this may be difficult to discern from the noise, therefore it is plausible that this enhancement was not detected. In the case of the 1300°C anneals the enhanced diffusion length was estimated at 10nm, while the actual detected diffusion at a concentration of $1x10^{18}cm^{-2}$ was 5nm. The predicted diffusion lengths were on the same order of magnitude, which confirmed the enhancement in the diffusion observed. The enhanced diffusion was also consistent with the reductions in the trapped interstitials observed between these two temperatures.

As seen in Figure 8-11 there was no difference in the boron pile up at the oxide interface, which was shown in Chapter 6 not to be consistent with boron uphill diffusion [WAN01, DUF03]. This behavior was shown to be simply a re-distribution of the boron from the profile peak to the Si-SiO_2 interface, which was confirmed from the SIMS data.

Based on the above arguments therefore, it was obvious that most of the diffusion occurred in the first low temperature anneal step, while boron was still in the amorphous

phase prior to application of the 700°C iRTP and 1100°C fRTP anneal. The additional thermal budget associated with the fRTP anneals effected diffusion levels which were found to be enhanced, however this enhanced diffusion did not dominate till an fRTP temperature of 1300°C was attained.

8.4.4 Electrical Data Analyses

The most obvious differences between the samples which were subjected to the low temperature preanneal and the experimental controls were found in the electrical data. In particular the sheet resistance values attained for preannealed sample for the 1100°C fRTP anneals was more than 25% higher than that of the control sample, as shown in Figure 8-15. However, very similar values were attained for the 700°C iRTP and the 1300°C fRTP. In order to gain better insight into these differences it was necessary to assess the active dose and carrier mobility data. The active dose attained for the preannealed 1100°C iRTP was found to be approximately 40% lower than that of the experimental control, with a value very similar to that of the 700°C iRTP samples, while the values attained for the 700°C iRTP and 1300°C fRTP anneals were more or less the same. Similarly, the carrier mobility for the 700°C iRTP and 1300°C fRTP anneals were very similar in both cases. But on comparing the carrier mobility values at 1100°C it was apparent that the mobility of the preannealed sample was higher than that of the control, since the measurements fell outside of the error bars. One may be inclined to believe that the mobility for this anneal temperature was within the experimental error of the Hall measurement, but further analysis of the data was required before a firm conclusion could be drawn.

8.4.4.1 Recrystallization temperature

The application of the low temperature preanneal effected changes in the temperature at which the amorphous layer was re-crystallized. The XTEM analyses confirmed that total re-crystallization of the amorphous layer occurred during the low temperature anneal at a temperature of 500°C prior to application of the second anneal stage. However in the experimental control the re-crystallization temperature was shown to differ for the 700°C iRTP anneal and the fRTP anneals. This was largely due to the relative distance of the boron profile and the amorphous-crystalline interface and hence the regrowth rate. Since the re-growth was initially governed by an intrinsic rate, re-crystallization of the amorphous layer was not completed once the 700°C iRTP anneal was attained. Hence for the sample which was subjected to the 700°C iRTP anneal, the re-crystallization was accomplished on the ramp down from this temperature. While in the samples which were annealed at the fRTP temperatures, re-crystallization was realized at a temperature of 1000°C.

In Chapter 7 it was concluded that the re-crystallization temperature governed the activation of boron. If the activation was a function of the re-crystallization temperature [GAB04, JAI04], then the active boron should have been the same for the wafers which were subjected to the low temperature preanneal. The corresponding data points at 700°C and 1100°C supported this supposition, since there was virtually no change in the active dose on application of these anneals, from that attained for the 500°C 30 minute furnace anneal. But the active dose attained at 1300°C fRTP practically doubled the active dose obtained at the lower anneal temperatures. This drastic increase in the active dose hinted that another mechanism may have been responsible for activating boron at this

temperature, provided the hypothesis that the activation was a function of the re-crystallization temperature was accurate.

The similar active doses attained for both sample sets at 700°C iRTP anneal, also substantiated the theory that the activation was controlled by the re-crystallization temperature. This was justified by the fact that the amorphous-crystalline interface sweep over the boron profile on the ramp down from the 700°C iRTP anneal, resulting in very comparable recrystallization temperature and hence analogous activation levels. Likewise, in the experimental control, since the fRTP anneals ranging 1000 through 1200°C were all demonstrated to re-crystallize at 1000°C, then higher activation levels were attained above that of the iRTP anneal. The higher activation levels achieved at the higher re-crystallization temperature were in accordance with Jain's findings which indicated the boron activation had a monotonically increasing dependence on the temperature [JAI04]. The seemingly higher activation achieved by the 1300°C fRTP anneal in the experimental control, concurred with the value attained for the sample which was preannealed and subjected to the same fRTP anneal. This significant detail confirmed that the activation was probably governed by another process at higher anneal temperatures, which occurred subsequent to the activation during the solid phase epitaxy.

8.4.4.2 Activation subsequent to solid phase epitaxy

To identify where the active boron concentrations were located in the structure, the active dose attained from the Hall measurements were matched to the integrated area below the chemical concentration-depth curves obtained from SIMS. These calculations yielded the maximum active concentrations achieved by the anneals. Figure 8-18 contains these plots for the wafers which were preannealed and the experimental control. The maximum active concentration attained for the 500°C 30minute anneal was found to be

approximately $1.5x10^{20}cm^{-3}$. Additionally, the active concentrations were observed not to increase over this value on application of the 700°C iRTP and 1100°C fRTP second stage anneals. The fact that the maximum attainable active concentration matched for these cases confirmed that the boron activation may in fact be related to the re-crystallization temperature. It should be noted that the active concentration attained subsequent to the low temperature anneal was much higher that the equilibrium solid solubility in crystalline silicon [TRU60], and were comparable the findings of other authors [SOL90, LIN03, JAI04]. The 1300°C anneal resulted in an active concentration of roughly $3x10^{20}cm^{-3}$, which represented approximately twice the active concentration over that achieved by the low temperature anneal. Inspection of the diffused profiles revealed that the majority of the increase in active concentration above that of the low temperature anneal resided in the profile peak and not in the diffused tail. This represented 90% of the entire increase in the active dose compared to 10% due to diffusion into the bulk. This striking characteristic indicated that the 1300°C fRTP anneal supplied enough thermal budget to effect activation of boron from an inactive, immobile boron configuration. Therefore it could be inferred that the supplemental activation was not due to the processes which occurred during the re-growth.

In the experimental control a progressive increase in active concentration could be seen as the peak anneal temperature was increased from 700°C to 1200°C. This data also substantiated the theory that the temperature at which the re-crystallization was completed, dictated the amount of active boron in the silicon lattice. The apparent higher active concentration observed for the 1200°C fRTP anneal was determined to fall within the error of the Hall measurement. Most of the elevated active boron concentrations

above the 1000°C fRTP at 1300°C were located in profile peak, which accounted for 70% of the increase in active boron, versus 30% in the tail region. This was very similar to the effects observed for the preannealed wafers and indicated that boron was activated in the peak subsequent to re-crystallization of the amorphous layer. This strongly implied that the thermal budget associated with the 1300°C fRTP was sufficient to activate boron from some unknown configuration which was present in the structure succeeding re-growth.

Figure 8-19 highlights the effects of the low temperature preanneal at 500°C on the maximum active concentration relative to the experimental control. All three plots emphasize different concepts and provide evidence thereof. The first plot (Figure 8-19a) compares the effects of the low temperature anneal on the 700°C iRTP, in which it was clear that there was virtually no difference in the peak active concentration, since the re-cystallization temperatures were practically the same. Figure 8-19b which contrasts the preannealed sample and experimental control for the 1100°C fRTP anneal stands out since the differences were most blatant. In this case the re-crystallization temperatures differed by an estimated 500°C such that the experimental control exhibited an active concentration, which was 80% higher than the preannealed wafer. The active concentrations were found to be approximately $1.4x10^{20}$ and $2.5x10^{20}cm^{-3}$, for the preannealed and control wafers, respectively. It is interesting to note that the increase in active concentration was due to activation of boron located mainly in the profile peak which contained more than 90% of the additional activated dose. It is important to note that in these cases the differences were related directly to the temperatures at which the re-crystallization occurred, which indicated that a larger fraction of boron was located at

substitutional sites during the re-crystallization process itself. Hence it provided further evidence that the activation was governed by the re-crystallization temperature. Clearly doubling the re-crystallization temperature effected a 60% increase in substitutional boon in the peak.

Conversely in Figure 8-19c, few differences could be discerned in the wafers which were annealed at the 1300°C fRTP anneal temperature, despite the differing re-crystallization temperatures. Based on the above hypothesis the activation level subsequent to the re-crystallization should have been higher in the experimental control and comparable to the values attained for the 1000 through 1200°C fRTP anneals. Similarly, the boron active fractions for the preannealed wafer should have compared to that attained for the 500°C 30 minute preanneal. But the values attained were found to be substantially higher than the post re-crystallization activation, which led to the inference that this supplemental activation in both cases did not originate from the re-growth of the layer. Rather it further endorsed the theory that the 1300°C fRTP anneal supplied enough thermal budget to effect activation of boron from some inactive, immobile boron configuration, which existed subsequent to SPER of the layer. This may have been from two possible sources, which included diffusion of the layer or activation of boron in the peak of the profiles.

Figure 8-20 further illustrates the differences in the active concentrations effected between the temperatures at which re-crystallization was determined to occur and the 1300°C fRTP anneal. In the case of the low temperature preanneal the initial active condition was assumed to be the 500°C 30minute anneal only, compared to the 1000°C fRTP anneal for the experimental control. In these cases it was observed that both the

diffusion of boron into the bulk of the material and activation of boron in the peak of the profile, contributed to the increase in the active boron fraction above the re-crystallization activation. Clearly this increase was higher for the sample which was subjected to the low temperature preanneal as the active dose doubled, compared to a 30% increase in active dose in the control. It was also evident that in the case of the low temperature anneal a larger fraction of this supplemental activation resided in the peak, which represented 90% of the newly activated boron. While in the experimental control, the opposite was observed, as 70% of the supplemental active boron resided in the tail region of the profile. Closer inspection of the active concentrations divulged that the peak active concentration was a little higher for the sample which was preannealed at 500°C. However, further analyses of the discrepancies in the active concentrations in the profile revealed that they coincided with the error in the Hall measurement and were therefore not due to the differences in the experiments.

The analyses presented above clearly suggested that the supplemental activation was the result of diffusion of boron into the bulk of the material and also activation in the peak from some initial inactive boron configuration. The fact that maximum active concentrations coincided for both cases despite the fact that the initial active fraction immediately subsequent to amorphous layer re-crystallization differed, was peculiar. One would have expected the sample with the higher initial active concentration prior to the fRTP anneal to yield a higher active dose, assuming the source of the additional boron activation was the same. The total dose activated in the peak after re-crystallization was determined to be smaller for the experimental control (no preanneal). The differences in additional thermal budget applied subsequent to the re-growth, may account for the

different activated fractions of boron in the peak. Since the amorphous layer in the experimental control re-crystallized at the higher temperature, then less thermal budget was available for additional activation in the peak, hence a smaller fraction of boron was activated. Alternatively, the existence of a threshold for boron activation subsequent to the re-crystallization is proposed to account for the similar peak active concentrations obtained despite the differences in the active dose upon re-crystallization.

8.4.4.3 Carrier mobility variations

The mobility data for the experimental control was consistent and therefore it was much easier to pinpoint the processes which were responsible for the decreases in sheet resistance which were observed in this instance. Clearly it was the increase in the active dose which dictated the final sheet resistance in the control. But a conclusion was not as clear cut for the samples which were preannealed since the mobility attained for the 1100°C fRTP was undoubtedly higher than those of the other temperatures, with a value of approximately 54cm^{2}/Vs. One may argue that within the 10% error associated with the Hall measurement, the mobility was in the expected 40-50cm^{2}/Vs range for such dopant concentrations [KLA92]. However, on comparing the mobility and active doses attained immediately subsequent to the re-crystallization of the layer (i.e. after the 500°C 30 minute anneal) to those values accomplished on application of the 1100°C anneal, it was evident an increase in mobility did occur. The active doses at these temperatures were within 10% of each other, compared to a 25% change in the mobility. A similar trend was observed for the other germanium preamorphizing energy investigated in this work, in which the 1100°C fRTP anneal effected a 20% increase in the mobility over that value attained after re-crystallization of the layer at 500°C, demonstrated in Appendix _. These

similarities compelled us to believe that these mobility changes were real and not just an artifact of the experiment.

An increase in the mobility is expected if there is an increase in the time between scattering events. If one considers scattering by the ionized impurities in the material, one cannot argue substantial differences between the anneal temperatures since the active concentrations were observed to be similar and therefore the probability of such scattering should have been similar. Hence this argument cannot explain the differences observed between the experimental control and the sample annealed at 1100°C. These trends were found to be analogous to the higher mobilities attained for the 8keV germanium preamorphizing implant in the fRTP range 1000 to 1200°C. The prime cause for such a mobility enhancement is unclear at this time and would need to be the focus of additional investigations which are not encompassed in this work.

Nonetheless, the mobility values attained for the 700°C iRTP and 1300°C fRTP anneals were found to be very similar and coincided with those of the experimental control. They were also consistent with determinations from standard mobility models for this dopant concentration range [KLA92]. Hence, since the mobility did not change significantly, the differences in the sheet resistance between these two anneals could be attributed to the change in the active concentrations with reasonable certainty.

8.4.5 Models for Boron Activation

Effective solute-trapping at the amorphous-crystalline interface is one theory which exists in the literature to account for the high activation levels which can be achieved by low temperature furnace anneals. Such activation levels are known to exceed solid solubility limits in crystalline silicon [BLO79, NAR82, LIN03]. This solute trapping occurs once the impurity residence time at the interface exceeds time required for re-

growth of the monolayer [CAM80]. It has also been postulated that impurity solubility in amorphous silicon is significantly greater than that in crystalline silicon. The increased solubility has been ascribed to the large density of defects trapping and gettering the impurities [ELL85, POL90, COF92], as well as to the distorted atomic structure of the amorphous phase [CAL89]. To account for the higher boron activation levels yielded by higher re-crystallization temperatures a number of theories have been proposed which stem from these hypotheses.

Jain et al [JAI04] proposed that higher activation levels are achieved by higher recrystallization temperatures because the faster sweeping amorphous-crystalline interface can trap much larger concentrations at substitutional sites, since the re-growth velocity is much higher than the corresponding dopant atom diffusion [CAM80, CLA04]. Melt laser annealing represents the extreme end of this spectrum, where all the dopants are incorporated onto lattice sites because of the exceptionally high regrowth velocity [JAI04]. In the case of the low temperature anneal the re-crystallization occurred at 500°C, but varied with the boron concentration levels. But the velocity was much lower than the experimental control. In this instance the amorphous-crystalline interface swept over the boron profile for temperatures between 700 and 1000°C, at a much higher re-growth velocity, hence in accordance with the proposed theory the faster re-growth should have resulted in higher concentrations of boron atoms trapped at substitutional sites. Higher activation levels immediately subsequent to the re-crystallization were observed for the 30keV germanium preamorphizing implant layers subjected to the fRTP anneals, which agreed with this conjecture.

An alternative proposal stemmed from the fact that boron exhibited a higher solubility in the amorphous phase relative to the crystalline phase [GAB04]. This was thought to be the responsible factor for the higher active fractions obtained at higher re-crystallization temperatures. The boron profiles in amorphous silicon were subjected to different temperatures since the re-crystallizations occurred at different stages in the anneal sequence. Those profiles which were re-crystallized during the low temperature anneal were only subjected to a 500°C temperature, hence the solubility may have been temperature limited. On the contrary, the amorphous region in the experimental control experienced much higher temperatures on the ramp up to the 1000°C anneal. The boron solubility in the amorphous phase may have therefore been much higher for experimental control, which concurred with the higher active doses attained subsequent to re-crystallization of the layer. Gable's supposition can account for the higher active doses achieved at the higher re-crystallization temperatures in these experiments. However, the reasons why a higher solubility was attained in the amorphous phase have not been presented.

Based on the most recent discussion, I am inclined to believe that the higher active doses achieved at higher re-crystallization temperatures could have been the result of either one of these theories; the effective solute trapping at substitutional sites during the re-growth [JAI04] or the higher boron solid solubility in the amorphous phase [GAB04].

8.5 Conclusion

The aim of this chapter was to resolve the underlying principles which governed the boron activation during the Flash-assist RTP process. This was attempted by varying the initial wafer condition prior to the application of the Flash-assist RTP process, by the application of a low temperature furnace anneal. Hence the experiment entailed a

constant germanium preamorphizing implant condition at an energy of 30keV and a constant dose of $1x10^{15}cm^{-2}$. Boron was subsequently implanted at a constant energy and dose of 1keV and $1x10^{15}cm^{-2}$, respectively. The low temperature furnace anneal was conducted at $500^{o}C$ for 30minutes such that total re-crystallization of the amorphous region was accomplished prior to application of the Flash-assist RTP. The experimental control wafers were not subjected to this low temperature anneal.

Analyses of the experimental data indicated that the initial wafer condition had a significant impact on the final junction characteristics for fRTP temperatures. The re-crystallization temperature was shown to dictate the boron activation level for anneals conducted at temperatures less than $1300^{o}C$. Subsequent to the re-crystallization process thermal budgets associated with fRTP anneal temperatures as high as $1200^{o}C$, were determined to be insufficient to result in increased activation levels, thus the final activation was controlled by the re-crystallization temperature. Hence the Flash-assist RTP process had no effect on the final boron activation once the amorphous layer was previously re-crystallized. The corresponding activation mechanisms during the re-crystallization were attributed to the much more effective trapping of solute atoms at substitutional sites at the higher temperatures. The experimental findings also concurred with the possibility of higher boron solid solubility levels in amorphous silicon.

At $1300^{o}C$ fRTP increases in activation levels above the re-crystallization activation were observed to be a direct consequence of two processes which included increased diffusion in the tail of the boron profile and activation in the profile peak. This find demonstrated that boron was activated from some initial unknown, immobile, inactive configuration. This unknown configuration of boron was shown to be less stable

than the widely researched boron interstitial cluster (BIC) [LIL02, MIR03, DES05]. Application of BIC kinetics revealed that these thermal budgets were insufficient to activate boron from such a configuration, to yield the high active concentrations observed. Additionally, despite the differences in the active dose upon completion of the re-crystallization process, identical peak active concentrations were attained for the 1300°C anneal, which hinted at a possible threshold concentration for activating boron at these temperatures from such a configuration. This research strongly hints at the existence of boron in an alternate immobile, inactive configuration subsequent to the re-crystallization process, which is less stable than the well known BIC structure. At high enough thermal budgets boron can be activated from this structure.

It was also concluded that the sheet resistance was dictated by the active dose for the experimental control. Conversely, the mobility varied substantially for the samples which were preannealed, in particular for the 1100°C fRTP anneal. A firm conclusion could not be drawn regarding the factor which was responsible for the final sheet resistance, since the mobility changes are not fully understood at this time and need to be further investigated.

Reference to the experiments of the previous chapter indicated that the lower germanium energy implant demonstrated a higher mobility in the fRTP range of 1000 through 1200°C. The values of which were comparable to the preannealed 1100°C fRTP wafer. The similarities in the experiments lie in the fact that the amorphous layer re-crystallized at relatively low temperatures. This may provide some insight into the reasons why higher carrier mobilities were noticeable for these cases.

Figure 8-1. Picture of the ASM International A400 furnace used in these experiments.

Figure 8-2. Thermal profile of the 500°C low temperature anneal performed in these experiments, on which the 450°C stabilization can be seen.

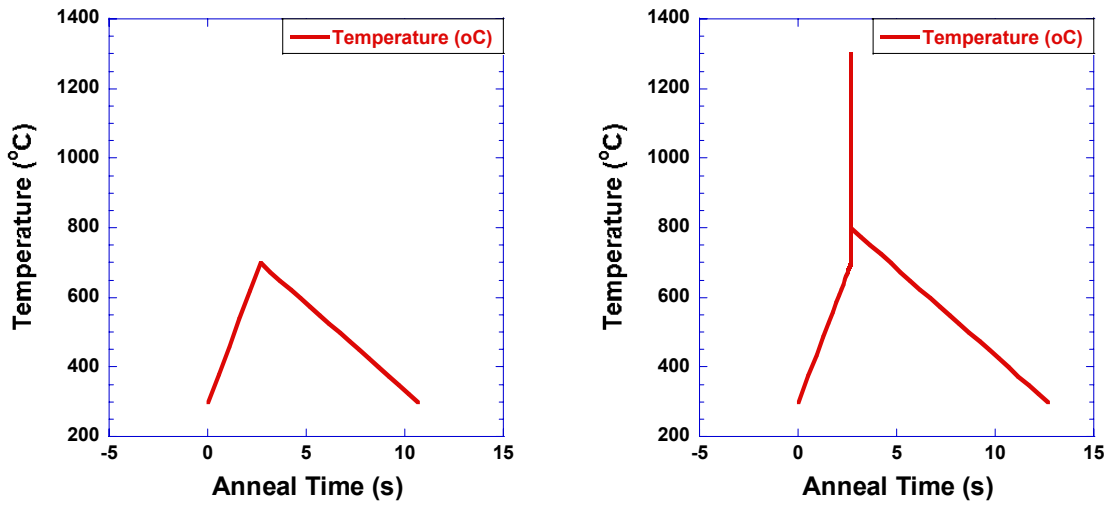

a) b)

Figure 8-3. Illustration of the temperature-time variations for the Flash-assist RTP thermal profiles used in these experiments. a) 700°C iRTP anneal b) 700°C iRTP, (1000-1300) °C fRTP

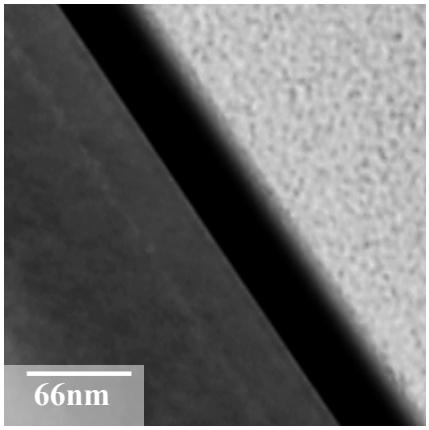

Figure 8-4. XTEM image of the re-crystallized amorphous layer for a 30keV germanium PAI after the 500°C 30 minute furnace anneal, taken under g_{110} bright field conditions. The EOR damage can be discerned just beyond the original amorphous-crystalline interface at an estimated depth of 55nm.

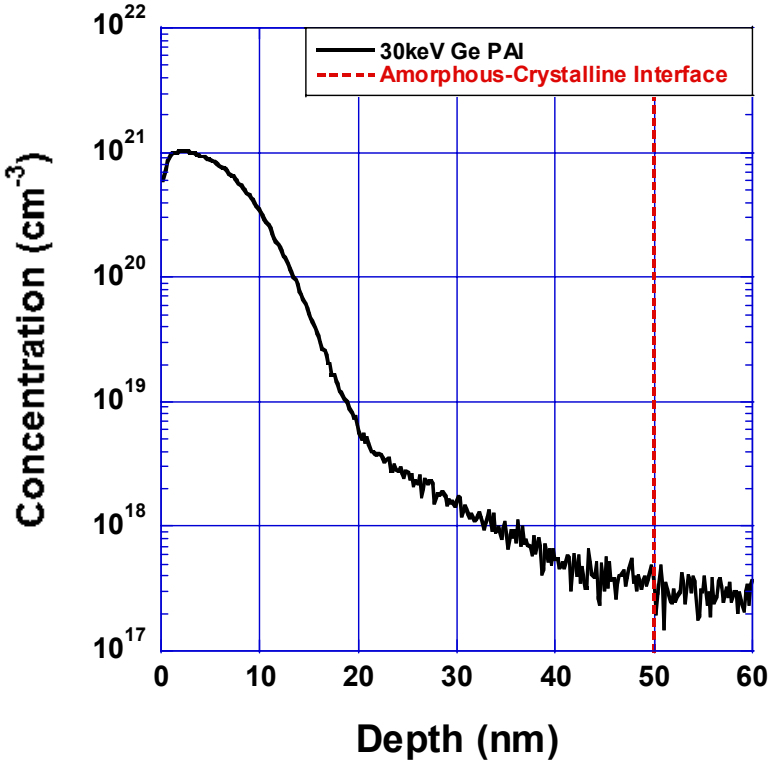

Figure 8-5. Concentration-depth profiles of the boron implant into an amorphous layer formed by a 30keV Ge PAI obtained from SIMS analyses.

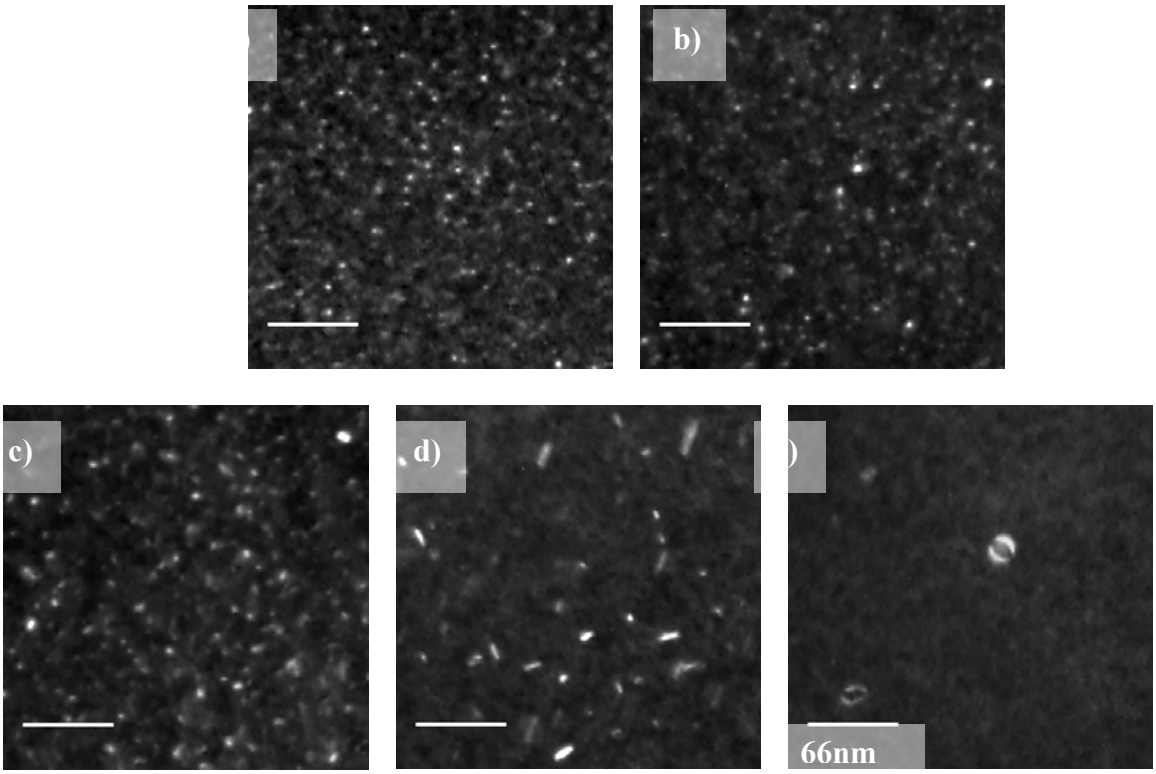

Figure 8-6. WBDF PTEM images of the EOR defects imaged under g_{220} two-beam conditions of the 30keV germanium PAI subjected to flash anneals. a)700°C iRTP, b) 700°C iRTP,1000°C fRTP, c) 700°C iRTP, 1100°C fRTP, d) 700°C iRTP, 1200°C fRTP, e) 700°C iRTP, 1300°C fRTP

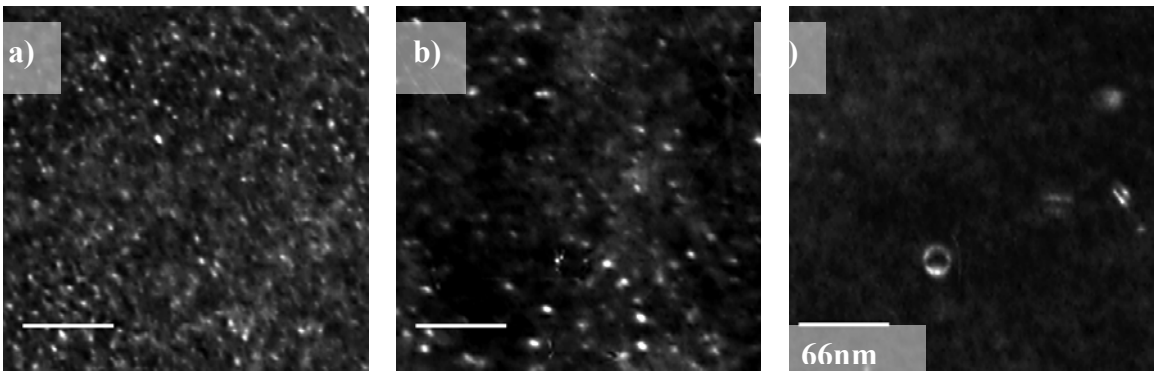

Figure 8-7. WBDF PTEM images of the EOR defects imaged under g_{220} two-beam conditions of the 30keV germanium PAI, which were subjected to a low temperature furnace anneal at 500°C for 30minutes and a flash anneals. a)700°C iRTP, b) 700°C iRTP, 1100°C fRTP and c) 700°C iRTP, 1300°C fRTP.

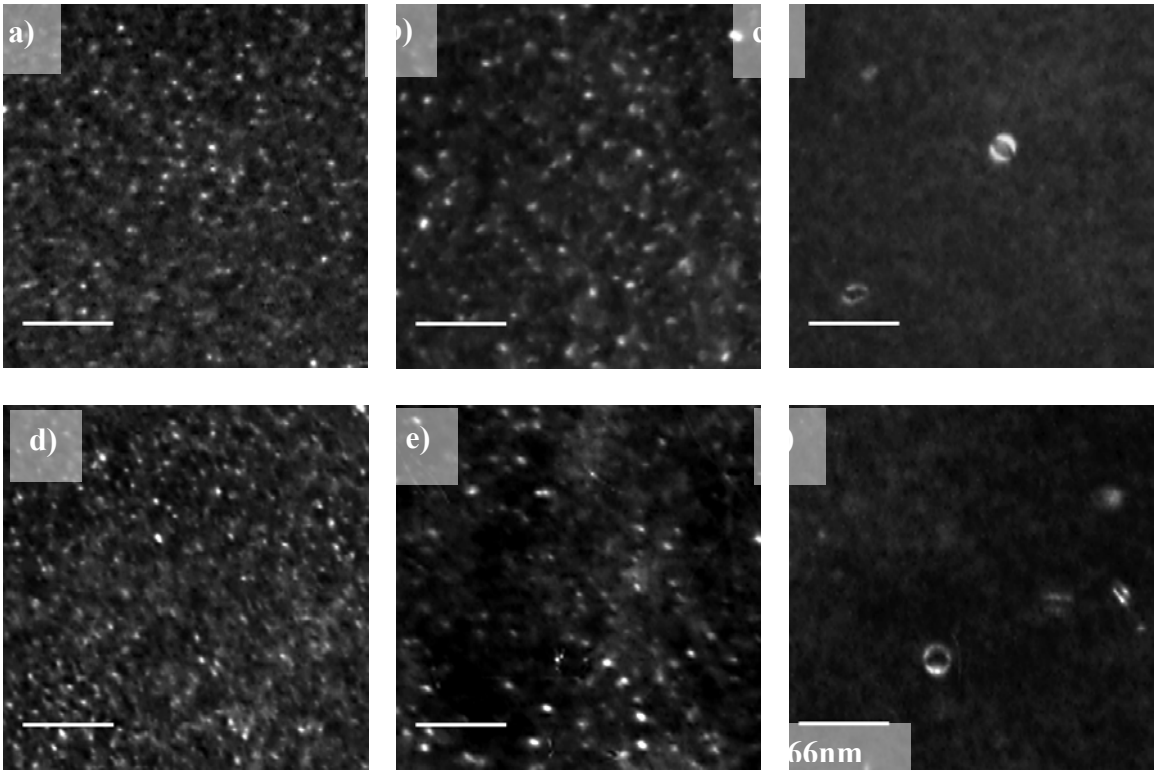

Figure 8-8. WBDF PTEM images of the EOR defects imaged under g_{220} two-beam conditions of the 30keV germanium PAI. Samples a, b, and c were subjected to a low temperature furnace anneal at 500°C for 30minutes prior to the fRTP anneal, while d, e and f were only subjected to the fRTP anneals. a)700°C iRTP, b) 700°C iRTP, 1100°C fRTP c) 700°C iRTP, 1300°C fRTP d) 700°C iRTP e) 700°C iRTP, 1100°C fRTP and f) 700°C iRTP, 1300°C fRTP.

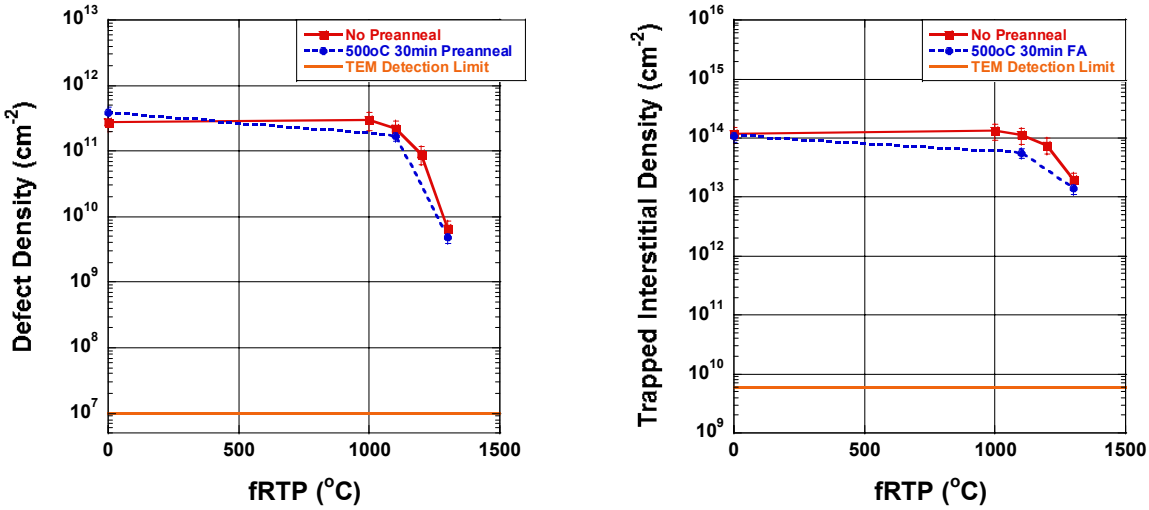

a) b)

Figure 8-9. Quantitative transmission electron microscopy results for a 30keV germanium PAI for samples which were subjected to two stage anneal process comprising a 500°C 30min furnace anneal and Flash-assist RTP anneals at 700°C iRTP, 700°C iRTP/1100°C fRTP and 700°C/1300°C fRTP temperatures. a) Defect density and b) Trapped Interstitial Density as a function of fRTP anneal temperature.

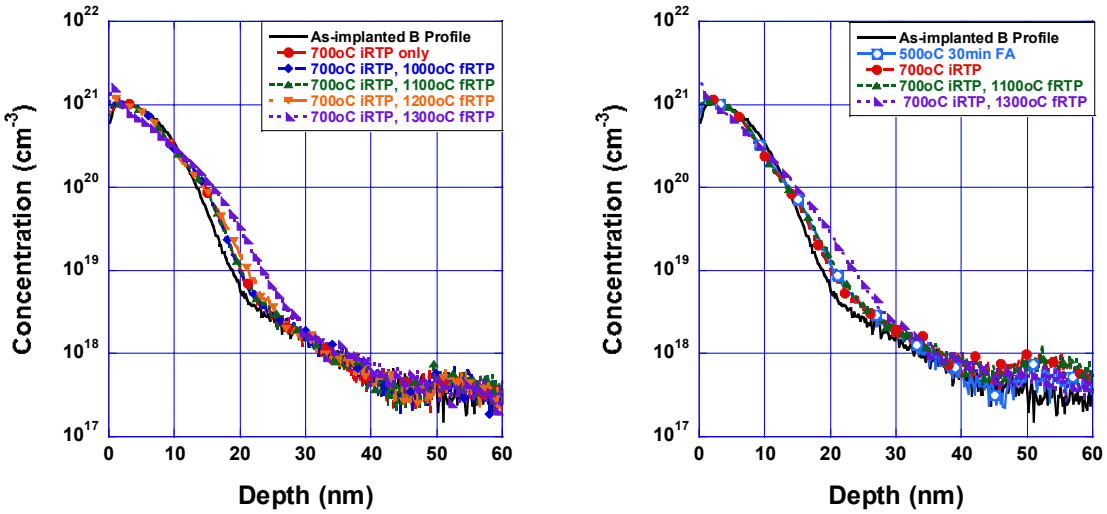

a) b)

Figure 8-10. Concentration-depth profiles of the diffused 1keV $1x10^{15}cm^{-3}$ boron implant processed by Flash-assist RTP for the $1x10^{15}cm^{-3}$, 30keV germanium PAI obtained from SIMS analyses for samples which were subjected to two stage anneal process comprising a $500^{o}C$ 30min furnace anneal and Flash-assist RTP anneals. a) Flash-assist RTP anneals only b) $500^{o}C$ 30min Furnace anneal and Flash-assist RTP anneals.

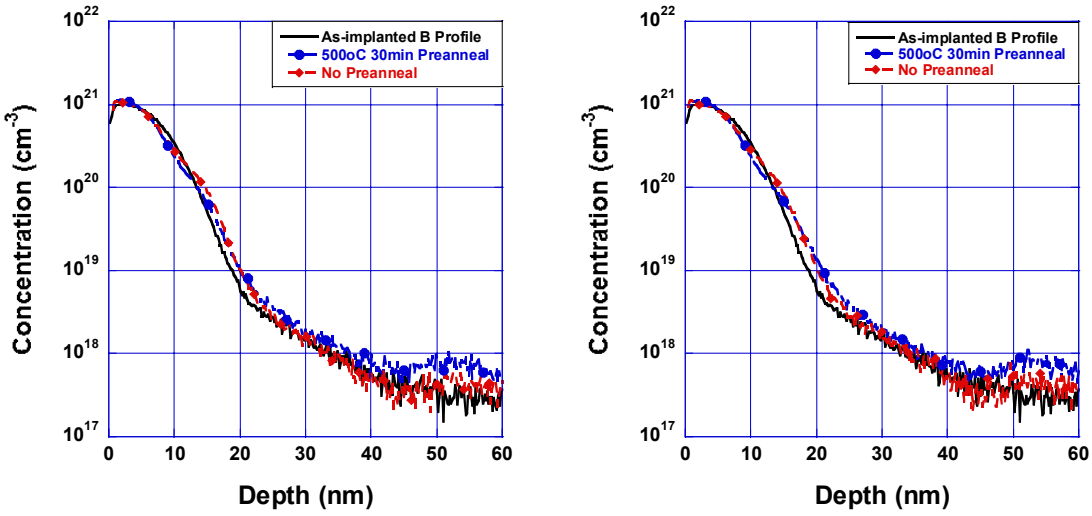

a) b)

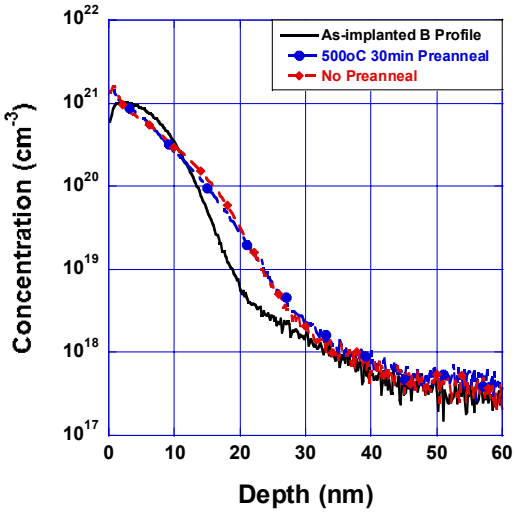

c)

Figure 8-11. Comparison of the diffused 1keV $1x10^{15}cm^{-2}$ boron profiles which were pre-annealed at 500°C for 30min and processed by Flash-assist RTP.a) 700°C iRTP b) 700°C iRTP/1100°C fRTP c) 700°C iRTP/1300°C fRTP.

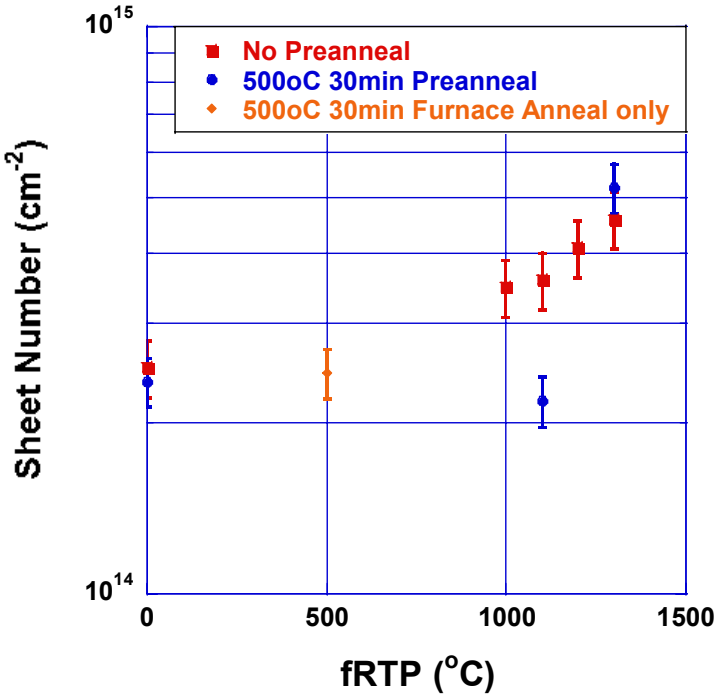

Figure 8-12. Active dose as a function of the fRTP anneal temperature of a 1keV $1x10^{15}cm^{-2}$ boron implant, into an amorphous layer formed by a 30keV $1x10^{15}cm^{-2}$ germanium implant. The samples were pre-annealed at 500°C for 30min and processed by Flash-assist RTP at 700, 1100, and 1300°C. The active dose obtained for the experimental control is also depicted for 700, 1000, 1100, 1200 and 1300°C.

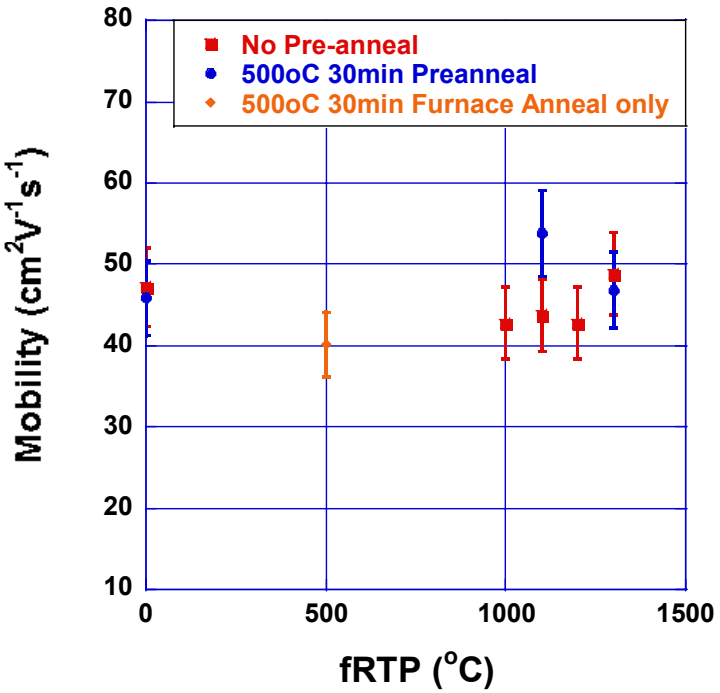

Figure 8-13. Carrier mobility as a function of the fRTP anneal temperature of a 1keV $1x10^{15}cm^{-2}$ boron implant, into an amorphous layer formed by a 30keV $1x10^{15}cm^{-2}$ germanium implant. The samples were pre-annealed at 500°C for 30min and processed by Flash-assist RTP at 700, 1100, and 1300°C. The carrier mobility obtained for the experimental control is also depicted for 700, 1000, 1100, 1200 and 1300°C.

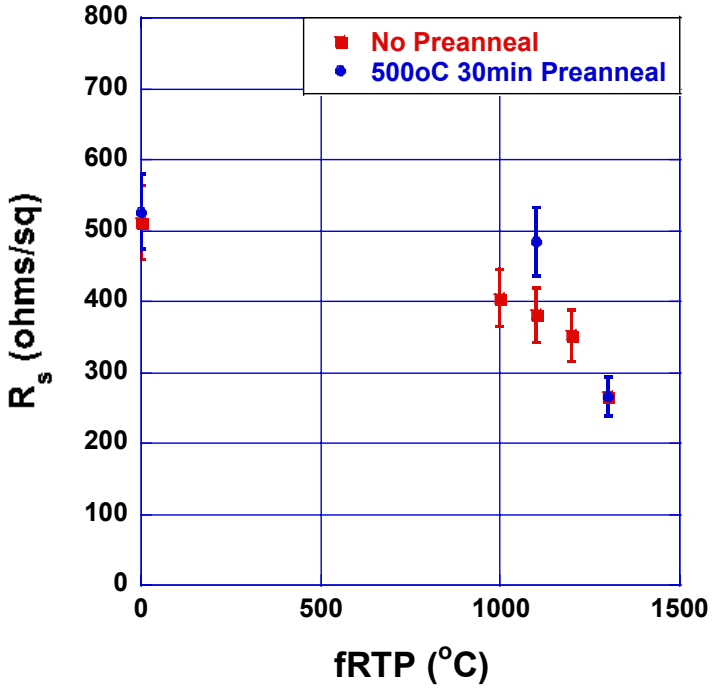

Figure 8-14. Sheet resistance, R_s of a $1x10^{15}cm^{-2}$, 1keV boron implant into an amorphous layer formed by a $1x10^{15}cm^{-2}$, 30keV germanium implant, as a function of the fRTP anneal temperature. Indicated are the R_s values for samples which were preannealed at 500°C for 30min prior to the Flash-assist RTP anneals and those samples which were annealed by Flash-assist RTP only.

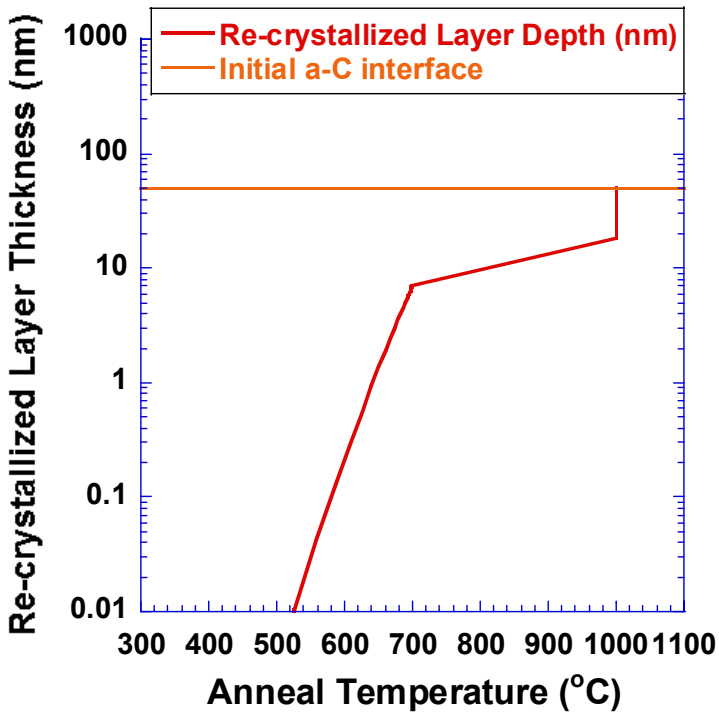

Figure 8-15. Re-crystallized layer depth as a function of anneal temperature for a 30keV germanium PAI generated in FLOOPS, utilizing both an intrinsic and extrinsic regrowth velocity relations.

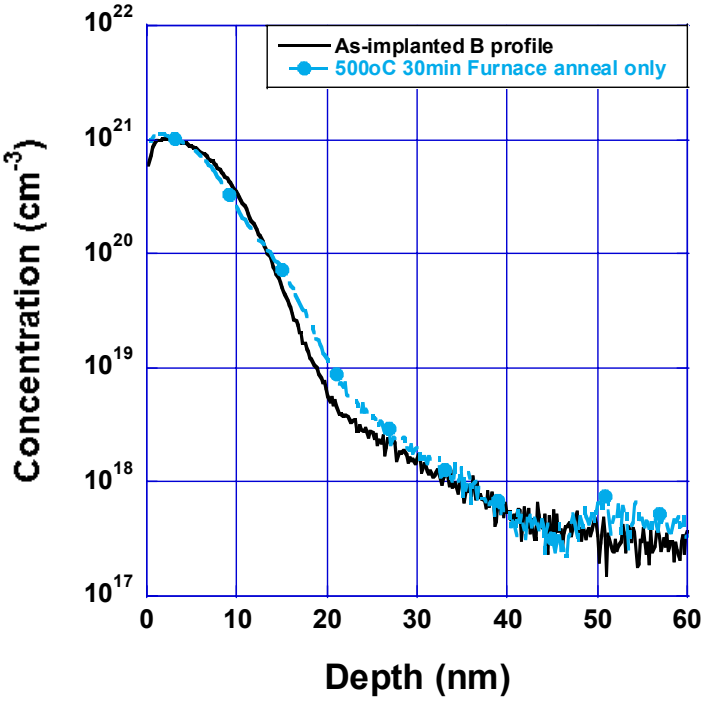

Figure 8-16. Concentration-depth profiles for a 1keV, $1x10^{15}cm^{-3}$ boron implant into a 50nm amorphous layer formed by a 30keV, $1x10^{15}cm^{-3}$ germanium preamorphizing implant, which was annealed at $500^{o}C$ for 30 minutes.

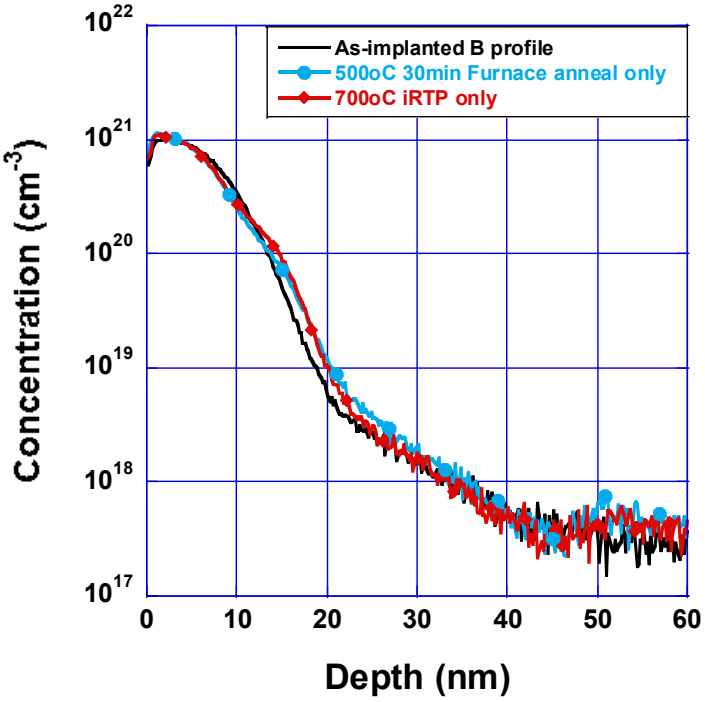

Figure 8-17. Comparison of the diffused 1keV $1x10^{15}cm^{-2}$ boron profiles, for a 30keV germanium preamorphizing implant, which were pre-annealed at $500^{o}C$ for 30min in a furnace and processed by Flash-assist RTP by a $700^{o}C$ iRTP

Table 8-1. Calculated boron intrinsic diffusion lengths in crystalline silicon for the fRTP

fRTP Temperature (^{o}C)	Intrinsic boron diffusion length (nm)
500	7.0×10^{-4}
700	3.5×10^{-2}
1100	4.4×10^{-1}
1300	1.03×10^{0}

Table 8-2. Estimated silicon interstitial supersaturation and boron enhanced diffusion length in crystalline silicon for the fRTP temperatures investigated.

fRTP Temperature (^{o}C)	Silicon interstitial supersaturation	Boron enhanced diffusion length (nm)
1100	2.68E+02	3
1300	1.11E+02	10

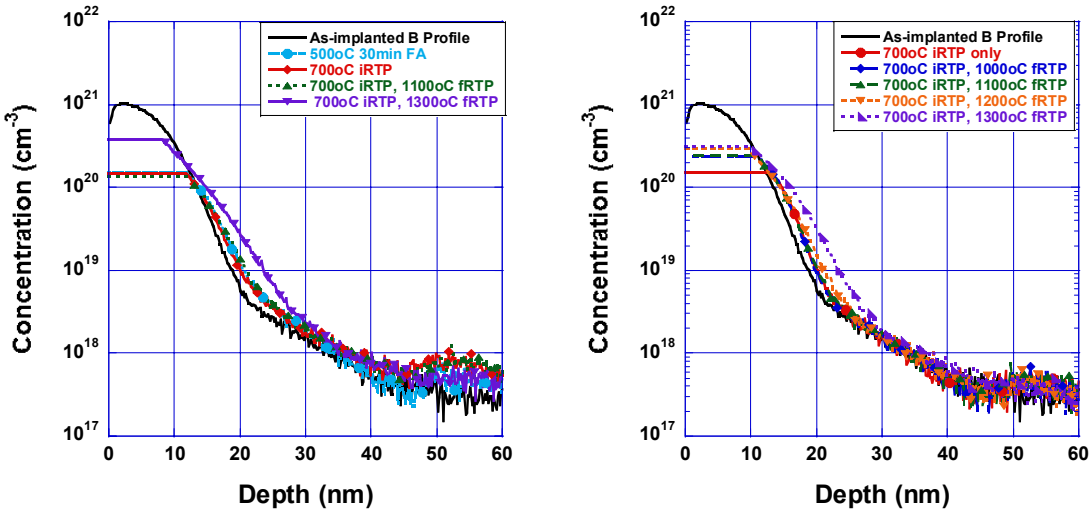

a) b)

Figure 8-18. Active portions of the SIMS boron profile, determined by matching the integrated area below the curve to the active boron dose obtained from the Hall measurement for a 30keV germanium PAI. Peak active concentrations are also highlighted for each anneal. a) 500°C 30min Preanneal b) No Preanneal (expt'l control).

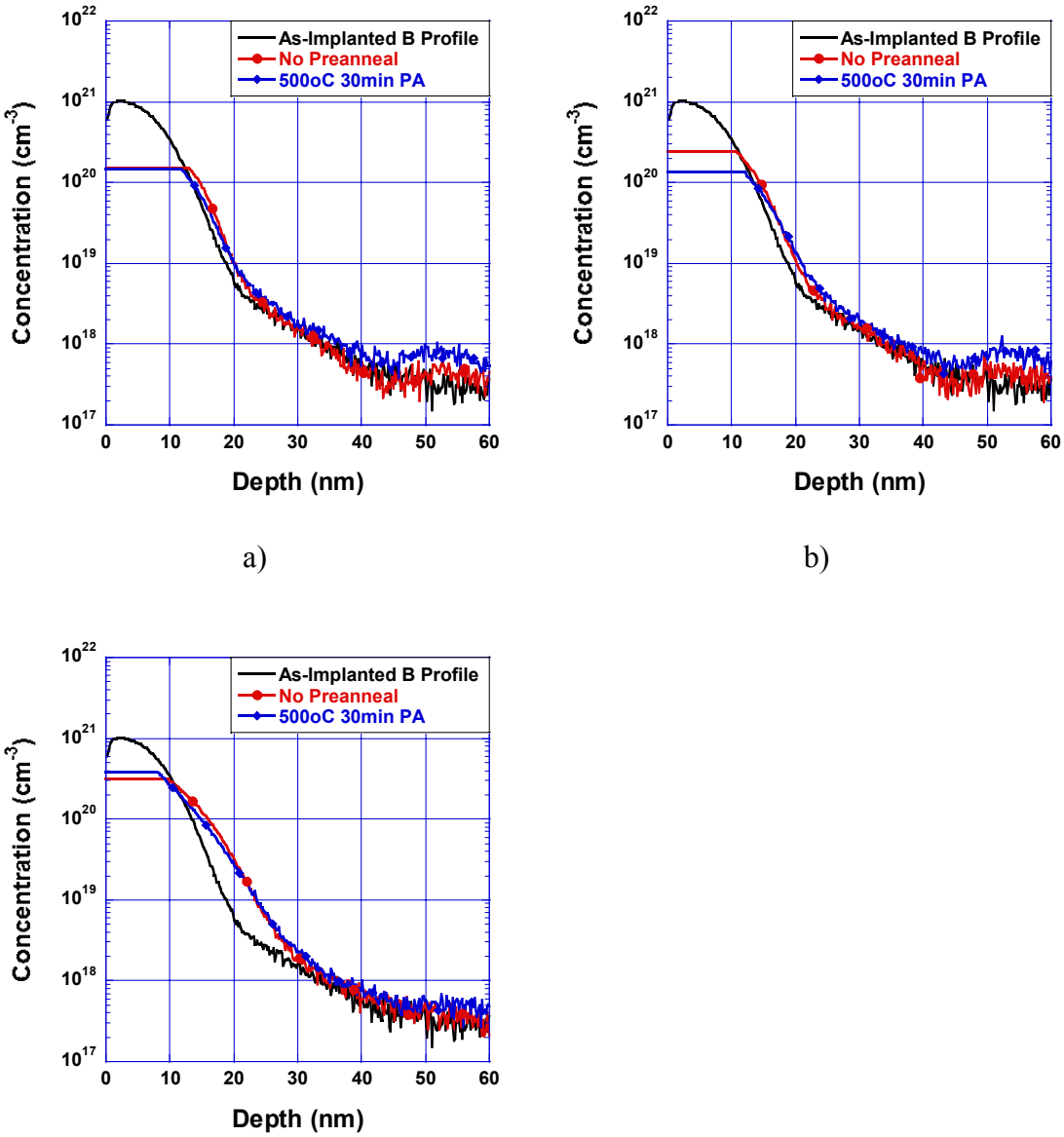

Figure 8-19. Comparison of the active boron concentrations for 1keV $1x10^{15}cm^{-2}$ boron profiles which were pre-annealed at 500°C for 30min and processed by Flash-assist RTP for a 30keV germanium PAI. a) 700°C iRTP b) 700°C iRTP/1100°C fRTP c) 700°C iRTP/1300°C fRTP.

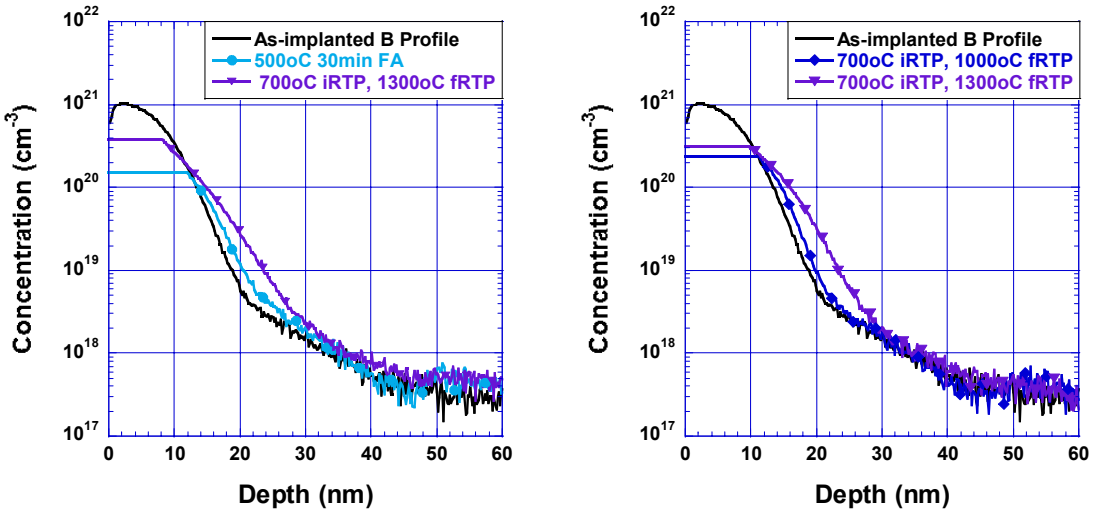

a) b)

Figure 8-20. Difference in the active boron concentrations upon re-crystallization of the amorphous layer and application of a 700°C iRTP/1300°C fRTP anneal. Recrystallization occurred during a) 500°C 30min preanneal b) 700°C iRTP/1000°C fRTP anneal.

CHAPTER 9
SUMMARY AND FUTURE WORK

9.1 Summary

9.1.1 Kinetics of the Dot-like Interstitial Cluster

The work presented in this dissertation has provided new insights into the processes which impact boron activation and diffusion in germanium preamorphized silicon during Flash-assist Rapid Thermal Processing (RTP). The fast ramp rates, on the order of $1x10^6$ $^oCs^{-1}$; short anneal times, which are typically less than 1 millisecond; and extremely high temperatures ranging 1000 through 1300°C; enabled by Flash-assist RTP allowed for such investigations at time scales not possible with past annealing tools such as the Rapid Thermal Annealer (RTA). The initial investigations surveyed the evolution of the End of Range (EOR) damage associated with amorphous layer formation, for which a defect believed to be the precursor for the {311}-type defect was detected. This defect occurred as a dot-like interstitial cluster in the silicon microstructure for the lower fRTP anneals and was observed to either dissolve or evolve into the {311}-type defect with additional thermal budget. Hence the defects were thought to evolve from point defects to sub-microscopic interstitial clusters [BEN97, COF00, LIB98] which then form these dot-like interstitial clusters, now believed to be the precursor for the {311}-type defect. The defect structures revealed at the higher fRTP anneal temperatures were consistent with previous studies on the End of Range damage evolution; in which {311}-type defects [EAG94, STO97, PAN97], which are metastable unfault to form dislocation loops [LIJ98].

The short anneal times which fall in the millisecond regime, characteristic of the Flash-assist RTP that makes it attractive as an annealing technique, presented challenges in evaluating its effectiveness in evolving the EOR damage, since time dependent studies of the evolution were impossible. Hence an alternative approach was necessitated, which utilized the initial interstitial density as that for the iRTP anneal, which was not varied for the experiment. Thus the interstitial decay rate over the fRTP portion of the anneal could be isolated, enabling the effectiveness of the flash to be evaluated. The kinetics of the dot-like interstitial cluster indicated a highly unstable defect, whose dissolution was related to the anneal temperature by an Arrhenius relation with an activation energy of 2.1eV. These kinetics were different from those of previously reported structures [SEI85,EAG94, KIN03], substantiating that this defect configuration was in fact different from known structures.

9.1.2 Varying the Germanium Preamorphization Energy

Varying the germanium preamorphization energy between 8 and 30keV had a significant influence on both the boron activation and diffusion. The relative distance of the amorphous-crystalline interface from the boron profile, effected differences in the recrystallization rate which induced changes in the boron diffusion and the final re-crystallization temperature. An increase in the relative distance between the boron profile and the interface allowed for an elevated re-crystallization temperature and higher diffusion levels of boron in the amorphous phase, prior to the recrystallization. This diffusion was observed to dictate the final diffused profiles, subsequent to application of the Flash-assist RTP and resulted in a more abrupt profile for the deeper amorphous layer. The shallower amorphous layer was found to have a lower active dose than the deeper amorphous layer, immediately subsequent to the re-crystallization process. This

was thought to be due to the differences in the temperature at which the amorphous layer re-crystallized.

At 1300°C fRTP increases in activation levels above the re-crystallization activation, were detected for the 8 and 30keV germanium implants. These were observed to be a direct consequence of two processes which included increased diffusion in the tail of the boron profile and activation in the profile peak. This find demonstrated that boron was activated from some initial unknown, immobile, inactive configuration, which did not conform to the dissolution kinetics of the extensively studied boron interstitial clusters (BICs) [LIL02, MIR03, DES05]. Hence it was concluded that the supplemental activation was the result of boron activation from another inactive configuration which was much less stable than the BIC. The final junction characteristics attained for the 1300°C fRTP anneal also appeared to be independent of the germanium preamorphization energy, since the junctions exhibited similar electrical and chemical profiles. Despite the differences in the active dose upon completion of the re-crystallization process, identical peak active concentrations were attained for the 1300°C anneal, independent of the preamorphization energy, which hinted at a possible threshold concentration for activating boron at these temperatures.

In the deeper amorphizing implant the sheet resistance was found to be undisputedly dictated by the active dose. Conversely, the mobility appeared to be the dominant parameter which governed the final sheet resistance for the lower energy implant for temperatures of 1200°C and below, since the active dose was demonstrated to be controlled by the re-crystallization temperature. But a firm conclusion could not be

drawn for the low energy germanium preamorphizing implant, as the mobility changes were not fully understood and needs to be further investigated.

9.1.3 Influence of the Recrystallization Temperature

In order to further explore whether the recrystallization temperature was responsible for the differences in boron activation observed when the germanium preamorphization was altered, an alternative experiment was performed. This experiment entailed re-crystallization of the amorphous layer by a low temperature anneal process, prior to application of the Flash-assist RTP.

The experimental data which confirmed that the activation was dictated by the re-crystallization temperature came from the sample which was preannealed and subsequently annealed at 1100°C fRTP. In this case the re-crystallization temperatures differed by an estimated 500°C such that the experimental control exhibited an active concentration, which was 80% higher than the preannealed wafer. Interestingly, the increase in active concentration was due to activation of boron located mainly in the profile peak which contained more than 90% of the additional activated dose. It is important to note that in these cases the differences were related directly to the temperatures at which the re-crystallization occurred, which indicated that a larger fraction of boron was located at substitutional sites during the re-crystallization process itself. Hence it provided further evidence that the activation was governed by the re-crystallization temperature.

Subsequent to the re-crystallization process, increases in the fRTP anneal temperature to temperatures as high as 1200°C, were determined to be insufficient to result in increased activation levels, thus the final activation was controlled by the re-crystallization temperature. Hence the Flash-assist RTP process for temperatures less

than 1300°C, had no effect on the final boron activation once the amorphous layer was previously re-crystallized. The corresponding activation mechanisms were attributed to the much more effective trapping of solute atoms at substitutional sites at the higher temperatures [CAM80, JAI04]. The experimental findings also concurred with the possibility of higher boron solid solubility levels in amorphous silicon [ELL85, POL90, COF92, CAL89, GAB04].

9.1.4 Activation Subsequent to Re-crystallization

The above experiments further substantiated the theory that at high enough anneal temperatures the activation was independent of the recrystallization temperature. At 1300°C fRTP increases in activation levels above the re-crystallization activation were observed to be a direct consequence of two processes which included increased diffusion in the tail of the boron profile and activation in the profile peak. This find demonstrated that boron was activated from some initial unknown, immobile, inactive configuration, as seen in the previous experiments where the germanium preamorphization energy was altered. This unknown configuration of boron was shown to be less stable than the widely researched boron interstitial cluster (BIC) [LIL02, MIR03, DES05]. Additionally, despite the differences in the active dose upon completion of the re-crystallization process, identical peak active concentrations were attained for the 1300°C anneal, which hinted at a possible threshold concentration for activating boron at these temperatures from such a configuration.

These research results strongly hinted at the existence of boron in an alternate immobile, inactive configuration subsequent to the re-crystallization process, which is less stable than the well known BIC structure. At high enough thermal budgets boron can be activated from this structure. It was also concluded that the sheet resistance was

dictated by the active dose for the experimental control. Conversely, the mobility varied substantially for the samples which were preannealed, in particular for the 1100°C fRTP anneal. A firm conclusion could not be drawn regarding the factor which was responsible for the final sheet resistance, since the mobility changes are not fully understood at this time and need to be further investigated.

Reference to the experiments in which the germanium preamorphization was altered, indicated that the lower germanium energy implant demonstrated a higher mobility in the fRTP range of 1000 through 1200°C. The values of which were comparable to the preannealed 1100°C fRTP wafer. The similarities in the experiments lie in the fact that the amorphous layer re-crystallized at relatively low temperatures. This may provide some insight into the reasons why higher carrier mobilities were noticeable for these cases.

9.2 Future Work

Although these studies have provided a better understanding of the mechanisms which dictate the activation and diffusion of boron in preamorphized silicon during Flash-assist Rapid Thermal Processing (RTP), the experiments herein indicated that further work is required. This work should focus on identifying the location of the additional activation in the peak observed for the 1300°C fRTP anneal temperature and also on investigating the high mobilities attained for the 8keV germanium preamorphizing implant and those samples which were subjected to a low temperature anneal.

9.2.1 Differential Hall Measurement of the Active Dose

The supplemental activation achieved for the 1300°C fRTP anneal in all the experiments conducted in this manuscript have been attributed in part to activation of

boron in the Gaussian peak, subsequent to amorphous layer re-crystallization. This was inferred by matching the active doses attained from the Hall measurement with the integrated area below the concentration-depth profiles obtained from the SIMS measurement, which entailed an assumption that all boron located in the profile tail was active. In order to identify the location of the active boron profile, the use of Differential Hall Measurements (DHM) [BEN05] is recommended.

The inherent nature of the Flash-assist RTP effects substantial differences in the temperatures to which the material layers are subjected during the regrowth, which can significantly affect the active dose on the atomic level. The DHM measurement will therefore provide data on the variation of the active dose and the carrier mobility with depth. It is also recommended that consecutive Four Point Probe (FPP) measurements of the sheet resistance be conducted, as a reference to be used during the DHM measurement.

The DHM technique entails stripping the material surface layers in successive steps. A Hall measurement is then conducted for each consecutive layer. The layer removal technique relies on the growth of an oxide, which is controlled by the water quality and reaction time. Hence these factors should not be manipulated, such that differences in the oxide thickness are minimized. A buffered Hydrogen Fluoride (HF) solution is then used to etch the oxide, subsequent to the Hall measurement. Consecutive oxide growth and removal steps are performed between each measurement. This technique relies on the assumption that a uniform amount of material is removed between each measurement, which impacts the depth resolution of DHM.

9.2.2. Resolve the Enhanced Mobility

The enhanced mobility detected in the temperature range 1000 through 1200°C, for the 8keV germanium preamorphizing implant cannot be resolved within the framework of these experiments. The values were found to much higher than determinations from standard mobility models for this dopant concentration range [KLA92], hence the following experiment is therefore proposed.

Boron box-shaped profiles should be grown via Chemical Vapor Deposition (CVD) at peak concentrations ranging $1x10^{18}$ through $1x10^{20}cm^{-3}$ in silicon (100) wafers, such that the active dose within each box-profile is the same. Hall measurements should then be conducted on these structures in order to extract the mobility. The question lies in whether the mobility in such a structure is actually higher and is subsequently degraded owing to the different scattering mechanisms in re-grown ion implanted material. Alternatively, one could consider whether the enhancement detected is an improvement in mobility simply due to a reduction in the scattering mechanisms.

APPENDIX A
END OF RANGE DAMAGE EVOLUTION FOR 8KEV GERMAMIUN PREAMORPHIZING IMPLANT

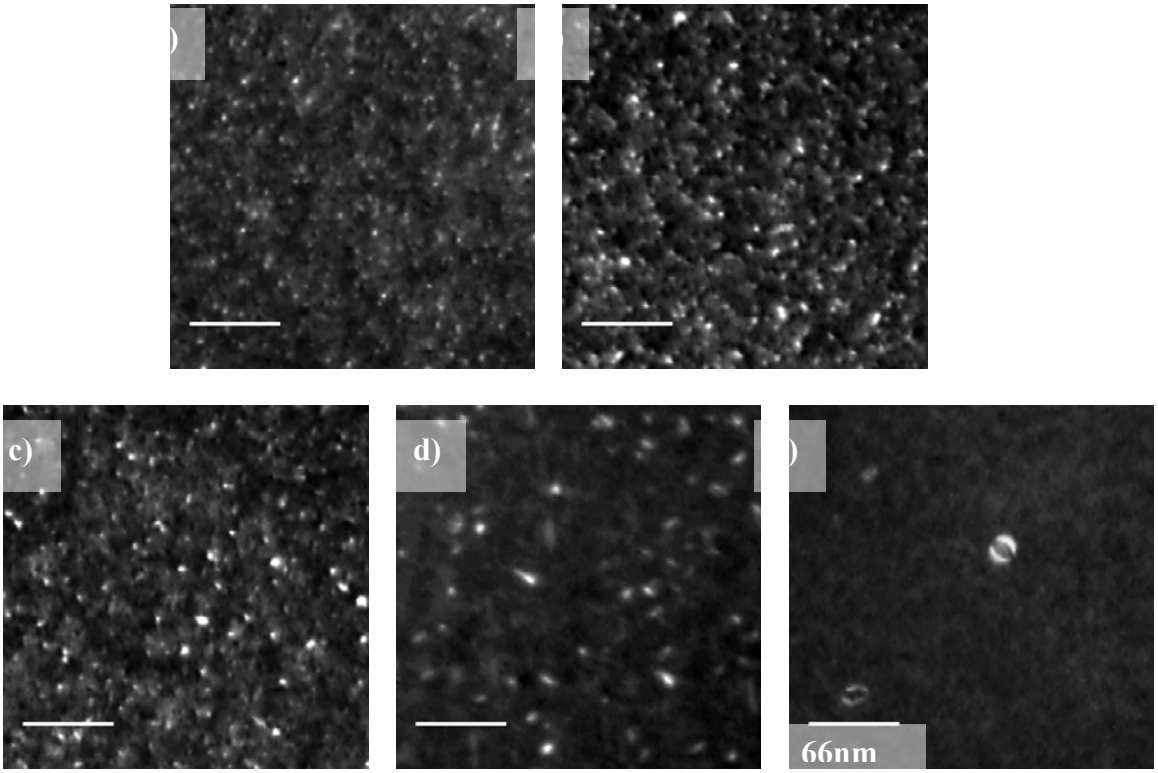

Figure A-1. WBDF PTEM images of the EOR defects imaged under g_{220} two-beam conditions of the 8keV $1x10^{15}cm^{-2}$ germanium amorphizing implant. a)700°C iRTP, b) 700°C iRTP,1000°C fRTP, c) 700°C iRTP, 1100°C fRTP, d) 700°C iRTP, 1200°C fRTP, e) 700°C iRTP, 1300°C fRTP

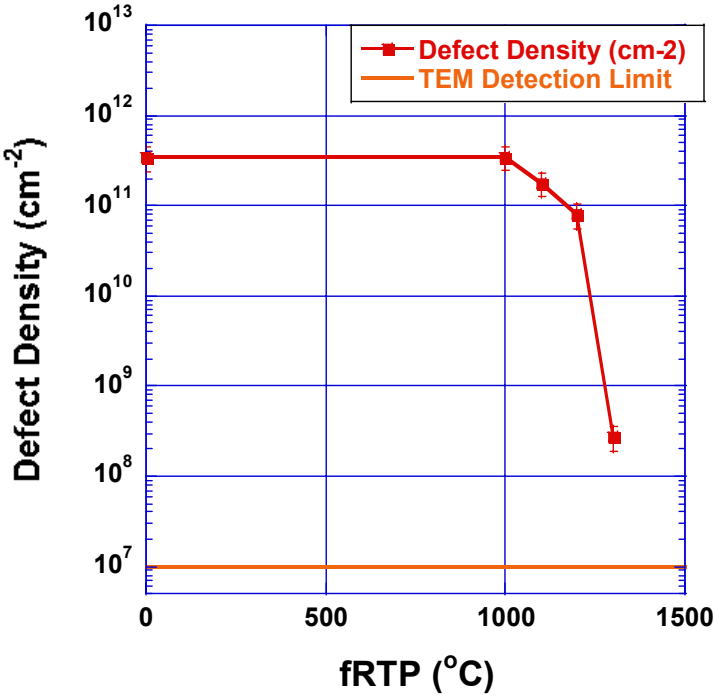

Figure A-2. Defect density as a function of fRTP anneal temperature for a $1x10^{15}cm^{-2}$ 8keV germanium amorphizing implant

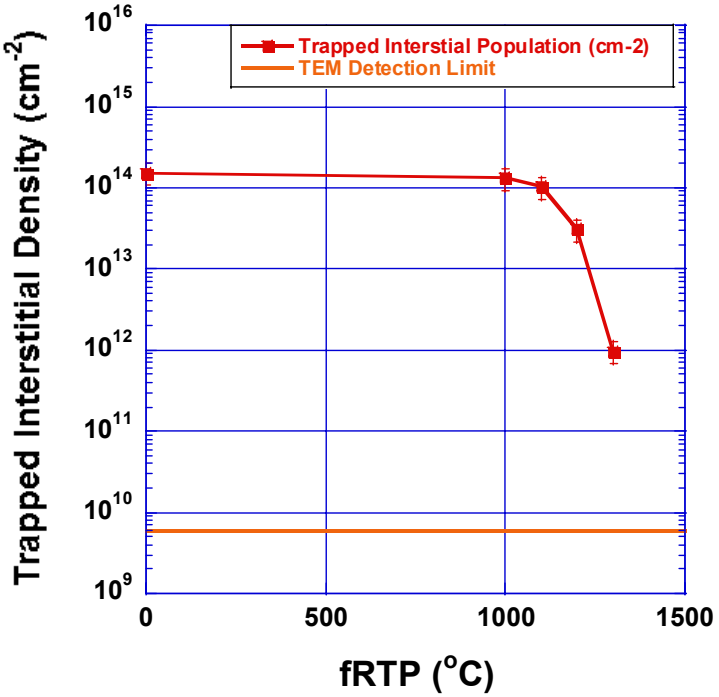

Figure A-3. Trapped interstitial density as a function of fRTP anneal temperature for a $1x10^{15}cm^{-2}$ 8keV germanium amorphizing implant

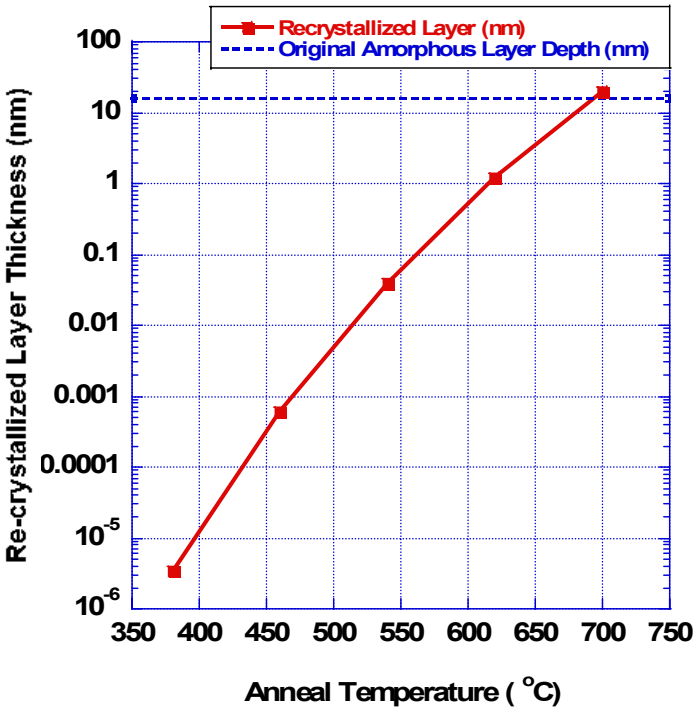

Figure A-4. Re-growth of a 16nm amorphous layer formed by an 8keV $1x10^{15}cm^{-2}$ Ge PAI, containing a 1keV $1x10^{15}cm^{-2}$ B implant. Regrowth as a function of temperature determined by taking the integral of the velocity-time plots.

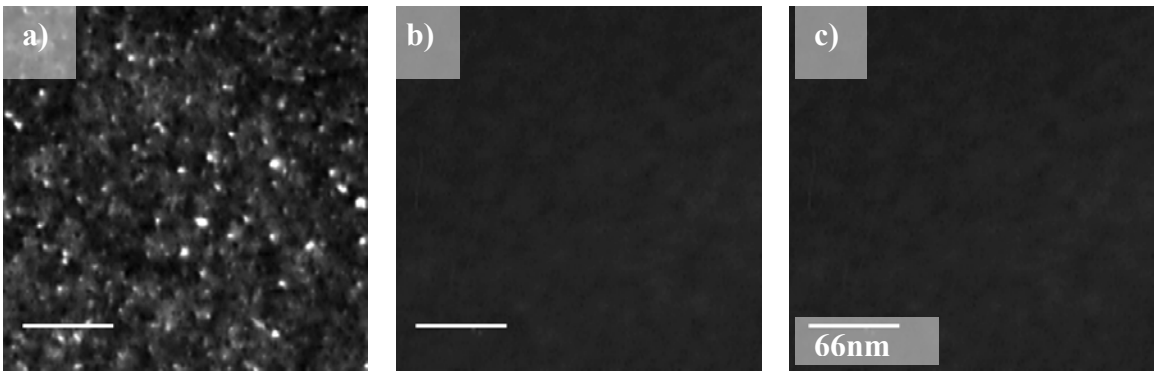

Figure A-5. WBDF PTEM images of the EOR defects imaged under g_{220} two-beam conditions of the 8keV $1x10^{15}cm^{-2}$ germanium amorphizing implant, subjected to a flash anneal and a spike RTA. a) 700°C iRTP, 1100°C fRTP b) 700°C iRTP, 1100°C + 950°C spike RTA c) 950°C spike RTA only

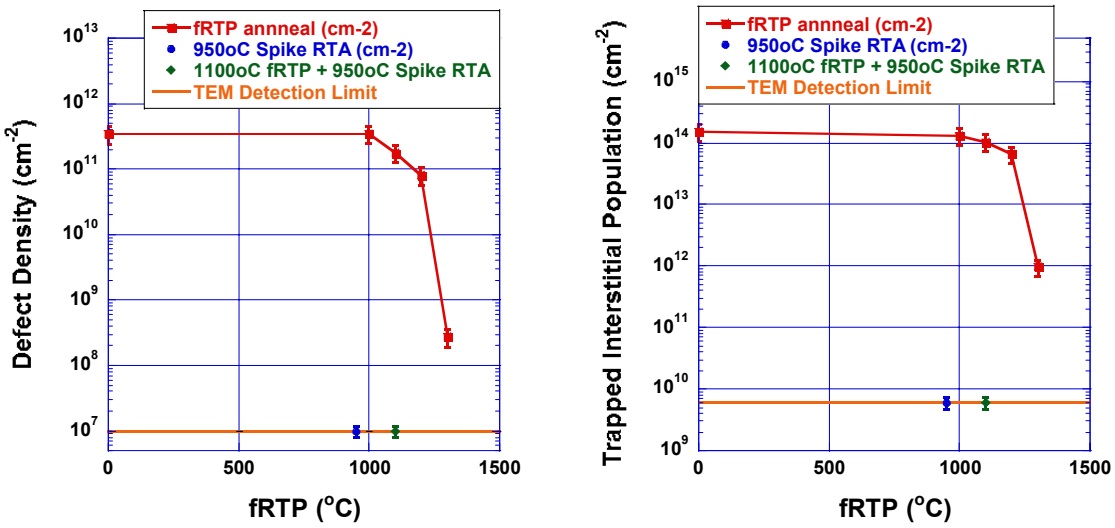

a) b)

Figure A-6. Defect density and trapped interstitial density as a function of fRTP anneal temperature for a $1x10^{15}cm^{-2}$ 8keV Ge amorphizing implant for the 700°C iRTP, 1100°C fRTP anneal only and 700°C iRTP, 1100°C fRTP anneal + 950°C spike RTA. a) Defect density and b) Trapped interstitial density.

APPENDIX B
KINETIC ANALYSIS OF THE END OF RANGE DAMAGE DISSOLUTION FOR FLASH-ASSIST RAPID THERMAL PROCESSING

Table B-1. Simulated and experimental trapped interstitial densities and associated errors for an 8keV germanium amorphizing ion implant into (100) silicon.

fRTP Anneal Termperature (^{o}C)	Simulated Trapped Interstitial Density (cm^{-2})	Experimental Trapped Interstitial Density (cm^{-2})	Error (%)
1300	$1.30x10^{12}$	$9.64x10^{11}$	-34.88
1200	$4.81x10^{13}$	$6.51x10^{13}$	26.17
1100	$1.19x10^{14}$	$1.02x10^{14}$	-16.37
1000	$1.48x10^{14}$	$1.31x10^{14}$	-12.76

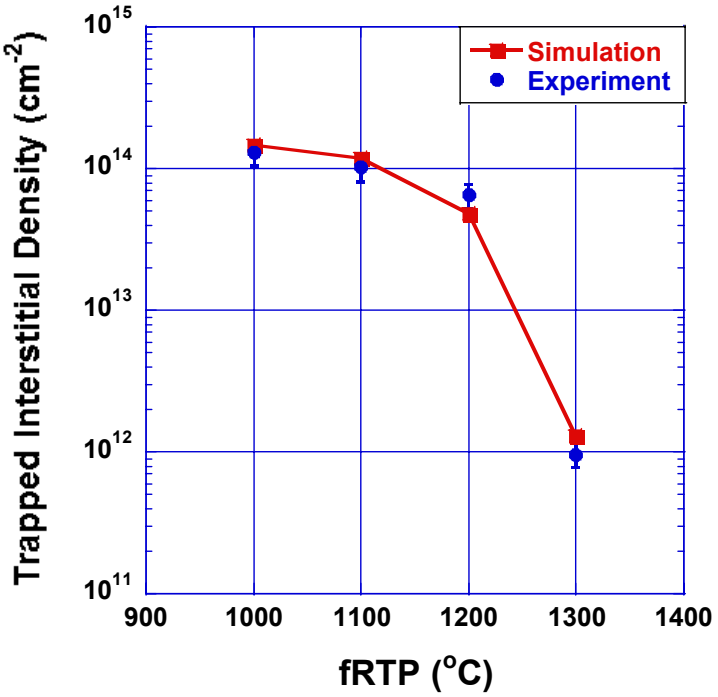

Figure B-1. Simulated and experimental trapped interstitial densities for a 8keV, $1x10^{15}cm^{-2}$ germanium amorphizing ion implant into (100) silicon

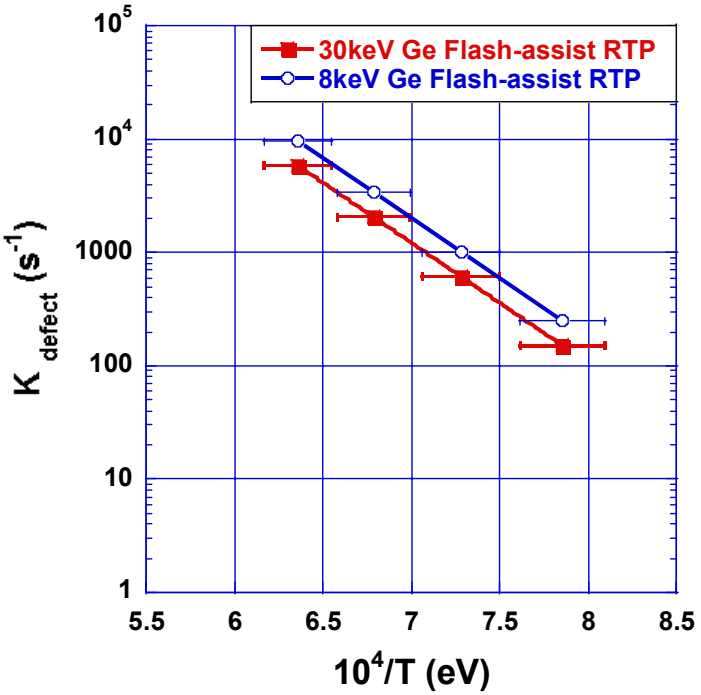

Figure B-2. Arrhenius plot of the time constant derived for the defect decay extracted from the simulated experimental data, indicating an activation energy, E_a of 2.1 ±0.05eV for dissolution.

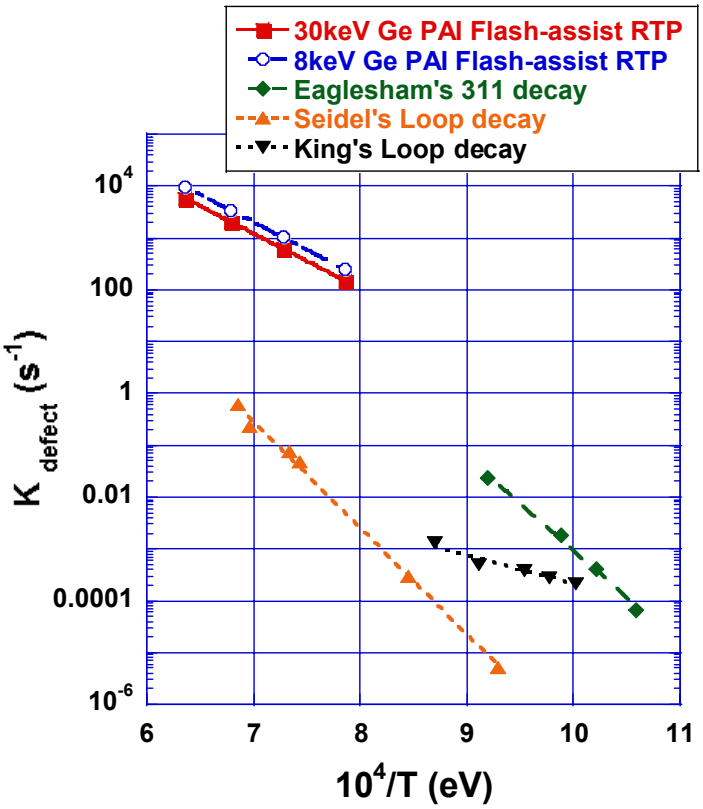

Figure B-3. Arrhenius plot of the time constant derived for defect decay from the literature, including decay rates for {311}-type defects [EAG94, STO97], dislocation loops [SEI85, KIN03] and the dot-like defects observed in this work.

APPENDIX C
FLOOPS SIMULATION CODES

C.1 Trapped Interstitial Decay

```
#Flash Experiment Defect Decay over Flash-assist RTP

proc SimAnneal { Temp } {

                    solution add name=test pde solve !negative

pdbSetString Si test Equation "ddt(test) + test/tau"

# define the grid

line x loc=0 spacing=0.05 tag=top

line x loc=4.0 spacing=0.25

line x loc=400.0 tag=bottom

region silicon xlo=top xhi=bottom

init

sel z=100.0 name=test; #initial defect density set at the value after the 700oC iRTP

term name=tau add eqn= {1.0e-11*exp(2.2/(8.62e-5*(T+273.0)))} silicon

# ramp up rate

term name=T add eqn= {700.0+1.0e6*[simGetDouble Diffuse time ]} silicon

diffuse time = [ expr (${Temp}-700.0)/(1.0e6*60.0) ]

# peak temp

term name=T add eqn= ${Temp} silicon

diffuse time = [expr (0.9e-3 - (${Temp}-700.0)/1.0e6)/60.0]

# ramp down rate
```

```
term name=T add eqn= {${Temp}-1.0e6*[simGetDouble Diffuse time]} silicon
diffuse time = [ expr (${Temp}-700.0)/(1.0e6*60.0) ]
sel z=test
puts "Defect density is [interpolate silicon x=1.0] "
return [interpolate silicon x=1.0]
}
# testing plot command
# plotting temperature profile
 set W [CreateGraphWindow]
 sel z=T
CreateLine $W Temperature_profile [slice y=0.0 silicon]
set temps {1000 1100 1200 1300}
foreach temp $temps {
append defect_percent_remaining [SimAnneal $temp]
}
puts "For temperatures ...\n${temps}\nthe remaining defect percentage is
...\n${defect_percent_remaining}"
```

C.2 Recrystallization Temperature Determination

```
# short simulation to calculate the effective regrowth of a given thermal process

# depth dimension used as time

# inputs : regrowth velocity of a species of interest

# temperature profile vs time

    #set D { 3.07e8*exp(-2.68/kT) } ;# intrinsic regrowth rate of Olson and Roth

    set D { 5.35e8*exp(-2.52/kT) } ;# extrinsic regrowth rate


#iRTP regrowth

    set Temperature_profile {} ;#700oC iRTP Temperature Ramp

    lappend Temperature_profile { 300 150 0.67 5e-5 }

    lappend Temperature_profile { 400 0 1 5e-5 }

    lappend Temperature_profile { 400 150 2 5e-5 }


#fRTP regrowth

    set initT 300.0

    set iRTP 700.0

    set iramp_rate 150.0

    set icool_rate -50.0

    set iflash_rate 10.0e6

    set back_temp 800.0

    set fRTP 1300.0

    lappend Temperature_profile " $initT $iramp_rate [expr ($iRTP-
    $initT)/$iramp_rate] 0.5 "
```

```
        lappend Temperature_profile " $iRTP $icool_rate [expr ($initT-
        $iRTP)/$icool_rate] 0.5 "

        lappend Temperature_profile " $iRTP $iflash_rate [expr ($fRTP-
        $iRTP)/$iflash_rate] 5e-5 "

        lappend Temperature_profile " $fRTP 0 9e-4 5e-5 "

        lappend Temperature_profile " $fRTP $iflash_rate [expr ($fRTP-
        $back_temp)/$iflash_rate] 5e-5 "

        lappend Temperature_profile " $back_temp $icool_rate [expr ($initT-
        $back_temp)/$icool_rate] 0.5 "

        set min_dt 1.0e-8 ;# minimal delta t [s]

# build the grid to have accurate account of the noncontinuous points in temperature
profile

        set previous_loc 0.0

        for {set i 0} {$i < [llength $Temperature_profile]} {incr i} {

                set step [lindex $Temperature_profile $i]

                set stepT [lindex $step 0]

                set step_rate [lindex $step 1]

                set step_t [lindex $step 2]

                set step_dt [lindex $step 3]


                if {$i == 0} {

                line x loc=$previous_loc spa=$step_dt tag=time_start

          #     puts "1st line command: line x loc=$previous_loc spa=$step_dt
        tag=time_start"

                } elseif {$i == [expr [llength $Temperature_profile]-1]} {

                line x loc=$previous_loc spa=$step_dt

          #     puts "line command: line x loc=$previous_loc spa=$step_dt"

                line x loc=[expr $previous_loc + $step_t] spa=$step_dt  tag=time_end
```

```
  #         puts "last line command: line x loc=[expr $previous_loc + $step_t]
spa=$step_dt tag=time_end"

            } else {

            line x loc=$previous_loc spa=$step_dt

  #         puts "line command: line x loc=$previous_loc spa=$step_dt"

            }

  set previous_loc [expr $previous_loc + $step_t]

  }

set total_time $previous_loc

region silicon xlo=time_start xhi=time_end

init quiet


# add the temperature profile T=f(x)

set previous_loc 0.0

set Temperature_expr {0.0}

for {set i 0} {$i < [llength $Temperature_profile]} {incr i} {

            set step [lindex $Temperature_profile $i]

            set stepT [lindex $step 0]

            set step_rate [lindex $step 1]

            set step_t [lindex $step 2]

            set step_dt [lindex $step 3]


            if {$i == [expr [llength $Temperature_profile]-1]} {

                        set step_expr "(${stepT}+(${step_rate})*(x-
${previous_loc}))*(x>=${previous_loc})*(x<=[expr
${previous_loc}+${step_t}])"
```

```
            } else {

            set step_expr "(${stepT}+(${step_rate})*(x-
    ${previous_loc}))*(x>=${previous_loc})*(x<[expr ${previous_loc}+${step_t} -
    ${min_dt}])"

            }

  #         puts "step number $i is: $step \n\t expression is $step_expr"

            append Temperature_expr " + ${step_expr} "

            set previous_loc [expr $previous_loc + $step_t]

  }

    puts "Full temperature expression is:\n$Temperature_expr\n"

    sel z=$Temperature_expr name=T


# plotting temperature profile

    set W [CreateGraphWindow]

    sel z=T

    CreateLine $W Temperature_profile [slice y=0.0 silicon]



# calculate the effective regrowth velocity, sum vt

    set X [CreateGraphWindow]

    sel z=(T+273.15)/11605.0 name=kT ;#11605 is the inverse of the Boltzmann
    constant

    sel z=$D ;# velocity

    CreateLine $X velocity_profile_$fRTP [slice y=0.0 silicon]

    set Dt_eff [expr [FindDose]*1.0e4] ;# sum(D * dt), conversion of microns to cm
    for the depth intergral

    puts "regrowth is $Dt_eff cm"
```

APPENDIX D
ALTERING THE RE-CRYSTALLIZATION TEMPERATURE OF THE AMORPHOUS LAYER AND ITS IMPACT ON FINAL BORON ACTIVATION

D.1 Results for the 8keV Ge PAI

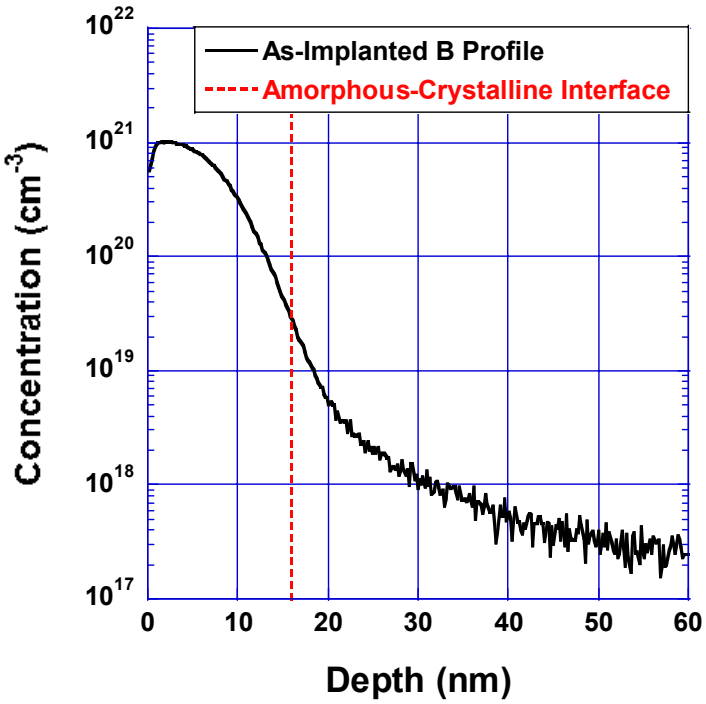

Figure D-1. Concentration-depth profiles of the boron implant into an amorphous layer formed by a $1x10^{15}cm^{-2}$, 8keV germanium preamorphizing implant obtained from SIMS analyses

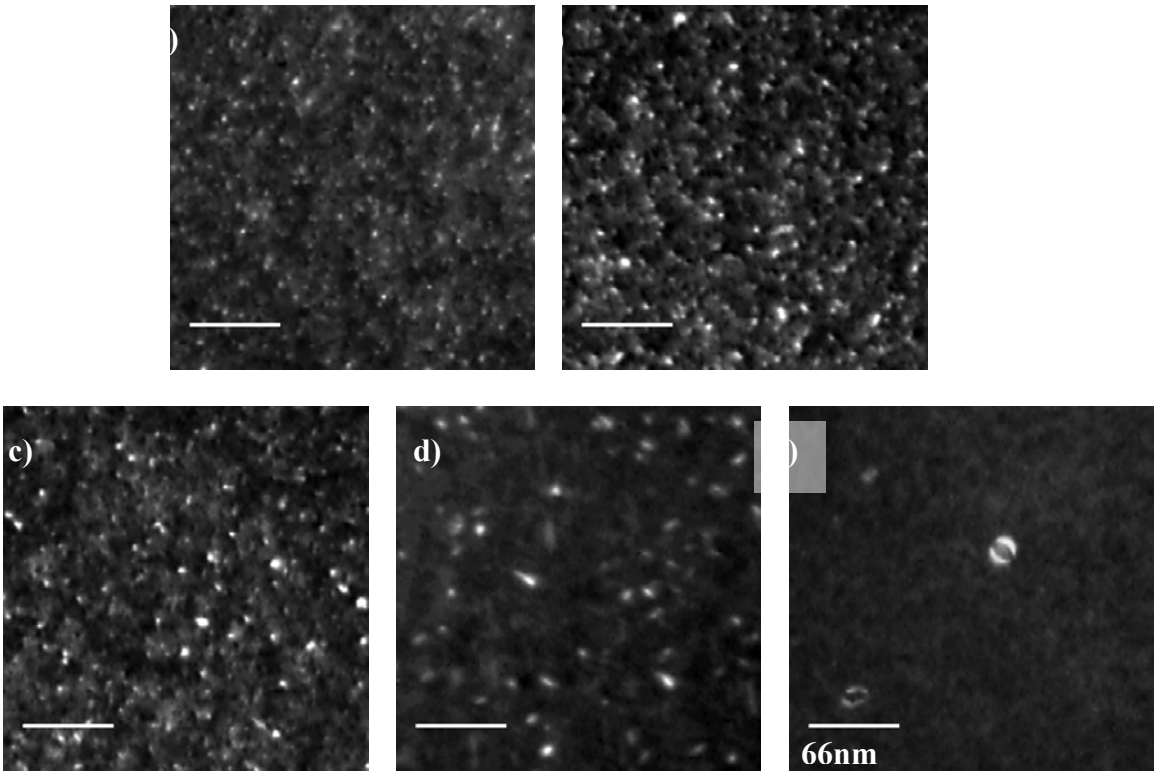

Figure D-2. WBDF PTEM images of the EOR defects imaged under g_{220} two-beam conditions of the 8keV germanium preamorphizing implant subjected to a flash anneal. a)700°C iRTP, b) 700°C iRTP,1000°C fRTP, c) 700°C iRTP, 1100°C fRTP, d) 700°C iRTP, 1200°C fRTP, e) 700°C iRTP, 1300°C fRTP

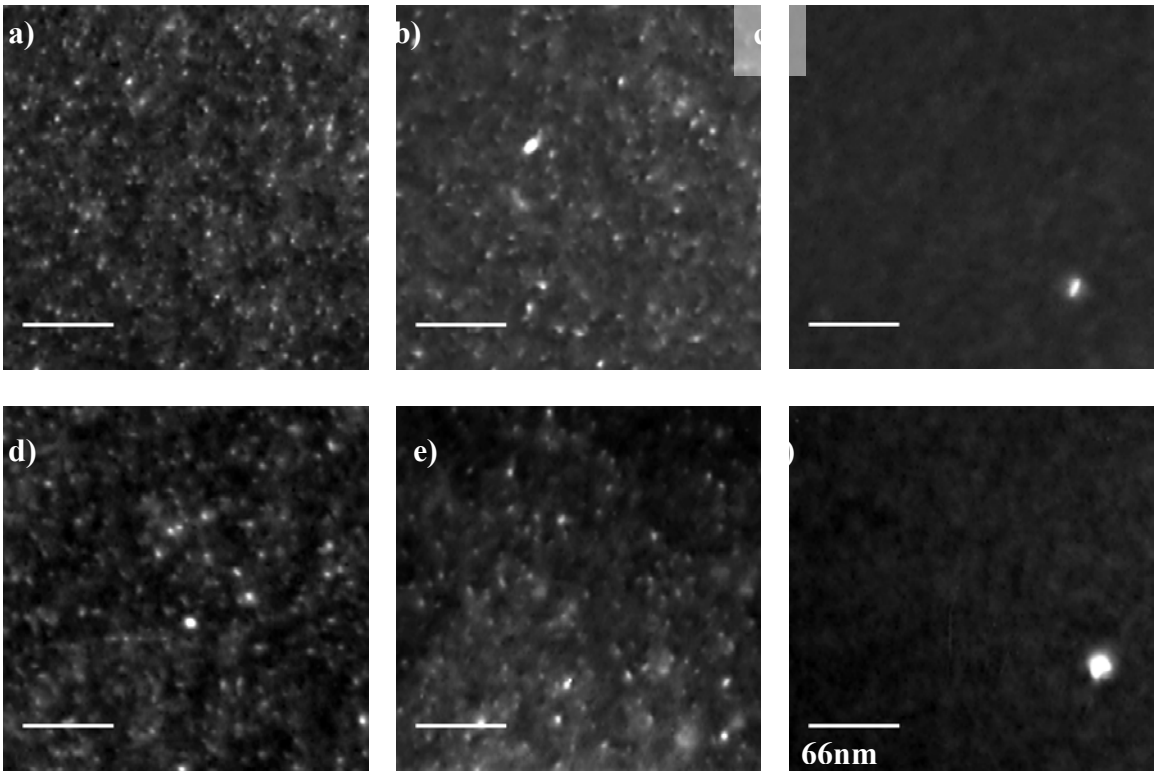

Figure D-3. WBDF PTEM images of the EOR defects imaged under g_{220} two-beam conditions of the 8keV germanium preamorphizing implant, which were subjected to a 450°C 8hr 30min low temperature furnace anneal and flash anneals. a)700°C iRTP, b) 700°C iRTP, 1100°C fRTP and c) 700°C iRTP, 1300°C fRTP. Also a 500°C for 30minutes low temperature furnace anneal and d)700°C iRTP, e) 700°C iRTP, 1100°C fRTP and f) 700°C iRTP, 1300°C fRTP

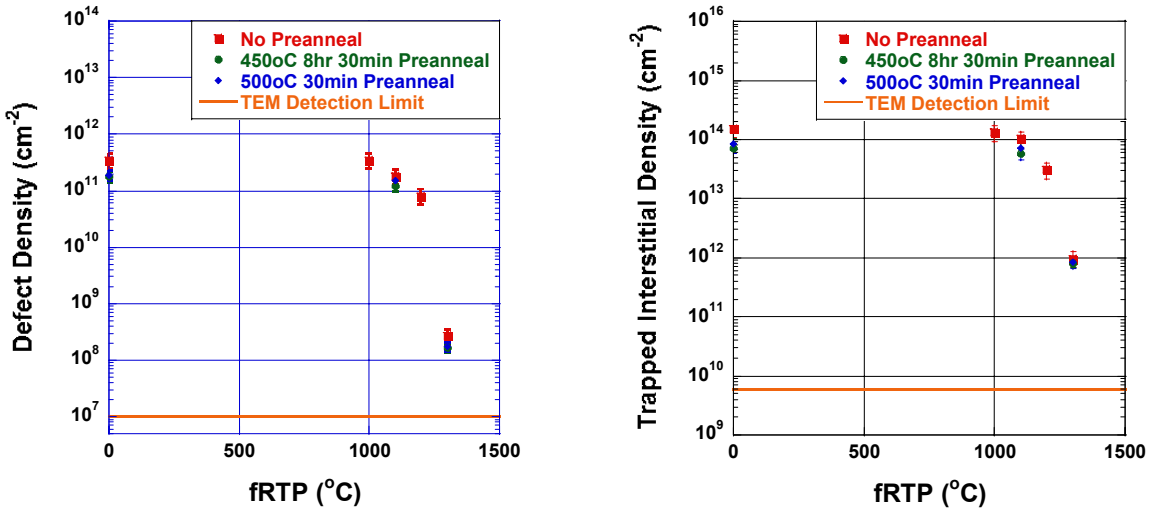

a) b)

Figure D-4. Defect density and trapped interstitial density as a function of fRTP anneal temperature for a $1x10^{15}cm^{-2}$, 8kev Ge PAI for samples which were subjected to two stage anneal process comprising a 450oC 8hr 30min or a 500°C 30min furnace anneal and Flash-assist RTP anneals at 700°C iRTP, 700°C iRTP/1100oC fRTP and 700°C/1300°C fRTP temperatures. The experimental control (no Preanneal) is also shown. a) Defect density and b) Trapped interstitial density.

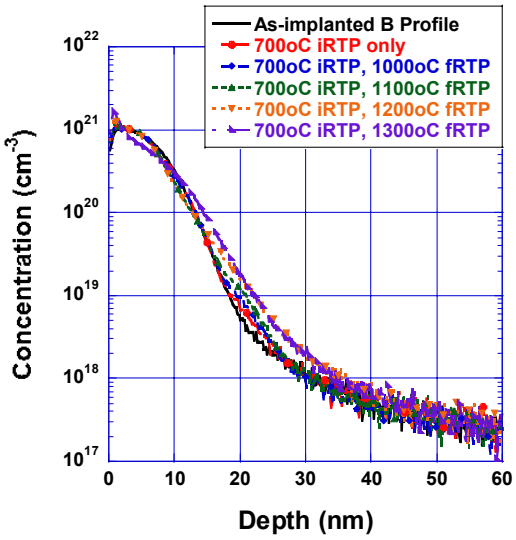

a)

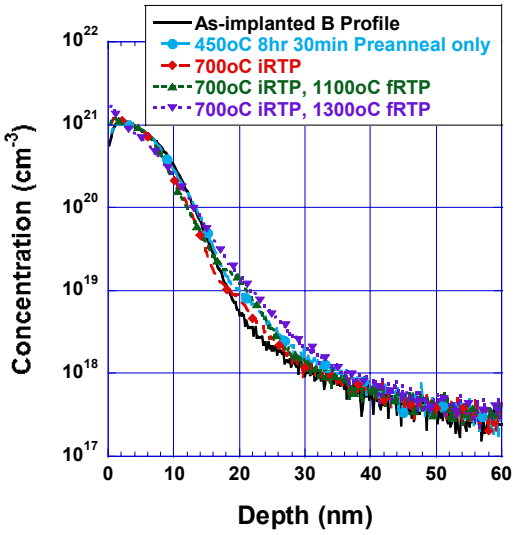

b)

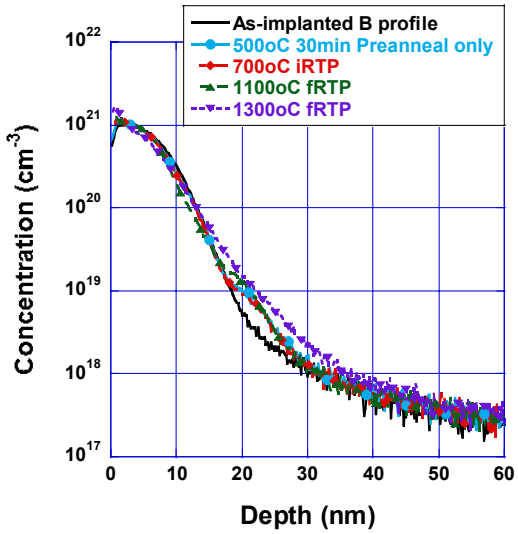

c)

Figure D-5. Concentration-depth profiles of the diffused 1keV $1x10^{15}cm^{-2}$ B implant processed by Flash-assist RTP for the $1x10^{15}cm^{-2}$, 8keV germanium preamorphizing implant for samples which were preannealed at 450 and 500°C and subsequently flash annealed, obtained from SIMS analyses. a) Flash-assist RTP anneals only b) 450°C 8hr 30min Furnace anneal and Flash-assist RTP anneals c) 500°C 30min Furnace anneal and Flash-assist RTP anneals.

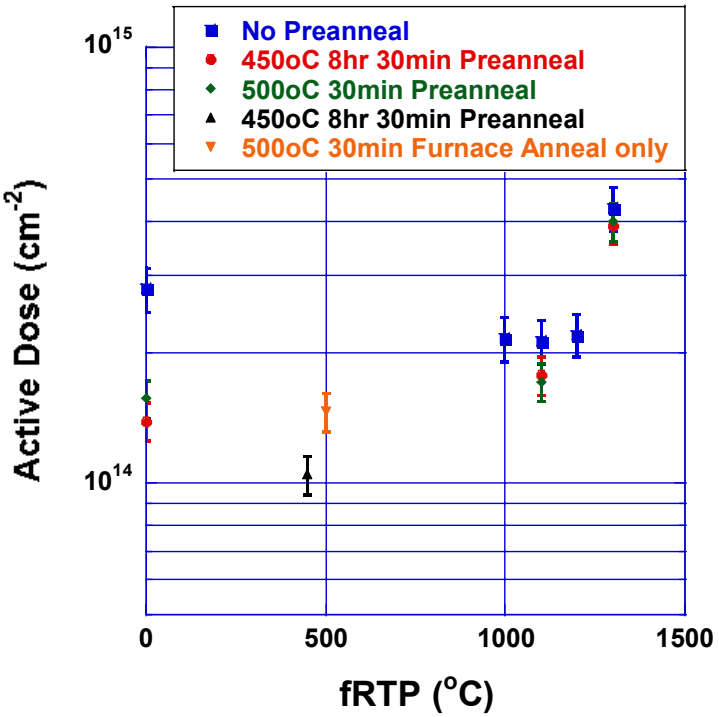

Figure D-6. Active dose as a function of the fRTP anneal temperature of a 1keV $1x10^{15}cm^{-2}$ boron implant, into an amorphous layer formed by an 8keV $1x10^{15}cm^{-2}$ germanium implant. The samples were pre-annealed at 450°C for 8hr 30min or at 500°C for 30min and processed by Flash-assist RTP at 700, 1100, and 1300°C. The active doses obtained for the experimental control are also depicted for 700, 1000, 1100, 1200 and 1300°C.

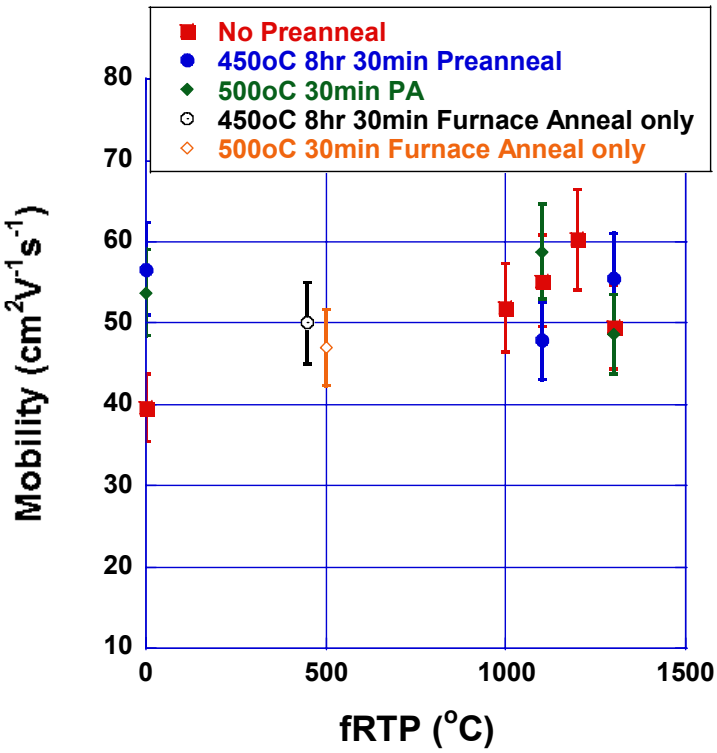

Figure D-7. Carrier mobility as a function of the fRTP anneal temperature of a 1keV $1x10^{15}cm^{-2}$ boron implant, into an amorphous layer formed by a 8keV $1x10^{15}cm^{-2}$ germanium implant. The samples pre-annealed at 450°C for 8hr 30min or at 500°C for 30min and processed by Flash-assist RTP at 700, 1100, and 1300°C. The carrier mobility obtained for the experimental control is also depicted for 700, 1000, 1100, 1200 and 1300°C.

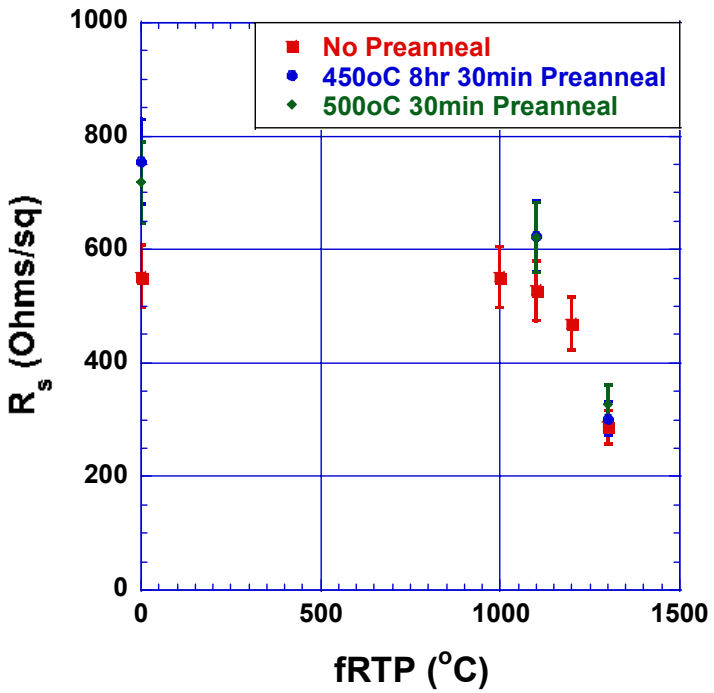

Figure D-8. Sheet resistance, R_s of a $1x10^{15}cm^{-2}$, 1keV boron implant into an amorphous layer formed by a $1x10^{15}cm^{-2}$, 30keV germanium implant, as a function of the fRTP anneal temperature. Indicated are the R_s values for samples which were preannealed at 450°C for 8hr 30min or at 500°C for 30min prior to the Flash-assist RTP anneals and those samples which were annealed by Flash-assist RTP only.

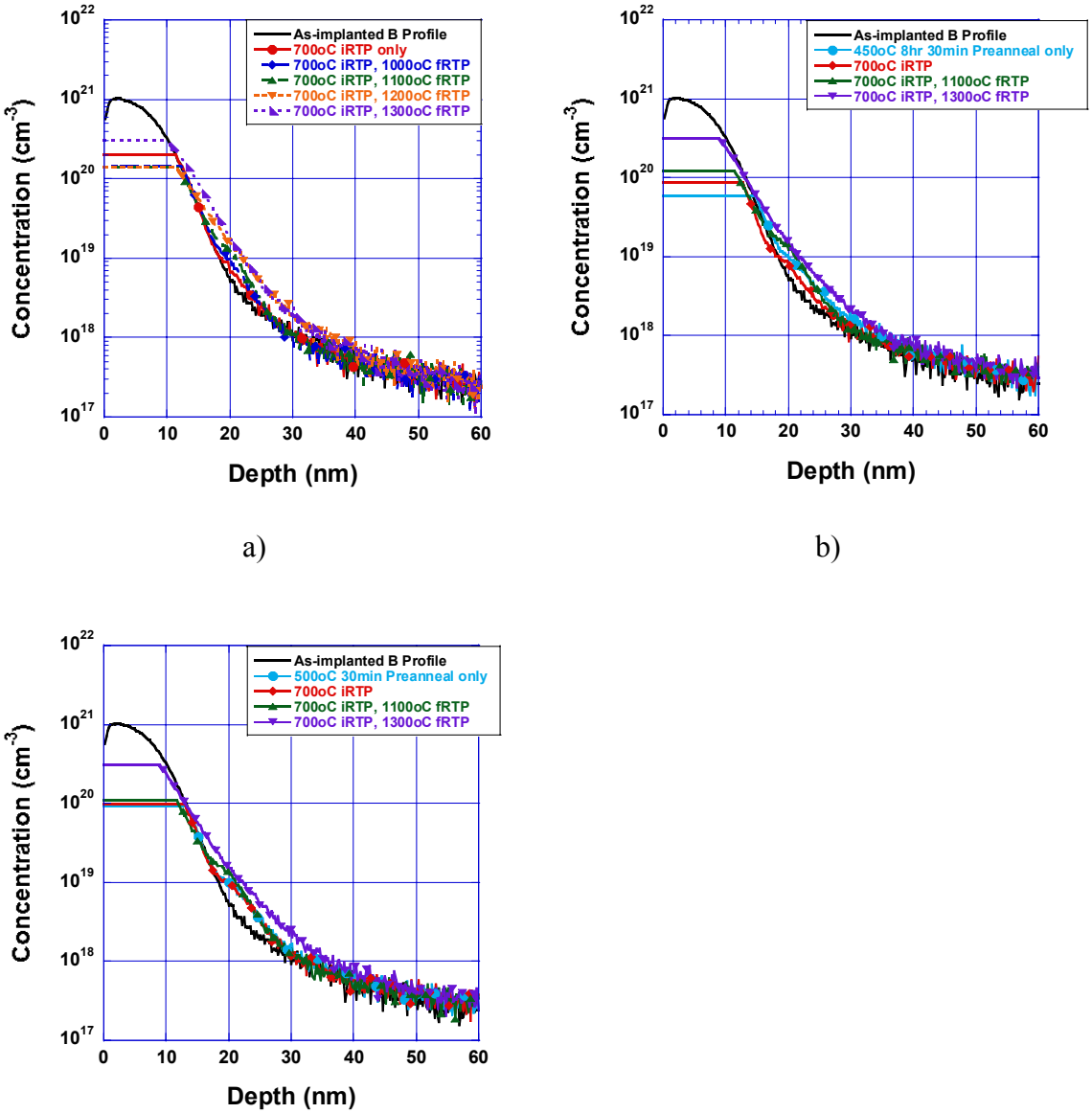

Figure D-9. Active portions of the SIMS boron profile, determined by matching the integrated area below the concentration curve to the active boron dose obtained from the Hall measurement for a $1x10^{15}cm^{-2}$ 8keV germanium preamorphizing implant. Samples were subjected to low temperature preanneals at 450°C for 8hr 30min and 500°C for 30min. a) No Preanneal (expt'l control b) 450°C 8hr 30min Preanneal c) 500°C 30min Preanneal. Peak active concentrations are also highlighted for each anneal.

D.2 Results for the 30 keV Ge PAI

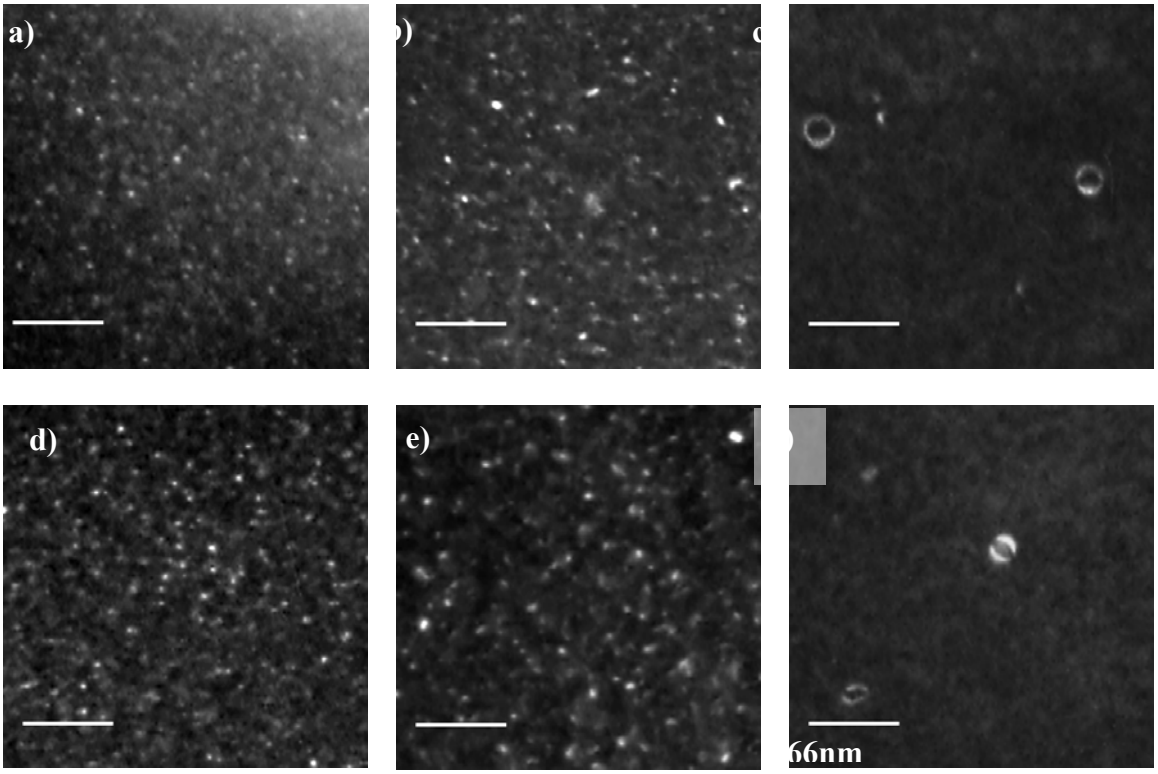

Figure D-10. WBDF PTEM images of the EOR defects imaged under g_{220} two-beam conditions of the 30keV germanium preamorphizing implant, which were subjected to a 450°C 8hr 30min low temperature furnace anneal and subsequently flash annealed. a)700°C iRTP, b) 700°C iRTP, 1100°C fRTP and c) 700°C iRTP, 1300°C fRTP. Also a 500°C for 30minutes low temperature furnace anneal and d)700°C iRTP, e) 700°C iRTP, 1100°C fRTP and f) 700°C iRTP, 1300°C fRTP

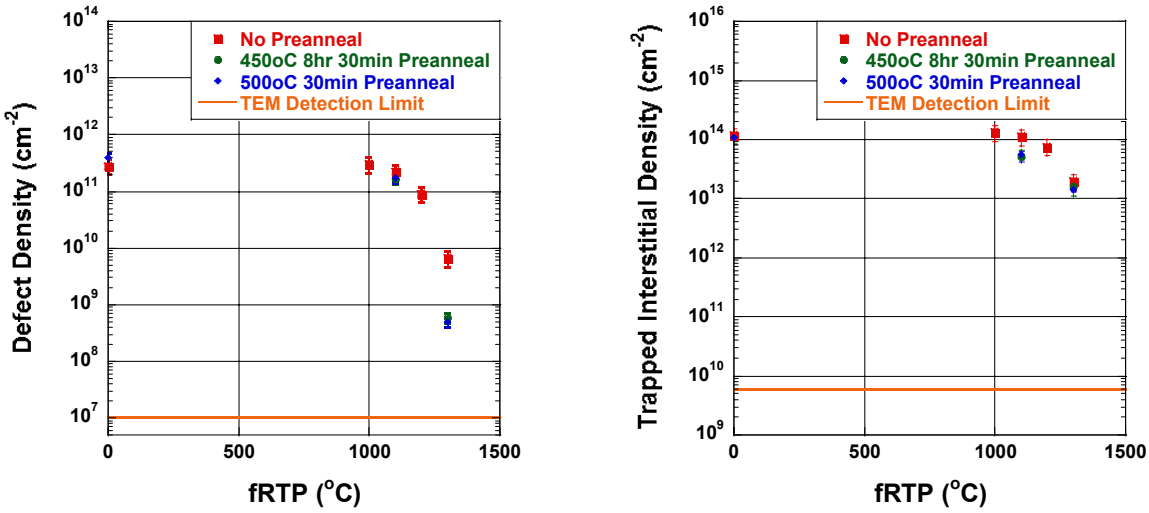

a) b)

Figure D-11. Defect density and trapped interstitial density as a function of fRTP anneal temperature for a $1x10^{15}cm^{-2}$, 8kev germanium preamorphizing implant for samples which were subjected to two stage anneal process comprising a 450°C 8hr 30min or a 500°C 30min furnace anneal and Flash-assist RTP anneals at 700°C iRTP, 700°C iRTP/1100°C fRTP and 700°C/1300°C fRTP temperatures. The experimental control (no Preanneal) is also shown. a) Defect density and b) Trapped interstitial density.

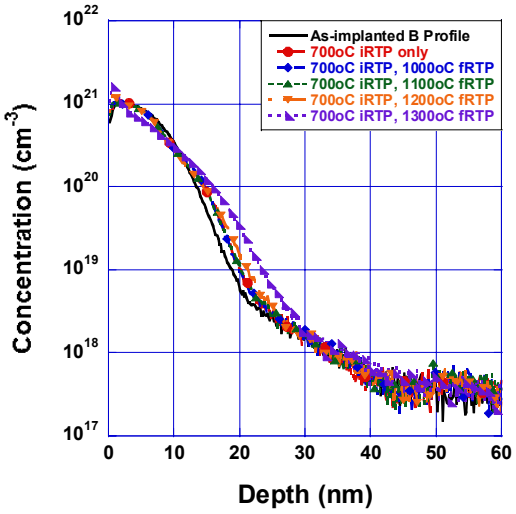

a)

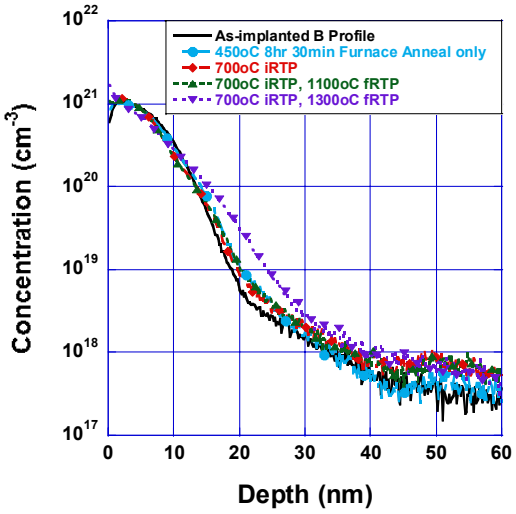

b)

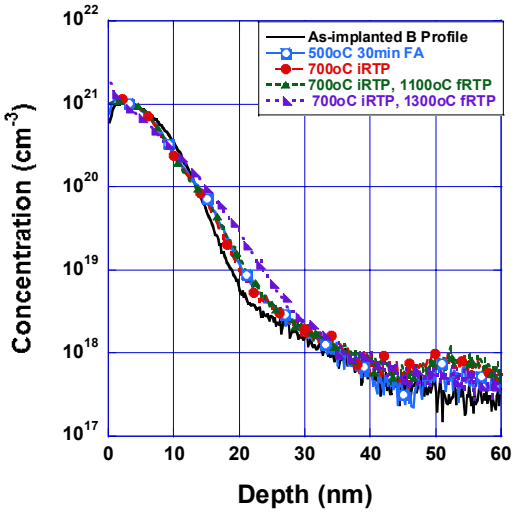

c)

Figure D-12. Concentration-depth profiles of the diffused 1keV $1x10^{15}cm^{-3}$ boron implant processed by Flash-assist RTP for the $1x10^{15}cm^{-3}$, 30keV germanium preamorphizing implant obtained from SIMS analyses, which were preannealed at 450 and 500°C. a) Flash-assist RTP anneals only b) 450°C 8hr 30min Furnace anneal and Flash-assist RTP anneals c) 500°C 30min Furnace anneal and Flash-assist RTP anneals.

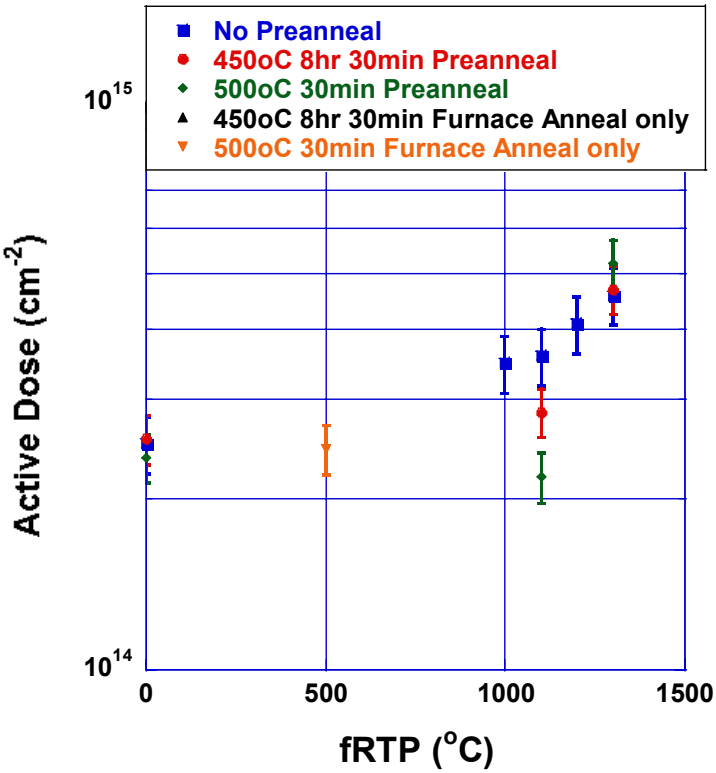

Figure D-13. Active dose as a function of the fRTP anneal temperature of a 1keV $1x10^{15}cm^{-2}$ boron implant, into an amorphous layer formed by an 30keV $1x10^{15}cm^{-2}$ germanium implant. The samples were pre-annealed at 450°C for 8hr 30min or at 500°C for 30min and processed by Flash-assist RTP at 700, 1100, and 1300°C. The active doses obtained for the experimental control are also depicted for 700, 1000, 1100, 1200 and 1300°C.

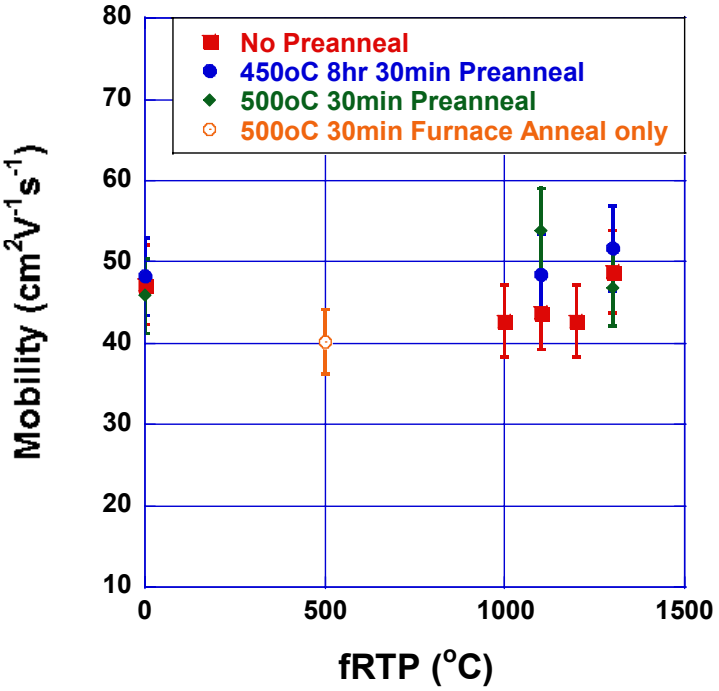

Figure D-14. Carrier mobility as a function of the fRTP anneal temperature of a 1keV $1x10^{15}cm^{-2}$ boron implant, into an amorphous layer formed by a 30keV $1x10^{15}cm^{-2}$ germanium implant. The samples pre-annealed at 450°C for 8hr 30min or at 500°C for 30min and processed by Flash-assist RTP at 700, 1100, and 1300°C. The carrier mobility obtained for the experimental control is also depicted for 700, 1000, 1100, 1200 and 1300°C.

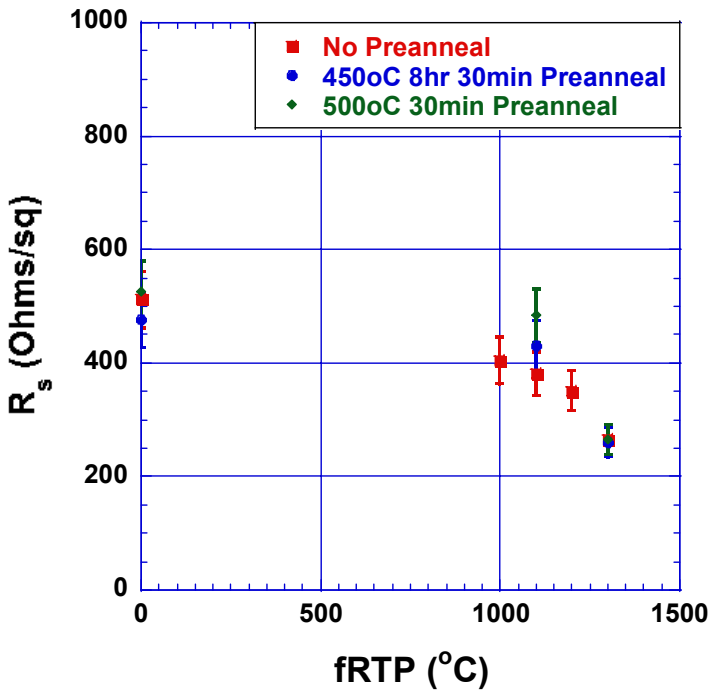

Figure D-15. Sheet resistance, R_s of a $1x10^{15}cm^{-2}$, 1keV boron implant into an amorphous layer formed by a $1x10^{15}cm^{-2}$, 30keV germanium implant, as a function of the fRTP anneal temperature. Indicated are the R_s values for samples which were preannealed at 450°C for 8hr 30min or at 500°C for 30min prior to the Flash-assist RTP anneals and those samples which were annealed by Flash-assist RTP only.

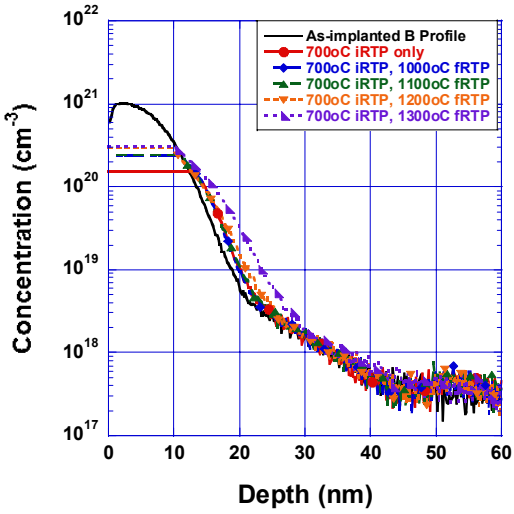

a)

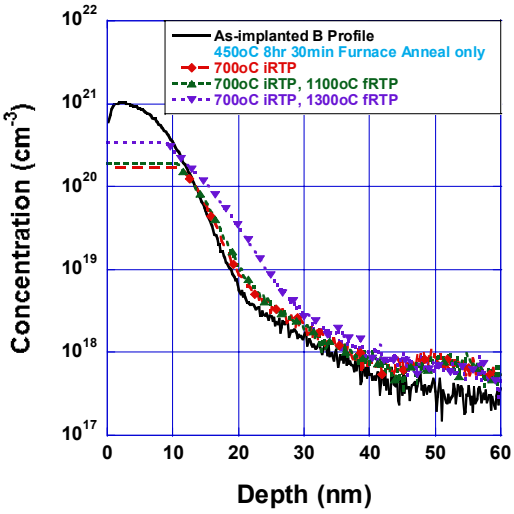

b)

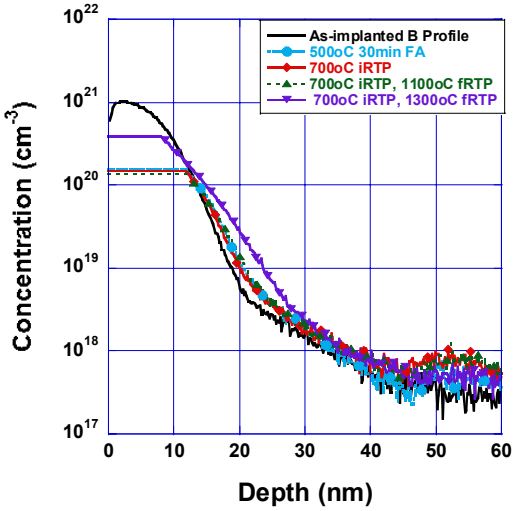

c)

Figure D-16. Active portions of the SIMS boron profile, determined by matching the integrated area below the curve to the active boron dose obtained from the Hall measurement for a $1x10^{15}cm^{-2}$ 30keVgermanium preamorphizing implant. a) No Preanneal (expt'l control b) $450^{o}C$ 8hr 30min Preanneal c) $500^{o}C$ 30min Preanneal. Peak active concentrations are also highlighted for each anneal.

APPENDIX E
THERMAL STABILITY STUDY

E.1 8keV Germanium Preamorphizing Implant

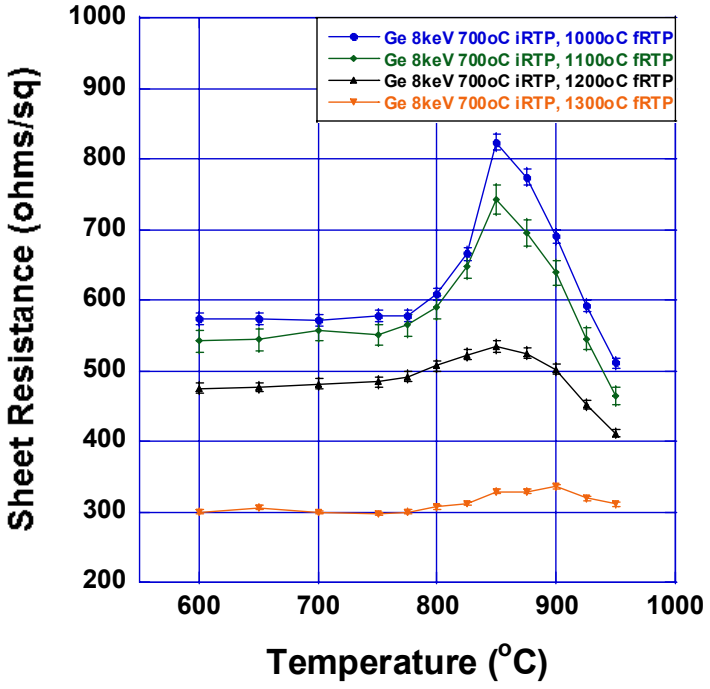

Figure E-1. Sheet resistance versus anneal temperature for a 1keV, $1x10^{15}cm^{-2}$ boron implant into Si (100) preamorphized with 8keV, $1x10^{15}cm^{-2}$ germanium implant. All anneals were performed in a Total Fab Solutions Heatpulse 610 Rapid Thermal Processing (RTP) System for 1 minute.

E.2 30keV Germanium Preamorphizing Implant

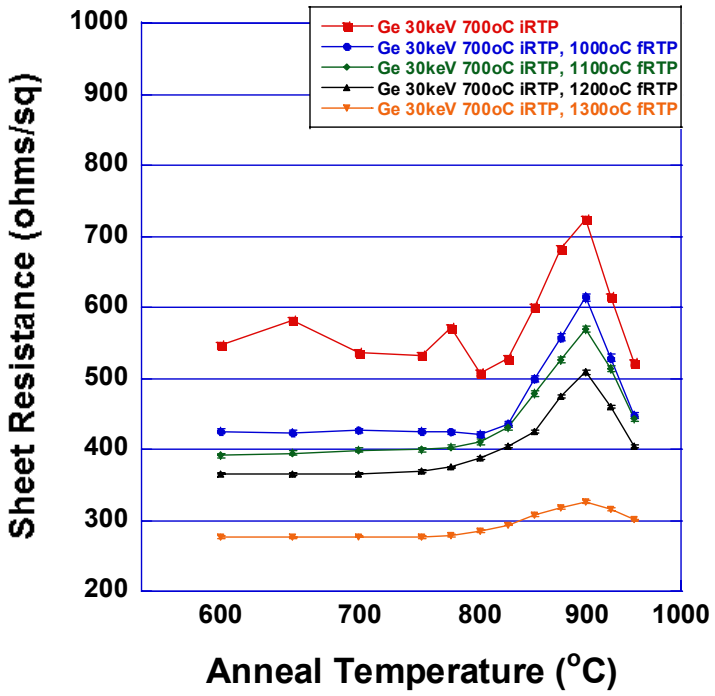

Figure E-2. Sheet resistance versus anneal temperature for a 1keV, $1x10^{15}cm^{-2}$ B implant into Si (100) preamorphized with 30keV, $1x10^{15}cm^{-2}$ germanium implant. All anneals were performed in a Total Fab Solutions Heatpulse 610 Rapid Thermal Processing (RTP) System for 1 minute.

.

LIST OF REFERENCES

[ADE03] J. Adey, J. P. Goss, R. Jones, and P. R. Briddon, Phys. Rev. B 67, 245325-1 (2003).

[ADE88a] W.O. Adekoya, M. Hage-Ali, J.C. Muller and P. Siffert, Appl. Phys. Lett. 53(6), 511 (1988)

[ADE88b] W.O. Adekoya, M. Hage-Ali, J.C. Muller and P. Siffert, Amer. Inst. Phys., 53(6), 511 (1988)

[AGA99] A. Agarwal, H.-J. Gossmann, and A. T. Fiory, J. Electron. Mater., 28, 1333 (1999).

[ALB00] A. Al-Bayati, IIT-2000, (Alpbach, Austria, 2000), p.54

[ANG86] R. P. Angelucci, P. Negrini, and S. Solmi, Appl. Phys. Lett. 49(21), 1468 (1986).

[ANG87] R. Angelucci, F. Cembali, P. Negrini, M. Servidori, and S. Solmi, J. Electrochem. Soc. 134, 3130 (1987).

[ARA97] N. Arai, S. Takeda, and M. Kohyama, Phys. Rev. Lett. 78, 4265 (1997).

[AVC02] I. Avci, Ph.D. Dissertation, University of Florida, Gainesville, FL (2002).

[BEN05] N.S. Bennett, Author, A.J. Smith, B. Colombeau, R. Gwilliam, N.E.B. Cowern and B.J. Sealy, Mat. Sci. Eng. B. 124/125, 305 (2005).

[BEN97] J.L. Benton, S. Libertino, P. Kringhoj, D. J. Eaglesham and J. M. Poate, J. Appl. Phys. 82 (1), 120 (1997).

[BEN97] J.L. Benton, S. Libertino, P. Kringoi, D. J. Eaglesham, J. M. Poate, and S. Coffa, J. Appl. Phys. 82, 120 (1997).

[BEN98] J.L. Benton, K. Halliburton, S. Libertino, D. J. Eaglesham and S. Coffa, J.Appl. Phys. 84 (9), 4749 (1998)

[BHA97] S. Bharatan, J. Desrouches, and K. S. Jones, *Materials and Process Characterization of Ion Implantation Volume 4*, (Ion Beam Press, Austin, TX, 1997), p. 222

[BLO79] P. Blood, W. L. Brown, and G. L. Miller, J. Appl. Phys. 50, 173 (1979).

[BON96] C. Bonafos, D. Alquier, A. Martinez, D. Mathiot and A. Claverie, Nucl. Instr. Meth. Phys. Res. B 112(1-4), 129 (1996).

[BON97a] C. Bonafos, M. Omri, B. de Mauduit, G. BenAssayag, A. Claverie, D. Alquier A. Martinez and D. Mathiot, J. Appl. Phys. 82, 2855 (1997).

[BON97b] C. Bonafos, A. Claverie, D. Alquier, C. Bergaud, A. Martinez, L. Laanab and D. Mathiot, Appl. Phys. Lett. 71(3), 365 (1997)

[BON98] C. Bonafos, D. Mathiot and A. Claverie, J. Appl. Phys. 83(6), 3008 (1998).

[BOR01] J.O. Borland, Mat. Res. Soc. Proc. 717, C1.1.1 (2001)

[BRA99] H. Bracht, E.E. Haller and R. Clark-Phelps, Phys. Rev. Lett. 81(2), 393, (1998).

[BRO69] M. H. Brodsky, R.S. Title, K.Weisser and G.D. Pettit, Phys. Rev. B1, 2632 (1969)

[BRU92] C. R. Brundle, C. A. Evans, Jr., and S. Wilson, *Encyclopedia of Materials Characterization*, (Butterworth-Heinemann, Boston, MA, 1992) pp. 40-41.

[CAL89] L. Calcagno, S. U. Campisano, and S. Coffa, J. Appl. Phys. 66, 1874 (1989).

[CAM02] R. A. Camillo-Castillo, K.S. Jones, M.E. Law and L.M. Rubin, Mat. Res. Soc. Proc. 717, C1.4.1 (2002).

[CAM04] R. A. Camillo-Castillo, M. E. Law and K. S. Jones, J. Appl. Phys. 96, 4939 (2004).

[CAM80] S. U. Campisano, G. Foti, P. Baeri, M. G. Grimaldi, and E. Rimini, Appl. Phys. Lett. 37, 719 (1980).

[CAM94] D. M. Camm, B. Lojek, Proc. 2nd Int. Conf. Advanced Thermal Processing of Semiconductors (RTP, Round Rock, TX 1994), p.259.

[CAT98] M. J. Caturla, M. D. Johnson and T. D. de la Rubia, Appl. Phys. Lett. 72, 2736 (1998).

[CHA96] H.S. Chao, S.W. Crowder, P.B. Griffin and J.D. Plummer, J. Appl. Phys., 79, 2352 (1996).

[CHE99] P.-S. Chen, T. E. Hsieh, Y.-C. Hwang and C.-H. Chu, J. Appl. Phys. 86, 5399 (1999).

[CHI02] M. P. Chichkine, M. M. De Souza, and E. M. Sankara Narayanan, Phys. Rev. Lett. 88, 085501 (2002).

[CHO85] K. Cho, M. Numan. T. Finstad, W.Chu, J. Liu and J. Wortman, Appl. Phys. Lett. , 47, 1321 (1985).

[CHR81] L.A. Christel, J. F. Gibbons and T. W. Sigmon, J. Appl. Phys. 52, 7143 (1981).

[CLA00] A. Claverie, B. Colombeau, G.B. Assayag, C.Bonafos, F. Cristiano, M. Omri and B. de Mauduit, Mat. Sci. Semi. Proc. 3, 269 (2000).

[CLA01] A. Claverie, B. Colombeau, F. Cristiano, A. Altibelli and C. Bonafos, Mat. Res. Soc. Proc., 669, J9.4 (2001).

[CLA02] A. Claverie, B. Colombeau, F. Cristiano, A. Altibelli and C. Bonafos, Nucl. Instr. Meth. Phys. Res. B 186 (1-4), 281 (2002).

[CLA03] A. Claverie, B. Colombeau, B. De Mauduit, C. Bonafos, X. Hebras, G. Ben Assayag, and F. Cristiano, Appl. Phys. A 76, 1025 (2003).

[CLA04] M.H. Clark, PhD Dissertation, University of Florida, Gainesville, FL (2004).

[CLA95] A. Claverie, L.Laanad, C. Bonafas, C. Bergaud, A. Martinez and D. Mathiot, Nucl. Instr. Meth. Phys. Res. B. 96, 202 (1995).

[CLA97] A. Claverie, C. Bonafos, M. Omri, B. De Mauduit, G. Ben Assayag, D. Alquier, A. Martinez and D. Mathiot, Mat. Res. Soc. Proc. 438, 3, (1997).

[COF00] S. Coffa, S. Libertino and C. Spinella, Appl. Phys. Lett, 76(3), 321 (2000).

[COF92] S. Coffa, J. M. Poate, D. C. Jacobson, W. Frank, and W. Gustin, Phys. Rev. B 45, 8355 (1992).

[COF97] S. Coffa, V. Privitera, F. Priolo, S. Libertino, and G. Mannino, J. Appl. Phys. 81, 1639 (1997).

[COW90] N.E. B. Cowern, J.T.F. Janssen and H.F.F. Jos, J. Appl. Phys. 68, 6191 (1990).

[COW94] N.E.B. Cowern, G.F.A. Van de Walle, P.C. Zalm and D.E.W. Vandenhout, Appl. Phys. Lett, 65, 2981 (1994).

[COW94] N. E. B. Cowern, Appl. Phys. Lett. 64(20), 2646 (1994).

[COW99a] N.E.B. Cowern, G. Mannino, P. A. Stolk, F. Roozeboom, H. G. A. Huizing, J. G. M. van Berkum, F. Cristiano, A. Claverie and M. Jaraı´z, Phys. Rev. Letts. 82 (22), 4460 (1999).

[COW99b] N.E. B. Cowern, M. Jaraiz, F. Cristiano, A. Claverie and G. Mannino, Tech. Dig. Int. Elec. Dev. Meet. 333 (1999).

[CSE75] L. Csepregi and J. W. Mayer. Phys. Letts., 54A (2), 157 (1975)

[CSE76] L. Csepregi, J. W. Mayer and T.W. Sigmon. Appl. Phys. Lett., 29(2), 92 (1976)

[CSE77] L. Csepregi, E.F. Kennedy, T.J. Gallagher and J.W. Mayer, J. Appl. Phys. 48(10), 4234 (1977).

[CSE78] L. Csepregi, E.F. Kennedy, J.W. Mayer and T.W. Sigmon. J. Appl. Phys., 49(7), 3906 (1978).

[DEA73] G. Dearnaley, J. H. Freeman, R. S. Nelson and J. Stephen, Ion Implantation (1973).

[DEM90] B. de Mauduit, L. Laanab, C. Bergaud, M.M. Faye, A. Martinez and A. Claverie, Nucl. Instr. Meth. Phys. Res. B84, 190 (1990).

[DES00] M.M. De Souza, M.P. Chichkine and E.M. Sankara Narayanan, Mat. Res. Soc. Proc. No. 610, B11.3.1, (2000).

[DES05a] D. De Salvador, E. Napolitani, G. Bisognin, A. Carnera, E. Bruno, S. Mirabella, G. Impellizzeri, and F. Priolo, Appl. Phys. Lett. 87, 221902 (2005).

[DES05b] D. De Salvador, E. Napolitani, G. Bisognin, A. Carnera, E. Bruno, S. Mirabella, G. Impellizzeri, and F. Priolo, Mat. Sci. Eng. B 124–125 (2005).

[DRO78] R. Drosd and J. Washburn, J. Appl. Phys., 51, 1656 (1978)

[DRO82] R. Drosd and J. Washburn, J. Appl. Phys. 53, 397 (1982).

[DUF03] R. Duffy, V. C. Venezia, A. Heringa, T. W. T. Hu¨sken, M. J. P. Hopstaken, N. E. B. Cowern, P. B. Griffin and C. C. Wang, Appl. Phys. Lett. 82 (21), 3647 (2003).

[DUF04] R. Duffy, V. C. Venezia, A. Heringa, B. J. Pawlak, M. J. P. Hopstaken, G. C. J. Maas, Y. Tamminga, T. Dao, F. Roozeboom and L. Pelaz, Appl. Phys. Lett. 84 (21), 4283 (2004).

[EAG94] D.J. Eaglesham, P. A. Stolk, H.-J. Gossmann and J. M. Poate, Appl. Phys. Lett. 65 (18) (1994).

[EAG95a] D. J. Eaglesham, P.A. Stolk, H-J. Grossman, T.E. Haynes and J. M. Poate, Nucl. Inst. Meth. Phys. Res.106, 191 (1995).

[EAG95B] D. J. Eaglesham, P.A. Stolk, J-Y Cheng, H-J. Grossman, T.E. Haynes and J. M. Poate, Inst. Phys. Conf. Ser. No.146, 451 (1995).

[EAG96] D. J. Eaglesham, A. Agrawal, T.E. Haynes, H-J. Grossman, D. C. Jacobson and J. M. Poate, Nucl. Inst. Meth. Phys. Res.120,1 (1996).

[ELL85] R. G. Elliman, J. M. Gibson, D. C. Jacobson, J. M. Poate, and J. S. Williams, Appl. Phys. Lett. **46**, 478 (1985).

[ELL87a] R. G. Elliman, J. S.Williams, S. T. Johnson and E. Nygren, Mat. Res. Soc. Proc. 74, 471 (1987)

[ELL87b] R. G. Elliman, J. S.Williams, W. L. Brown, A. Leiberich, D. M. Mayer and R. V. Knoel, Nucl. Instr. Meth. Phys. Res. B. B19/20, 435 (1987)

[ELL98] R. G. Elliman, S. M. Hogg, and P. Kringhøj, 1998 Intl. Conf. on Ion Imp. Tech. Proc., 1055 (1998).

[FAH89] P. M. Fahey, P. B. Griffin, and J. D. Plummer, Rev. Mod. Phys. 61, 289 (1989).

[FAI81] R. B. Fair, *Impurity Doping Processes in Silicon*, edited by F. F. Y. Wang, (North-Holland, New York, 1981), 315.

[FAI84] R. B. Fair, J.J. Wortman and J. Liu, J. Electrochem. Soc. 131, 2387 (1984).

[FAI90] R. Fair, J. Electrochem. Soc. 137, 667 (1990).

[FAU62] J. Faust and H. John, J. Phys. Chem. Coll. 23, 1119 (1962)

[FEL00] S.B. Felch, S. Talwar, C. Gelatos, Y. Wang, D.F. Downey and E.A. Arevalo, Ion Implant Technology 2000, IEEE (2000).

[FIO99] A.T. Fiory and K.K. Bourdelle, Appl. Phys. Lett. 74(18), 2658 (1999).

[GAB04] K.A.Gable, PhD Dissertation, University of Florida, Gainesville, Fl. (2004).

[GAN89] E. Ganin and A. Marwick, *Ion Beam Processing of Advanced Electronic Materials*, (Materials Research Society, Pittsburgh, PA, 1989), Mat. Res. Soc. Proc. 147, 13, (1989).

[GIB77] J.F. Gibbons, Lectures on Ion Implantation and Proton Enhanced Diffusion, Univ. of Tokyo, Tokyo, Japan (Jap. Soc. Appl. Phys.) (1977).

[GIL91] M.D. Giles, J. Electrochem. Soc., 138, 1160 (1991).

[GIL95] G. H. Gilmer, T. Diaz de la Rubia, D. M. Stock and M. Jaraiz, Nucl. Instr. Meth. Phys. Res. B 102, 247 (1995).

[GIL99] L. F. Giles, M. Omri, B. de Mauduit, A. Claverie, D. Skarlatos, D. Tsoukalas, and A. Nejim, Nucl. Instr. and Meth. B 148, 273 (1999).

[GOE96] U. Go¨sele, A. Plo¨ssl, and T. Y. Tan, Process Phys. Model. Semi. Tech. edited by G. R. Srinivasan, C. S. Murthy and S. T. Dunham, Electrochem. Soc., Pennington, NJ, 309 (1996).

[GRI87] P.B. Griffin, S.T. Ahn, W.A. Tiller and J.D. Plummer, Appl. Phys. Lett. 51(2), 115 (1987).

[GRI93] P.B. Griffin, R.F. Lever, R.Y.S. Huang, H.W. Kennel, P.A. Packan. J.D. Plummer, Tech. Dig. Int. Elec. Dev. Meet., 295 (1993).

[GUT01] A.F. Gutierrez, M.S. Thesis, University of Florida, Gainesville (2001).

[HAD00] Y.M. Haddara, B.T. Folmer, M.E. Law and T Buyuklimanli, Appl. Phys. Lett., 77(13), 1976 (2000).

[HOD84] R.T. Hodgson, V. Deline, S.M. Mader, F.F. Morehead and J.C. Gelpey, Appl. Phys. Lett. 44, 589 (1984).

[HOF73] W.K. Hofker, H. W. Werner, D.P. Oosthoek and H.A.M. de-Grefte, Appl. Phys. 2, 265 (1973).

[HOF74] W. K. Hofker, H. W. Werner, D. P. Oosthoek, and N. J. Koeman, Appl. Phys. Lett. 4, 125 (1974).

[HUA99] M. B. Huang and I. V. Mitchell, J. Appl. Phys. 85, 174 (1999).

[HUI96] H.G.A. Huizing, C. C. G. Visser, N.E.B. Cowern, P.A. Stolk and R.C. M. de Kruif, Appl. Phys. Lett. 69(9), 1211 (1996).

[HWA03] G. S. Hwang and W. A. Goddard, Appl. Phys. Lett. 83, 1047 (2003).

[JAC05] J. Jacques, PhD. Dissertation, University of Florida, Gainesville, FL (2005).

[JAG87] K. Jagannadham and J. Narayan, J. Appl. Phys. 62, 1694 (1987).

[JAI02] S.C. Jain, W. Schoenmaker, R. Linsday, P.A. Stolk, S. Decoutere and H.E. Maes, Appl. Phys. Revs. 91, 8918 (2002).

[JAI04] S. H. Jain, P. B. Griffin, J. D. Plummer, S. McCoy, J. Gelpey, T. Selinger, and D. F. Downey, J. Appl. Phys. 96, 7357 (2004).

[JAS99] C. Jasper, A. Hoover and K.S. Jones, Appl. Phys. Lett., 75(17), 25 (1999).

[JON88] K.S. Jones, S. Prussin and E. R. Weber, Appl. Phys. A 45, 1 (1988).

[JON91] K.S. Jones and D. Venables, J. Appl. Phys., 69(5) (1991).

[JON93] K.S. Jones and G.A. Rozgonyi, *Rapid Thermal Processing Science and Technology*, 5, 123 (Academic Press, 1993).

[JON96] K. S. Jones, R. G. Elliman, M. M. Petravic, and P. Kringhøj. Appl. Phys. Lett. 68, 3111 (1996)

[JON96] K.S. Jones, V. Krishnamoorthy, L.H. Zhang, M. Law, D.S. Simmons, P.H. Rubin and R.G. Elliman, Appl. Phys. Lett., 68, 2672 (1996).

[JON97] K.S. Jones, K. Moller, J. Chen and M. Puga-Lambers, IEEE Proc. Ion Impl. Tech. Conf., 96, 618 (1997).

[JUN03] M.Y. Jung, L., R. Gunawan, R. D. Braatz, and E. G. Seebauer, J. Elec. Soc., 150 (12), (2002).

[KER84] H. Kerkow, G. Kreysch and B. Lukasch. Phys. Stat. Sol. 82, 125 (1984)

[KEY01] P. Keys, PhD. Dissertation, University of Florida, Gainesville, FL (2001).

[KIM89] J. Kim, J. W. Wilkins, F. S. Khan, and A. Canning, Phys. Rev. B 40, 10351 (1989).

[KIN03a] A.C. King, A. F. Gutierrez, A. F. Saavedra, K. S. Jones and D. F. Downey, J. Appl. Phys. 93(5), 2449 (2003).

[KIN03b] A.C. King, M.S. Thesis, University of Florida, Gainesville FL (2003).

[KLA92] D.B.M. Klaasse, Solid-State Electronics 35(7), 953 (1992)

[KOY99] M. Kohyama and S.Takeda, Phys. Rev. B 60 (11), 8075 (1999)

[LAN93] L. Laanab, C. Bergaud, M.M. Faye, A. Martinez and A. Claverie, Mat. Res. Soc. Proc. 279, 381 (1993).

[LAN95] L. Laânab, C. Bergaud, C. Bonafos, A. Martinez, and A. Claverie, Nucl. Inst. Meth. B 96, 236 (1995).

[LAW00] M.E. Law, G.H. Gilmer and M. Jairaz, MRS Bull., June, 45 (2000).

[LAW03] FLOOPS, Mark Law, University of Florida, Electrical and Computer Engineering Department (2003).

[LAW98] M. E. Law, Y. M. Haddara, and K. S. Jones, J. Appl. Phys. 84, 3555 (1998).

[LEF99] M. E. Lefrancois, D. M. Camm, and B. J. Hickson, Proc. 7th Int. Conf. Advanced Thermal Processing of Semiconductors, 93 (1999).

[LEN00] T. J. Lenosky, B. Sadigh, S. K. Theiss, M. J. Caturla, and T. D. de la Rubia, Appl. Phys. Lett. 77, 1834 (2000).

[LI79] S. S. Li, Semiconductor Meas. Tech. 400-47, 1 (1979).

[LIB00] S. Libertino, S. Coffa, C. Spinella, J.L. Benton and D. Arcifa, Mat. Sci. Eng. B17, 137 (2000).

[LIB98] S. Libertino, J. L. Benton, S. Coffa, and D. J. Eaglesham, Mat. Res. Soc. Proc. 504, 3, (1998).

[LIB99] S. Libertino, S. Coffa , J.L. Benton, K. Halliburton and D. J. Eaglesham, Nucl. Inst. Meth. Phys. Res.B 148, 247 (1999).

[LIC86] C. Licoppe and Y. I. Nissim, J. Appl. Phys. 59(2), 432 (1986)

[LIJ98] J. Li and K.S. Jones, Appl. Phys. Lett. 73 (25), (1998).

[LIL02] A.D. Lilak, M. E. Law, L. Radic, K.S. Jones and M. Clark, Appl. Phys. Lett., 81(12) (2002).

[LIL99] A. D. Lilak, S. K. Earles, M. E. Law and K. S. Jones, Appl. Phys. Lett. 74(14), 2038 (1999).

[LIN00] C.D. Lindfors, K. S. Jones., M.E. Law, D.F. Downey and R.W. Murto, Mat. Res. Soc. Proc. 610, B10.2.1 (2000).

[LIN01] C.D. Lindfors , K. S. Jones and M. J. Rendon, Mat. Res. Soc. Proc. 669, J8.5.1 (2001).

[LIN03] C.D. Lindfors, Ph.D. Dissertation, University of Florida, Gainesville, FL (2003).

[LIN81] J.F. Lin, S.S. Li, L.C. Linares and K.W. Teng, Sol.State Elec. 24(9), 827 (1981).

[LIS93] J. K. Listebarger, K. S. Jones, and J. A. Slinkman, J. Appl. Phys. 73, 4815 (1993).

[LIU00] X. Y. Liu, W. Windl, and M. P. Masquelier, Appl. Phys. Lett. 77, 2018 (2000).

[LIU95] J. Liu, M.E.Law and K.S. Jones, Solid State Elec., 38, 1305 (1995).

[LOR91] E. Lorenz, L. Frey, J. Gyulai, H. Ryssel and N.Q. Khanh, J. Mat. Res., 6, 1695 (1991).

[LUO01] W. Luo and P. Clancy, J. Appl. Phys. 89, 1596 (2001).

[MAN00] G. Mannino, N. E. B. Cowern, F. Roozeboom, and J. G. M. van Berkum, Appl. Phys. Lett. 76, 855 (2000).

[MAN01] G. Mannino, P. A. Stolk, N. E. B. Cowern, W. B. de Boer, A. G. Dirks, F. Rooze-boom, J. G. M. van Berkum, P. H. Woerlee, and N. N. Toan, Appl. Phys. Lett., 78, 889, (2001).

[MAN02] G. Mannino, V. Privitera, S. Solmi and N.E.B. Cowern, Nucl. Instr. Meth. Phys. Res. B 186 (2002).

[MAT04] A. Mattoni and L. Colombo, Phys. Rev. B 69, 045204 (2004).

[MAZ86] A.M. Mazzone, Phys. Stat. Sol. A, 95, 149 (1986)

[MIC87] A.E. Michel, W. Rausch, P.A. Ronsheim and R.H. Kastl, Appl. Phys. Lett. 50(7), 416, (1987).

[MIR02] S. Mirabella, A. Coati, D. De Salvador, E. Napolitani, A. Mattoni, G. Bisognin, M. Berti, A. Carnera, A. V. Drigo, S. Scalese, S. Pulvirenti, A. Terrasi, and F. Priolo, Phys. Rev. B., 65(4), 045209 (2002).

[MIR03] S. Mirabella, E. Bruno, F. Priolo, D. De Salvador, E. Napolitani, A. V. Drigo, and A. Carnera, Appl. Phys. Lett., 83(4), 680 (2003).

[MOK02] A. Mokhberi, P. B. Griffin, J. D. Plummer, E. Paton, S. McCoy, and K. Elliot, IEEE Trans. Electron Dev. 49, 1183 (2002).

[MOO65] G. E. Moore, Electronics 38, 114 (1965).

[MOR70] F.F. Morehead and B.L. Crowder, Rad. Eff., 6, 27 (1970).

[NAR82] J. Narayan and O. W. Holland, Phys. Stat. Sol., 78, 225 (1982).

[NAR93] J. Narayan, O.W. Holland and B. R. Appleton, J. Vac. Sci. Technol. B1(4), 871(1993)

[OEH84] G.S. Oehrlein, R. Gbez, J.D. Fehribach, E.F. Gorey, T.O. Sedgwick, S. Cohen and V.R. Deline, Proc. 13th Int. Conf. Defects in Semicond., 593 (1984).

[OLS84] L. Olson, J. A. Roth, L.D. Hess and J. Narayan, Mat. Res. Soc. Proc. 23, 375 (1984)

[OLS85a] G.L. Olson, Mat. Res. Soc. Proc., 35, 25 (1985).

[OLS85b] G.L. Olson, J. A. Roth, Y. Rytz-Froidevaux and J. Narayan, Mat. Res. Soc. Proc., 35, 211 (1985).

[OLS88] G.L. Olson and J. A. Roth, Mat. Sci. Rep. 3, 1-78 (1988).

[OMR96] M. Omri, C. Bonafos, A. Claverie , A. Nejim, F. Cristiano, D. Alquier, A. Martinez and N.E.B. Cowern, Nucl. Instrum. Meth. Phys. Res. B 120, 5 (1996).

[OMR99] M. Omri, L. F. Giles and A. Claverie, Mat. Res. Soc. Proc. 568, 219 (1999).

[PAC90] P.A. Packan and J.D. Plummer, Appl. Phys. Lett. 56 (18), 1787 (1990).

[PAN97] G.Z. Pan, K.N. Tu and A. Prussin, J. Appl. Phys. 71(5), 659, (1997).

[PAU58] L. J. van der Pauw, Philips Res. Repts. 13, 1 (1958).

[PEL97] L. Pelaz, M. Jaraiz, G. H. Gilmer, H. J. Gossmann, C. S. Rafferty, D. J. Eaglesham, and J. M. Poate, Appl. Phys. Lett. 70, 2285 (1997).

[PEL98] L. Pelaz, G.H. Gilmer, M. Jairaz, S.B. Herner, H-J. Gossman, D.J. Eaglesham, G. Hobler, C.S. Rafferty and J. Barbolla, Appl. Phys. Lett., 73(10), 1421 (1998).

[PEL99a] L. Pelaz, G. H. Gilmer, H. –J. Gossmann, C. S. Rafferty, M. Jaraiz and J. Barbolla, Appl. Phys. Lett. 74, 3657 (1999).

[PEL99b] L. Pelaz, V. C. Venezia, H. –J. Gossmann, G. H. Gilmer, A. T. Fiory, C. S. Rafferty, M. Jaraiz and J. Barbolla, Appl. Phys. Lett. 75, 662 (1999).

[PLU00] J.D. Plummer, M.D. Deal and P.B. Griffin, *Silicon VLSI Technology. Fundamentals, Practice and Modeling,* (Prentice Hall, Upper Saddle River, NJ, 2000).

[POA74] J. M. Poate and J.S. Williams, *Ion Implantation and Beam Processing* (Academic Press, New York 1984), p. 27

[POL90] A. Polman, D. C. Jacobson, S. Coffa, J. M. Poate, S. Roorda, and W. C. Sinke, Appl. Phys. Lett. 57, 1230 (1990).

[RAD02] L. Radic, A.D. Lilak, and M.E. Law, Appl. Phys. Lett. 81, 826 (2002).

[RAF96] C.S. Rafferty, G.H. Gilmer, M. Jaraiz, D.J. Eaglesham and H-J. Gossmann, Appl. Phys. Lett., 68, 2395 (1996).

[RAM99a] R. Raman, M. E. Law, V. Krishnamoorthy and K. S. Jones, Appl. Phys. Lett., 74(5), 700 (1999).

[RAM99b] R. Raman, M. E. Law, V. Krishnamoorthy, K. S. Jones and S. B. Herner, Appl. Phys. Lett., 74(11), 1591 (1999).

[ROB00] L.S. Robertson, K.S. Jones, L.M. Rubin and J. Jackson, J. Appl. Phys. 87(6), 2910 (2000).

[ROT90] J.A. Roth, G.L. Olson, D.C. Jacobson and J.M. Poate, Appl. Phys. Lett. 57(13) (1990).

[SED85] T.O. Sedgwick, Symp. Red. Temp. Proc. for VLSI, Fall Meet. Electrochem. Soc., (1985).

[SEI85] T.E. Seidel, D.J. Lischerner, C.S. Pai, R.V. Knoell, D.M. Maher and D.C. Jacobson, Nucl. Instr. Meth. Phys. B 7/8, 251, (1985).

[SEI94] M. Seibt, J. Imschweiler and H. A. Hefner, Mat. Res. Soc. Proc. 316, 167 (1994).

[SEM05] Semiconductor Industry Association. International Semiconductor Technology Roadmap. http://www.itrs.net/Common/2005ITRS/Home2005.htm (2005).

[SER87] M. Servidori, Z. Sourek, and S. Solmi, J. Appl. Phys. 62, 1723 (1987).

[SHI01] A. Shima, T. Jinbo, N. Natsuaki, J. Ushio, J.-H. Oh, K. Ono, and M. Oshima, J. Appl. Phys. 89, 3458 (2001).

[SHI85] Y.Shih, Ph.D. Dissertation., University of California, Berkeley (1985).

[SHI99] S. Shishiguchi, A.Mineji, T.Y. Matsuda and H.Kitajima, Electrochem. Soc. Symp. Proc. 99(10), 105 (1999).

[SHO03] W. Shockley, "Forming Semiconductive Devices by Ionic Bombardment," U.S. Patent 2,787,654.

[SOL00] S. Solmi, M. Bersani, M. Sbetti, J. L. Hansen and A. N. Larsen, J. Appl. Phys. 88, 4547 (2000).

[SOL86] S. Solmi, S. Guimaraes, E. Landi and P. Negrini, Semicond. Si. 86 (4), 583 (1986).

[SOL90] S. Solmi, E. Landi and F. Baruffaldi. J. Appl. Phys.68, 3250 (1990).

[SOL91] S. Solmi, F. Baruffaldi and R. Canteri, J. Appl. Phys. 69, 2135 (1991).

[SPA79] F. Spaepen and D. Turnball, Laser –Solid Interactions and Laser-Processing, editors S. Ferris et al. AIP Conf. Proc., 50, 73 (1979)

[STE70] H.J. Stein, F. Vook, D.K. Brice, J.A. Borders and S.T. Picraux, Rad. Eff., 6, 19 (1970).

[STO95] P.A. Stolk, H-J. Gossmann, D. J. Eaglesham, D. C. Jacobson, J. M. Poate and H. S. Luftman, Appl. Phys. Lett. 66 (5), 570 (1995).

[STO97] P.A. Stolk, H.-J. Gossmann, D. J. Eaglesham, D. C. Jacobson, C. S. Rafferty, G. H. Gilmer, M. Jaraı´z, J. M. Poate, H. S. Luftman and T. E. Haynes, J. Appl. Phys. 81 (9), (1997).

[STU02] G.C. Stuart, D.M. Camm, J. Cibere, L. Kaludjercic, S.L. Kervin, B. Lu, K.J. McDonnell and N. Tam, 10th IEEE International Conference of Advanced Thermal Processing of Semiconductors, pg. 77 (2002).

[SUN82a] I. Suni, G. Goltz, M.G. Grimaldi, M-A Nicolet and S.S. Lau, Appl. Phys. Lett., 40(3), 269 (1982).

[SUN82b] I. Suni, G. Goltz, M. G. Grimaldi, M-A. Nicolet and S.Lau, Thin Solid Films, 93, 171 (1982)

[SUN82c] I. Suni, G. Goltz, M. G. Grimaldi, M-A. Nicolet and S.Lau, Mat. Res. Soc. Pro., 10, 175 (1982)

[TAK94] S. Takeda, M. Kohyama, and K. Ibe, Phil. Mag. A 70, 287 (1994).

[TIM85] P.J. Timans, R.A. McMahon and H. Ahmed, Mat. Res. Soc. Proc., 45, 337 (1985).

[TIM86] P. J. Timans, R.A. McMahon and H. Ahmed, Mat. Res. Soc. Proc. 52, 123 (1986).

[TRU60] F.A. Trunbore, Bell System Tech. Jour., 39, 205 (1960).

[TUK72] K.N. Tu, S.I. Tan, P. Chaudhari, K. Lai and B.L. Crowder, J. Appl. Phys. 43, 4262, (1972).

[URA98] A. Ural, P. B. Griffin and J. D. Plummer, Appl. Phys. Lett., 79(26), 24, (2001).

[VAN89] P. VanDenabeele, K. Maex and R. De Kerrsmaecker, Mat. Res. Soc. Proc. 146, 316 (1989).

[VIC69] G.L. Vick and K. M. Whittle, J. Electrochem. Soc. 116, 1142 (1969).

[VOL26] M. Volmer and A. Weber, J. Phys. Chem., 119, 227, (1926).

[WAN01] H. C.-H. Wang, C.-C. Wang, C.-S. Chang, T. Wang, P. B. Griffin and C. H. Diaz, IEEE Electron Device Lett. 22,65 (2001).

[WAS83] J. Washburn, C.S. Murty, D.K. Sadana, P. Byrne, R. Gronsky, N. Cheung and R. Kilaas, Nucl. Inst. Meth., 209, 345 (1983).

[WIL84] J. S. Williams and J. M. Poate, *Ion Implantation and Beam Processing*, (Academic Press Australia 1984), p.15

[WIL96] D. B. Williams and C. B. Carter, *Transmission Electron Microscopy*, (Plenum Press, New York, NY, 1996), pp. 423-437.

[YAN01] S. Yang and M.O.Thompson, Mat. Res. Soc. Proc. 669, J7.4. (2001)

[ZHA95] L.H. Zhang, K. S. Jones, P. H. Chi and D. S. Simons, Appl. Phys. Lett. 67 (14), 2025, (1995).

[ZHU96] J. Zhu, T. D. de la Rubia, L. H. Yang, C. Mailhiot and G. H. Gilmer, Phys. Rev. B 54, 4741 (1996).

[ZIE00] J. F. Ziegler, *Ion Implantation Science and Technology* (Ion Implantation Technology Co., Edgewater, MD, 2000).

BIOGRAPHICAL SKETCH

Renata Camillo-Castillo was born in Sangre Grande, Trinidad and Tobago, on September 17th, 1974. She attended high school at St. Joseph's Convent, St. Joseph, in Trinidad from 1986 to 1993. In 1994 she commenced her tertiary education at the University of the West Indies, St. Augustine, Trinidad, in the Faculty of Engineering, from which she graduated in 1998 with a Bachelor of Science in chemical and process engineering, under the advisement of Dr. Hamid Farabi. Subsequently she joined Petrotrin, the national oil company of Trinidad and Tobago, as a process engineer. Her graduate work commenced in the field of electronic materials in the Department of materials science and engineering at the University of Florida in 2001. There she studied under Drs. Mark E. Law and Kevin S. Jones in the areas of ion implantation, dopant diffusion and activation for advanced silicon devices. She received her Master of Science in materials science and engineering in 2003. During her graduate career she conducted collaborative research at the Inter-University Micro Electronics Center (IMEC) in Leuven, Belgium, under the auspices of Dr. Karen Maex and Dr. Richard Lindsay. Upon receipt of her Doctor of Philosophy in materials science and engineering in May 2006, she will join IBM in Burlington, VT.